New Fabrication Strategies for Smart Window Prototype Devices Using Invisible Metal Mesh Electrodes

A Thesis

Submitted for the Degree of

Doctor of Philosophy

By

S. Kiruthika

Chemistry and Physics of Materials unit

Jawaharlal Nehru Centre for Advanced Scientific Research

(A Deemed University)

Bangalore – 560064 (INDIA)

May 2017

Dedicated to

Almighty for His Blessings

DECLARATION

I hereby declare that the thesis entitled "**New Fabrication Strategies for Smart Window Prototype Devices Using Invisible Metal Mesh Electrodes**" is an authentic record of research work carried out by me at the Chemistry and Physics of Materials Unit, Jawaharlal Nehru Centre for Advanced Scientific Research, Bangalore, India under the supervision of Professor **G. U. Kulkarni** and that it has not been submitted elsewhere for the award of any degree or diploma.

In keeping with the general practice in reporting scientific observations, due acknowledgment has been made whenever the work described is based on the findings of other investigators. Any omission that might have occurred due to oversight or error in judgment is regretted.

S. Kiruthika

CERTIFICATE

Certified that the work described in this thesis titled **"New Fabrication Strategies for Smart Window Prototype Devices Using Invisible Metal Mesh Electrodes"** has been carried out by **S. Kiruthika** at the Chemistry and Physics of Materials Unit, Jawaharlal Nehru Centre for Advanced Scientific Research, Bangalore, India under my supervision and that it has not been submitted elsewhere for the award of any degree or diploma.

Professor G. U. Kulkarni

(Research Supervisor)

ACKNOWLEDGEMENTS

First and foremost, I would like to thank my research supervisor ***Professor G. U. Kulkarni*** for his constant guidance throughout this research journey. I am very grateful to him for suggesting very interesting projects and encouraging and motivating me towards new explorations. His passion for doing research is a great motivation for me. The forum he created for research discussion is highly appreciable. I always admire the working style of him. Sir, you will ever remain as a role model on how to decide thoughtfully a scientific problem and to pursue and dissect it meaningfully. Also, he is the one who taught me to think beyond laboratory research and how to explore industrial demand in the field of study. I express my deep sense of gratitude and profound feeling of admiration for him.

Prof. C. N. R. Rao, a constant source of inspiration and it is always a great opportunity to listen to encouraging words about research by the legend. I learned more about him through my research supervisor, who himself is a great disciple of Prof. Rao.

I thank past and present ***Presidents of JNCASR*** for their immense support in various activities. It is a pleasure to thank the past and present ***Chairman of CPMU*** for allowing me to use department instrumentation facilities.

I thank all ***my collaborators***; Prof. Krishna Prasad, Prof. Geetha Nair, Dr. B. Radha, Dr. K. Narendra, Dr. N. Padmavathy, Dr. Shubra Singh, Dr. Ritu Gupta, Dr. Mallik, Dr. Ashutosh Singh, Mr. Ankush, Ms. Chaitali, Mr. Indrajit, Mr. Aman Anand, Ms. Swati Chakraborty, Ms. Madhavi, Ms. Vimala, Ms. Janani for their fruitful discussion and collaboration.

I thank all ***the faculty members of CPMU and NCU*** for their cordiality, especially my teachers, Prof. G. U. Kulkarni, Prof. A. Sundaresan, Prof. S. M. Shivaprasad, Prof. Ranjan Datta, Prof. Subi George, Prof. Govindaraju, Prof. Ujjal Gowtham, Prof. Ranjani Viswanatha and Prof. Sebastian C Peter for their courses. I thank Prof. S. N. Bhat for giving me an opportunity to help POCE students in chemistry lab.

Timely and ready assistance and also friendly attitude from ***technical staffs*** is greatly acknowledged. I thank Mrs. Selvi (FESEM), Mr. Srinath, Mr. Srinivas, Dr. S. Basavaraja (AFM), Mrs. Usha (TEM), Mr. Anil (XRD), Mr. Vasu (UV, IR, PL, TGA) and Mr. A. Srinivasa Rao for their invaluable technical assistance. Special thanks to Mrs. Vanitha and Mr. Sunil for their assistance in various activites. Mr. Dilip, Mr. Gowda and Mr. Peer are acknowledged for their assistance.

I am grateful to **my *past and present lab mates***, Dr. Radha, Dr. Narendra, Dr. Abhay, Dr. Ritu, Dr. Mallik, Dr. Ganga, Dr. Padmavathy, Dr. Rashmi, Dr. Umesh, Dr. Murali, Dr.Ashutosh, Dr. Shobin, Dr. Remya Govind and ***going to be Drs*** Sunil, Bharath, Chatali, Nikita, Rajashekhar, Ankush, Indrajit, Suman, Karthik, Sanjit, Amala, Veena Navneet, Swati, Prahlada, Thripurantaka, Veeresh, Govind, Ramya, Vandana, Dipa, Shikha, Janani,; POCE and summer students-Tripti, Guratinder, Aman, Vetri; visiting student Gugu for their support and friendly nature. A special note of thanks goes to, ***Ms. Amala and all my present lab mates for proof reading of the thesis***.

I thank the ***staff of academic and administrative*** section in JNC for their assistance, especially Dr. Princy and Mrs. Sukanya for their help and friendly nature. I also thank the ***library staffs*** for their help. I am thankful to the ***computer lab staffs*** and ***purchase office staffs***. ***Hostel staffs*** are gratefully thanked for their cooperation and help. I would like to thank ***Dhanvantri staffs*** for their timely help.

I thank ***JNCASR and DST-INSPIRE*** for residential, financial assistance and DST for providing facilities. I thank ***IGSTC*** for my fellowship. I acknowledge ***Indo-EU project*** for travel grant to attend meeting in Brussels.

I thank all ***my JNC friends cum siblings*** Gopal, Vijay & Vino, Suresh, Gowsica, Ram, Prabu & family, Senthil & family, Meha, Gangaru, Sel, Baki, Bheem, Pavithra, Gedda, Sanjit, Puttu, Karthik & Krutika, Rajaji, Thara, Susila, Shashi, Manoj, Swati, Shivaprasad, Sunita, Meenakshi, Divya for their wonderful friendship and unconditional love and affection. Special thanks to ***cheerful badminton friends***. I thank all my CPMU, NCU and TSU friends for memorable days in JNC. I thank all ***my teachers and well-wishers.*** Dr. Azhagan anna, Mrs. Lavanya, Mrs. Asin, Mrs. Aruna, Mrs. Devi, Dr. Sengoden and Dr. Sindhuja and other B.Sc and M.Sc friends for their constant encouragement.

Besides the research life, ***Prof. G. U. Kulkarni's and his family's*** personal care and affection are greatly acknowledged for providing me a home away from home. I thank Mrs. Indira Kulkarni, Teju and Poorna for their warmth and hospitality.

I would like to thank ***my parents*** (Mr. Shanmugam and Mrs. Renuga Devi), ***my husband*** (Mr. Jai)***, my grandparents, sisters*** (Mrs. Priya and Ms. Revathy), ***brothers*** (Aathy and Mr. KP) ***master Aakshay*** and ***other family members*** for their continuous and consistent, support and encouragements; otherwise I could have not come thus far. Last but not least I would like to thank ***Almighty for His Grace Blessings***.

Preface

The thesis work pertains to fabrication of new generation transparent conducting electrodes and transparent functional devices. It is organized into five chapters.

Chapter I introduces the concept of functional materials and their important properties. As examples of functional materials directly useful in devices, transparent conducting materials such as ultra-thin metal electrodes, metal wire networks, hybrid electrodes etc. are given. In the latter part, the scope of the thesis work is presented. **Chapter II** introduces characterization techniques used in the thesis work.

Chapter III deals with fabrication of transparent conducting electrodes (TCEs) using the crackle templating method. This chapter contains four sections. *Chapter IIIA* describes TCE fabrication using TiO_2 colloidal dispersion as crackle precursor. The prepared TCEs have been examined by optical microscopy, SEM, UV-vis spectroscopy as well as by adhesion tests. *Chapter IIIB* describes a solution based process for large area TCE fabrication. Commercially available crackle precursors such as paints have been used as they are inexpensive and stable. *Chapter IIIC* describes the spray and roll coating process for large throughput TCEs involving simple solution processes. *Chapter IIID* deals with the fabrication of hybrid transparent conducting electrodes in which the shortcomings of the bare metal meshes such as high peak-to-valley roughness, the presence of an electric field gradient away from the wires, are overcome with a coating of transparent and conducting metal oxide over the metal mesh. The TCEs thus formed exhibit optoelectronic properties superior to commercial indium tin oxide films and other alternatives.

Chapter IV describes the fabrication of a few functional transparent devices. Transparent electrodes can be made high temperatures by joule heating process. This heat may be used effectively in avoiding frost or fog on the TCE surface (*Chapter IVA*). The transparent heaters find many applications in smart glazing window technology as well. In *Chapters IVA and B*, aspects related to fabrication and device performance have been dealt with in respect of phase changing devices, thermochromic and liquid crystal devices where mesh electrodes serve as functional electrodes. In another application, the mesh electrodes act as potential current collector in transparent and electrochromic supercapacitors yielding high

areal capacitance while retaining high transmittance (*Chapter IVC and IVD*). Highly transparent UV photodetector was also fabricated using metal meshes and ZnO as the current collector and the photoconductive material, respectively (*Chapter IVE*).

Chapter V deals with the miscellaneous work. In the final pages, a summary of the thesis work and an outlook are provided.

Table of contents

Chapter IVD: Smart Electrochromic Supercapacitors

Chapter IVE: A Smart Window Based UV-Photodetector

Chapter V: Miscellaneous work

Chapter VA: Sun Baked Electrodes for Supercapacitors

Chapter VB: Highly Stable Supercapacitor Electrodes for Harsh Electrolytes

Acronyms

0D	Zero Dimension
1D	One Dimension
2D	Two dimension
3D	Three dimension
AC	Alternating Current
AFM	Atomic Force Microscope
Al_2O_3	Aluminium oxide
aq.	Aqueous
AZO	Aluminium doped Zinc Oxide
BOPP	Biaxially Oriented Polypropylene films
CA	Contact Angle
CD	Charge-Discharge
CdO	Cadmium oxide
CNT	Carbon Nanotubes
CP	Crackle Precursor/Crackle Patterns
CVD	Chemical Vapour Deposition
CV	Cyclic Voltammogram
DC	Direct Current
DI	Deionised
EBL	Electron beam Lithography
EC	Electrochromic
ED	Electron Diffraction
EDL	Electrochemical Double Layer
Fe_2O_3	Ferric Oxide
Fe_3O_4	Iron (II,III) Oxide
FESEM	Field Emission Scanning Electron Microscope
FOM	Figure of Merit
FTO	Fluorine doped Tin Oxide
GaN	Gallium nitride
HOPG	Highly Oriented Pyrolytic Graphite
InGaAs	Indium Gallium Arsenide

InGaZnO	Indium Gallium Zinc Oxide
ITO	Tin doped Indium oxide
JCPDSPDF	Joint Committee on Power diffraction Standards Power Diffraction Files
LCD	Liquid Crystal Display
LCE8	Liquid Crystal E8
LED	Light Emitting Diode
LSC	Luminescent Solar Concentrator
Micro	10^{-6} m
MgF_2	Magnesium Fluoride
MWNT	Multi Walled Carbon Nano- Tube
Nano	10^{-9} m
nc-Pd/C	nano crystalline Pd in carbon matrix
NIL	Nanoimprint Lithography
NIR	Near field Infrared Spectroscopy
NOA	Norland Optical Adhesive
NW	Nanowire
OLED	Organic Light Emitting Diode
OP	Optical Profiler
OSC	Organic Solar cell
PANI	Polyaniline
PC	Polycarbonate
PCM	Phase Changing Materials
PDMS	Polydimethylsiloxane
PDLC	Polymer dispersed Liquid Crystal
PEDOT:PSS	Poly(3,4- ethylenedioxythiophene) : poly (styrenesulfonate)
PET	Polyethylene terephthalate
PL	Photoluminescence
PMMA	Poly-methyl-methacrylate
PPY	Polypyrrole
PT	Polythiophene
PV	Photovoltaics
PVA	Poly vinyl alcohol
PVD	Physical Vapour Deposition
QD	Quantum Dot

R2R	Roll-to-roll
RF	Radio Frequency
R_{rms}	Root mean square roughness
R_s	Sheet resistance
RT	Room temperature
R2RNIL	Roll-to-roll Nanoimprint Lithography
SAED	Selected area electron diffraction
SAM	Self-assembled monolayers
SEM	Scanning electron microscopy
SERS	Surface Enhanced Raman Scattering
Si	Silicon
SiC	Silicon carbide
SiO_2	Silicon dioxide
SnO_2	Tin oxide
SP	Surface Plasmon
SPR	Surface Plasmon Resonance
STM	Scanning Tunnelling Microscopy
Superacid	Acidity > 100% pure sulphuric acid
SWNT	Single Walled Carbon Nanotubes
TBABr	Tetrabutylammonium Bromide
TOABr	Tetraoctylammonium Bromide
TCE	Transparent conducting electrodes
TEM	Transmission electron microscopy
TFT	Thin Film Transistor
TiO_2	Titanium dioxide
T%	Transmittance
UV	Ultraviolet
UV-vis	Ultraviolet-visible
UHV	Ultra-High Vacuum
UTMF	Ultra-Thin Metal Films
XPS	X-ray Photoelectron Spectroscopy
XRD	X-ray Diffraction
ZnO	Zinc Oxide

Chapter I

Introduction

IA Functional Materials

A material is something known for its properties and finds application accordingly. For instance, stone is the first material known to mankind which was used for hunting animals and protection in Stone Age (Figure I.1). Naturally available wood has played a crucial role in the history of civilization as fuel, weapons, and tools, the raw material for building constructions, papers, etc. Around 5000 BC, after the invention of fire, the first ceramic was made by sintering clay at high temperatures to increase the hardness of the material. Ceramics are mainly composed of inorganic oxides (Al_2O_3, SiO_2, Fe_3O_4), nitrides, carbides (SiC) and silicates.

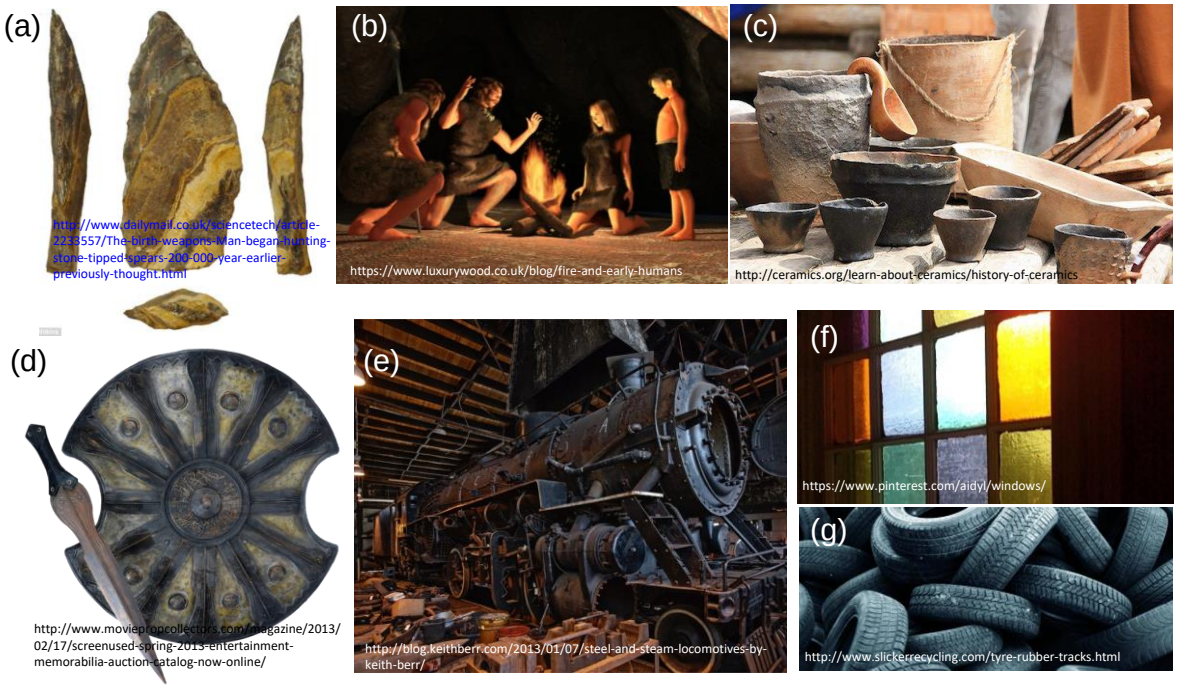

Figure I.1 Photographs of materials (stones, wood, ceramic, iron, steel, glass and rubber) useful for mankind. [References are given on the images]

In the Iron Age, metal tools and utensils were invented and helped in emerging several civilizations. The industrial revolution took place after the invention of steel, an alloy of the iron and carbon (Fe-C). Glass, an optically transparent material, was

used in windows and mirrors. The Space Age has brought composite materials which are durable as well as lightweight. The multi-phase composite materials are obtained by an artificial combination of various materials to attain properties which are absent in individual materials.

Functional materials are those which are attributed with the range of properties and sometimes combination of unique properties. In this aspect, nanomaterials have gained importance. Nano is a scale (= 10^{-9} m) that refers to one-billionth of the meter. When the material dimensions are confined to nm, surface to volume ratio of materials increase drastically leading to unusual properties that depend on the size of the system. For instance, the melting point of nanomaterials is much lower than the bulk due to low mean coordination number. Besides the size, shape and dimensionality (0D, 1D, 2D, and 3D) of nanomaterials also influence the properties.

Figure I.2 Examples of functional materials. (a) Carbon fiber reinforced racket, (b) concrete, (c) polymer sports shoes and (d) glass-fibre reinforced panels. [References are given on the images]

An example of functional nanomaterial composite is carbon fiber reinforced polymers which possess attractive properties such as high strength and stiffness, excellent fatigue resistance, high chemical and corrosion resistance, etc. (Figure I.2a). Another widely used composite material in day-to-day life is concrete, a composite of cement, water, sand, gravel and other admixtures such as fine SiO_2 particulates (Figure I.2b). In this era of light-weight materials, polymer-matrix composites are used for the fabrication of various equipment such as sporting goods, wheel chairs, aircraft items to name but a few. (Figure I.2c). Fiber reinforced glasses are used in space applications such as booms and antenna structures, mirror back structures etc. These glasses possess high thermal conductivity with increased strength, toughness and modulus (Figure I.2d). Due to high wear resistance and environmental degradation resistance, it is used in gas turbine engine components.

The surface of materials can be tuned for controlled wetting, adhesion, chemical resistance, etc. by various protective coatings. Commonly known paints and lacquer coatings are mostly used for protecting and decorating the surface. For instance, adhesion properties on the surface can be tuned either by non-stick PTFE or by release/primer coatings. Protective coatings with hydrophobic paint and concrete cement finish help in bringing waterproofing and damp proofing in buildings. In this context, self-assembled monolayers (SAMs) are unique which are formed spontaneously by surface adsorption of organic molecules. The transparent conductive coating is a specialty coating on the surface of transparent substrates which is vital for many optoelectronic devices.

IB Transparent Conducting Materials

A transparent conductor is a key component of any optoelectronic or transparent device. With increasing number of large area applications, there is growing demand to replace the conventional oxide based transparent conducting films with nanomaterials, primarily to reduce the cost. This introduction deals with a range of materials and processes forming new generation transparent electrodes while giving some insight into the cost.

In a scenario, where light photons have to traverse in or out of an active material, it is mandatory that the electrode(s) hosting the active material is kept transparent to

light photons. Thus, optoelectronic devices such as display screens use transparent conducting materials to carry electrical signals while making the display visible [1]. In a touchscreen, on the other hand, the transparent conductors not only keep the display visible but also translate touch into electrical signals for further processing [2]. In new generation solar cells such as organic and dye-sensitized cells, the transparent conductors while allowing (light) photons to fall on the active layer, extract charge carriers generated due to the photovoltaic effect [3,4]. There are non-optoelectronic (optoelectronic) applications as well where transparent conductors are required. In defogging or defrosting applications, a transparent conducting material is joule heated to make the surface stand above the dew or frost point, respectively [5]. It is becoming fashionable to make conventional electronics transparent with the aid of transparent conductors leading to transparent electronics, be it a gas sensor [6], H_2 catalyst [7], lithium-ion battery [8], flexible capacitor [9], supercapacitor [10–11] or charge trap memory [12].

A transparent electrode typically consists of a transparent conducting material coated on a transparent substrate such as glass or PET. Conventionally, tin-doped indium oxide (ITO) sputtered on the substrate such as glass is used practically in all currently existing devices. A well-prepared film of ITO exhibits excellent optoelectronic properties, the transmittance of over 90% and sheet resistance (R_S) of 10 Ω/sq, which explains its widespread use [1].

The TCEs are ranked by evaluating the figure of merit (FOM) from the ratio of optical and DC conductivities, σ_{OP}/σ_{DC} that relates transmission with sheet resistance (R_S). The electrical and optical properties of these electrodes are optimized by engineering the material design and architecture. Commonly, parameters such as the thickness of the film, network density, area occupied by the material, % of conducting phase, the fractal dimension of the network are varied for tuning the transmittance and resistance of a given TCE [13a]. The demand for transparent electrodes is becoming huge due to increasing production with newer and newer products being added to the consumer list. Parallelly, the active user area within a product is also increasing. The limited abundance of indium and the process cost towards its extraction and deposition are indeed the stumble blocks in the progress of new

industrial products based on transparent electrodes. In addition, high brittleness of ITO films makes it implausible to adapt to futuristic flexible electronics. The above issues have given rise to the high impetus to alternate materials and methods to produce transparent conducting electrodes (TCE) with the clear focus on making larger area electrodes at an affordable cost [13b]. The new generation materials that have emerged in the last few years can be classified broadly into ultra-thin conducting materials and conducting networks. This introduction essentially covers all the above topics environmentally benign TCEs for next generation flexible and low weight optoelectronic devices. The TCEs can be broadly classified as ultra-thin conducting electrodes, conducting networks and hybrid as shown in the schematic *tree* below (Scheme I.1).

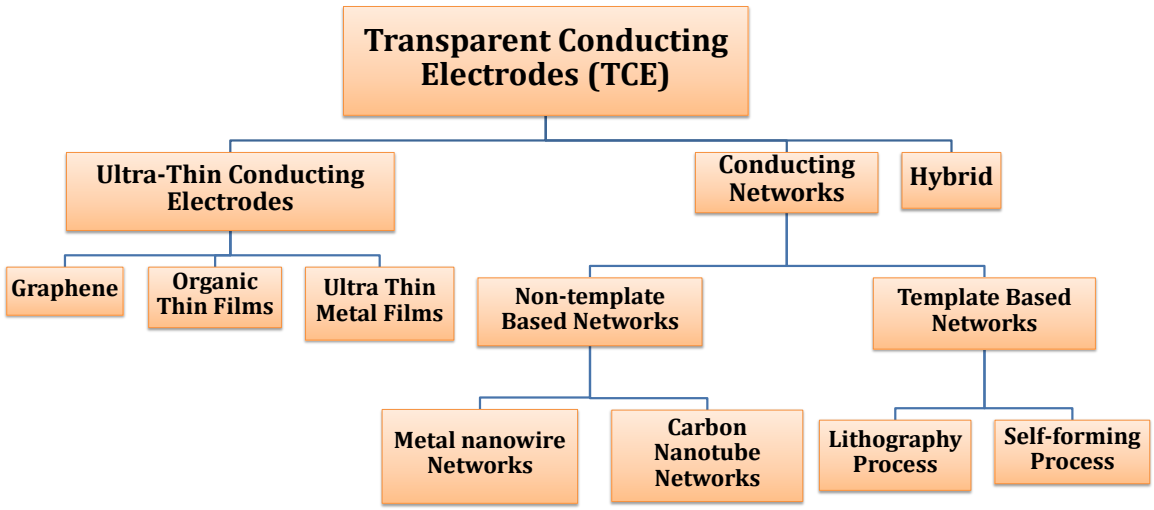

Scheme I.1 Classification of transparent conducting electrodes.

IB.1 ULTRA-THIN CONDUCTING ELECTRODES

Graphene as a transparent conductor

Graphene is one carbon atom thick two dimensional sheet with sp^2-hybridization exhibiting extraordinary thermal, electrical and mechanical properties due to long range π-conjugation [14]. Novoselov *et al*. obtained single-layer graphene by mechanical exfoliation of highly oriented pyrolytic graphite (HOPG) [15]. Further, various physical and chemical routes have been established to fabricate graphene [16]. First ever application proposed for single layer graphene has been a transparent

conductor as it can transmit about 97.7% of visible light while sheet resistance being reasonably low (60 Ω/sq) [17]. The first demonstration of graphene based transparent electrodes was by Kang *et al*., in which reduced graphene oxide film used as TCE was shown to exhibit 75% transmittance with the sheet resistance of 0.9 kΩ/sq. However, the performance of solar cells made out of this electrode was poorer compared to the standard ITO-based devices [18].

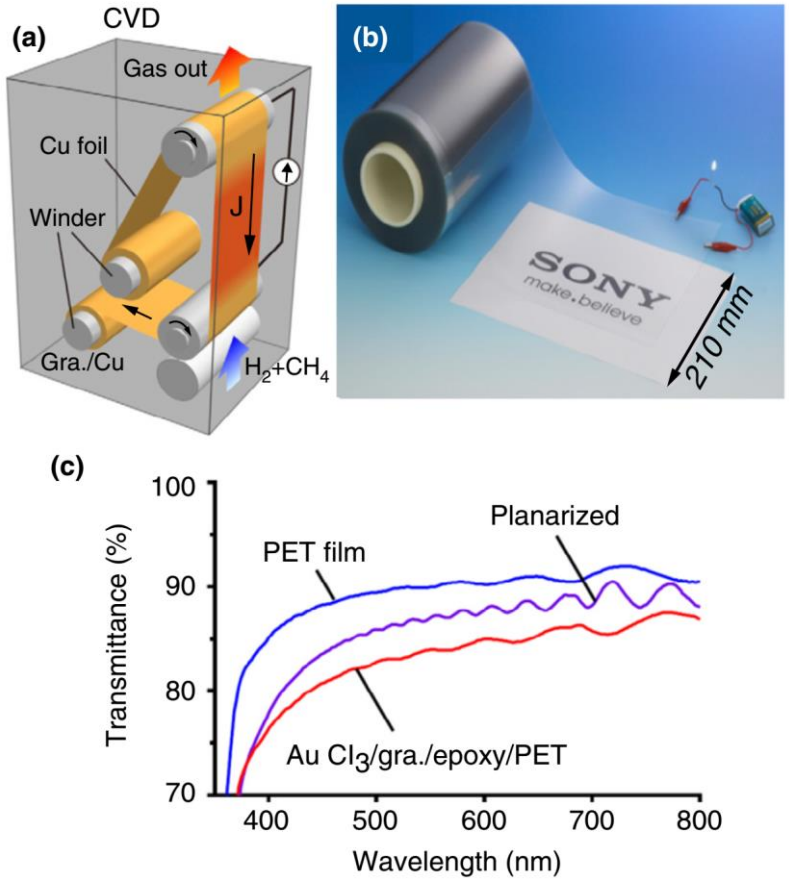

Figure I.3 Roll-to-roll synthesis of graphene. (a) Schematic illustration of the roll-to-roll synthesis of graphene on Cu foil (Gra./Cu). Stainless steel vacuum chamber with current-feeding electrode rollers to joule heat Cu foil. The precursor gasses (CH_4 and H_2) are introduced into a chamber (1000 Pa) where Cu foil (230 mm wide, >100 m long, 36 μm thick, >99.9% pure) is selectively joule heated to 1000 °C. The Cu foil moves with the velocity of 0.1 m/min. (b) Photograph of a roll of graphene/epoxy/ PET film. The graphene/epoxy width is marked in the photograph. The film was later doped with $AuCl_3$. Optical transmittance of PET film (blue), $AuCl_3$/graphene/epoxy/PET (red) and planarized film, purple color (PET/Adhesive/$AuCl_3$/graphene/ epoxy/PET) is shown in (c).

The graphene-based transparent electrodes find applications in several (flexible) lightweight optoelectronic devices [19]. However, fabricating them over a large area is quite challenging. Iijima and coworkers have realized 30 inch graphene film by chemical vapor deposition method (CVD) [20]. Recently, Hobara and coworkers successfully prepared 100 m long high-quality graphene using a roll-to-roll CVD technique (see Figure I.3a) [21]. As the Cu foil was selectively annealed, there was less heat load on the system. Thus, the CVD process was quite stable throughout the experiment (>16 hours). The photograph of thus formed roll of the TCE (graphene/epoxy/PET film) is shown in Figure I.3b whose sheet resistance is reported to be 500 Ω/sq. The sheet resistance was brought down to 250 Ω/sq by wet chemical doping of graphene with the $AuCl_3$ solution but of course at the cost of transmittance (Figure 1.3c). Ni *et al*. have achieved R_S of 120 Ω/sq with 95% transmittance by doping graphene with non-volatile ferroelectric polymers [22]. The reliability of graphene-based transparent electrodes for practical applications has been analyzed recently by Shi *et al*. [23]. Although high-quality graphene with roll-to-roll CVD fabrication is a success, its large scale production at low cost is still at large.

Organic thin films as transparent conductor

Another promising transparent electrode material for flexible and stretchable devices which can be coated as a thin film is poly(3,4 ethylenedioxythiophene) (PEDOT), discovered by Heywang *et al*. [24]. Upon polymerization with poly-(styrenesulfonate) (PSS), a polyanion, it forms an intrinsically conducting polymer (PEDOT:PSS), highly preferred as its work function (5–5.2 eV) is electronically suited for optoelectronic applications. Among other organic conducting polymers such as polyaniline (PANI), polypyrrole (PPY) and polythiophenes (PT), PEDOT:PSS is more promising. However, its low intrinsic conductivity ($\sim 10^{-3}$–10^{-4} S cm^{-1}) is a matter of concern. The conductivity can be enhanced further by doping with high boiling polar solvents termed as 'secondary dopants', though the exact mechanism of the enhancement is yet to be understood [25]. In the literature, dimethyl sulfoxide (DMSO), ethylene glycol (EG), diethylene glycol, sorbitol, sulphuric acid (H_2SO_4), zonyl, etc. have been used to improve PEDOT:PSS conductivity [26–28]. For example, the sheet resistance of zonyl doped PEDOT:PSS on the poly(dimethylsiloxane)

substrate was 42 Ω/sq with 82% transmittance. Zonyl besides improving conductivity also enhances wettability even on hydrophobic surfaces [28]. In another report, the non-ionic surfactant (Triton X-100) was used to produce the conformal coating on hydrophobic substrates by reducing the surface tension of the polymer solution. Also, it induces the formation of nanofibrils of PEDOT which increases the mechanical stability of the polymer and thereby, of the devices [29]. Extending the electrode formation over the large area by the simple roll-to-roll process has also been already realized and commercialized [30]. The reduction in electrical conductivity of polymers upon exposure to humidity, high temperature, and UV light are vital issues inhibiting practical implementation of conducting polymers [31].

Ultra- thin metal films (UTMF) as transparent conductors

Highly conducting noble metal films of 1–5 nm thickness on mica substrate were reported as early as the 1970s. At such small thicknesses, metal films tend to be optically quite transparent, but are exceptionally fragile ending up with high sheet resistances. Depositing a bimetal layer on a transparent substrate such as glass is shown to improve the mechanical stability of the TCE. For instance, a sub-nm thick Ag layer yielded a well conducting Au overlayer with the total thickness of only 3.2 nm. Later, Pt was used as nucleating layer for better adhesion and stability [32]. Briggs and coworkers demonstrated that depositing gold (7 nm) over pre-treated (3-mercaptopropyl(methyl)dimethoxysilane) substrate led to lower surface roughness. Besides improving adhesion, it provides better average transmittance (75%) and the low sheet resistance of 20 Ω/sq [33]. Such thin metal films possess great advantage of being compatible with flexible devices as metals by nature are malleable and ductile. While UTMF can be a potential substitute for ITO, corrosion and oxidation of the metal (like Ag) in the ambient atmosphere tend to deteriorate transmittance and conductivity. Among many proposed permeation blocking layers, thin Ni layer is shown to serve well as a stable, flexible barrier layer [34]. In another report, 7 nm Cu with Al shell of 0.8 nm served as low work function window electrodes for OPV with 65% transmittance at 550 nm with the sheet resistance of 15.7 Ω/sq [35]. UTMF were even sandwiched between metal oxide thin films to fabricate better performing TCEs.

This method of fabricating TCE is highly cost effective since it can be extended for large scale roll-to-roll processes as well.

IB.2 CONDUCTING NETWORKS

Unlike thin conducting electrodes, in network structures, only designated paths conduct electricity while the rest of the regions transmit light. These can be classified into non-template based networks and template based networks. Naturally, in template-based methods, the formation of conducting paths is guided by lithography processes, and the paths tend to remain in a plane with seamless junctions, but suffer from diffraction effects due to the orderliness of the patterns. In contrast, the non-template based networks are usually formed by brute-force, and therefore, the conducting paths are typically random in nature forming cross-bar junctions and therefore, the electrical conduction takes place mainly through the percolative paths. There are many theoretical studies to relate their behavior to bulk-like systems such as continuous thin films. For networks with T > 90%, the expected bulk-like behavior does not occur. The main reason is that below a critical density, termed as percolation threshold, the network conductivity decreases drastically with the decrease in the density of the wires and therefore, the conduction can only be described by percolation theory. By increasing the wire lengths or the number of wire junctions, the conductivity is seen to increase due to increasing conduction paths, following a percolation scaling law [36]. Such theoretical treatments have helped researchers to optimize conditions for nanowire deposition.

IB.2.1 NON-TEMPLATE BASED NETWORKS

Metal nanowire networks

Metal nanowires prepared by simple solution processes are deposited onto large area transparent substrates by various coating techniques (rod, spray, drop, etc.). The density and length of nanowires decide the trade-off between optical transmittance and sheet resistance. Thus, longer nanowires even with low wire density provide well-conducting network with high transmittance [37]. The key merits of metal nanowires are simple solution processing, large area amenability, stability towards flexing and highly tunable optoelectronic properties. Among metals, Ag is highly

conducting with the lowest resistivity (1.67 nΩ. m). Coleman and coworkers were the first to use Ag nanowire networks as transparent electrodes and achieved 85% transmittance with sheet resistance of 13 Ω/sq [36].

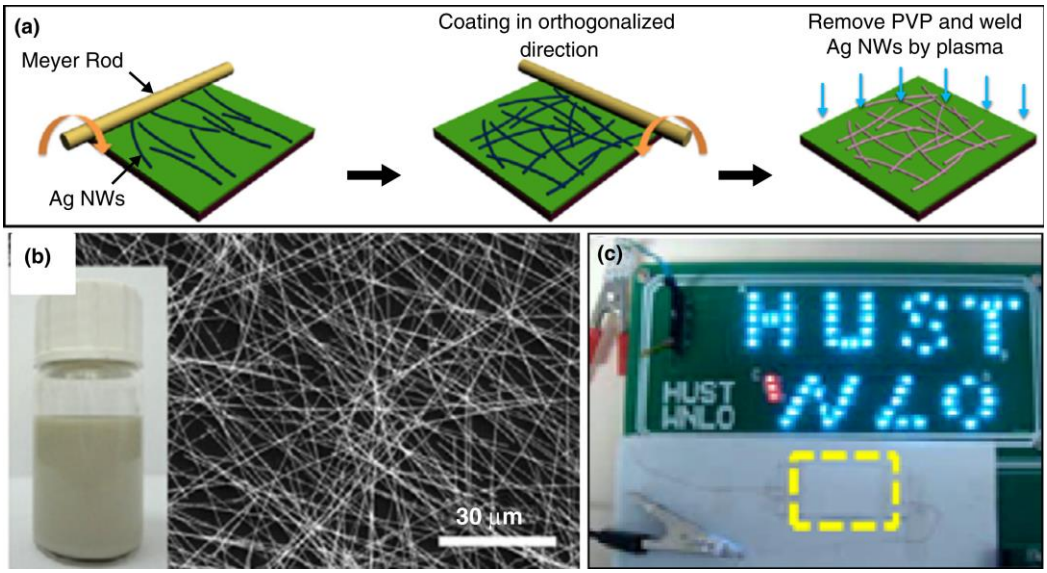

Figure I.4 Meyer rod coating method to fabricate Ag nanowire-based TCE. (a) Schematic of the process and SEM image of silver nanowire network (b). Inset in (b) is a photograph of their suspensions in alcohol. (c) An OLED device fabricated using Ag nanowire TCE.

Many researches have attempted to minimize junction resistances of nanowire networks (Figure I.4) [38–40] by decreasing the density of the junctions or by post annealing or plasmonic welding. Flexible organic solar cells, fabricated with Ag nanowires were highly stable even to a bending radius of 200 μm [41]. As process costs involved are minimal in the case of solution processed Ag nanowires, roll-to-roll processing can be easily realized. Although resistivity of Cu (1.59 nΩ m) is about the same as that of Ag, in terms of abundance and cost, it outdoes Ag. In the last half-decade, Cu nanowires have emerged as a potential candidate for next generation TCEs for the realization of low cost and flexible optoelectronic devices [42]. Wiley and coworkers have developed a simple solution route to prepare the large quantity of Cu nanowires and shown that thus fabricated TCE has transmittance and the sheet resistance of 67% and 61 Ω/sq, respectively [43]. The aggregation problem of nanowires along with its shorter lengths (10 ± 3 μm) and larger diameters (90 ± 10

nm) have been the main reasons for its poor performances. Modified processes have been reported to synthesize longer (>20 μm) and thinner (<60 nm) Cu nanowires and transmittance of 85% with the sheet resistance of 30 Ω/sq have been achieved [44,45]. However, highly oxidizing nature of the Cu surface and its reddish orange haze hinder its practical implications in display devices. Alloying Ni with Cu does provide the solution to abovementioned problems, however, with some loss in transmittance due to the increase in diameter of nanowires [46]. Ferromagnetic Ni shell is shown to assist in self-assembling Cu nanowires with the aid of a guiding magnetic field [47]. A more effective way to improve the stability towards oxidation was offered by forming transparent oxide shell over Cu nanowires, without affecting the transmittance [48]. Im *et al*. demonstrated that embedding Cu nanowires in polymers provides the smoother surface with high thermal/dimensional stability and also improved adhesion to the substrate [49]. On the other hand, other metal nanowires such as Au has been tried out as TCEs [50], but those are quite expensive.

Carbon nanotube networks

Carbon nanotubes (CNTs) are known to exhibit excellent electrical, optical and mechanical properties. Synthesis procedures yield CNTs with varieties of tube numbers, diameters, lengths, and chiralities along with the mixture of amorphous or non-tubular carbon and catalyst particles. Obtaining well-defined CNTs in large scale is the major challenge for real applications [51]. CNT based transparent electrodes have been fabricated by dry transfer as well as solution based methods. The dry or solvent-less method to fabricate CNT electrodes using vertically grown MWNT was pioneered by Baughman's group [52]. The electrodes fabricated using solution methods are more promising for industrial scale process. Falco *et al*. have fabricated SWCNT-based TCE with low surface roughness by a spray coating process, and achieved the sheet resistance of 160 Ω/sq with 84% transmittance [53]. The high sheet resistances resulting from poor electrical contact between nanotube network were resolved by exfoliation/doping by the superacid (60 Ω/sq and 90.9%) [54]. Limited environmental stability of CNT networks has prevented its practical applications.

IB.2.2 TEMPLATE BASED NETWORKS

Lithography processes

In these methods, the conducting feature in the network is produced by various printing and lithography processes. Using a maskless direct laser writing on a film of Ag nanoparticles, Ag grid patterns were produced which showed high transmittance (>85%) and low sheet resistance (30 Ω/sq) [55]. Lewis and coworkers developed a concentrated Ag nanoparticle ink for direct writing. Thus formed electrodes have shown the optical transmittance of 94% [56]. The overlapping ring pattern of Ag nanoparticles was obtained by inkjet printing [57] for making a TCE. Interconnected Cu mesh structure realized through polystyrene microsphere lithography has shown excellent robustness towards thermal, bending and abrasion tests [58]. Grayscale xerographic lithography was adopted to fabricate Ag TCE by spreading Ag ink over toner patterned region. After thermal curing of Ag ink and removal of the toner, thus obtained electrodes have shown 72% transmittance [59]. Krebs and coworkers have fabricated a promising hybrid TCE with printed silver grids on polymer substrates interlaced with PEDOT:PSS and ZnO layers, termed as flextrode [60]. These electrodes exhibit low sheet resistance (10 Ω/sq) with the transmittance of 60%. Importantly, the TCE can be processed at a high speed of 10 m/min. Another possible technique to realize metallic patterns over rigid glass/flexible PET is nanoimprint lithography (NIL) which makes use of a hard mold [61]. Such lithography techniques involve multistep processes, and the instrumentation is usually expensive. However, few attempts have been made to realize fabrication using continuous roll-to-roll nanoimprint lithography (R2RNIL) [62].

Self-forming process

Different innovative techniques have recently evolved under this category of transparent conducting electrodes. This involves the formation of uncontrolled junctionless metal wire network in a random process. For example, bubble template method [63], inorganic crystal growth template [64], interconnected coffee rings [57] have been observed to form itself resulting in patterns that are utilized for TCE fabrication. However, these are limited to small areas with limited success. Using low-

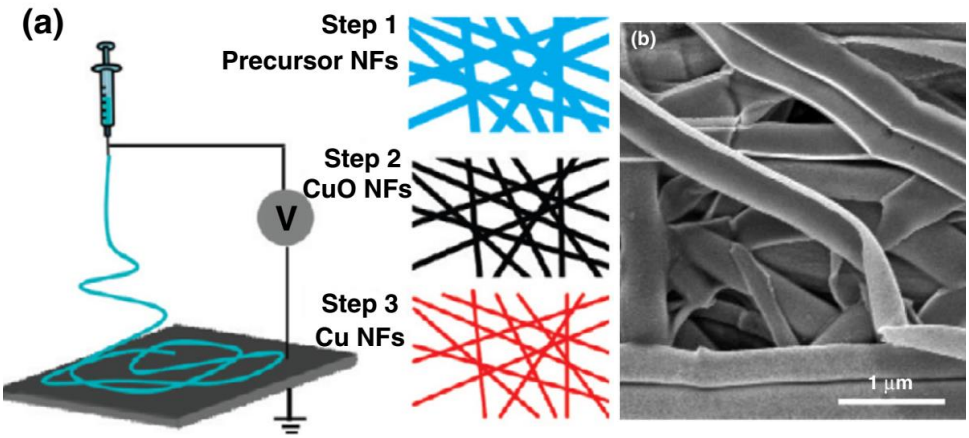

Figure I.5 Fabrication of TCE using electrospun process. (a) Schematic of an electrospinning process with syringe pump is shown on left side whereas systematic process steps are shown right. SEM image of Ag nanotroughs clearly shows its concave shape (b).

cost and scalable electrospinning process, ultralong polymeric fibers with nanoscale dimension can be synthesized (see Figure I.5a). By successive calcination steps, Cu fiber networks have been obtained [65,66]. In another work, fiber networks were electrospun, and metals of choice were deposited onto fibers depending on the application. The dissolution of fiber material resulted in the formation of metal nanotroughs (see Figure I.5b) with excellent optoelectronic properties and mechanical stability [67]. Combination of the electrospun process and simple electroless deposition technique was employed to obtain metal wire network over the large area [68].

IB.3 HYBRID TCEs

As evident from the above sections, ultra- thin graphene, organic and metal films possess high electrical uniformity over the TCE but suffer from high sheet resistance. On the other hand, metal and carbon nanowires and metal meshes afford low sheet resistance with poor electrical uniformity on its surface. In this context, the combination of metal meshes with a thin layer of conducing films improves the TCE performance. Few such examples are shown in Figure I.6. Such metal wire network based hybrid TCEs are fabricated following different approaches: (1) by introducing

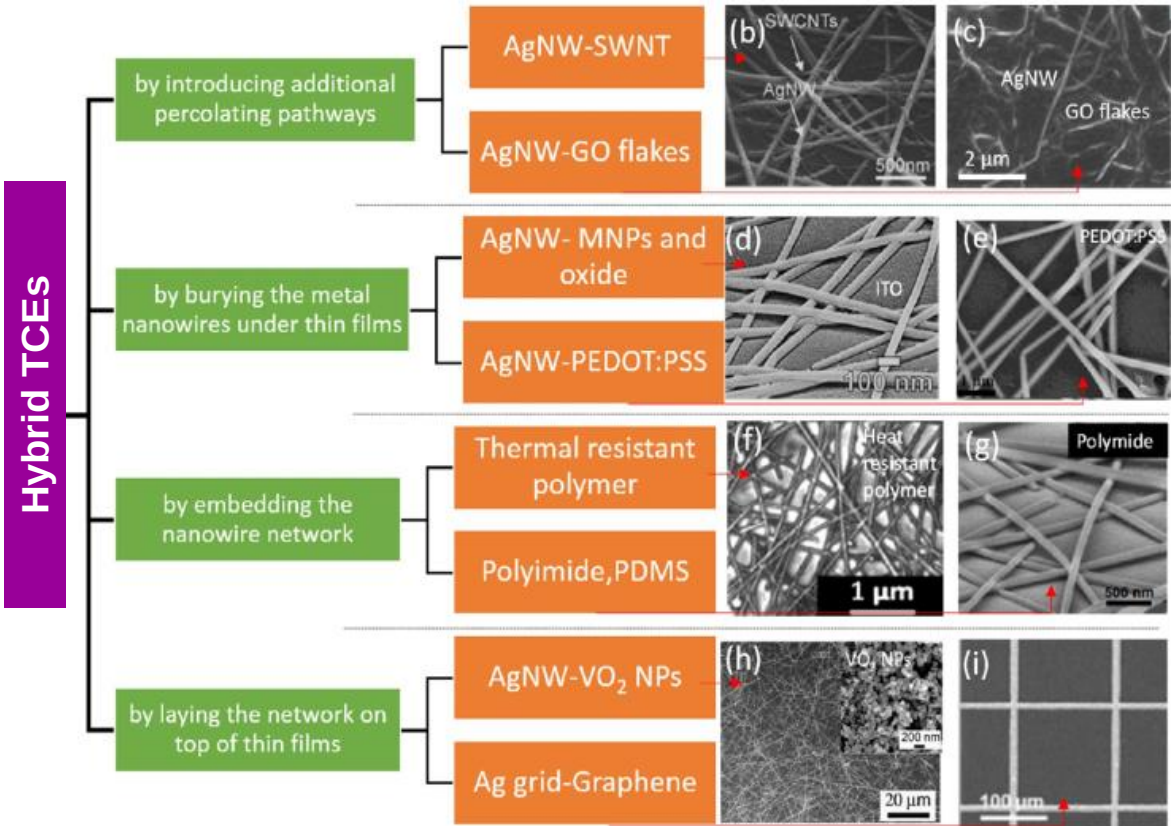

Figure I.6 (a) Schematic categorizing the hybrid TCE (b) SWNTs-AgNW, (c) Graphene oxide flakes- AgNW, (d) ITO-AgNW, (e) PEDOT:PSS-AgNW, (f) Heat resistant polymer-AgNW, (g) Polyimide-AgNW, (h) VO_2 nanoparticles (NP)-AgNW and (i) Graphene-Ag grid.

additional percolating conducting pathways using CNTs or graphene flakes, (2) by burying the wire network under thin films of metal oxides or polymers, (3) by embedding the wire network in insulating polymers or (4) by laying the network on top of thin films. These approaches not only lower the overall R_S of the nanowire networks but also result in homogeneous electric field on the surface. Few examples of hybrid TCE based on abovementioned approaches are shown in Figure I.6. An AgNW/ SWNT based hybrid TCE (Figure I.6a) is proposed as an electrically robust and scalable method for transparent conductors [69,70]. By the addition of functionalized SWNTs (2.5 wt %) to Ag nanowires in solution, a hybrid TCE has been realized [69]. Importantly, SWNTs tend to connect with AgNWs conformably leading to the higher contact area (see Figure I.6b) unlike junctions among the AgNWs. The individual AgNWs are more rigid as compared with SWNTs, and as a result, the

contact area varies largely among the AgNW junctions. Moreover, few AgNW junctions may not even be connected in the network as shown in Figure I.6b. In spite of a large number of junctions in the network, only a few percolative current paths are possible, whereas in the case of AgNW/SWNT based TCEs, the junctions are engineered to have more contact area leading to lesser junction resistance. Zhang *et al*. [71] reported another strategy where AgNWs were first mixed with small and large flakes of reduced graphene oxide (rSGO, rLGO) and vacuum filtered to obtain a continuous film (Figure I.6c). Graphene oxide and AgNW hybrid electrodes formed a continuous film instead of a network. The large graphene oxide flakes spanning over a few micrometers may connect several AgNWs simultaneously, thus enhancing both electrical and thermal energy transport. GO flakes also prevent areal oxidation and melting of AgNWs. Recently, a hybrid heater of AgNW and graphene oxide film was fabricated by electrostatic interaction between charged layers and AgNW [72]. The device was transparent up to 90% with a resistance of ~11 Ω/sq. Following approach 2, Cheong *et al*. [73] covered the Ag nanowire network using Ag nanoparticles and sputtered ITO films (Figure I.6d). Similarly, in another example, an Ag mesh fabricated using microsphere lithography was obtained as buried under ITO [74]. PEDOT:PSS is a conducting polymer that can also be easily spin coated for filling the voids in a nanowire network. Ji *et al*. [75] coated a PEDOT:PSS layer over an Ag nanowire network film and reduced its R_S to 4 Ω/sq (Figure I.6e). PEDOT:PSS is highly efficient in redistributing the heat from the hot wires, resulting in uniform temperature distribution [76]. Li *et al*. [77] have designed heat-resistant polymers that can tolerate high temperatures at low operation voltages. The heat resistant polymer is bonded to the AgNW network as shown in Figure I.6f. In another attempt, Lu *et al*. [78] embedded the AgNWs in polyimide resulting in a hybrid TCE (Figure I.6g). This resulted in excellent mechanical and thermal stability. In another study, a functional thermo-electrochromic heater was fabricated by coating a layer of VO_2 nanoparticles on Ag nanowires (Figure I.6h) [79]. A large area hybrid TCE has been fabricated by the printing of Ag mesh over a graphene film (Figure I.6i) resulting in R_S of ~4 Ω/sq and transmittance of 78% [80].

Table I.1 Parameters for optimum designing of materials for transparent conductors[#].

Features	ITO and oxides	CNTs	Graphene	Metal nanowires	hybrid
Sheet resistance	****	***	***	**	*
Transmittance	***	***	****	****	***
Haze	**	*	*	***	**
Roughness	**	****	*	***	*
Processing Cost	**	**	***	*	**

[#] The number of asterisks indicates relative magnitude of the property.

IC Scope of the thesis

An ideal transparent conductor should have the high transmittance (~ 90%), low sheet resistance, low haze, zero color, highly flexible and stable towards all environmental conditions, feasible for large area fabrication and should exhibit uniformity in properties such as R_S, T% over the large area. The discussion presented in the previous section clearly implies that most conventional ITO and other oxides and all recently developed alternatives such as graphene, CNT, etc. suffer from many deficiencies which are summarized in Table I.1. The thesis explores new processes on how all the above can be addressed effectively. Much of it has been possible due to the newly developed crackle template method which has the capability to produce transparent conductors with high transmittance, low sheet resistance, and low haze. Having made such transparent conductors using the crackle template method, various device fabrications have been tried out as part of the thesis work.

References

1. U. Betz, M. Kharrazi Olsson, J. Marthy, F. Escolá, F. Atamny, Thin films engineering of indium tin oxide: Large area flat panel displays application, *Surf.Coat. Technol.,* 2006, **200**, 5751-5759.

2. C-H. Hong, J-H. Shin, B-K. Ju, K-H. Kim, N-M. Park, B-S. Kim, W-S. Cheong, Index-matched indium tin oxide electrodes for capacitive touch screen panel applications, *J. Nanosci. Nanotechnol.,* 2013,**1**,7756-7759.

3. CG. Granqvist, Transparent conductors as solar energy materials, A panoramic review, *Sol. Energy Mater. Sol. Cells.,* 2007, **91**,1529-1598.

4. FC. Krebs, SA. Gevorgyan, J. Alstrup, A roll-to-roll process to flexible polymer solar cells: model studies, manufacture and operational stability studies, *J. Mater. Chem.,* 2009, **19,**5442-5451.

5. K. Im, K. Cho, K. Kwak, J. Kim, S. Kim, Flexible transparent heaters with heating films made of indium tin oxide nanoparticles, *J. Nanosci. Nanotechnol.,* 2013,**13**,3519-3521.

6. H. Choi, JS. Choi, J-S. Kim, J-H. Choe, KH. Chung, J-W. Shin, JT. Kim, D-H. Youn, K-C. Kim, J-I. Lee, *et al*., Flexible and transparent gas molecule sensor integrated with sensing and heating graphene layers, *Small.,* 2014,**10**,3685-3691.

7. Z. Chen, S. Ye, AR. Wilson, Y-C. Ha, BJ. Wiley, Optically transparent hydrogen evolution catalysts made from networks of copper-platinum core-shell nanowires, *Energy Environ. Sci.* 2014.,**7**,1461-1467.

8. Y. Yang, S. Jeong, L. Hu, H. Wu, SW. Lee, Y. Cui, Transparent lithium-ion batteries, *Proc. Natl. Acad. Sci.,* 2011, **108**,13013-13018.

9. T. Chen,H. Peng, M. Durstock, L. Dai, High-performance transparent and stretchable all solid supercapacitors based on highly aligned carbon nanotube sheets, *Sci. Rep.,*2014*,* **4.**

10. T. Chen, Y. Xue, AK. Roy, L. Dai, Transparent and stretchable high-performance supercapacitors based on wrinkled graphene electrodes, *ACS Nano.,* 2014,**8**,1039-1046.

11. HY. Jung, MB. Karimi, MG. Hahm, PM. Ajayan, YJ. Jung, Transparent, flexible supercapacitors from nano-engineered carbon films*., Sci. Rep.* 2012,**2**.

12. SM. Kim, EB. Song, S. Lee, J. Zhu, DH. Seo, M. Mecklenburg, S. Seo, KL. Wang, Transparent and flexible graphene charge-trap memory, *ACS Nano* 2012., **6**:7879-7884.

13. (a) G. Zhu, WQ. Yang,, T. Zhang, Q. Jing, J. Chen, Y. S. Zhou, P. Bai, Z. L. Wang,, Self-Powered, Ultrasensitive, Flexible Tactile Sensors Based on Contact Electrification., *Nano Lett.*2014, **14,** 3208- 3213. (b) S. Ye, AR. Rathmell, Z. Chen, IE. Stewart, BJ. Wiley**,** Metal nanowire networks: the next generation of transparent conductors., *Adv. Mater.,* 2014,**26**,6670-6687.

14. MJ. Allen, VC. Tung, RB. Kaner, Honeycomb carbon: a review of graphene, *Chem. Rev.,* 2009, **110**:132-145.

15. KS. Novoselov, AK. Geim, SV. Morozov, D. Jiang, Y. Zhang, SV. Dubonos, IV. Grigorieva, AA. Firsov, Electric field effect in atomically thin carbon films. *Science* 2004, **306**,666-669.

16. A. Reina, X. Jia, J. Ho, D. Nezich, H. Son, V. Bulovic, MS. Dresselhaus, J. Kong, Large area, few-layer graphene films on arbitrary substrates by chemical vapor deposition, *Nano Lett.,* 2008, **9**, 30-35.

17. RR. Nair, P. Blake, AN. Grigorenko, KS. Novoselov, TJ. Booth, TS. tauber, NMR. Peres, AK. Geim, Fine structure constant defines visual transparency of graphene, *Science* 2008, **320**,1308.

18. X. Wang, L. Zhi, K. Müllen, Transparent, conductive graphene electrodes for dye-sensitized solar cells, *Nano Lett.,* 2007, **8**,323-327.

19. K. Rana, J. Singh, J-H. Ahn, A graphene-based transparent electrode for use in flexible optoelectronic devices, *J. Mater. Chem. C* 2014*,* **2**,2646-2656.

20. S. Bae, H. Kim, Y. Lee, X. Xu, J-S. Park, Y. Zheng, J. Balakrishnan, T. Lei, H. Ri Kim, YI. Song, *et al*., Roll-to-roll production of 30-inch graphene films for transparent electrodes, *Nat Nano* 2010*,* **5**,574-578.

21. T. Kobayashi, M. Bando, N. Kimura, K. Shimizu, K. Kadono, N. Umezu, K. Miyahara, S. Hayazaki, S. Nagai, Y. Mizuguchi, *et al*., Production of a 100-m-long high-quality graphene transparent conductive film by roll-to-roll chemical vapor deposition and transfer process, *Appl. Phys. Lett.,* 2013, **102**,023112.

22. G-X. Ni, Y. Zheng, S. Bae, CY. Tan, O. Kahya, J. Wu, BH. Hong, K. Yao, B. Özyilmaz, Graphene ferroelectric hybrid structure for flexible transparent electrodes, *ACS Nano,* 2012,**6**,3935-3942.

23. Y. Shi, Y. Ji, F. Hui, H-H. Wu, M. Lanza, Ageing mechanisms and reliability of graphene-based electrodes, *Nano Res.,* 2014,**7**,1820-1831.

24. G.Heywang, F. Jonas, Poly(alkylenedioxythiophene)s-new, very stable conducting polymers, *Adv. Mater.,* 1992, **4**,116-118.

25. T. Takano, H. Masunaga, A. Fujiwara, H. Okuzaki, T. Sasaki, PEDOT nanocrystal in highly conductive pedot:pss polymer films, *Macromolecules,* 2012, **45**,3859-3865.

26. N. Kim, S. Kee, SH. Lee, BH. Lee, YH. Kahng, Y-R. Jo, B-J. Kim, K. Lee, Highly conductive PEDOT: PSS nanofibrils induced by solution-processed crystallization, *Adv. Mater.,* 2014, **26**, 2268-2272.

27. R. Po, C. Carbonera, A. Bernardi, F. Tinti, N. Camaioni, Polymer- and carbon-based electrodes for polymer solar cells: Toward low-cost, continuous fabrication over large area, *Sol. Energy Mater. Sol. Cells.,* 2012, **100**, 97-114.

28. M. Vosgueritchian, DJ. Lipomi, Z. Bao, Highly conductive and transparent PEDOT:PSS films with a fluorosurfactant for stretchable and flexible transparent electrodes, *Adv. Funct. Mater.,* 2012, **22**,421-428.

29. JY. Oh, M. Shin, JB. Lee, J-H. Ahn, HK. Baik, U. Jeong, Effect of PEDOT nanofibril networks on the conductivity, flexibility, and coatability of PEDOT:PSS films, *ACS Appl. Mater. Interfaces.,* 2014,**6**,6954-6961.

30. FC. Krebs, T. Tromholt, M. Jorgensen, Upscaling of polymer solar cell fabrication using full roll-to-roll processing., *Nanoscale,* 2010, **2**,873-886.

31. AM. Nardes, M. Kemerink, MM. de Kok, E. Vinken, K. Maturova, RAJ. Janssen, Conductivity, work function, and environmental stability of PEDOT:PSS thin films treated with sorbitol. *Org. Electron.* 2008, **9**,727-734.

32. HK. Chaurasia, WAG. Voss, Ultra-thin conducting films of gold on platinum nucleating layers. *Nature,* 1974, **249**,28-29.

33. RA. Hatton, MR. Willis, MA. Chesters, D. Briggs, A robust ultrathin, transparent gold electrode tailored for hole injection into organic light-emitting diodes, *J. Mater. Chem.,* 2003, **13**,722-726.

34. N. Formica, D. Sundar Ghosh, TL. Chen, C. Eickhoff, I. Bruder, V. Pruneri, Highly stable AgNi based transparent electrodes on PET substrates for flexible organic solar cells, *Sol. Energy Mater. Sol., Cells* 2012,**107**,63-68.

35. OS. Hutter, HM. Stec, RA. Hatton, An indium-free low work function window electrode for organic photovoltaics which improves with in-situ oxidation, *Adv. Mater.,* 2013, **25**, 284-288.

36. S. De, TM. Higgins, PE. Lyons, EM. Doherty, PN. Nirmalraj, WJ. Blau, JJ. Boland, JN. Coleman, Silver nanowire networks as flexible, transparent, conducting films: extremely high DC to optical conductivity ratios. *ACS Nano,* 2009, **3**,1767-1774.

37. J. Lee, P. Lee, H. Lee, D. Lee, SS. Lee, SH. Ko, Very long Ag nanowire synthesis and its application in a highly transparent, conductive and flexible metal electrode touch panel *Nanoscale* 2012*,* **4**,6408-6414.

38. S. Zhu, Y. Gao, B. Hu, J. Li, J. Su, Z. Fan, J. Zhou, Transferable self-welding silver nanowire network as high performance transparent flexible electrode, *Nanotechnology,* 2013,**24**,335202.

39. J. Liang, L. Li, K. Tong, Z. Ren, W. Hu, X. Niu, Y. Chen, Q. Pei, Silver nanowire percolation network soldered with graphene oxide at room temperature and its application for fully stretchable polymer light-emitting diodes, *ACS Nano,* 2014,**8**,1590-1600.

40. H. Lu, D. Zhang, X. Ren, J. Liu, WCH. Choy, Selective growth and integration of silver nanoparticles on silver nanowires at room conditions for transparent nano-network electrode, *ACS Nano*, 2014,**8**,10980-10987.

41. M. Song, DS. You, K. Lim, S. Park, S. Jung, CS. Kim, D-H. Kim, D-G. Kim, J-K. Kim, J. Park, *et al*., Highly efficient and bendable organic solar cells with solution-processed silver nanowire electrodes, *Adv. Funct. Mater.,* 2013,**23**,4177-4184.

42. H. Guo, N. Lin, Y. Chen, Z. Wang, Q. Xie, T. Zheng, N. Gao, S. Li, J. Kang, D. Cai, *et al*., Copper nanowires as fully transparent conductive electrodes. *Sci. Rep.,* 2013,**3**.

43. AR. Rathmell, SM. Bergin, Y-L. Hua, Z-Y. Li, BJ. Wiley, The growth mechanism of copper nanowires and their properties in flexible, transparent conducting films, *Adv. Mater.,* 2010,**22**,3558-3563.

44. AR. Rathmell, BJ. Wiley, The synthesis and coating of long, thin copper nanowires to make flexible, transparent conducting films on plastic substrates, *Adv. Mater.* 2011, **23**, 4798-4803.

45. D. Zhang, R. Wang, M. Wen, D. Weng, X. Cui, J. Sun, H. Li, Y. Lu: Synthesis of ultra-long copper nanowires for high-performance transparent electrodes, *J. Am. Chem. Soc.,*2012, **134**,14283-14286.

46. AR. Rathmell, M. Nguyen, M. Chi, BJ. Wiley, Synthesis of oxidation-resistant cupronickel nanowires for transparent conducting nanowire networks, *Nano Lett.,*2012,**12**,3193-3199.

47. S. Zhang, HC. Zeng, Solution-based epitaxial growth of magnetically responsive Cu@Ni nanowires, *Chem. Mater.,*2010,**22**,1282-1284.

48. Z. Chen, S. Ye, IE. Stewart, BJ. Wiley, Copper nanowire networks with transparent oxide shells that prevent oxidation without reducing transmittance, *ACS Nano,* 2014,**8**: 9673-9679.

49. H-G. Im, S-H. Jung, J. Jin, D. Lee, J. Lee, D. Lee, J-Y. Lee, I-D. Kim, B-S. Bae, Flexible transparent conducting hybrid film using a surface-embedded copper nanowire network: a highly oxidation-resistant copper nanowire electrode for flexible optoelectronics, *ACS Nano,* 2014,**8**,10973-10979.

50. A. Morag, V. Ezersky, N. Froumin, D. Mogiliansky, R. Jelinek, Transparent, conductive gold nanowire networks assembled from soluble Au thiocyanate. *Chemical Communications,* 2013,**49**,8552-8554.

51. DS. Hecht, L. Hu, G. Irvin, Emerging transparent electrodes based on thin films of carbon nanotubes, graphene, and metallic nanostructures, *Adv. Mater.,* 2011, **23**,1482-1513.

52. M. Zhang, S. Fang, AA. Zakhidov, SB. Lee, AE. Aliev, CD. Williams, KR. Atkinson, RH. Baughman: Strong, transparent, multifunctional, carbon nanotube sheets, *Science,* 2005, **309**,1215-1219.

53. A. Falco, L. CinÃ , G. Scarpa, P. Lugli, A. Abdellah, Fully-sprayed and flexible organic photodiodes with transparent carbon nanotube electrodes, *ACS Appl. Mater. Interfaces.,* 2014, **6**,10593-10601.

54. DS. Hecht, AM. Heintz, R. Lee, L. Hu, B. Moore, C .Cucksey and S. Risser ,High conductivity transparent carbon nanotube films deposited from superacid, *Nanotechnology,* 2011, **22**,075201.

55. S. Hong, J. Yeo, G. Kim, D. Kim, H. Lee, J. Kwon, H. Lee, P. Lee, SH. Ko, Nonvacuum, maskless fabrication of a flexible metal grid transparent conductor by low-temperature selective laser sintering of nanoparticle ink, *ACS Nano,* 2013,**7**,5024-5031.

56. BY. Ahn, DJ. Lorang, JA. Lewis, Transparent conductive grids via direct writing of silver nanoparticle inks, *Nanoscale,* 2011**3**,2700-2702.

57. M. Layani, M. Gruchko, O. Milo, I. Balberg, D. Azulay, S. Magdassi, Transparent conductive coatings by printing coffee ring arrays obtained at room temperature, *ACS Nano,* 2009, **3**,3537-3542.

58. T. Gao, B. Wang, B. Ding, J-k. Lee, PW. Leu, Uniform and ordered copper nanomeshes by microsphere lithography for transparent electrodes, *Nano Lett.,* 2014,**14**,2105-2110.

59. R. Gupta, M. Hosel, J. Jensen, FC. Krebs, GU. Kulkarni, Digital grayscale printing for patterned transparent conducting Ag electrodes and their applications in flexible electronics, *J. Mater. Chem.C*., 2014,**2**,2112-2117.

60. M. Hösel, RR. Søndergaard, M. Jørgensen, FC. Krebs, Fast inline roll-to-roll printing for indium-tin-oxide-free polymer solar cells using automatic registration, *Energy Technol.,* 2013,**1**,102-107.

61. MG. Kang, LJ. Guo: Nanoimprinted semitransparent metal electrodes and their application in organic light-emitting diodes, *Adv. Mater.,* 2007, **19**,1391-1396.

62. SH. Ahn, LJ. Guo, Large-area roll-to-roll and roll-to-plate nanoimprint lithography: a step toward high-throughput application of continuous nanoimprinting, *ACS Nano,* 2009, **3**,2304-2310.

63. T. Tokuno, M. Nogi, J. Jiu, T. Sugahara, K. Suganuma, Transparent electrodes fabricated via the self-assembly of silver nanowires using a bubble template, *Langmuir*,2012,**28**,9298-9302.

64. D-E. Lee, S. Go, G. Hwang, BD. Chin, DH. Lee, Two-dimensional micropatterns via crystal growth of Na_2CO_3 for fabrication of transparent electrodes, *Langmuir,* 2013, **29**,12259-12265.

65. H. Wu, L. Hu, MW. Rowell, D. Kong, JJ. Cha, JR. McDonough, J. Zhu, Y. Yang, MD. McGehee, Y. Cui, Electrospun metal nanofiber webs as high-performance transparent electrode, *Nano Lett.,* 2010,**10**,4242-4248.

66. P-C. Hsu, H. Wu, TJ. Carney, MT. McDowell, Y. Yang, EC. Garnett, M. Li, L. Hu, Y. Cui, Passivation coating on electrospun copper nanofibers for stable transparent electrodes. *ACS Nano* 2012,**6**,5150-5156.

67. H. Wu, D. Kong, Z. Ruan, P-C. Hsu, S. Wang, Z. Yu, TJ. Carney, L. Hu, S. Fan, Y. Cui, A transparent electrode based on a metal nanotrough network, *Nat Nano* 2013,**8**,421-425.

68. P-C. Hsu, D. Kong, S. Wang, H. Wang, AJ. Welch, H. Wu, Y. Cui, Electrolessly deposited electrospun metal nanowire transparent electrodes, *J. Am. Chem. Soc.,* 2014,**136**,10593-10596.

69. JS. Woo, JT. Han, S. Jung, JI. Jang, HY. Kim, HJ. Jeong, SY. Jeong, KJ. Baeg, GW.Lee, Electrically Robust Metal Nanowire Network Formation by in-situ Interconnection with Single Walled Carbon Nanotubes, *Sci. Rep*., 2014, **4**, 4804.

70. D. Kim, L. Zhu, DJ. Jeong, K. Chun, YY. Bang, SR. Kim, JH. Kim, SK. Oh, Transparent Flexible Heater Based on Hybrid of Carbon Nanotubes and Silver Nanowires, *Carbon* 2013, **63**, 530-536.

71. X. Zhang, X. Yan, J. Chen, J. Zhao, Large-Size Graphene Microsheets as a Protective Layer for Transparent Conductive Silver Nanowire Film Heaters, *Carbon*,2014, **69**, 437-443.

72. SM. Lee, JH. Lee, S. Bak, K. Lee, Y. Li, H. Lee, Hybrid Windshield-Glass Heater for Commercial Vehicles Fabricated Via Enhanced Electrostatic Interactions Among a Substrate, Silver Nanowires, and an Over-Coating Layer, *Nano Res*., 2015, **8**, 1882- 1892.

73. HG. Cheong, DW. Song, JW. Park, Transparent Film Heaters with Highly Enhanced Thermal Efficiency Using Silver Nanowires and Metal/Metal-Oxide Blankets, *Microelectron. Eng.,* 2015, **146**, 11-18.

74. N. Kwon, K. Kim, J. Heo, I. Yi, I. Chung, Study on Ag Mesh/ Conductive Oxide Hybrid Transparent Electrode for Film Heaters. *Nanotechnology,* 2014, **25,** 265702.

75. S. Ji, W. He, K. Wang, Y. Ran, C. Ye, Thermal Response of Transparent Silver Nanowire/PEDOT:PSS Film Heaters, *Small,* 2014, **10**, 4951-4960.

76. C. Hunger, KDM. Rao, R. Gupta, CR. Singh, GU. Kulkarni, M. Thelakkat, Transparent Metal Network with Low Haze and High Figure of Merit Applied to Front and Back Electrodes in Semitransparent ITO-Free Polymer Solar Cells, *Energy Technol*., 2015, **3**, 638-645.

77. J. Li, J. Liang, X. Jian, W. Hu, J. Li, Q. Pei, A Flexible and Transparent Thin Film Heater Based on a Silver Nanowire/HeatResistant Polymer Composite, *Macromol.Mater. Eng*., 2014, **299**, 1403-1409.

78. HY. Lu, CY. Chou, JH. Wu, JJ. Lin, GS. Liou, Highly Transparent and Flexible Polyimide-AgNW Hybrid Electrodes with Excellent Thermal Stability for Electrochromic Applications and Defogging Devices, *J. Mater. Chem. C.,* 2015, **3**, 3629-3635.

79. M. Li, S. Ji, J. Pan, H. Wu, L. Zhong, Q. Wang, F. Li, G. Li, Infrared Response of Self-Heating VO_2 Nanoparticles Film Based on Ag Nanowires Heater, *J. Mater. Chem. A.,* 2014, **2,** 20470- 20473.

80. J. Kang, Y. Jang, Y. Kim, SH. Cho, J. Suhr, BH. Hong, JB. Choi, D. Byun, Ag-Grid/Graphene Hybrid Structure for LargeScale, Transparent, Flexible Heaters, *Nanoscale* 2015, **7**, 6567-6573.

Chapter II

Characterization Techniques

Several spectroscopic, microscopic and electrochemical techniques have been used to characterize the prepared transparent conductors (samples) reported in this thesis. In the present chapter, the basic principles and details of the instruments used and the sample preparation and characterization methods are described.

Field Emission Scanning Electron Microscopy (FESEM) and Energy-Dispersive X-ray Spectroscopy (EDS)

In FESEM, the focussed electron beam scans (raster) across the sample surface and generates the secondary (inelastic scattering) and backscattered (elastic scattering) electrons which are detected by detectors to generate the surface topography of the sample. Inelastic scattering also produces X-rays and Auger electrons which are used for chemical composition analysis [1].

FESEM measurements were performed using a Nova NanoSEM 600 equipment (FEI Co., The Netherlands). Energy dispersive spectroscopic (EDS) mapping was performed using EDAX Genesis V4.52 (USA) attached to the SEM column. The EDS mapping was performed at 10-15 kV (energy window, 10 eV) with a beam current of 1.1-2 nA, the dwell time per pixel being 25 μs. Low vacuum imaging were performed on the same instrument using helix detectors. Under low vacuum environment, the chamber was maintained at 0.4 Torr and filled with water vapor.

Electron beam lithography (EBL) was performed at 10^{-6} Torr vacuum. The silicon samples were grounded to avoid charging while patterning, as it broadens the patterned features. The pattern designs were fed through the e-beam write software available with the instrument. The e-beam energies were varied from 5-30 kV according to the pattern features. For large area patterning, low energy was preferred whereas for small fine features high energy was employed. The beam current was varied between 91 pA to 24 nA. The dwell time (exposure time per pixel) and number of passes varied from 0.1-50 μs and 1-15000.

Transmission Electron Microscope (TEM) and Electron Diffraction (ED)

The first transmission mode electron microscope was built by Ruska and Knoll in 1930s. In TEM, a beam of electrons is transmitted through an ultra-thin sample and transmitted electrons are used to create an image of the sample by an area sensor such as CCD camera. Electromagnetic lens are used to focus electron beam and TEM provides 0.2 nm resolution. ED pattern helps to understand the local crystal structure of the sample [2].

Transmission electron microscopy (TEM) measurements were carried out with a JEOL-3010 instrument operating at 300 kV (λ= 0.0196 Å) and selected area electron diffraction (SAED) patterns were collected at a camera length 20 cm (calibrated with respect to the standard polycrystalline Au thin film). Samples for TEM were prepared by depositing a drop of the nanomaterial on a holey carbon copper grid, allowing it to dry overnight.

Atomic Force Microscopy (AFM)

Fundamental principle of AFM is based on interaction between a sharp tip and sample surface for assessing morphology and other physical properties. It was developed in the year 1986 by Binnig, Quate and Gerber. Probe (combination of cantilever and tip assembly) was mounted on piezo scanner which allows its movement independently in X, Y and Z axes. A laser beam was made to fall on cantilever whose deflections were recorded by quadrupole photodetector. Repulsive and attractive van der Waals is two kinds of forces encountered during AFM operation. AFM measurement can be done in static contact mode or dynamic non-contact mode. In contact mode, repulsive interaction between tip and surface provides the information about topography of the sample. While imaging, tip exerts local pressure of nearly GPa over the sample surface. Thus, non-contact mode is highly preferred for soft samples such as polymers and bio-molecules. AFM has also been used to study mechanical, electrical and magnetic properties of surface [3].

Veeco Dimension 3100 SPM with Nanoscope-IV controller and Veeco diInnova SPM with Nanodrive controller was used for AFM measurements. Si and Si_3N_4 cantilevers were used for tapping and contact (lateral force) mode imaging,

respectively. Both the height and deflection/ amplitude information were recorded at a scan rate of 1 Hz, and stored in a 512 × 512 pixel format. Images were processed using the offline softwares.

Raman Spectroscopy

Raman spectra of nanocrystalline metal composite was recorded in the backscattering geometry using a 532 nm excitation from a diode pumped frequency doubled Nd:YAG solid state spectrometer equipped with a SPEX TRIAX 550 monochromator and a liquid nitrogen cooled CCD detector (Spectrum One with CCD3000 contrller, ISA Jobin Yuon). Signal accumulation was performed for 30 s with a spot size of ~ 2 μm.

Optical Microscope

An optical microscope consists of a simple lens system for magnifying small objects. The objective lens first creates an image of the object in the intermediate image plane which is further magnified through eye-piece lens [4]. The optical microscope from Laben microscope, India with magnification of 50-1000 X was used to capture images in reflective and transmission modes.

Optical Profiler

Optical profiler, a non-contact profilometer, provides information about sample surface such as thickness, roughness etc. This can provide information even about 3D surface due to optical interference [5,6]. For film thickness measurements, a Wyko NT9100 (Veeco, USA) optical profiler (OP) was used. The vertical scanning interferometry (VSI) was used for samples having more than 160 nm roughness whereas phase shifting interferometry (PSI) mode for less than 160 nm roughness. The field of view and objective lens magnifications ranges from 0.5x–2x and 5x–50x respectively.

UV-vis and IR spectroscopy

Transmittance, reflectance, absorption and haze measurements were performed using a Perkin-Elmer Lambda 900 UV/vis/NIR spectrophotometer. Fourier transform

infrared (FTIR) measurements were done using a Bruker IFS66v/s spectrometer with a resolution of ~2 cm^{-1}.

X-ray Photoelectron Spectroscopy (XPS)

XPS was carried out with OMICRON spectrophotometer (1 x 10^{-10} Torr vacuum) with X-ray source of Al Kα (1486.6 eV). Samples for XPS (solid substrates) were mounted on the stub using high vacuum compatible Ag paint and drying in a vacuum. For sputtering the samples, a beam (focus 1 keV) energy of 1 keV with a current of 44. 2 μA was used at a base pressure of 10^{-5} mbar.

X-ray Diffraction

Powder X-ray diffraction measurements were performed using a Siemens Seifert 3000TT diffractometer employing Cu Kα (λ= 1.5406 Å) radiation. Samples were prepared by depositing the materials in the form of films on glass slides/PET/Si and typical scan rate was 1 degree min^{-1}. The X-ray tube was set at 40 kV and 30 mA. With a receiving slit of 0.3 mm wide and a scintillation counter as detector, the θ-2θ scans were performed. High-purity silicon powder was used as an internal standard. The coherently diffracting crystallographic domain size (D) of the nanoparticles was calculated from X-ray diffraction (XRD) line broadening after subtracting the contribution from the Cu Kα component (Rachinger correction) and correcting for the instrumental width. The integral line width was used in the Scherrer formula [7] to calculate d_{XRD} of the high intensity peak.

$$D = 0.9\lambda/\beta_{1/2}\, cos\theta$$

where λ is the wavelength of the X-ray beam, $\beta_{1/2}$ is the angular width at the half-maximum intensity and θ is the Bragg angle.

Thermogravimetric Analysis (TGA)

TGA measurements were carried out with a Mettler Toledo Star instrument (Weinheim, Germany) in the temperature range 30 – 450 °C under N_2 or O_2 or ambient atmosphere at a flow rate of 100 mL/min and a heating rate of 3- 5 °C/min. Typically using 5-25 mg of the sample in solid form mounted on a porcelain boat.

Electrochemical Measurements

The electrochemical properties were investigated in three electrode and two electrode configurations with the potentiostat equipment from Technoscience Instruments (Model PG 16250) and CH instruments 650 Electrochemical station (Austin, TX, USA).

Contact Angle (CA) Measurements

For contact angle measurements, a Rame´-Hart digital contact angle (CA) goniometer was used to measure the surface wetting properties of films at room temperature. A deionized (DI) water or solvents (3 μL) were dropped gently on the sample surface using an automatic pipet, and a photograph of the water droplet was taken immediately with the goniometer camera. CA values were given by the DROP image advanced software measurement; the CA values obtained from the software were also crosschecked with the CA values measured manually on the printed photograph of the water droplet. For each point, a few images were recorded and measured. The typical error of the CA measurements is ±3°.

Infrared Thermal Imaging

For thermal imaging of conducting samples, the electrode contacts were established using thick epoxy Ag paint. The substrate was mounted with supports at both ends such that it is kept hanging in air while the imaging is done from either front or rear view of the electrode. The voltage was applied using Keithley 2400 and thermal imaging was carried out using Testo thermal imager (Testo 885). The thermal images were analysed using the offline software.

References

1. J. Goldstein, D.Newbury, D. Roy, C. Lyman, D. Echlin et al., *Scanning Electron Microscopy and X-ray Microanalysis*, 3rd Edition, Springer Science and Business Media, Inc., USA (**2003**).

2. D. B. Williams & C.B. Carter, *Transmission Electron Microscope*, Plenum Press, Newyork (**1996**).

3. R. Wiesendanger in *Handbook of Microscopy, Methods II,* S. Amelinckx, D. Van Dyck, J. Van Landuyt, G. Van Tendeloo, Eds., Wiley VCH, Weinheim (**1997**).

4. Pluta, Maksymilian. *Advanced Light Microscopy vol.1 Principles and basic properties*, Elsevier (**1988**).

5. https://en.wikipedia.org/wiki/Profilometer

6. http://www.nanoscience.com/technology/optical-profiler-technology/howprofilometer-works/#sthash.LFtP1rwy.dpuf

7. B. D. Cullity and S. R. Stock, *Elements of X-Ray Diffraction*, Prentice-Hall Inc., (**2001**).

Chapter III

A Variety of Transparent Conducting Electrodes by Crackle Templating Method

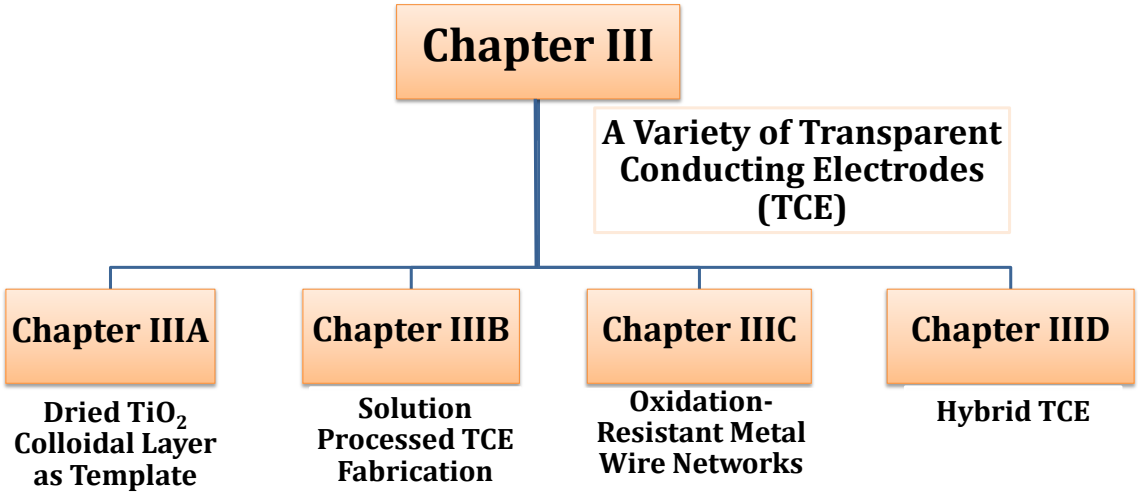

Chapter IIIA

Dried TiO_2 Colloidal Layer as Crackle Template

Summary

A metal (Au) wire network, nearly invisible to the naked eye, has been realized on common substrates such as glass, to serve as a transparent conducting electrode (TCE). The process involves coating of a TiO_2 nanoparticle dispersion to a film thickness of ~10 μm, which following solvent evaporation, spontaneously forms a crackle network; the film is then used as a sacrificial template for metal deposition. The TCE thus formed exhibited visible transmittance of ~82% and sheet resistance of 3–6 Ω/sq. With PET substrate, flexible and robust TCE could be produced and with quartz, the spectral range could be widened to cover UV and IR regions.

IIIA.1 Introduction

Particulate films exhibit cracks above a critical thickness, due to the stress induced by solvent evaporation [1], which is widely seen in nature such as in mud cracking [2–4]. Cracks, by definition, are unpredictable and widely varied [5,6]. Indeed, a crack is something one wishes to avoid at any cost. In thin film based device fabrication, the occurance of cracking is considered detrimental to the device performance and its reproducibility [7]. There have been efforts in the literature to inhibit crack formation by manipulating the stress [6–8]. Thus, Prosser et al [8] followed an unconventional deposition process, in which a thick film of ~500 nm was obtained by sequential deposition of thin layers, each below the critical thickness. In another instance [9], the crack formation in a TiO_2 nanoparticle layer used in solar cell fabrication, was suppressed by applying pressure during drying. In contrast to the above reports, there are recent indications in the literature of exploiting cracks for material deposition and patterning [10]. In an interesting report using cracks formed in a TiO_2 nanoparticle layer coated on graphene, the latter was given mild exposure to acid vapor through cracks so as to control its doping [11]. This is an example of using a cracked layer as a lithography template. Recently, Wei Han et al [12] have reported crack formation in films of polystyrene beads which formed a template for Au wires.

Paper based on this study: Mater. Res. Express, 1, 026301 (2014)

There is much emphasis in the literature given to the fabrication of transparent conducting electrodes using nanomaterials such as CNTs [13–15], metal nanowires [16–20] and graphene [21–27] as possible replacements for the conventional electrode material, tin doped indium oxide (ITO), as the processing costs are high and In is relatively less abundant [28,29]. ITO possesses properties rightly suited to optoelectronic applications; typically, ITO films exhibit transmittance of 92% for visible wavelengths and sheet resistance, 10 Ω/sq, which explains the widespread use [30–32]. The new generation alternative electrodes, which essentially consist of percolative conducting networks of 1D nanomaterials (CNTs or Ag nanowires) deposited on common substrates such as glass or PET wherein the nude areas amidst the network transmit light [33]. In such a situation, as is obvious, there is always a trade-off between the transmittance and the sheet resistance, which is achieved by optimizing the nanomaterial loading. Thus, performance specifications close to if not better than ITO, have been reported [34,35]. The challenge is, of course, the optimization step of ensuring uniform loading of the conducting network over macro-areas while minimizing the contact resistance and occurrence of redundant wires (or tubes), which remain unconnected to rest of the network [36,37]. Secondly, the roughness associated with the network can be a nightmare in thin film device fabrication involving macro-areas [38, 39]; a few nanowires or tubes which, during deposition and subsequent processing, happen to raise themselves from the average network thickness, can actually shunt the device [40–44]. Prompted by the above observations, it is considered to be interesting to explore the possibility of forming a wire network by metal vapor deposition, using a cracked layer of TiO_2 nanoparticles as a sacrificial template.

IIIA.2 Scope of the present investigation

One encounter cracks in daily lives, popular examples being mud cracks and aged wall paint. Inspired by Nature, cracks have been used in a new way for fabricating large area transparent conducting electrodes (TCEs). The work described in this chapter exploits cracking of TiO_2 colloidal film in fabricating transparent conductors. Cracking of dried colloidal layers is a classic problem in soft matter physics that is mostly revisited for remedial measures on how to avoid

cracks. Contrary, a recipe was developed which produces crackles in a continuous network, over large area yet with a fair degree of control on the crackle groove width and density. Usually, the new generation TCEs, rely on CNT or metal nanowire networks but suffer from junction scattering and contact resistance, besides other issues. In this study, a metal wire network close with low resistance (3-6 Ω/sq) and transmittance of nearly 84% in a wide spectral range was obtained.

IIIA.3 Experimental Details

Fabrication of transparent conducting electrodes

TiO_2 nanoparticle powder (80 mg, P25 Degussa) was dispersed in 1 mL of ethanol by rigorously ultrasonicating for 1 h to form a suspension. Further, 0.16 mL of ethyl acetate was added to the suspension to enhance the crackle formation with lesser film thickness. It was then used directly for drop coating on various substrates (glass, quartz and PET). The volume of solution varied with respect to the substrate size. Typically, 30 µL was drop-coated per cm square area of the substrate. The crackle network pattern formed spontaneously in the coated.

IIIA.4 Results and Discussion

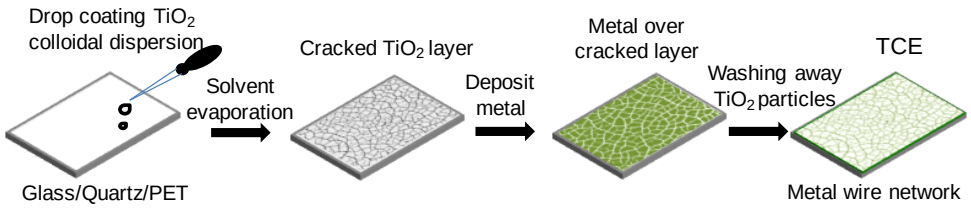

Figure IIIA.1 Schematic of the TCE fabrication.

The process consists of only three steps (schematic in Figure IIIA.1). A smooth transparent substrate (glass, quartz or PET) is drop coated with a colloidal dispersion of TiO_2 nanoparticles (~21 nm) in ethanol-ethyl acetate mixture (0.08 g mL^{-1}) to a thickness of ~13 µm which was allowed to dry under ambient conditions. The dispersion was chosen after several optimisation trials (Figure IIIA.2). It may be noted that the thicknesses of the films prepared from 14:86 and 23:77 ratios may be less than the critical thickness to form crackles but for 23:77, the presence of

additional ethyl acetate (crack inducing solvent) may be reason for formation of few cracks.

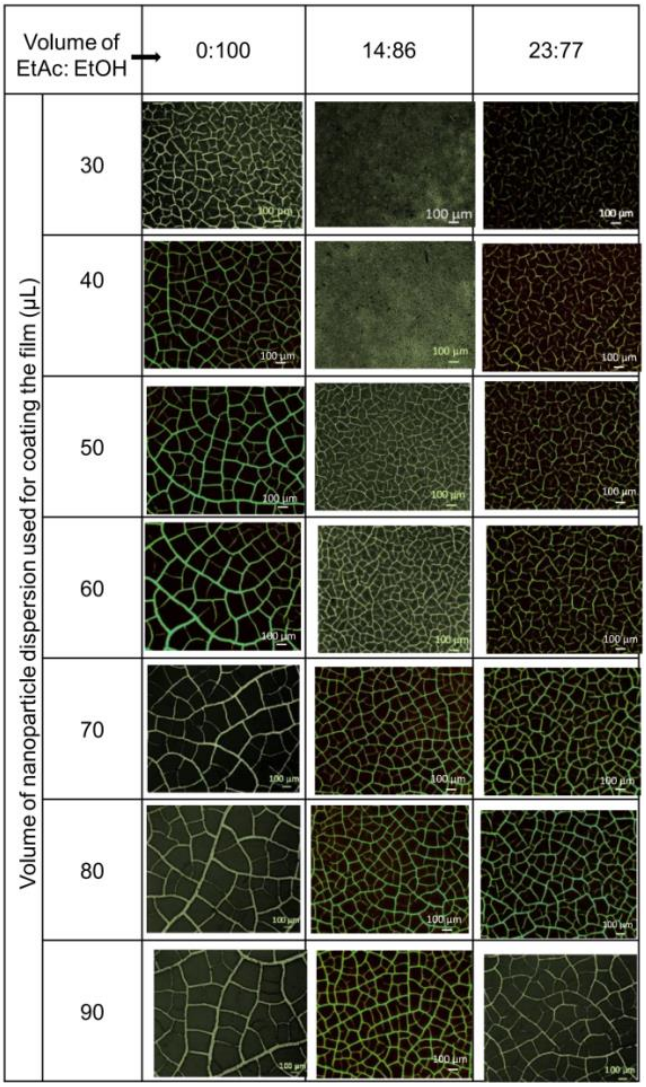

Figure IIIA.2 The process of optimization for crackles formed in TiO_2 nanoparticle film: The volume ratio of ethyl acetate (EtAc) and ethanol (EtOH) and the volume of nanoparticle dispersion used for controlling film thickness have been varied. In the absence of ethyl acetate, the TiO_2 nanoparticle dispersion in ethanol (0.08 g/mL) produced polygons that were relatively large in size, while addition of 0.3 mL to the dispersion made cracks less interconnected. In general, increasing volume of the dispersion for coating increased crack width and the polygonal size. A coating obtained with 70 µL of the dispersion containing 0.16 mL ethyl acetate, was found appropriate.

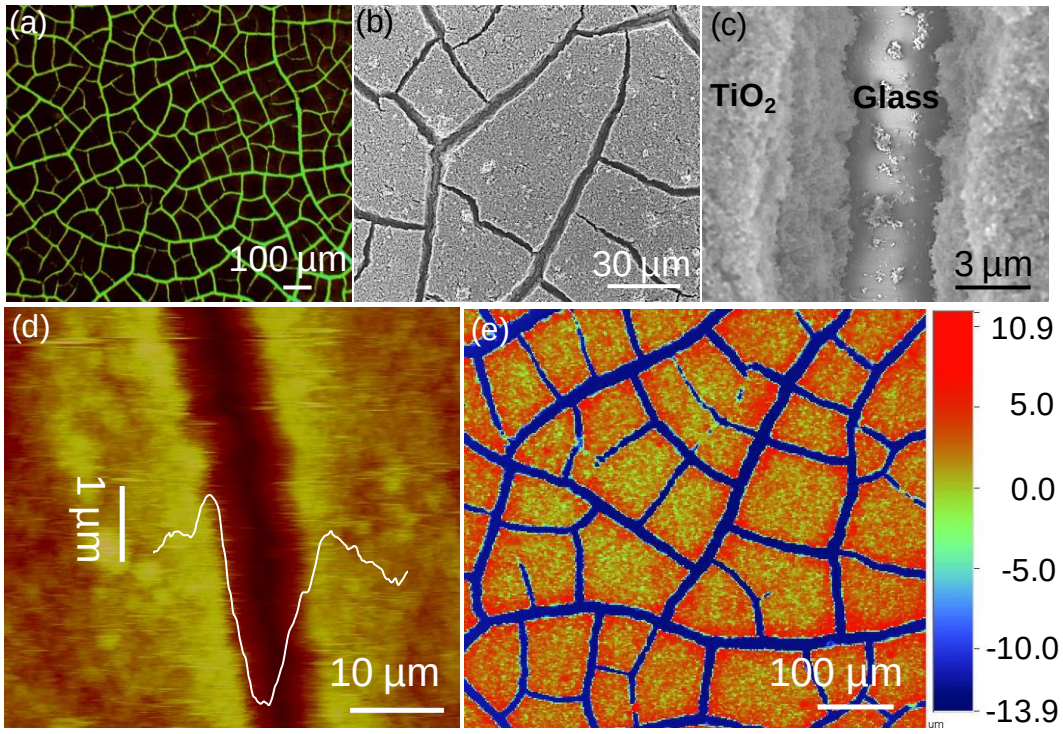

Figure IIIA.3 (a) Optical microscopy image showing a network of cracks in a dried TiO_2 nanoparticle layer on glass. The image was recorded in the transmission mode with a green light source illuminating from below. (b) SEM image of the cracked layer. (c) A magnified image showing densely packed TiO_2 nanoparticles on the wall of the crackle. (d) AFM image of a crackle along with its depth profile. (e) Optical profiler image shows the depth of the highly interconnected TiO_2 crackle network on glass substrate.

As shown in Figure IIIA.3a, the TiO_2 layer formed cracks all over the substrate with two remarkable features-all cracks were interconnected to give rise to a single network and the cracking was complete with no residual layer at the bottom, as revealed by the light tracks seen in the transmission mode microscopy (Figure IIIA.3a). More appropriately, these are crackles. Importantly as shown in the SEM, AFM and optical profiler images in Figure IIIA.3b-e, the crack width is in the range of few microns and the crack spacing, 50–200 µm, which makes the study worthwhile. The TiO_2 nanoparticles are seen densely stacked in the dried film (Figure IIIA.3c) giving way to clean cracked regions-lines, curves and junctions alike.

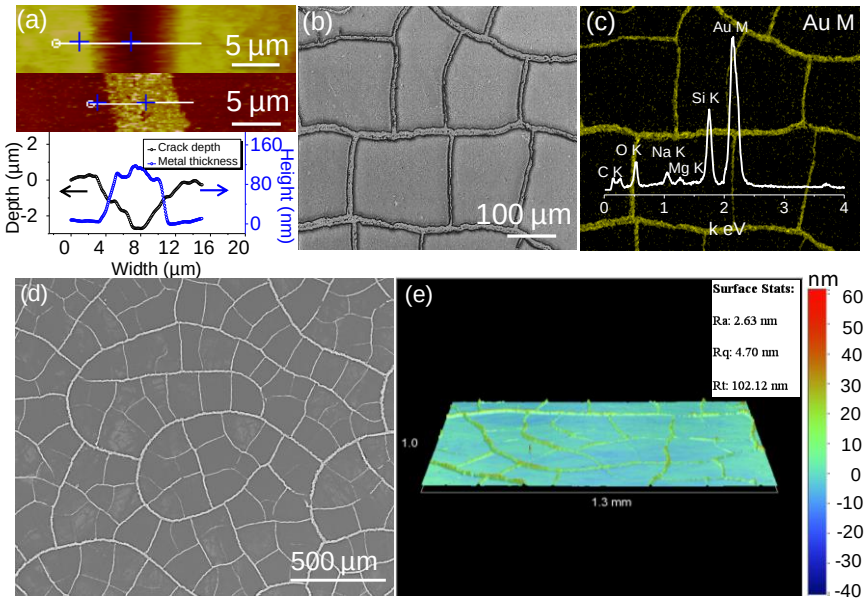

Figure IIIA.4 (a) AFM topography images of a crack (top) and metal wire (middle) and the corresponding z-profiles (bottom). (b) SEM image of the Au wire network and (c) Au M EDS map and the total spectrum. Other peaks are due to the glass substrate. (d) SEM and (e) optical profilometry images of a large area Au metal network. The measured roughness of the Au wire is shown in the right inset.

In the second step, Au was deposited by vacuum evaporation to a thickness of ~100 nm. Following developing in water (third step), the TiO_2 nanoparticles could be lifted-off the substrate leaving behind the metal trapped inside the cracked regions (see schematic in Figure IIIA.1). The AFM topography images and the z-profiles derived from them (Figure IIIA.4a) showed that the widths associated with the crack and the metal retained on the substrate after lift-off are similar. The Au wire network thus formed was examined using SEM and Au M signal in energy-dispersive spectroscopy (EDS). As shown in the images in Figures IIIA.4b-d the material retained on the substrate was indeed the Au wire network (see EDS spectrum in Figure IIIA.4c). The wire roughness measured over 1.3 mm^2 using optical profilometry is shown in Figure IIIA.4e. The arithmetic mean value (R_a) was 2.63 nm from the wire network surface, while the maximum roughness height (R_t) was 102 nm due to the thickness of nanowire.

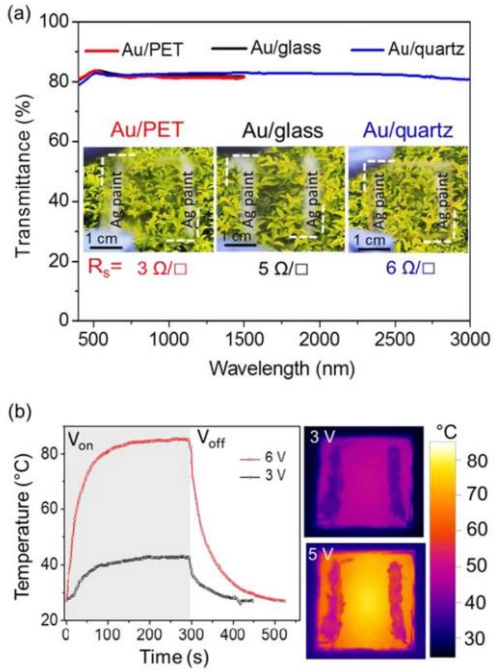

Figure IIIA.5 (a) A plot of transmittance versus wavelength of light obtained for Au wire networks on glass (black), quartz (blue) and PET (red). Photographs of the substrates held using fingers against a plant are shown along with four probe sheet resistance values. (b) Variation in the temperature as measured using an IR camera, of Au/quartz based TCE with time, after applying different voltages across silver contact pads. The corresponding thermographs depicting temperature variations after reaching saturation are shown on the right.

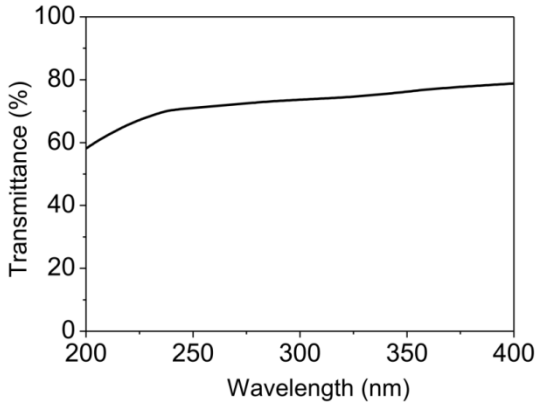

Figure IIIA.6 Transmittance spectrum of the Au wire network on quartz substrate in the UV region (200- 400 nm). Transmittance of over 60% was possible even at such low wavelengths.

The Au wire network based TCEs supported on glass, quartz and PET, exhibited transmittance of ~82% (Figure IIIA.5a), not only in the visibly relevant region (see photographs) but also beyond, up to 1500 nm for PET and glass, and 3000 nm for quartz. Quartz allowed UV light down to 200 nm (Figure IIIA.6), qualifying as a TCE with wide spectral range. The sheet resistance values measured using a four-pin setup was in the range of 3–6 Ω/sq for the different TCEs. These values are comparable to, or in many instances, even better than those of ITO films and other nanowire or nanotube based TCEs. What may further attract one's attention are the simplicity of process steps, inexpensive tools and environmentaly friendly raw materials. In order to reveal the overall presence of the Au wire network, a small bias across two Ag epoxy contacts was applied and joule heated the TCE. As shown in Figure IIIA.5b, the temperature of the Au/quartz TCE rose, in a matter of seconds, to a value which increased with increasing bias voltage. This is, in principle, a transparent heater. The thermographs shown on the right in Figure IIIA.5b, confirm the presence of the resistive wire network across the substrate. The uniform temperature distribution indicates good electrical connectivity of the network throughout the substrate, devoid of junction contact resistance.

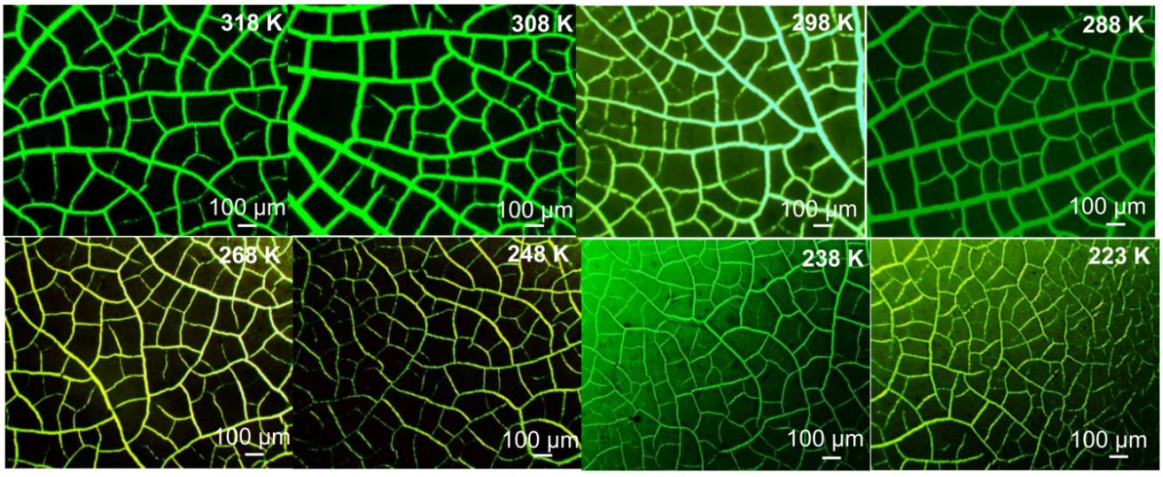

Figure IIIA.7 Optical micrographs of TiO_2 crackle networks formed at different temperatures from 318 K to 223 K. The crackle widths as well as the polygon areas are found to decrease with temperature due to slower evaporation of the solvents.

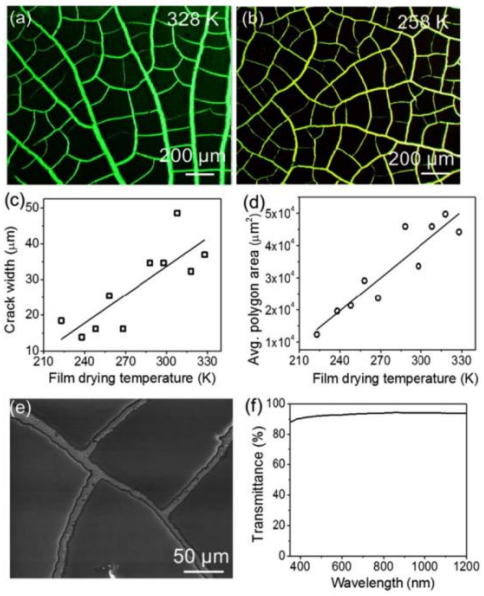

Figure IIIA.8 Optical microscopic images of interconnected crackles formed in TiO_2 nanoparticle film when dried at 328 K (a) and 258 K (b) under nitrogen flow. (c) A plot of maximum crack width versus the drying temperature. (d) A plot of average polygon area of crackles versus the drying temperature. (e) SEM image of Au networked wire on glass obtained using the 258 K dried film. (f) Transmittance spectrum of the Au/glass TCE.

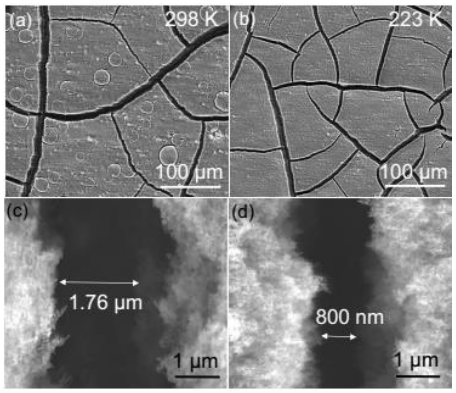

Figure IIIA.9 (a) and (b) shows SEM images of the crackle networks on TiO_2 film formed at 298 K and 223 K on glass. High magnification images in (c) and (d) show the narrow crackles from the respective drying temperatures. With lower drying temperatures, crackle width of less than a micrometre is possible.

For efficient active layer-electrode interface in optoelectronic devices, it is required to produce smaller metal wire widths which in turn demands, in this study,

fine crackles in the nanoparticle film. Crack spacing and width can be reduced by decreasing the thickness of the film, but this is limited by the critical film thickness, below which less interconnected cracks are observed (Figure IIIA.2). The possibility of reducing crackle width by reducing the film drying temperature was explored, thereby slowing down solvent evaporation. Crackle networks in TiO_2 nanoparticle films (all ~30 μm thick) dried at various temperatures are shown in Figure IIIA.7. Low temperature measurements were done using a THMS600 stage from Linkam Scientific Instruments Ltd, UK. As is evident, the crackle widths as well as the polygon areas are found to decrease at lower drying temperature (compare Figures IIIA.8a and b) due to slower evaporation of the solvents, which obviously influences the stress release in the film. At low drying temperatures, the network often contained fine crackles of width <1μm (Figure IIIA.9). The maximum crackle width decreased from 37 μm at 328 K to 18 μm at 223 K and the variation was nearly linear with some spread (Figure IIIA.8c). Concomitantly, the average area per polygon, calculated by dividing the total area (~2.4 mm^2) with the number of polygons, was also found to vary linearly (Figure IIIA.8d). Below 223 K, drying the nanoparticle film proved practically difficult. A Au wire TCE (Figure IIIA.8e) fabricated using a 258 K dried film exhibited transmittance of ~93% (Figure IIIA.8f), much higher than the metal network formed from the room temperature crackle network (~82%, Figure IIIA.5a). The sheet resistance of TCE fabricated from film dried at 258 K was 32.5 Ω/sq. However, this process needed further optimisation for producing large area TCEs.

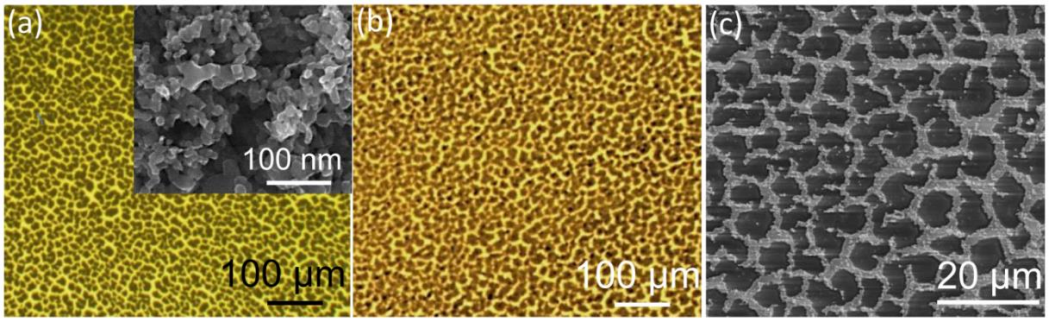

Figure IIIA.10 (a) Optical microscopic images of crackles formed with colloidal TiO_2. Inset shows the SEM images of colloidal TiO_2 particles. (b) Optical micrograph of metal network and SEM image of the same is shown in (c).

Another important parameter which can be explored to tune crack spacing and width, is the particle size [1,45,46]. TiO_2 nanoparticles having diameter of ~16 nm were prepared [47] which produced cracks with much finer widths (see Figure IIIA.10). The procedure adopted is similar to synthesis method reported in literature [47]. To synthesis TiO_2 colloid, 2.5 mL of titanium orthobutoxide was added to 11.5 mL of ethanol. After thorough mixing, 250 µL of ethyl acetate was added. Separately hydrolysate solution was prepared by mixing 750 µL of HNO_3 to equal volume of water and 6 mL ethanol. Then hydrolysate solution was slowly added to the precursor solution at the rate of 1 mL/min under stirring at 1000 rpm and continued stirring for 12 h at room temperature. Later, top clear solution was used as crackle precursor. The optical microscope image of the formed crackles on glass substrate is shown in Figure IIIA.10a. The diameter of nanoparticle is ~ 16 nm. Figure IIIA.10b and c shows the optical microscope and SEM images of metal network having resistance of 0.5 Ω and transmittance of ~ 50%.

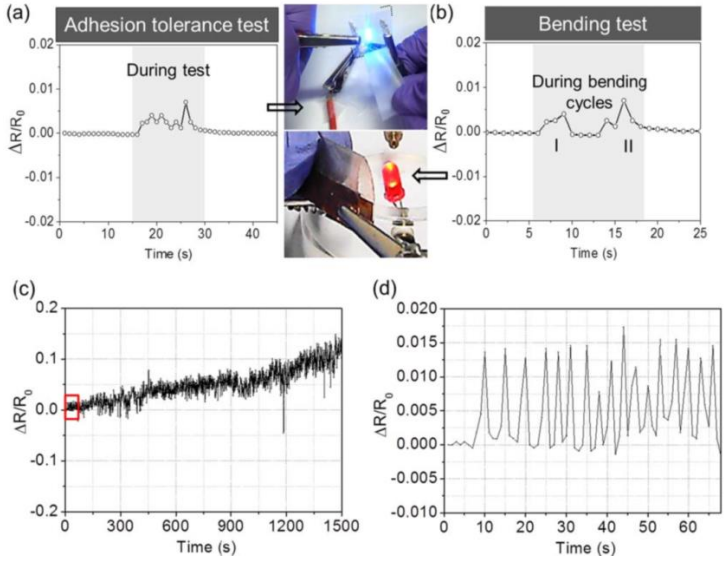

Figure IIIA.11 (a) A Au/PET substrate subjected to scotch tape adhesion test. The Au wire network was connected in series to an LED circuit. The relative change in resistance during the test is shown left. (b) The relative change in resistance during the bending cycles. The glowing LED is shown on the left. (c) The resistance of the TCE during several cycles of bending. The portion marked in the red box is shown magnified in (d). The resistance variation during each cycle is less than 2%.

PET is commonly used as a substrate for flexible optoelectronics. In this context, the robustness of the Au/PET based TCE was examined by taking it through adhesion and flexibility tests (Figure IIIA.11). Sticking a scotch tape, pressing and peeling off from the TCE surface caused less than 1% change in the resistance, that being temporary (Figures IIIA.11a and 12a and Movie IIIA.S1 in CD). Upon bending over several cycles (Figures IIIA.11b–d), mild changes in the TCE resistance was observed. Such was the case during crumbling, rolling and twisting (Figure IIIA.12b). The PET substrate hosting the delicate Au wire network could withstand all aggressive handling.

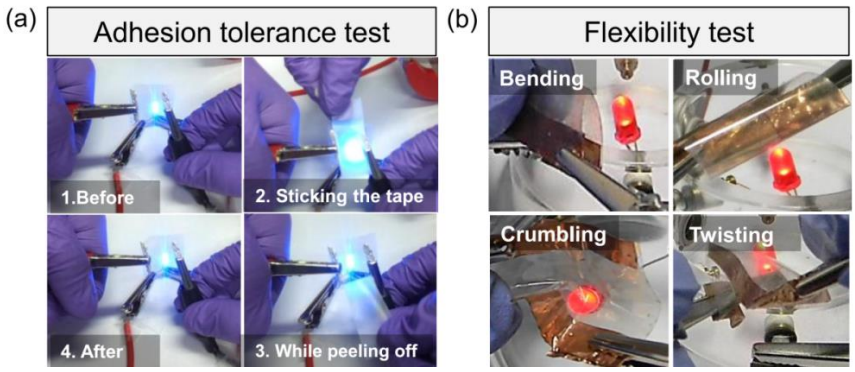

Figure IIIA.12 Photographs taken during the scotch tape peel-off test (a) and the various flexibility tests (b).

IIIA.5 Conclusions

A simple method for the fabrication of transparent conducting electrodes was developed which consist of an Au micro/nanowire network on a transparent substrate produced using a crackled TiO_2 nanoparticle film as a template. This is a spontaneously formed template unlike those used in conventional lithography techniques. The fabricated TCEs are commendable-they are inexpensive and robust, yet can perform with the desired optoelectronic properties required in industry. The fabrication process involves materials that are environmentally benign. A typical TCE produced by this method exhibited transmittance ~82% in the visible range with sheet resistance of 3–6 Ω/sq. Depending on the substrate property, the property of the TCE could be tuned. By using quartz as substrate, appreciable

transmittance was achieved in the UV and IR ranges. Similarly, a flexible TCE was obtained using PET as the host supporting Au wire network. The method opens up a wide range of possibilities for future studies, such as the choice of metal (or material), the deposition process-physical or chemical, controlling the nanostructure etc.

References

1. W. P. Lee and A. F. Routh, Why do drying films crack? *Langmuir*, 2004, **20,** 9885–8.

2. K. Pasricha, U. Wad, R. Pasricha and S. Ogale, Parametric dependence studies on cracking of clay *Physica. A.,* 2009,**388**, 1352–8.

3. L. Goehring, R. Conroy, A. Akhter, W. J. Clegg and A. F.Routh, Evolution of mud-crack patterns during repeated drying cycles, *Soft Matter*, 2010, **6**, 3562–7.

4. V. Groisman and E. Kaplan, An experimental study of cracking induced by desiccation, *EPL*, 1994, **25**, 415.

5. M. J. Alava, P. K. Nukala and S. Zapperi, Statistical models of fracture, *Adv. Phys.,* 2006, **55**, 349–476.

6. A. T. Ngo, J. Richardi and M. P. Pileni, Crack patterns in superlattices made of maghemite nanocrystals, *Phys. Chem. Chem. Phys*. 2013, **15**, 10666–72.

7. J. T. Park, W. S. Chi, D. K. Roh, S. H. Ahn and J. H. Kim, Hybrid templated synthesis of crack free, organized mesoporous TiO_2 electrodes for high efficiency solid state dye sensitized solar cells, *Adv. Funct. Mater*. 2013, **23**, 26–33.

8. J. H. Prosser, T. Brugarolas, S. Lee, A. J. Nolte and D. Lee, Avoiding cracks in nanoparticle films, *Nano Lett*. 2012, **12**, 5287–91.

9. S. Senthilarasu, T. A. N. Peiris, J. García-Cañadas and K. G. U. Wijayantha Preparation of nanocrystalline TiO_2 electrodes for flexible dye-sensitized solar cells: influence of mechanical compression *J. Phys. Chem. C*, 2012, **116**, 19053–61.

10. T. Bhuvana and G. U. Kulkarni, Polystyrene as a zwitter resist in electron beam lithography based electroless patterning of gold Bull. Mater. Sci. 2008, **31**, 201–6.

11. E. Shi et al, Colloidal antireflection coating improves graphene–silicon solar cells *Nano Lett*. 2013, **13**, 1776–81.

12. W. Han, B. Li and Z. Lin, Drying-mediated assembly of colloidal nanoparticles into large-scale microchannels, *ACS Nano*, 2013, **7,** 6079–85.

13. Z. Wu et al, Transparent, conductive carbon nanotube films, *Science,* 2004, 305 1273–6.

14. E. M. Doherty, S. De, P. E. Lyons, A. Shmeliov, P. N. Nirmalraj, V. Scardaci, J. Joimel, W. J. Blau, J. J. Boland and J. N. Coleman, The spatial uniformity and

electromechanical stability of transparent, conductive films of single walled nanotubes, *Carbon*, 2009, **47,** 2466–73.

15. H. Z. Geng, K. K. Kim, K. P. So, Y. S. Lee, Y. Chang and Y. H. Lee, Effect of acid treatment on carbon nanotube-based flexible transparent conducting films J. Am. Chem. Soc. 2007, **129**, 7758–9.

16. T. Tokuno, M. Nogi, M. Karakawa, J. Jiu, T, Nge, Y. Aso and K. Suganuma Fabrication of silver nanowire transparent electrodes at room temperature, Nano Res., 2011, 4, 1215–22.

17. J. Y. Lee, S. T. Connor, Y. Cui and P. Peumans, Solution-processed metal nanowire mesh transparent electrodes, *Nano Lett*. 2008, **8**, 689–92.

18. A. Madaria, A .Kumar, F. Ishikawa and C. Zhou, Uniform, highly conductive, and patterned transparent films of a percolating silver nanowire network on rigid and flexible substrates using a dry transfer technique, *Nano Res.,* 2010, **3**, 564–73.

19. S. De, T. M. Higgins, P. E. Lyons, E. M. Doherty, P. N. Nirmalraj, W. J. Blau, J. J. Boland and J. N. Coleman, Silver nanowire networks as flexible, transparent, conducting films: extremely high dc to optical conductivity ratios, *ACS Nano*, 2009, **3** 1767–74.

20. A. S. Iglesias, B. R. Murias, M. Grzelczak, J. P. Juste, L. M. L. Marzán, F. Rivadulla and M. A. Correa-Duarte, Highly transparent and conductive films of densely aligned ultrathin Au nanowire monolayers *Nano Lett*., 2012, **12**, 6066–70.

21. I. Jung, D. A. Dikin, R. D. Piner and R. S. Ruoff, Tunable electrical conductivity of individual graphene oxide sheets reduced at 'low' temperatures *Nano Lett*. 2008, **8**, 4283–7.

22. L. G. D. Arco, Y. Zhang, C. W. Schlenker, K. Ryu, M. E. Thompson and C. Zhou Continuous, highly flexible, and transparent graphene films by chemical vapor deposition for organic photovoltaics, *ACS Nano*, 2010, **4**, 2865–73.

23. G. Jo et al, Large-scale patterned multi-layer graphene films as transparent conducting electrodes for GaN light-emitting diodes, *Nanotechnology*, 2010, **21,** 175201–6.

24. S. Gilje, S. Han, M. Wang, K. L. Wang and R. B. Kaner, A chemical route to graphene for device applications, *Nano Lett.* 2007, **7**, 3394–8.

25. J. Wu, M. Agrawa, H. A. Becerril, Z. Bao, Z. Liu, Y. Chen and P. Peumans, Organic light-emitting diodes on solution-processed graphene transparent electrodes *ACS Nano*, 2010, **4**, 43–8.

26. Bae S et al Roll-to-roll production of 30-inch graphene films for transparent electrodes *Nat. Nanotech*., 2010, **5**, 574–8.

27. K. S. Kim, Y. Zhao, H. Jang, S. Y. Lee, J. M. Kim, K. S. Kim, J. H. Ahn, P. Kim, J. Y. Choi and B. H. Hong, Large-scale pattern growth of graphene films for stretchable transparent electrodes *Nature*, 2009*,* **457**, 706–10.

28. A. C. Tolcin, Indium: US Geological survey mineral commodity summaries 2012, **2012**, 74–75.

29. A. Kumar and C. Zhou, The race to replace tin doped indium oxide: which material will win? *ACS Nano*, 2010, **4,** 11–14.

30. D. S. Ginley, H. Hosono and D. C. Paine Handbook of Transparent Conductors (*Berlin: Springer*) 2011.

31. K. L. Chopra, S. Major and D. K. Pandya, Transparent conductors—a status review, *Thin Solid Films,* 1983, **102**, 1–46.

32. C. S. Tao, J. Jiang and M, Tao, Natural resource limitations to terawatt scale solar cells, *Sol. Energy Mater. Sol*., 2011, **95**, 3176–80.

33. R. Gupta and G. U. Kulkarni, Holistic method for evaluating large area transparent conducting electrodes, *ACS Appl. Mater. Interfaces*, 2013, **5**, 730–6.

34. H. Wu et al, A transparent electrode based on a metal nanotrough network *Nat. Nanotechnol.* 2013, **8**, 421–5.

35. H. Guo et al, Copper nanowires as fully transparent conductive electrodes *Sci. Rep.,* 2013, **3** 2323.

36. Y. Lu, J. Y. Huang, C. Wang, S. Sun and J. Lou, Cold welding of ultrathin gold nanowires, *Nat. Nanotechnol*. 2010, **5** 218–24.

37. E. C. Garnett, W. Cai, J. J. Cha, F. Mahmood, S. T. Connor, M. G. Christoforo, Y. Cui, M. D. McGehee and M. L. Brongersma, Self-limited plasmonic welding of silver nanowire junctions, *Nat. Mater*. 2012, **11,** 241–9.

38. S. Zhu, Y. Gao, B. Hu, J. Li, J. Su, Z. Fan and J. Zhou, Transferable self-welding silver nanowire network as high performance transparent flexible electrode, *Nanotechnology,* 2013, **24**, 335202–8.

39. R. C. Tenent, T. M. Barnes, J. D. Bergeson, A. J. Ferguson, B. To, L. M. Gedvilas, M. J. Heben and J. L. Blackburn, Ultrasmooth, large-area, high-uniformity, conductive transparent single walled carbon nanotube films for photovoltaics produced by ultrasonic spraying, *Adv. Mater*., 2009, **21**, 3210–6.

40. L. Hu, H. S. Kim, J. Y. Lee, P. Peumans and Y. Cui, Scalable coating and properties of transparent, flexible, silver nanowire electrodes, *ACS Nano*, 2010, **4**, 2955–63.

41. S. L. Hellstrom, H. W. Lee and Z. Bao, Polymer-assisted direct deposition of uniform carbon nanotube bundle networks for high performance transparent electrodes, *ACS Nano*, 2009, **3**, 1423–30.

42. W. Gaynor, G. F. Burkhard, M. D. McGehee and P. Peumans, Smooth nanowire/polymer composite transparent electrodes, *Adv. Mater*. 2011, **23**, 2905–10.

43. C. H. Chung, T. B. Song, B. Bob, R. Zhu and Y. Yang, Solution-processed flexible transparent conductors composed of silver nanowire networks embedded in indium tin oxide nanoparticle matrices, *Nano Res.,* 2012, **5,** 805–14.

44. C. Sahin, A. E. Selen and U. H. Emrah, Optimization of silver nanowire networks for polymer light emitting diode electrodes, *Nanotechnology*, 2013, **24**, 125202–9.

45. P. Xu, A. S. Mujumdar and B. Yu, Drying-induced cracks in thin film fabricated from colloidal dispersions, *Drying Technol.* 2009, **27** 636–52.

46. H. Y. Yow, M. Goikoetxea, L. Goehring and A. F. Routh, Effect of film thickness and particle size on cracking stresses in drying latex films, *J. Colloid Interface Sci.,* 2010, **352**, 542–8.

47. E. Shi et al, TiO_2-coated carbon nanotube-silicon solar cells with efficiency of 15%, *Sci. Rep*., 2012, **2***,* 884.

Chapter IIIB

Solution Processed Fabrication of Cu Wire Mesh

Summary

Virtually unlimited and highly interconnected Cu wire networks have been fabricated on PET substrates with sheet resistance of <5 Ω/sq and transmittance of ~75%, as alternatives to the commonly used ITO based electrodes. This is a four step process involving deposition of commercially available colloidal dispersions onto PET, drying to induce crackle network formation, nucleating Au or Pd seed nanoparticles inside the crackle regions, washing away the sacrificial layer and finally, depositing Cu electrolessly or by electroplating. The formed Cu wire network is continuous and seamless, and devoid of crossbar junctions, a property which brings high stability to the electrode towards oxidation in air even at 130 °C. The flexible property of the PET substrate is easily carried over to the TCE. The sheet resistance remained unaltered even after a thousand bending cycles. The as-prepared Cu wire network TCE is hydrophobic (contact angle, 80°) which, upon UV–ozone treatment, turned to hydrophilic (40°).

IIIB.1 Introduction

With the developments in optoelectronics during last few decades, ITO has become the most suitable transparent conducting material in optoelectronic devices, namely solar cells [1], displays [2], organic light emitting diodes [3] and touch screens [4]. As mentioned in Chapter I, there are, however, some critical issues associated with ITO related to its mechanical, high temperature and chemical instabilities and brittleness [5-7]. The increasing price of indium is indeed prohibitive for large area applications. Although many oxide formulations such as Cu_2O, PbO and Al or Ga doped ZnO, have been developed by physical and solution based processing [8], these alternative oxides are still not able to meet the required standards of a transparent conducting electrode (TCE) in terms of the sheet resistance (10 Ω/sq) and transmittance (90%), as does ITO. In the last few years, there have been several new generation TCEs based on nanomaterials such as graphene films [9,10], carbon nanotube (CNT) [11–14],

Paper based on this study: J. Mater. Chem.C, 2, 2089 (2014)

metal nanowire networks [15–17], and nanofibers [18] as well as thin metal films [19]. Although carbon as a material is inexpensive and abundant, the process of conversion to useful forms, CNTs or graphene, is highly energy intensive and the cost is prohibitive, particularly for large area applications [20]. Often, physical deposition methods from the vapour phase are involved, which could be time consuming and expensive. On the other hand, Ag nanowires can be produced in large quantities by simple solution processing [17], but Ag as a material is scarce and expensive. The best alternative would be to use a cheaper metal such as Cu without much compromise in other factors. Copper has a resistivity of 1.59 nΩ m (Ag, 1.67 nΩ m) and is abundant (1000 times the abundance of Ag) [21]. There has been some effort in the literature towards TCE fabrication using Cu in the form of grating structures, either by physical deposition [22] or through a solution route [23]. The other methods include electrospun fibres [15,18,24] or solution dispersed Cu nanowires [25–31]. Zhang et al., for example, developed a novel recipe for synthesizing ultra-long single crystalline Cu nanowires and dispersing them over a transparent substrate [26]. The nanowire based electrodes, in general, suffer from junction resistance and the situation is even worse with Cu due to its surface being highly reactive [27]. A Cu nanowire TCE can become oxidised in ambient operation, giving it a very high sheet resistance [28]. Kholmanov et al. synthesized Cu-graphene hybrid electrodes to prevent oxidation of Cu nanowires [29]. Meanwhile, Rathmell et al. covered the Cu fibres with PVA to prevent the surface oxidation [30,31], Hsu et al. performed atomic layer deposition of aluminium zinc oxide and passivated the surface of Cu nanofibers [27]. While passivating nanowire surface should enhance stability, the root cause appears to be the junction resistance which triggers the oxidation process [32]. It is considered to be important to address this issue.

IIIB.2 Scope of the present investigation

This chapter proposes a new way of making alternate electrode entirely by solution processing. The conducting material is Cu in the form of a well-connected wire network on PET, with no crossbar junctions, commonly found in nanowire network based electrodes. Given that this is a solution process, the transmittance values are commendable (~ 75%) and low sheet resistance (<5 Ω/sq). As the

electrode is junction free, it exhibits extra stability towards oxidation at annealing temperatures. This is indeed a novel finding which should make this study distinct from other such studies in the literature (which have been compared in this chapter). The wetting property of the electrode can be tuned by UV exposure.

IIIB.3 Experimental Details

Fabrication of crack template by rod coating

A commercial SiO_2 nanoparticle dispersion termed here as CP-1 is a crackle paint (Premium Coatings & Chemicals, India) and CP-2 is a water based acrylic resin sold as a cosmetic product (Ming Ni Cosmetics Co., Guangzhou, China). Typically, CP-1 or CP-2 dispersion in diluter (0.3 g ml^{-1}) was rigorously ultrasonicated for 30 min. The dispersion was left overnight in an air-tight bottle. The suspended solution was extracted as needed and ultrasonicated prior to drop, spin or rod coating on a PET substrate (80 μm thick). The substrate was then left to dry in air while a crackle network pattern formed spontaneously in the coated layer. The crackle precursor formulations (CP-1 and CP-2) contain film forming agents that enable smooth and uniform coating of the template over large areas as shown in Figure IIIB.3. Moreover, the solvents present in the CP impart additional qualities. For example, ethyl acetate improves the spreading while pentyl acetate helps in levelling off the dispersion.

Fabrication of Cu wire network based TCE

For metal deposition by electroplating (EP) and electroless (ELD) methods, a thin Au layer was deposited over the crackled network by sputtering technique. This acts as a seed layer for further deposition of copper by EP and ELD. The copper electroplating solution is prepared by dissolving 230 g of copper sulphate solution in 1 L of water, and to that 140 mL of conc. H_2SO_4 was added. To electroplate Cu over the Au network on PET, the substrate with the Ag contact was taken as the cathode and Cu foil as the anode. By applying a potential between the two electrodes, Cu was deposited over the Au seed network and the reaction was stopped after obtaining the required thickness. The Cu plating bath used for the electroless deposition was composed of 3 g of $CuSO_4$, and 14 g of sodium potassium tartrate mixed with 4 g of NaOH in 100 mL of distilled water (solution A). Solution B was an aqueous formaldehyde solution (37.2 wt%). Solutions A and B were mixed in a 10 : 1 ratio. To

deposit Cu, the Au seed network on PET was immersed in the freshly prepared mixture for 10 min at room temperature. The plating process was stopped by removing the sample and rinsing with distilled water.

Flexibility test

The flexibility tests were performed for Cu/PET based electrodes using a custom designed setup with one side fixed while the other was kept movable using a screw gauge attachment. Silver epoxy adhesive was used for making contact pads on both sides of the Cu/PET electrode. The resistance change during bending at different bending radii was recorded through a digital multimeter (Test Link, India) interfaced with a computer using DMM viewer software. The stability of the electrodes over 1000 bending cycles (sinusoidal) was tested at a rate of 0.05 Hz with a bending radius of 4 mm.

IIIB.4 Results and Discussion

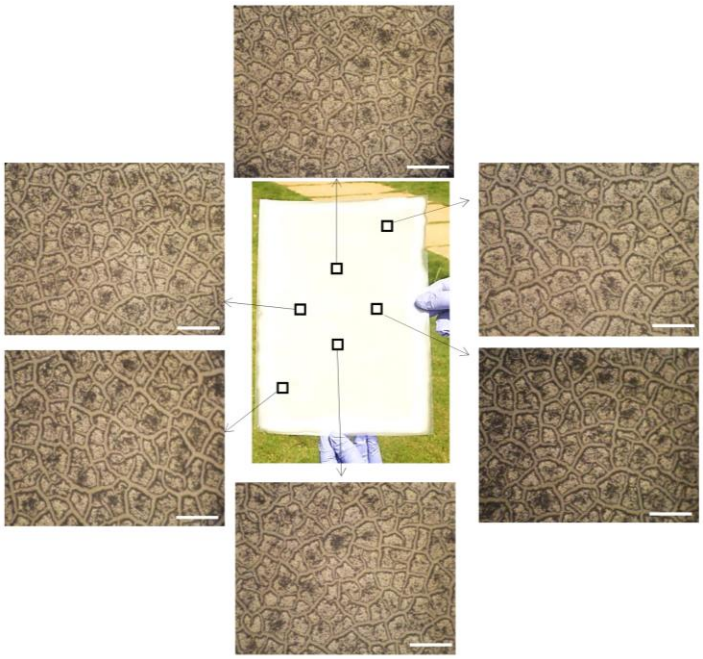

Figure IIIB.1 Photograph of crackle template formed from CP-1 on a A4-size PET substrate (centre). Optical micrographs taken from different positions of the template show crackles formed uniformly with high level of interconnection all over the substrate. Scale bar 1 mm.

A colloidal dispersion upon drying on a substrate tends to crack due to the stress induced by solvent evaporation [33]. A well-formed crack pattern may be in the

form of a network with crack regions exposing the substrate surface underneath, which is termed as a crackle network. The crackle network template is highly scalable and based on the colloidal particle size, concentration of the dispersion and the template thickness, a crackle network of a given length scale can be achieved over large areas with a high degree of uniformity (Figure IIIB.1). The crackle networks of two different length scales have been produced, using two crackle dispersions; both are inexpensive and available commercially (Figure IIIB.2 and 3).

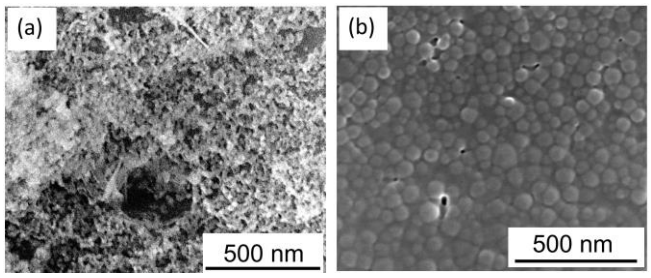

Figure IIIB.2 SEM images of crackle dispersions showing (a) colloidal SiO_2 in CP-1 and (b) acrylic resin in CP-2.

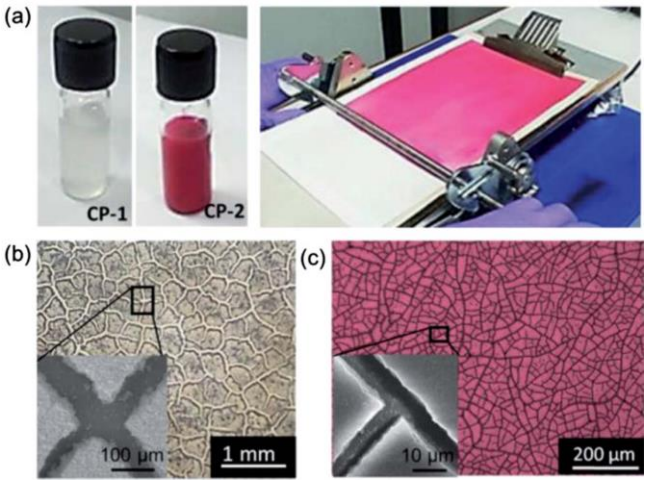

Figure IIIB.3 Fabrication of crackle template: (a) crackle dispersions used in this study are commercially available, a wall paint containing colloidal SiO_2 (CP-1) and a cosmetic containing acrylic emulsion (CP-2). Both are amenable to rod coating. High magnification photographs along with SEM images (in insets) of crack network formed in CP-1 (b) and (c) CP-2.

The CP-1 dispersion, which is essentially a dispersion of SiO_2 nanoparticles (20 nm, see Figure IIIB.2a), is available as a wall paint while CP-2 is an acrylic resin (50 nm, Figure IIIB.2b). In each case, the concentration of the crackle dispersion was optimized in such a way that upon drying, it resulted in a dried layer hosting highly interconnected cracks. The crackle dispersions were pipetted on PET substrates and spread over the surface using a Meyer rod coater (Figure IIIB.3a). First, it resulted in a wavy wet layer of thickness 45 μm which settled into a smooth and uniform film as the solvent evaporated in few seconds. As drying continued, a crackle network appeared spontaneously (Figure IIIB.3b and c) due to the internal stresses in the film.

Under the given experimental conditions, CP-1 produced cracks with widths in the range of 50–100 μm while CP-2 gave rise to much finer cracks (4–8 μm). Moreover, the crackle width can be altered by optimizing the concentration of the CP dispersion (Figure IIIB.4). In both cases, the cracks went deep down to the substrate surface (see insets in Figure IIIB.3b and c). These crack patterns were exploited as sacrificial templates for the site selective deposition of Cu metal.

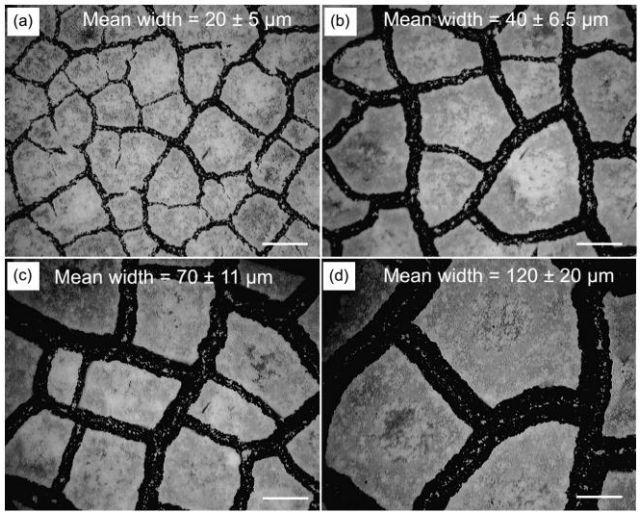

Figure IIIB.4 Optical microscopy of crackle network obtained for different concentrations of CP-1 dispersion. (a) 0.15 g/mL (b) 0.3 g/mL (c) 0.6 g/mL and (d) 0.9 g/mL. The estimated mean crackle widths are 20, 40, 70 and 120 μm, respectively. In each case, 700 μL dispersion was used for 5 cm^2 area. Scale bar: 200 μm.

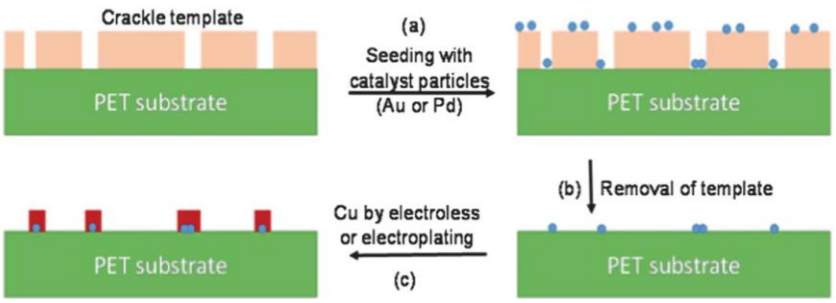

Figure IIIB.5 Schematic showing Cu metal wire network based TCE fabrication using solution route. (a) Seeding of catalyst particles in the crackle grooves, (b) removal of cracked template, (c) Cu deposition by electroless method or by electroplating.

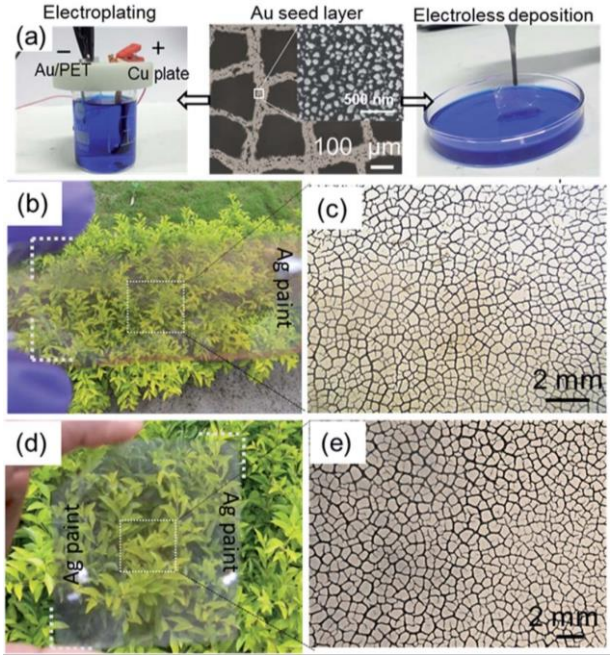

Figure IIIB.6 (a) Cu deposition over Au seeds by electroless and electroplating methods. Photographs of the substrates electroplated (b) and electrolessly deposited (d) with Cu, and the respective magnified microscopic images are in (c) and (e).

Selective deposition of Cu in the crackle regions was achieved by first depositing Pd or Au catalyst particles over the dried template (Figure IIIB.5a). As ultralow quantities of the metal catalyst are sufficient for Cu deposition, the additional cost of catalyst per unit area of the substrate is rather low. The CP-1 and CP-2 substrates were dosed with Pd by dipping the substrate carrying the crackle template in $PdCl_2$

solution (3 mM in ethylene glycol) and heating to 120 °C for 30 min to nucleate Pd catalyst particles. Alternatively, Au sputtering was also used for seeding the catalyst particles. Au sputtering is considered highly applicable for roll-to-roll coating [34], unlike other physical methods. The crackle layer was then washed away with acetone (CP-1) or chloroform (CP-2) to leave catalyst particles in the crackle network pattern on the substrate as shown in Figure IIIB.5b. This was followed by electroless and electroplating deposition of Cu to the desired thickness (see Figure IIIB.5c and Experimental section for details).

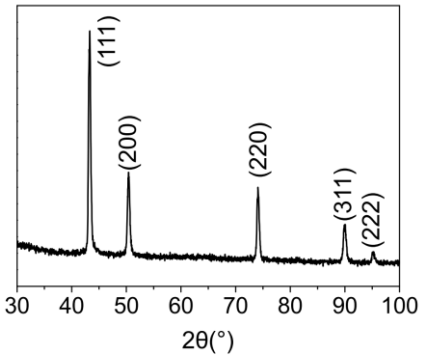

Figure IIIB.7 X-ray diffraction pattern of a Cu network formed from CP-1.

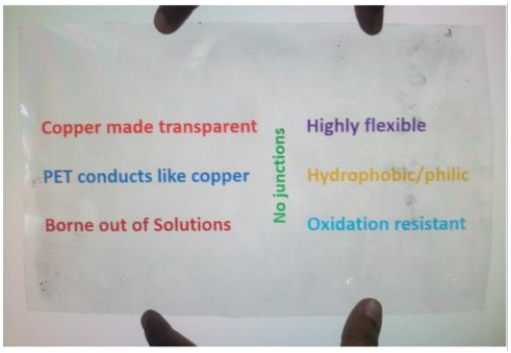

Figure IIIB.8 Large area Cu wire network/PET transparent conducting electrode prepared from CP-1 crackle precursor, by dipping the Au seed layer in Cu electroless bath solution. Underneath is a computer screen display and the text is clearly visible. The measured transmittance is ~75% and sheet resistance, 4.5 Ω/sq.

The process of Cu deposition on Au seed particles in the CP-1 crackle network is illustrated in Figure IIIB.6. Both electroplating and electroless depositions could be

easily achieved on the patterned Au seed layer. For electroplating (Figure IIIB.6a, left), the Au seed coated substrate was made the working electrode and a Cu plate was the counter electrode in a Cu plating bath containing copper sulphate (0.2 g mL^{-1}) and sulphuric acid (0.050 g mL^{-1}) solution. The thickness could be controlled by the deposition time and the applied voltage. For the electrode shown in Figure IIIB.6b and c, the deposition was carried out with an applied voltage of 0.6 V for 45 s to result in a Cu network ~ 300 nm thick. The Cu metal was deposited selectively on Au such that regions devoid of Au were kept clear to result in a transparent electrode (Figure IIIB.6b). Figure IIIB.6c shows a highly interconnected Cu network formed by electroplating, further confirmed by XRD (Figure IIIB.7). In electroless deposition, the Au network containing substrate was dipped in a plating bath (copper : formaldehyde, 10 : 1) for different times without any external voltage and Cu networks of varying thicknesses were obtained (Figure IIIB.6a, right). The photograph in Figure IIIB.6d shows a transparent electrode obtained with electroless deposition with the network image in Figure IIIB.6e. The network formed is continuous and extends over a large area (Figure IIIB.8).

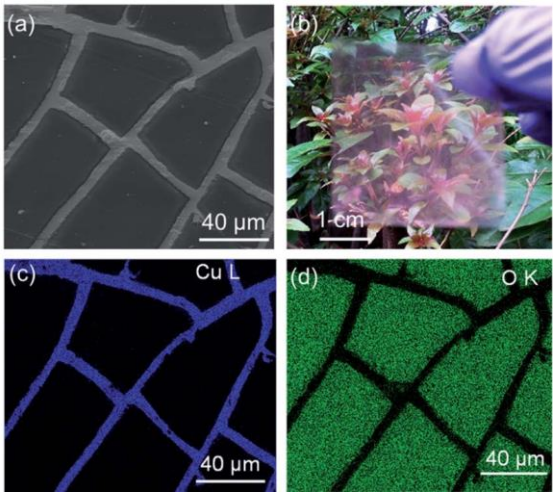

Figure IIIB.9 (a) SEM image of Cu electrolessly deposited on Pd; (b) a photograph of a flowering plant as seen through a Cu wire network TCE. EDS maps corresponding to (c) Cu L and (d) O K for the SEM image in (a). In the O K map, the Cu network region is dark indicating no detectable surface oxidation, while the signal from the PET substrate may be seen from other regions.

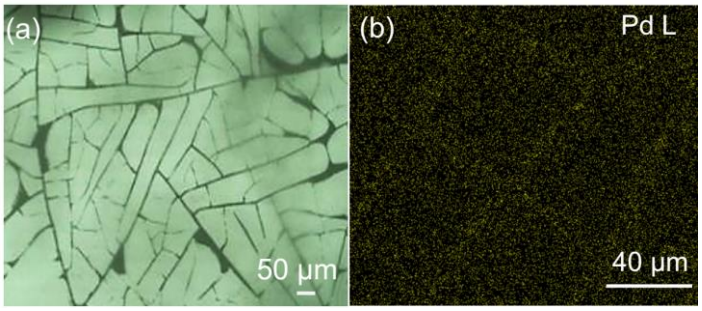

Figure IIIB.10 (a) Optical microscopic images of Pd seed layer formed over CP-2 crackle. (b) Pd L EDS map after Cu electroless deposition over Pd seed layer. Only a weak Pd signal may be seen.

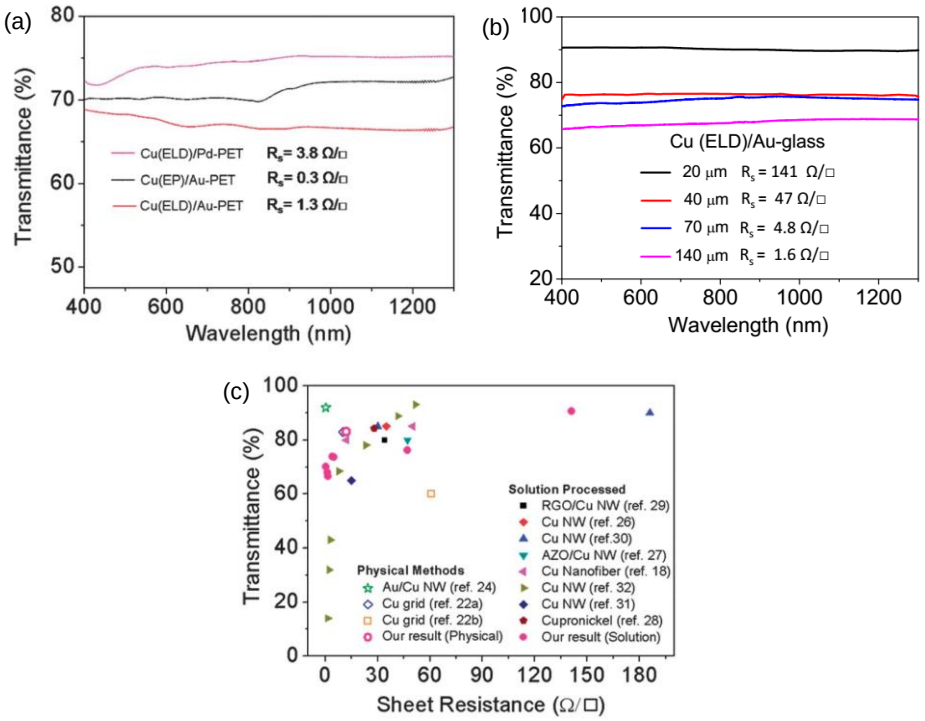

Figure IIIB.11 (a) Transmittance spectra and resistance values of the various Cu wire network based TCEs; EP and ELD refer to electroplating and electroless deposition, respectively. The seed particle (Pd or Au) is indicated. Sheet resistance values are also shown. (b) Transmittance spectra and resistance values of Cu network TCEs prepared from different crackle width templates. (c) Transmittance (at 550 nm) versus sheet resistance for the TCEs prepared in this study and their comparison with Cu based TCEs from the literature. Those produced by a physical method are shown with open symbols and those from solution processing are represented by solid symbols.

The crackle network obtained in CP-2 was replicated with a Pd seed layer (Figure IIIB.9a) by thermal decomposition of $PdCl_2$ dosed from solution and washing away the crackled layer with chloroform. The substrate was then dipped in an electroless plating bath wherein uniform coverage of Cu took place to give rise to a Cu wire network as shown in Figure IIIB.9a. A view of the substrate carrying the network (Figure IIIB.9b) clearly shows its transparency to the visible light. The presence of Cu over the Pd seed layer is confirmed by EDS mapping (Figure IIIB.9c and d). As expected, the Pd seed layer gives very low signal as the layer is quite thin (Figure IIIB.10) and buried underneath. The Cu L signal clearly indicates that the surface is composed of Cu with no detectable signal from oxidation (see Figure IIIB.9d).

Figure IIIB.11a and b shows the transmittance spectra that are nearly flat and featureless over the entire visible region, even extending to the IR region. The flat transmittance is advantageous for display devices while transmittance in the IR range is useful for solar application. The transmittance at 550 nm is 70%, 68% and 74%, for Cu EP and ELD (referring to electroplating and electroless deposition, respectively) on the CP-1 pattern and Cu ELD on the CP-2 electrodes, respectively. The sheet resistance values were very low, ~ 0.3 (EP, CP-1), 1.3 (ELD, CP-1) and 3.8 Ω/sq (ELD, CP-2). In the case of EP, the deposited metal tends to closely pack with good electrical connectivity between the neighbouring grains. Under the experimental conditions employed, the thickness of Cu deposited is greater in case of EP (~300 nm) compared to ELD (~100 nm). This resulted in a lower resistance for EP deposited electrodes as compared to ELD. In Figure IIIB.11c, the performance of this TCEs were compared with Cu nanowire based TCEs reported in the literature (from both physical and solution processing). It is clear from the plot that the performance parameters obtained in this study well compare and are somewhat better than the values reported for solution processed TCEs.

In solution processing, a small amount of non-specific deposition is unavoidable (Figure IIIB.12) which lowers the transmittance value. As is obvious, the physical deposition of Cu can be directly performed over the crackle template giving rise to a TCE with higher transmittance (Figure IIIB.13). However, resorting to physical

deposition would be a big compromise on the cost and simplicity offered by solution processing.

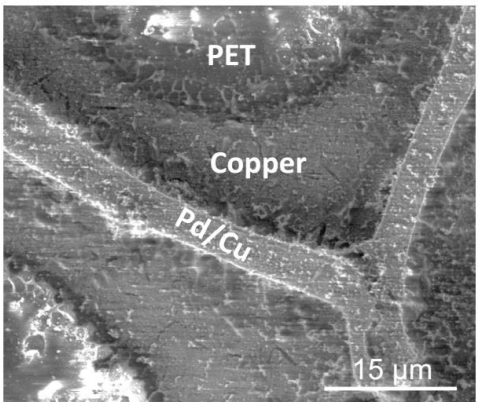

Figure IIIB.12 Excessive dipping in Cu bath solution can lead to non-specific deposition as shown in the image.

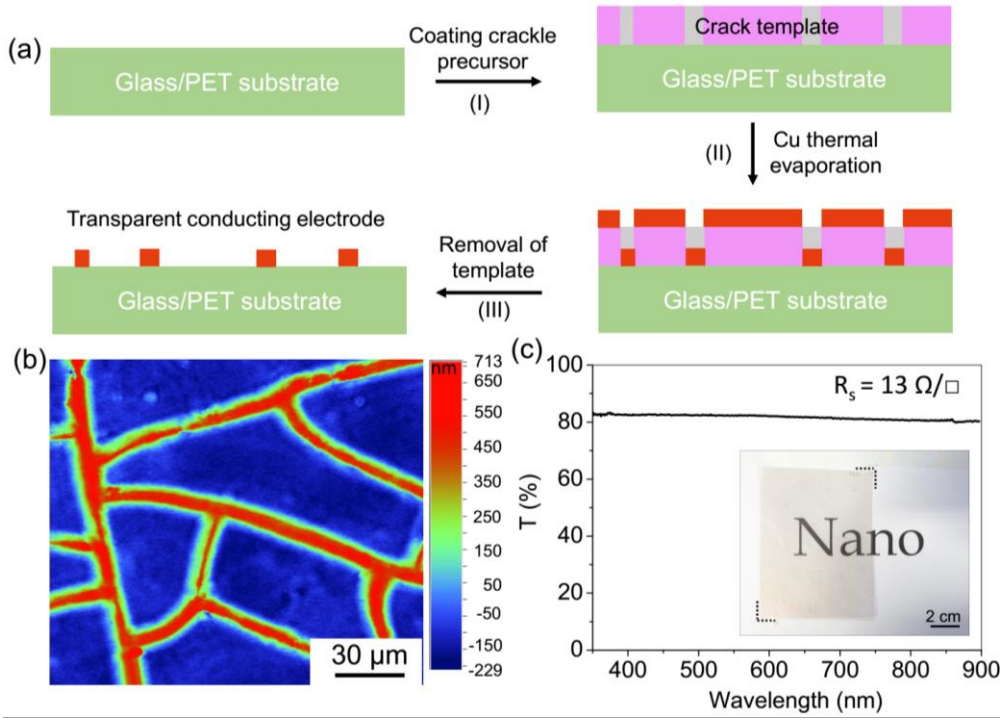

Figure IIIB.13 (a) Schematic showing the fabrication of TCE by physical deposition of metal over a crackle template. (b) Optical profiler image of Cu TCE fabricated from CP-2. (c) Transmittance of the Cu wire network. Photograph of the sample is shown in the inset.

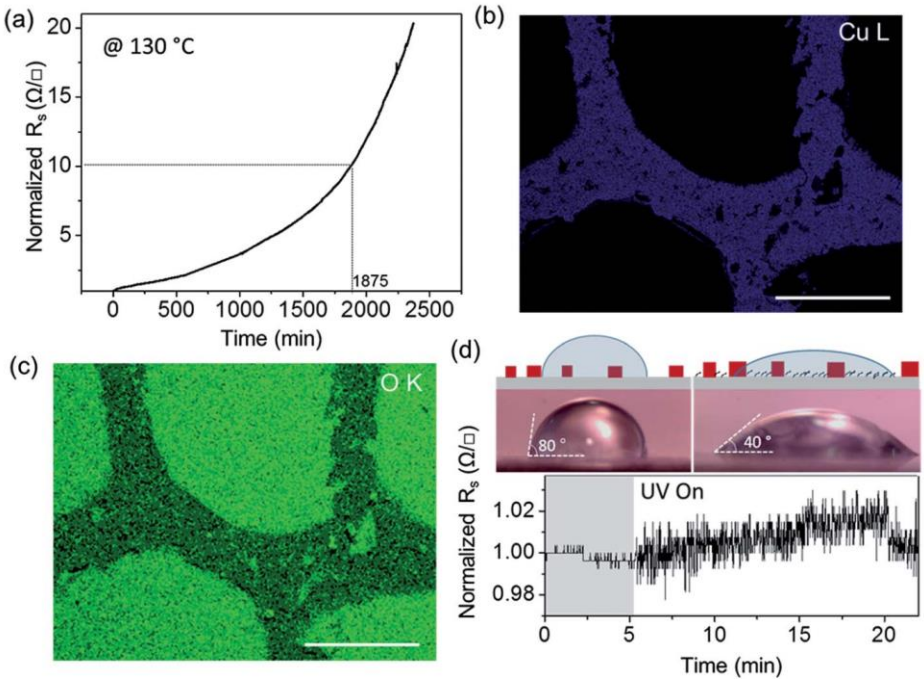

Figure IIIB.14 Thermal oxidation stability: (a) variation in the normalized sheet resistance with time at 130 °C. (b) Cu L and (c) O K EDS maps at the end of the heat treatment. Scale bar 200 μm. (d) Variation in the normalized sheet resistance with time for another TCE, under UV–ozone treatment with the top insets showing water contact angle measurements before and after UV–ozone exposure.

Stability against oxidation is an important aspect of a Cu wire network based TCE, as many devices require annealing of the overlaid active layer at mild temperatures. This is done also to improve the coupling between the active layer and the electrode. This aspect has been examined in detail by heating a TCE (Cu ELD/PET) at 130 °C on a hot plate under ambient conditions while monitoring the variation in its resistance with time (see Figure IIIB.14). As can be seen from Figure IIIB.14a, the change in the resistance is very slow. Eventually, there was some oxygen uptake on the Cu wire surface (compare Figure IIIB.14c with 9d). Thus, it took ~ 31 hours to increase the resistance by an order of magnitude. This observation is remarkable compared to literature results, where an order of magnitude increase in the sheet resistance in just a few hours is quite common upon heating to mild temperatures [28].

In some examples, Cu wires needed extra treatment such as passivation [27, 29] or thermal annealing in vacuum [32]. Hydrogen annealing above 300 °C is often adopted for obtaining good conductivity [18], but it is not feasible in the case of flexible electrodes using substrates such as PET. The enhanced stability of TCEs towards oxidation is understandable as these Cu wire networks are virtually devoid of crossbar junctions, which is found in TCEs prepared by depositing nanowire dispersions. Crossbar junctions may behave like hotspots with respect to oxidation. In these TCEs, the Cu wires are highly interconnected and the junctions are seamless (Figure IIIB.9a) and therefore, the junction resistance is no longer a serious concern. This explains the enhanced stability of the TCE even at elevated temperatures. At room temperature, the TCE showed only 2% change in resistance over a period of 4 months. The relatively higher wire widths may also contribute to enhanced stability [26].

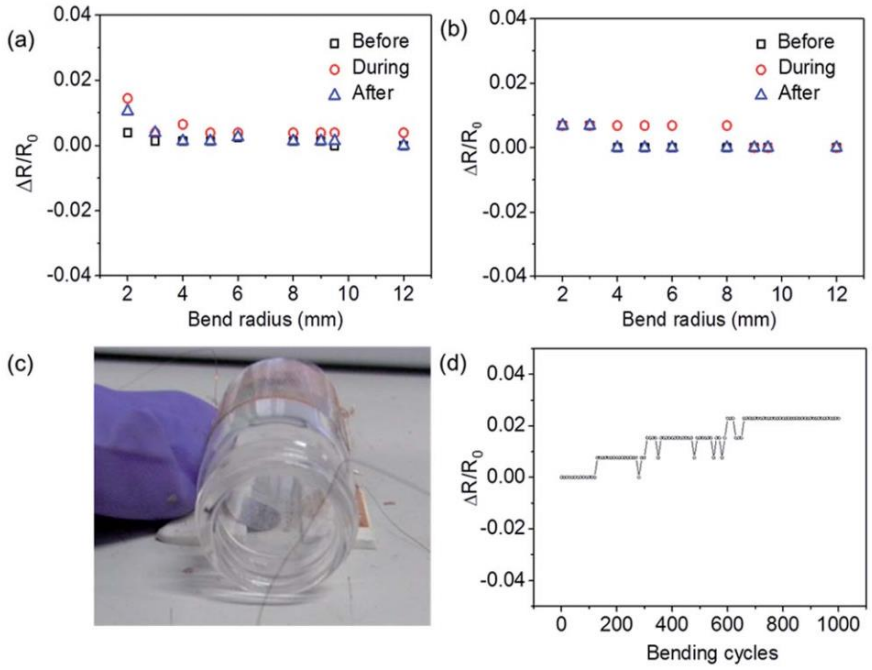

Figure IIIB.15 Flexibility tests. Variation in the normalised sheet resistance as Cu ELD/PET (a) and Cu EP/PET (b) were bent to different radii. (c) A photograph showing a TCE bent around a vial of diameter 12 mm. (d) Variation in the normalised sheet resistance with a large number of bending cycles with a bending radius of 4 mm. Every 10th data point is shown for clarity.

The wetting behaviour of Cu TCEs has been explored. A TCE used as a transparent heater, if hydrophobic, will have the advantage of self-cleaning. The hydrophilic nature of a TCE plays an important role at the interface with an electrolyte as in an electrochromic device. In either case, the back side being hydrophobic is clearly an advantage. The substrate, PET, used in this study does exhibit high water contact angles (~ 80°). The as-prepared Cu ELD/PET also exhibited a similar contact angle (see left inset in Figure IIIB.14d), as the metal covered region is only a small fraction (~ 25%). In order to decrease the contact angle, the exposed PET region of TCE was treated with UV–ozone plasma for 10 min (at 4.6 mW cm^{-2} with an ozone level of 180 mg m^{-3}) which should enhance the wetting behaviour [35]. Following this treatment, the contact angle decreased to ~ 40° (see right inset in Figure IIIB.14d). However, the resistance of the TCE was unchanged implying that the Cu wire network was practically unaffected.

Due to the extended interconnection between the wire networks without any junctions, the electrodes exhibit excellent flexibility. The bending of the electrode was performed at different bend radii followed by several bending cycles. The Cu wire network electrode prepared by ELD as well as EP did not show any significant change in resistance on bending to different radii from 12 mm to 2 mm and after release (Figure IIIB.15a - c). The overall resistance of the electrodes was unaffected. The Cu wire network was subjected to several bending cycles as well, to test the mechanical stability of the electrode (Figure IIIB.15d).

IIIB.5 Conclusions

In this study, a solution based method to produce a large area TCE consisting of a Cu wire network on a flexible PET substrate was developed. The Cu wire network was obtained by electroplating or by electrolessly coating Cu onto a sacrificial template hosting a crackled network. Pd or Au nanoparticles were used as seeds to grow Cu. Commercially available, inexpensive colloidal dispersions which upon coating on PET and drying, spontaneously formed networks of crackles. Cu wire network TCEs were produced at two different length scales (wire widths ~ 10 and 100 μm) by choosing different crackle dispersions and optimising the coated layer thickness. The TCEs with broader wire networks may be of interest in large panel

displays, while finer networks may be useful in touch screens and solar cells. The Cu TCEs produced in this study exhibit high transmittance (~ 67–75%) with low sheet resistance values (<5 Ω sq^{-1}). With 141 Ω sq^{-1}, transmittance of ~ 90% was achieved. These values compare well with those from Cu TCEs reported in the literature based on solution processing. Large area (~ A4 size) TCEs have also been made by this method. Importantly here, the Cu wire networks were highly interconnected in a single plane with no crossbar junctions, leading to extreme stability towards oxidation in air, even at elevated temperatures. The TCEs were also found to be highly flexible, a property borrowed from the PET substrate, but with no appreciable change in resistance upon increasing the number of bending cycles. The water wetting properties of the TCE could be switched from hydrophobic to hydrophilic by UV– ozone treatment, importantly, without changing the resistance. Being a solution process, the method should be of high significance for the optoelectronics industry. Future efforts will include solution based processing without the use of metal catalysts [36].

References

1. C. G. Granqvist, *Sol. Energ. Mat. Sol. C.*, 2007, **91**, 1529.
2. M. Katayama, *Thin Solid Films*, 1999, **341**, 140.
3. Y. Yang et al., *Adv. Mater.*, 2004, **16**, 321.
4. U. Betz, M. K. Olsson, J. Marthy, M. F. Escola and F. Atamny, *Surf. Coat. Tech.*, 2006, **200**, 5751.
5. C. Y. Lim, J. K. Park, Y. H. Kim and J. I. Han, *J. Intern. Coun. Elect. Engg.,* 2012, **2**, 237.
6. O. J. Gregory, Q. Luo, E. E. Crisman, *Thin Solid Films*, 2002, **406**, 286.
7. Y. Gassenbauer and A. Klein, *J. Phys. Chem. B*, 2006, **110**, 4793.
8. R. M. Pasquarelli, D. S. Ginley and R. O' Hayre, *Chem. Soc. Rev.*, 2011, **40**, 5406.
9. S. Bae, et al*., Nat. Nanotechnol.*, 2010, **5**, 574.
10. J. Zhang, P. A. Hu, X. Wang, Z. Wang, D. Liu, B. Yangc and W. Caoc, *J. Mater. Chem.*, 2012, **22**, 18283.
11. Q. Zheng, B. Zhang, X. Lin, X. Shen, N. Yousefi, Z. D. Huang, Z. Lia and J. K. Kim, *J. Mater. Chem.*, 2012, **22**, 25072.

12. C. M. Aguirre, S. Auvray, S. Pigeon, R. Isquierdo, P. Desjardins, R. Martel, *App. Phys. Lett.* 2006, **88**, 183104.

13. D. S. Hecht, L. Hu, G. Irvin, *Adv. Mater.* 2011, **23**, 1482.

14. R. Wang, J. Sun, L. Gao and J. Zhang, ACS Nano, 2010,**4**, 4890.

15. H. Wu et al., *Nat. Nanotech.*, 2013, **8**, 421.

16. A. Kim , Y. Won, K. Woo, C. H. Kim, and J. Moon, *ACS Nano*, 2013, **7**, 1081.

17. J. Y. Lee, S. T. Connor, Y. Cui, P. Peumans, *Nano Lett.*, 2008, **8**, 689.

18. H. Wu, L. Hu, M. W. Rowell, D. Kong, J. J. Cha, J. R. McDonough, J. Zhu, Y. Yang, M. D. McGehee and Y. Cui, *Nano Lett.*, 2010, **10**, 4242.

19. D. S. Ghosh, T. L. Chen and V. Pruneri, *Appl. Phys. Lett.*, 2010, **96**, 091106.

20. A. Reina et al., *Nano Lett.*, 2008, **9**, 30.

21. D. R. Lide, CRC handbook of chemistry and physics, 85th ed., CRC press, Boca Raton, FL 2004.

22. (a) M. G. Kang, M. S. Kim, J. Kim and L. J. Guo, *Adv. Mater.*, 2008, **20**, 4408; (b) D. S. Ghosh, R. Betancur, T. L. Chen, V. Pruneri, J. Martorell, *Sol. Energ. Mater. Sol. Cells*, 2011, **95**, 1228.

23. R. Gupta and G. U. Kulkarni, ACS Appl. Mater. Interfaces, 2013, 5, 730.

24. P. Hsu, S. Wang, H. Wu, V. Narasimhan, D. Kong, H. R. Lee, Y. Cui, *Nat. Commun.*, 2013, **4**, 2522.

25. C. Sachse, N. Weib, N. Gaponik, L. M. Meskamp, A. Eychmuller and K. Leo, *Adv. Energy Mater.*, 2013, **4,** 1300737.

26. D. Zhang, R. Wang, M. Wen et al., *J. Am. Chem. Soc.*, 2012, **134**, 14283.

27. P. C. Hsu et. al., *ACS Nano*, 2012, **6**, 5150.

28. A. R. Rathmell, M. Nguyen, M. Chi and B. J. Wiley, *Nano Lett.*, 2012, 12, 3193.

29. I. N. Kholmanov, S. M. Domingues et al, *ACS Nano*, 2013, DOI: 10.1021/nn3060175.

30. A. R. Rathmell, S. M. Bergin, Y. L. Hua, Z. Y. Li, and B. J. Wiley, *Adv. Mater.*, 2010, **22,** 3558.

31. A. R. Rathmell, B. J. Wiley, *Adv. Mater.*, 2011, **23**, 4798.

32. H. Guo, N. Lin et al., *Sci. Rep.*, 2013, **3**, 2323.

33. H. Kim et al. *J. Appl. Phys.***1999***, 86*, 6451-6461.

34. M. Manceau, D. Angmo, M. Jørgensen and F. C. Krebs, Organic Electronics, 2011, 12, 566.

35. I. K. Moon, J. I. Kim, H. Lee, K. Hur, W. C. Kim and H. Lee, Sci. Rep. 2013, 3, 1112, doi:10.1038/srep01112.

36. W. P. Dow, G. L. Liao, S.E. Huang and S.W. Chen, J. Mater. Chem., 2010, **20**, 3600.

Chapter IIIC

Fabrication of Oxidation-Resistant Metal Wire Networks

Summary

Roll and spray coating methods have been employed for the fabrication of highly oxidation resistant transparent and conducting electrodes by a simple solution process using crackle lithography technique. A crackle paint-based precursor was spray-coated to produce highly interconnected crackle network on PET roll mounted on a roll coater with web speed of 0.6 m/min. Ag TCE with a transmittance of 78% and sheet resistance of ~20 Ω/sq was derived by spraying Ag precursor ink over the crackle template followed by lift-off and annealing under ambient conditions. The Ag wire mesh was stable toward bending and sonication tests but prone to oxidation in air. When electrolessly coated with Pd, its robustness toward harsh oxidation conditions was enhanced. A low-cost transparent electrode has also been realized by using only small amounts of Ag as seed layer and growing Cu wire mesh by electroless method. Thus, made Ag/Cu meshes are found to be highly stable for more than a year even under ambient atmosphere.

IIIC.1 Introduction

Transparent conducting electrodes (TCE) with excellent optoelectronic properties are key components in various devices such as touch screens [1,2], organic solar cells [3], smart phones [4], etc. Large area TCEs are increasingly in demand because of the increasing size of the active parts of these devices [5], and in this context, large area manufacturing techniques such as roll-to-roll gain significance. For example, large area flexible organic tandem solar cell modules have been achieved through a roll-to-roll process, recently [6,7]. Perovskite solar cells fabricated by slot-die coating technique yielded ~12% conversion efficiency, showing the possibility toward mass production using roll-to-roll method [8]. The roll-to-roll system has been used to deposit/grow materials such as carbon nanotubes (CNT) on aluminum strips which find use as electrodes in battery and supercapacitors [9,10]. In most optoelectronic devices, the use of a transparent electrode is a must. It has become fashionable to

Paper based on this study: ACS Appl.Mater. Interfaces 2015, 7, 27215−27222

make even the non-optoelectronic devices, transparent [11–13]. Obviously, it requires high-volume, large-area manufacturing of transparent conducting electrodes. In this direction, there have been efforts to make roll-to-roll TCEs with ITO, the most commonly used transparent material [14,15]. Limitations of ITO as discussed in Chapter I such as brittleness, high material and process cost, and chemical instability have prompted the search for alternate materials amenable for large area manufacturing.

With the recent successes in new generation materials such as graphene [16,17], conductive polymers [18], metallic grids [19], random networks of carbon nanotubes (CNTs)[20], metal nanowire networks (Ag, Cu) [21,22], their hybrids [23–26], etc., scalability and cost effectiveness of the TCE are set to be the next achievable goals. In comparison to ITO, new generation materials and their hybrids are highly versatile for large scale fabrication. Undoubtedly, Ag and Cu nanowire electrodes can be easily produced by additive coating method over large areas by roll coating. The hybrid nanostructures are also produced by multiple coating steps to address the issues of high surface roughness, poor adhesion to substrate, high junction resistance between the nanowires, and non-uniform distribution of nanowires on substrate. Despite the fact that fabrication of hybrid electrodes involves extensive processing and multiple optimization steps, it is still considered to be highly promising. For example, Ag nanowires embedded in graphene or in PEDOT:PSS are being obtained by a roll-to-roll process [24,25].

IIIC.2 Scope of the present investigation

Templating methods such as bubble template [27], electrospun fibers [28], etc., are considered superior compared to networks obtained by simple coating of the pre-synthesized nanowires on a substrate. The templating methods offer well-defined fill-factors across the substrate area as well as seamless junctions. Among the templating methods, metal meshes have been produced using a rather simple process involving crack templates [29,30] as discussed in Chapter IIIA and B. However, considering the advantages of metal mesh electrodes over nanowires and hybrid electrodes, it is worthwhile to explore the possibility for scale-up of template-based methods. There are no reports for the scalability of template-based methods, since it is a highly

challenging to obtain uniform templates over large areas. Previously it has been demonstrated that metal meshes by crack lithography method can be derived over areas limited only by the size of metal evaporation chamber [29,30]. The process can be extended to roll-to-roll only if metal can be brought by complete solution based processing. This work aims at scalability of crack lithography method by exploring different strategies shown in Scheme IIIC.1 that includes solution based deposition of metal in crackle grooves by a spray and roll coating process.

Scheme IIIC.1 Schematic Representation of Different Methods Adopted for Solution-Based Processing of Metal Electrodes from Crackle Lithography[a]

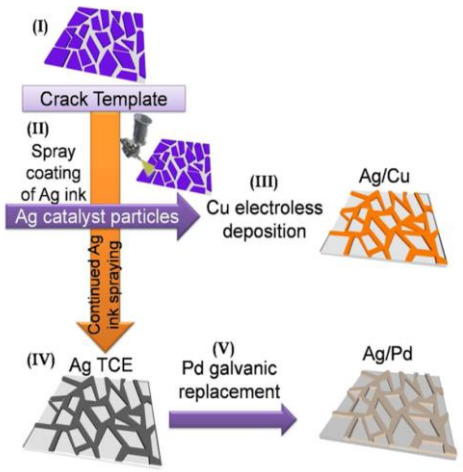

[a]Interconnected crack template (I) was obtained by spray coating crackle precursor over PET substrate. In step (II), Ag precursor ink was spray coated over template under ambient conditions. With a minimal usage of Ag as a seed layer in crackle grooves, the desired connectivity and conductivity was brought in by depositing Cu through an electroless process (III). Alternatively by continuing Ag deposition, highly interconnected conducting Ag wire network was obtained (IV). Highly oxidation resistant Ag/Pd mesh was obtained by a simple galvanic replacement process (V).

IIIC.3 Experimental Details

Fabrication of Crackle Template by Roll Coating

Commercially available silica nanoparticle-based dispersion (Premium Coatings and Chemicals, India) was used to obtain crackle template on PET substrate. The nanoparticle based dispersion was diluted with diluter to achieve the required concentration of 0.6 g/mL. The dispersion was always kept in an airtight bottle in

order to avoid evaporation of organic solvents. The crackle precursor (CP) was spray coated at the nitrogen pressure of ~25 psi on a clean and dried PET substrate. The custom designed roll coater as shown in Figure IIIC.1 was set to rotate at 2 rpm. The crackle precursor was spray deposited manually at a fixed distance of 5 cm with a 135A airbrush with 0.2 mm nozzle from United Traders, Bangalore. The crackle widths were tuned by increasing the wet layer thickness, controlled by number of passes of spray coating. The substrate was then left to dry in air while a crackle network pattern formed spontaneously in the coated layer. The crackle precursor formulations contain film forming agents that enable smooth and uniform coating of the template over large areas.

Fabrication of Ag Mesh

Ag precursor ink purchased from Kunshan Hisense Electronics Co., Ltd., China, 3 times diluted with isopropanol (IPA), was sprayed on the crackle network on PET maintained at 110 °C on the roller drum. All roll and spray coatings were performed in separate enclosure connected with exhaust in order to protect from strong smell of Ag precursor ink decomposition. According to the area of crackle template, appropriate volume of Ag ink was taken and was sprayed using spray gun. The spray gun was kept 5 cm away from the template for uniform spraying. The PET sheet carrying crackle template was detached from the roll coater and the template was removed by simple mechanical peeling. After the removal of template, Ag precursor ink was completely converted to metallic Ag by annealing at 140 °C for about 10 min in order to remove organic moieties from the Ag precursor ink.

Fabrication of Ag/Pd Mesh

Pd acetate (5.5 mM) in acetic acid was diluted with 20 mL of distilled water and maintained at 60 °C while depositing Pd by galvanic displacement over the Ag mesh. The deposition was carried out for 25 min.

Fabrication of Ag/Cu Mesh

To fabricate Ag/Cu TCE on PET substrate, Ag seed layer was formed on crackle grooves by spraying 5 times diluted Ag ink. After the removal of template and complete conversion to metallic Ag, it was dipped in Cu plating solution. The Cu plating bath was composed of solution A (1.5 g of $CuSO_4$ and 7 g of sodium

potassium tartrate mixed with 2 g of NaOH in 50 mL of distilled water) and formaldehyde as solution B. A freshly prepared plating solution (A:B = 10:1) was used for Cu electroless deposition on Ag seed layer. The plating process was stopped by taking out the sample from bath and rinsing with distilled water.

Characterization

Mechanical tests were performed by connecting electrical leads to DMM viewer software to record the change in resistance by interfacing a multimeter (Test Link, India) with a computer while performing test. A sonicator from Elmasonic P was used to perform ultrasonication test with a maximum power and at a frequency of 30 kHz. The bending tests were performed using a custom designed setup. After making contact pads with silver epoxy, one side of electrode was fixed, whereas other was kept movable to attain different bending radii with a help of screw gauge.

IIIC.4 Results and Discussion

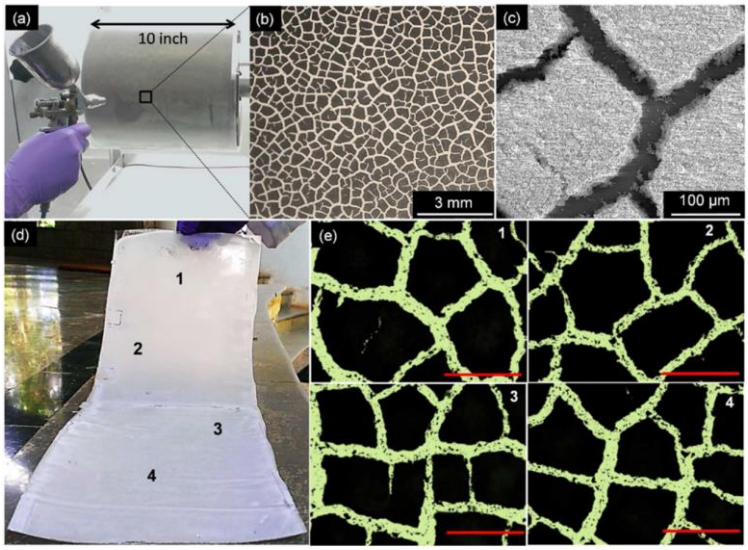

Figure IIIC.1 (a) Photograph demonstrating the formation of crackle template over large area PET substrate using the spray coat on roll technique. (b) Optical micrograph and (c) SEM image of thus formed interconnected crackle network. (d) Photograph of a roll of crackle template. The scratches observed are mainly due to template handling during photography. Few places on the sides are marks of the scotch tape used for sticking the PET substrate onto the roller drum. (e) Optical microscopic images of crackle template captured from different positions of the sample. Scale bar is 300 µm.

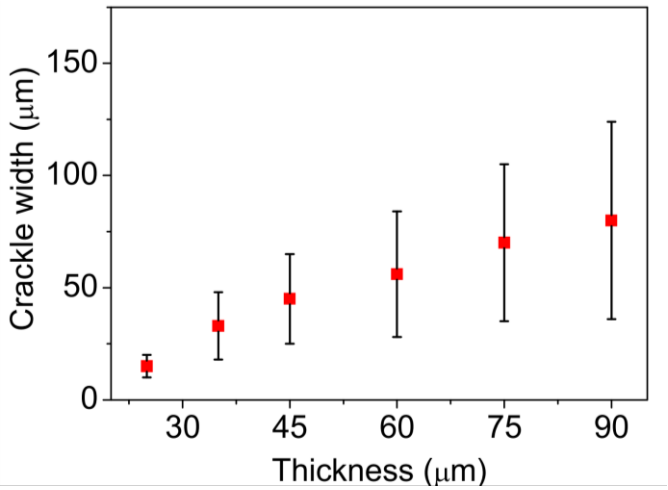

Figure IIIC.2 Dependence of crackle width on CP film thickness.

To develop a reliable method for producing solution-processed low-cost TCE over large area, a custom designed roll coater was employed. The silica nanoparticle based dispersion (CP) used for crack template formation was sprayed directly at the pressure of 25 psi on PET substrate wrapped around a 10 inch roller rotating at 2 rpm under ambient conditions (Figure IIIC.1a). The spray continued for over 5 passes such that the desired thickness for the interconnected crackle template could be achieved. The processing speed was 0.6 m/min. Once the precursor dried completely, highly interconnected spontaneously formed cracks were observed as shown in Figure IIIC.1b and c. The crackle widths were typically in the range of 50–150 μm. The thickness of the dried CP layer is dependent on the number of spray passes while other experimental conditions remain similar. An increase in the number of passes (3–15) led to higher thickness of the dried CP and hence wider cracks (150–180 μm) (see Figure IIIC.2). These cracks were down to the substrate which is term as crackles, and these crackle patterns were used as templates for metal deposition. Photograph of thus formed crackle template on a roll of PET is shown in Figure IIIC.1d. The optical micrographs of crackles formed at different positions are shown in Figure IIIC.1e.

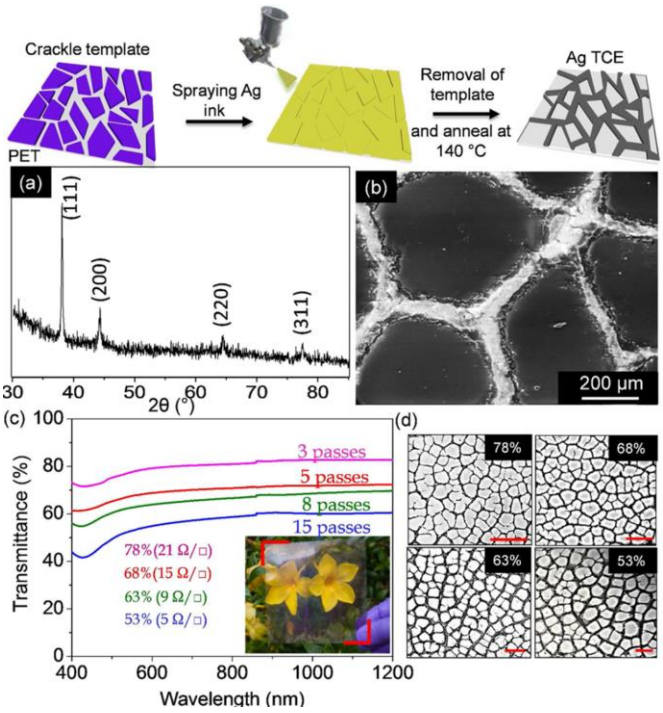

Figure IIIC.3 Schematic illustration of the key steps involved in the fabrication of Ag-TCE. (a) X-ray diffraction pattern of Ag mesh prepared by spraying Ag molecular ink. (b) SEM image of Ag mesh. (c) Specular optical transmittance of Ag mesh prepared from crackles of different widths. The sheet resistances of the samples are mentioned in parentheses. Photograph of the prepared TCE with 78% transmittance at 550 nm is shown as an inset. (d) Optical micrographs of Ag mesh of different widths. Scale bar is 1 mm.

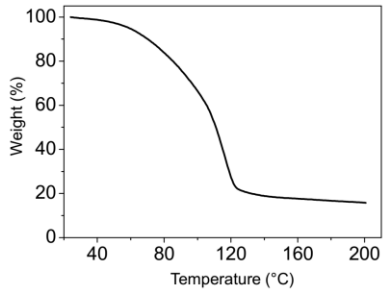

Figure IIIC.4 Thermo gravimetric analysis (TGA) of Ag precursor ink.

The Ag mesh was fabricated on transparent and flexible PET substrate following the procedures as shown in schematic in Figure IIIC.3. Briefly, Ag ink (3 times diluted with IPA) was sprayed (25 µL/cm^2) on the crackle network on PET maintained at 110 °C on the roller drum. After 10 min of coating, the PET sheet

carrying the crackle template was detached from the roller and the template was removed by simple mechanical peeling using adhesion tape. The dried ink pattern on PET was converted to metallic Ag by annealing at 140 °C (Figure IIIC.4) for about 10 min. This is confirmed by XRD measurement in Figure IIIC.3a, showing that the peaks match well with those of metallic Ag (JCPDS PDF, 89–3722). From the SEM image in Figure IIIC.3b, it is seen that the formed Ag mesh is interconnected with seamless junctions in a single plane. The width of Ag mesh is typically 50–150 μm. The optical transmittance spectra of Ag meshes of different widths are shown in Figure IIIC.3c. Transmittance spectra of meshes are constant in visible and near IR regions useful for display and solar applications, respectively. The transmittance of Ag mesh at 550 nm varies from 78 to 53% and sheet resistance from 21 to 5 Ω/sq Figure IIIC.3d shows the optical micrographs of Ag meshes with different widths on PET substrate. Interconnectivity between the meshes increases with increase in wire widths and thus leads to lower sheet resistance.

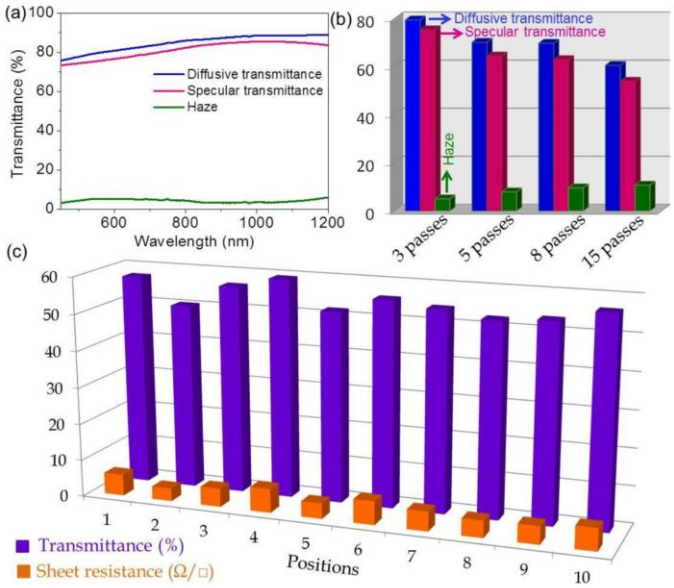

Figure IIIC.5 (a) Diffusive and specular transmittance along with calculated haze values of the Ag mesh fabricated from a crackle template (3 spray passes). (b) Histogram showing transmittance and haze value of various Ag mesh widths. (c) Sheet resistance and transmittance measured across 100 cm^2 area of Ag TCE prepared from a template (15 passes). Each measurement was done over 10 × 5 mm^2 randomly chosen areas.

The haze value is defined as $H = \Delta T/T_{dif} \times 100$, where $\Delta T = T_{dif} - T_{sp}$; T_{dif} is diffusive transmittance and T_{sp} is specular transmittance. The haze values of Ag meshes of different widths estimated from specular and diffusive transmittance measurements are found to be in the range 5–11% (see Figures IIIC.5a,b). The sheet resistance and transmittance values randomly measured from across 100 cm^2 area of Ag mesh are shown in Figure IIIC.5c. The uniformity in the measured parameters is thus evident. It may be noted that spray coating being directional avoids unnecessary spreading of the ink. Initial attempts by drop coating the Ag ink resulted in diffusion of the ink beneath the crackle template. This greatly affected the transmittance of the TCE because of uncontrolled mesh widths. The histogram comparing the width of crackles and Ag meshes fabricated thereof by spray coating is shown in Figure IIIC.6.

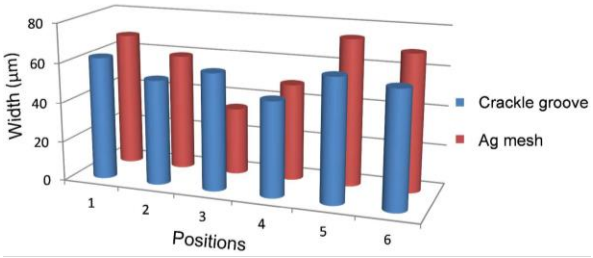

Figure IIIC.6 Histograms depicting the width of crackle grooves and Ag mesh fabricated thereof by spray coating.

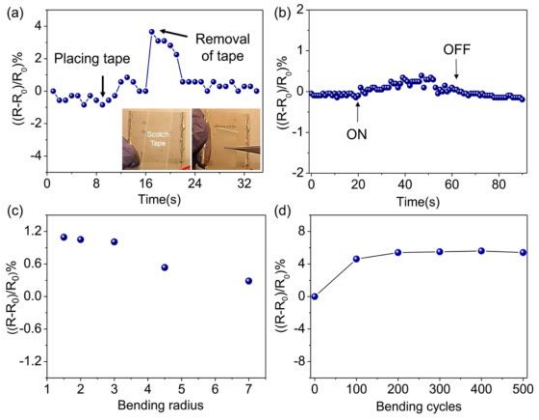

Figure IIIC.7 Relative variations in the resistance of the Ag mesh during (a) the scotch tape adhesion test, (b) sonication test, (c) bending to different radii, and (d) 500 bending cycles to radius of 1.5 mm. The photographs in the inset in (a) show the scotch tape pasted over the Ag mesh and while peeling off.

The mesh widths were almost comparable with crackle groove size (see Figure IIIC.6). In few positions, mesh widths became wider due to smearing effect and even narrower in some positions resulted from shadow effect while spraying Ag ink. Further, annealing at a moderate temperature of 110 °C while spraying enables quick evaporation of the solvents, thereby avoiding spreading of the ink beneath the crackle groove and also does not hinder in the subsequent lift-off process. Lift-off of crackle precursor through simple mechanical peeling becomes challenging beyond 110 °C because the template adheres well to the PET substrate.

Metallized Ag on PET with the experimental conditions used is known to adhere well on the substrate [6,31]. The mechanical stability of the metallized Ag in crackle network was examined using the standard scotch tape adhesion test and by repeated bending while monitoring the resistance. As shown in Figure IIIC.7a, the Ag mesh-based TCE showed minimal changes in the resistance (<0.5%) after performing the adhesion test. In addition, sonication test was performed by immersing Ag mesh in an ultrasonic water bath. The variation in resistance was less than 1% as shown in Figure IIIC.7b. These tests clearly suggest that the Ag mesh has good adhesion with the PET substrate. In order to examine the stability of Ag mesh in the context of flexible electronics, the Ag/PET was subjected to different bending radii. In spite of being bent to 1.5 mm, the variation in resistance was only ~1% (Figure IIIC.7c). Although, the mesh was subjected to 500 bending cycles with 1.5 mm radius, the change in the resistance remained within 5%, which demonstrates its robustness (Figure IIIC.7d). Importantly, the above tests required no encapsulation of the TCE.

In general, Ag and Cu nanowires tend to get oxidized in atmospheric conditions due to chemical instability which leads to deterioration of conductivity and thus the performance of optoelectronic devices [32,33]. Tarnishing of Ag is very harmful for electronic circuits in certain environments. Even in the presence of ppm level sulfide content in the atmosphere, silver sulfide nanoparticles get formed as a shell over Ag nanowires increasing the surface roughness [32,34]. With time, sulfide shell thickness increases at the cost of Ag core leading to higher resistance of the

nanowire network [35]. Therefore, it is essential to suppress the oxidation of nanowires in order to enhance the long-term stability.

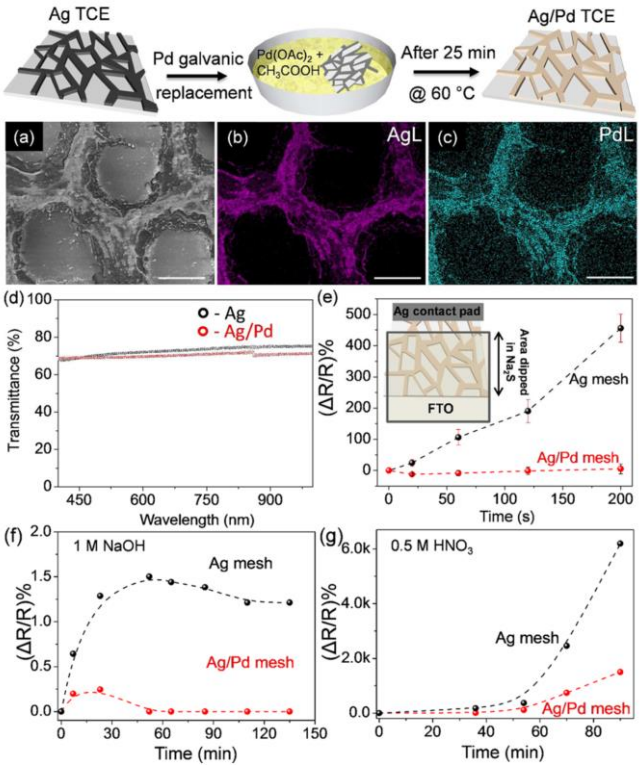

Figure IIIC.8 Schematic illustrating the fabrication of Ag/Pd mesh. (a) SEM image of Ag/Pd mesh. EDS mapping of mesh showing the presence of (b) Ag and (c) Pd. Scale bar is 100 μm. (d) Transmittance spectrum of Ag and Ag–Pd meshes. (e) Variation in electric resistance of Ag and Ag/Pd meshes vs dipping time in 50 mM Na_2S solution. Inset is the schematic of the process. To avoid exposure of Ag contacts to the sulfidic solution, only one Ag contact was taken from the network such that rest of it was free to be dipped in the solution. After dipping in solution for designated time followed by drying, the dipped part of the network was brought in contact with a fluorine-doped tin oxide (FTO) plate, which served as second contact. (f, g) Relative variation in resistance of the Ag and Ag/Pd meshes when exposed to 1 M NaOH and 0.5 M HNO_3, respectively.

Recent studies have shown that protective layer of reduced graphene oxide (r-GO) or graphene over Ag or Cu nanowires coated by dip-coating [36], spray-coating [37], spin-coating [38], or dry transfer processes [39] prevent its oxidation by forming passivation layer. These additional passivation coatings not only increase

number of process steps and also the cost of TCEs. Among the many protecting layers, thin coating of a noble or semi-noble metal by solution processing is highly promising as the coated metal can bring in highly resistant property to the nanowire. The surface stability of semi noble metal like Ag is improved by encapsulating with noble metals by simple galvanic replacement method [40,41]. Cui and coworkers have demonstrated that junction resistance between Ag nanowires could be reduced by encapsulating Au by galvanic replacement [42]. Besides being highly stable, the neutral grey color of Pd is highly desirable for display applications. Hence a simple process of coating Pd from a liquid carrier that produced a Pd-coated Ag mesh was adopted making it highly resistant to oxidation processes. The schematic in Figure IIIC.8 illustrates the fabrication process. SEM image of Ag/Pd mesh after galvanic displacement is shown in Figure IIIC.8a. EDS mapping of mesh (Figures IIIC.8b, c) clearly shows the presence of protective layer of Pd shell. The transmittance of Ag/Pd mesh is lower than Ag mesh to some extent (Figure IIIC.8d), as nonspecific deposition is unavoidable in case of solution process. The coating of Pd over the Ag mesh slightly increases the resistance of mesh (14 Ω/sq to 16 Ω/sq) likely due to the higher resistivity of Pd.

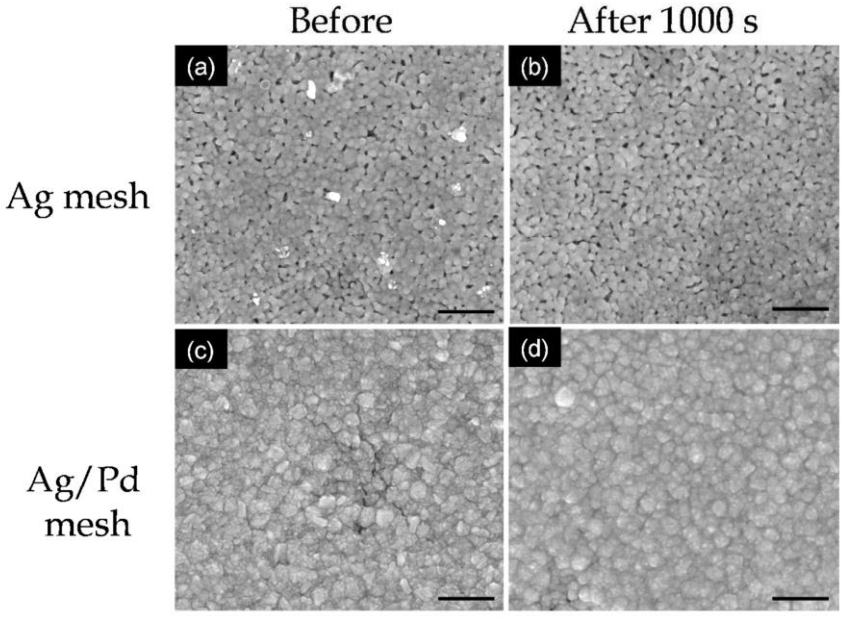

Figure IIIC.9 SEM images of Ag and Ag/Pd meshes before and after tested with Na_2S solution. Scale bar is 500 nm.

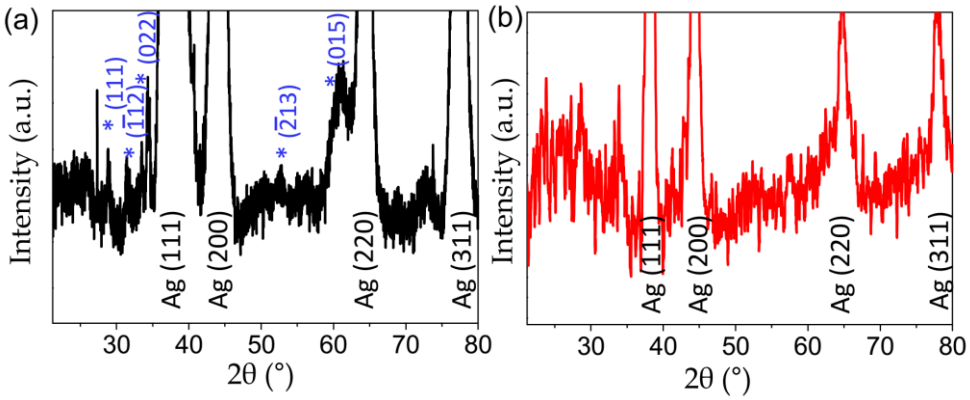

Figure IIIC.10 XRD patterns following Na_2S treatment (1000 s) of (a) Ag mesh (b) Ag/Pd mesh. Ag_2S peaks (*) though weak, are identifiable in (a) while in (b) the peaks are not distinguishable from noise.

Oxidation resistance of Ag/Pd was demonstrated by dipping the mesh in Na_2S solution. The Na_2S treatment has been performed as an accelerated test for estimating the stability of the TCE, and in this context, the performances of Ag/Pd with Ag have been compared. Schematic of the process is shown as the inset in Figure IIIC.8e. Despite the extreme oxidation environment, the resistance of the Ag/Pd mesh toward aqueous Na_2S solution was excellent and was superior to that of the Ag mesh (Figure IIIC.8e). After 200 s exposure, the resistance of the Ag mesh drastically increased to 450% whereas that of Ag/Pd mesh varied within 5%. Even after dipping for 1000 s, the resistance of the Ag/Pd mesh was less than a kΩ, whereas the resistance of the Ag mesh reached several GΩs. From the SEM images, it is observed that there is no major change in morphology of Ag and Ag/Pd meshes before and after dipping in the Na_2S solution. It is noteworthy that the XRD pattern of the Ag mesh showed distinct peaks of Ag_2S (see Figure IIIC.9 and 10). Further, the stability of the Ag and Ag/Pd meshes have been tested under HNO_3 and NaOH solutions (Figures IIIC.8f, g). The Ag/Pd mesh showed relatively long-term chemical stability superior to Ag mesh in both conditions. The simple process adopted here to enhance the stability can be used as a general strategy to improve the throughput and performance of transparent electrodes.

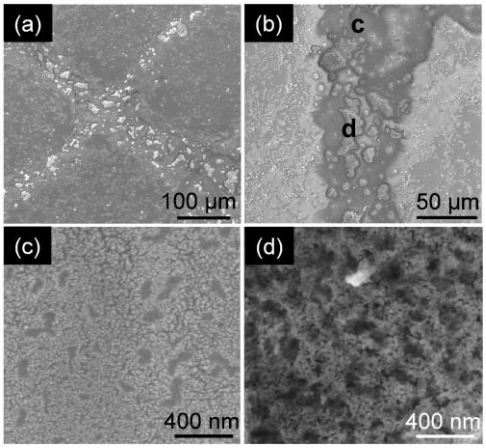

Figure IIIC.11 (a and b) SEM images of the metallized Ag seed layer in crackle pattern. The magnified regions of (b) are shown in (c) and (d).

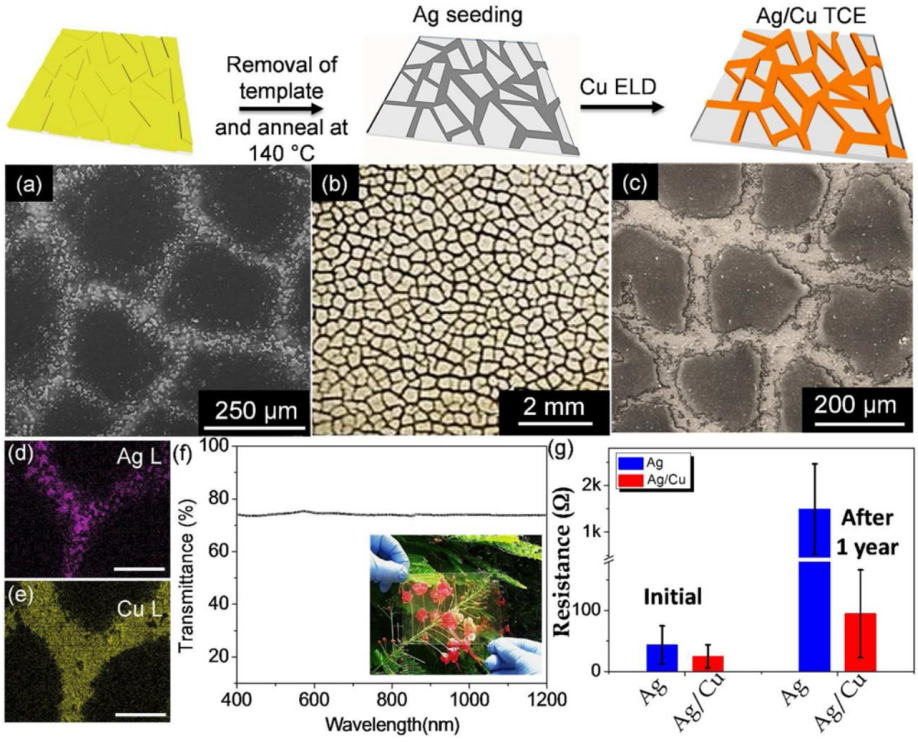

Figure IIIC.12 Schematic representation of the fabrication of Ag seeded Cu TCE. (a) SEM image of Ag seed layer. (b) Optical micrograph and (c) SEM image of Ag/Cu TCE. (d, e) Energy-dispersive X-ray spectroscopy images of Ag/Cu mesh on PET. Scale bar is 100 μm. (f) Transmittance spectrum of Ag/Cu meshes on a flexible PET substrate. Inset is the photograph of flexible transparent Ag/Cu electrode. (g) Resistance of Ag- and Ag/Cu-based TCEs after one year of storage in ambient atmosphere.

Although Ag offers versatile inks to work with, other cheaper metals such as Cu can only be brought into the TCE fabrication in a subsequent step using seed layer. In recent literature [43-46], wearable conducting electrodes for various applications have been reported fabricated through simple seed layer formation followed by electroless deposition process. A simple electroless method was followed to reduce Ag usage wherein only a small quantity of dilute Ag ink (dilution, 5 times and volume, 15 $\mu L/cm^2$) was initially sprayed and annealed which produced enough concentration of Ag catalyst nanoparticles (Figure IIIC.11) for Cu deposition.

SEM image of Ag seed layer is shown in Figure IIIC.12a. An inexpensive metal like Cu (100 times lower cost than Ag) was electroless deposited over Ag seed layer. The Cu metal was selectively deposited over Ag by dipping the PET substrate containing Ag network in a plating bath for 5 min without any external voltage. Optical micrograph and SEM image of thus fabricated Ag/Cu mesh clearly shows a highly interconnected network with seamless junctions (Figure IIIC.12b and c). The uniform coating of Cu over Ag was further confirmed by EDS mapping as shown in Figure IIIC.12d, e. The root mean-square (R_{rms}) roughness of the Ag/Cu mesh was found to be 43 nm (see Figure IIIC.13). A view of substrate carrying Ag/Cu mesh proves its transparency to the visible light (Figure IIIC.12f). The transmittance at 550 nm was 76% for a low sheet resistance of 9 Ω/sq. Large area uniformity of the prepared Ag/ Cu mesh is illustrated in Figure IIIC.14.

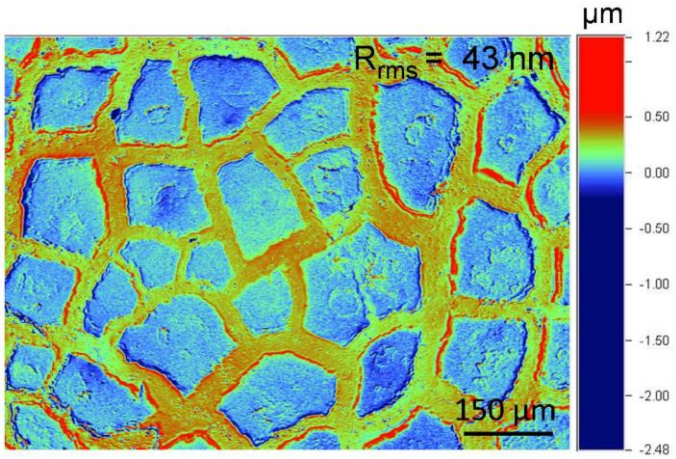

Figure IIIC.13 Optical profilometry of Ag/Cu mesh.

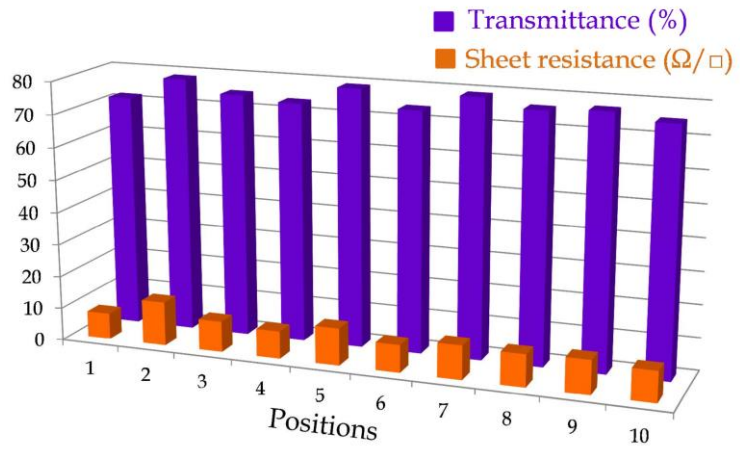

Figure IIIC.14 The sheet resistance and transmittance measured across 100 cm^2 area of Ag/Cu TCE. Each measurement was done over 10 × 5 mm^2 randomly chosen.

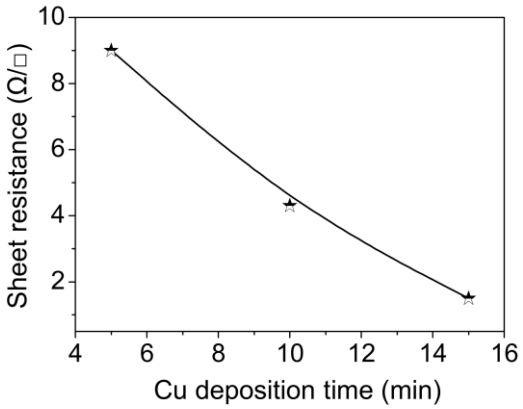

Figure IIIC.15 Dependence of sheet resistance on Cu electroless deposition time.

To explore the effect of Cu deposition time on the sheet resistance, the deposition process was carried out with increasing time duration, from 5 to 15 min. As shown in Figure IIIC.15, the sheet resistance values gradually decreased from 9 Ω/sq to 1.5 Ω/sq but beyond 5 min of deposition, nonspecific deposition of Cu occurred which greatly affected the transmittance as well as adhesion of Cu to the substrate. Besides reducing the cost of TCE fabrication, the Cu shell on Ag also enhances the stability of mesh. This is clearly seen from the sheet resistance values measured from the prepared meshes initially and after a year of storage in ambient atmosphere. Though the Ag/Cu TCE was exposed to ambient atmosphere for one year, it had excellent stability as shown in Figure IIIC.12g. In contrast, Ag TCE degraded

significantly because of ease of oxidation and highly porous surface unlike Ag/Cu (see Figure IIIC.16). Ag/Cu mesh being more stable is bit surprising. However, the porosity of the wire mesh also plays an important role. As shown in Figure IIIC.16, the Ag/Cu mesh is less porous compared to Ag mesh. In the presence of large number of pores and increased surface area, Ag tends to get oxidized relatively rapid. The pores formed in Ag are filled up by Cu in a latter step, thus bringing additional stability against oxidation. In the previous studies related to crackle lithography (as discussed in Chapter IIIB), the TCEs were realized by depositing metal on crackle grooves by physical deposition process except an attempt where Cu TCE was fabricated using Au and Pd as seed layer. Au seeding was done using sputtering process which demands vacuum system.

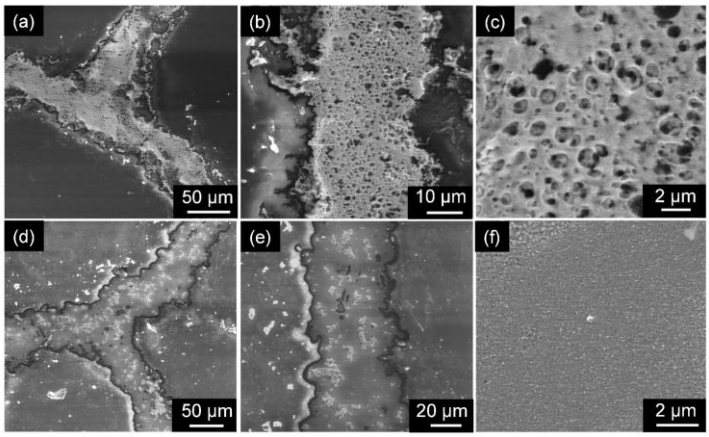

Figure IIIC.16 SEM images of (a-c) Ag mesh (d-f) Ag/Cu mesh at different magnifications. High magnification images clearly show the holey pattern of the Ag mesh (c) and the smooth Ag/Cu surface (f).

In general, thin layer of noble metals is coated for high stability rather than as a seed layer. In this work, Pd has been used as protection layer for Ag against oxidation environment. Also Ag as seed layer from spray coating of the precursor was used to successfully grow Cu wire meshes. Thus, the present work is the first step toward large scale production of TCEs using roll coating processes. The novelty of this work is that it is a complete solution-based recipe that is cost-effective and adaptable for roll-to-roll processing. Unlike spin coating or rod coating, spray roll process is significant for industrial processing.

IIIC.5 Conclusions

In summary, to upscale the fabrication of cost-effective TCE by adopting roll and spray coating techniques was executed. The processing speed for the template fabrication was 0.6 m/min under ambient conditions. However, the web speed could be improved with further optimization of processing parameters such as by increasing spray volume and faster drying conditions. These completely solution processed Ag, Ag/Pd, and Ag/Cu mesh-based TCEs have shown superior chemical and mechanical robustness. This method generates metal meshes adhering well to the PET substrate with seamless metal junctions and high degree of interconnectivity. The Ag/Cu meshes produced in this study exhibited low sheet resistance (9 Ω/sq) with high transmittance (~80%) which could be employed in a wide range of flexible and low-cost devices. In addition, Pd encapsulated Ag meshes have shown excellent stability toward oxidation. The developed process can be adopted as a general strategy to improve the throughput and performance of transparent electrodes, in place of relatively involved methods of nanowire encapsulation. The method adopted here opens up wide range of possibilities in future studies in terms of the metal or the material being deposited, which can be exploited for fine-tuning properties such as work function. The latter gains much significance in the context of optoelectronic device fabrication.

References

1. H. Wu, D. Kong, Z. Ruan, P.-C.Hsu, S. Wang, Z. Yu, T. J.Carney, L. Hu, S. Fan, Y. A Cui, Transparent Electrode Based on a Metal Nanotrough Network. *Nat. Nanotechnol.* **2013,** *8*, 421-425.

2. S. Bae et al, Roll-to-Roll Production of 30-Inch Graphene Films for Transparent Electrodes. *Nat. Nanotechnol.* **2010**, *5*, 574-578.

3. L. Huo, T. Liu, X. Sun, Y. Cai, A. J. Heeger, Y. Sun, Single-Junction Organic Solar Cells Based on a Novel Wide-Bandgap Polymer with Efficiency of 9.7%. *Adv. Mater.* **2015***, 27*, 2938-2944.

4. J. Ryu et al. Fast Synthesis of High-Performance Graphene Films by Hydrogen-Free Rapid Thermal Chemical Vapor Deposition. *ACS Nano* **2014,** *8*, 950-956.

5. G. U. Kulkarni, S. Kiruthika, R.Gupta, K. D. M. Rao, Towards Low Cost Materials and Methods for Transparent Electrodes. *Curr. Opin. Chem. Engineering* **2015***, 8*, 60-68.

6. R. Gupta, S. Walia, M. Hösel, J. Jensen, D. Angmo, F. C. Krebs, G. U. Kulkarni, Solution Processed Large Area Fabrication of Ag Patterns as Electrodes for Flexible Heaters, Electrochromics and Organic Solar Cells. *J. Mater. Chem. A* **2014,** 2, 10930-10937.

7. T. T. Larsen-Olsen, T. R. Andersen, B. Andreasen, A. P. L.Böttiger, E. Bundgaard, K. Norrman, J. W. Andreasen, M. Jørgensen, F. C. Krebs, Roll-to-Roll Processed Polymer Tandem Solar Cells Partially Processed from Water. *Sol. Energy Mater. Sol. Cells,* **2012***, 97*, 43-49.

8. K. Hwang, Y.-S. Jung, Y.-J. Heo, F. H. Scholes, S. E. Watkins, J. Subbiah, D. J. Jones, D.-Y. Kim, D. Vak, Toward Large Scale Roll-to-Roll Production of Fully Printed Perovskite Solar Cells. *Adv. Mater.* **2015***, 27*, 1241-1247.

9. M. R. Arcila-Velez, J. Zhu, A. Childress, M. Karakaya, R. Podila, A. M. Rao, M. E. Roberts, Roll-to-Roll Synthesis Of Vertically Aligned Carbon Nanotube Electrodes for Electrical Double Layer Capacitors. *Nano Energy* **2014**, *8*, 9-16.

10. L. Oakes, T. Hanken, R. Carter, W. Yates, C. L. Pint, Roll-to-Roll Nanomanufacturing of Hybrid Nanostructures for Energy Storage Device Design. *ACS Appl. Mater. Interfaces* **2015**, *7*, 14201-14210.

11. H. Choi et al., Flexible Electronics: Flexible and Transparent Gas Molecule Sensor Integrated with Sensing and Heating Graphene Layers. *Small* **2014***, 10*, 3812-3812.

12. S. M. Kim, E. B. Song, S. Lee, J. Zhu, D. H. Seo, M. Mecklenburg, S. Seo, K. L. Wang, Transparent and Flexible Graphene Charge-Trap Memory. *ACS Nano* **2012,** *6*, 7879-7884.

13. Y. Yang, S. Jeong, L. Hu, H. Wu, S. W. Lee, Y. Cui, Transparent Lithium-Ion Batteries. *Proc. Natl. Acad. Sci.* **2012***,* 108, 13013-13018.

14. A. Byoung-Joon, K. Ji-Youp, K. Sung-Lim, Roll-to-Roll Microimprinting Process for Indium Tin Oxide Layer Patterning. *Jpn. J. Appl. Phys.* **2013***, 52*, 05DB09.

15. Y.-H. Shin, H.-K. Kim, Effects of Ar Ion Beam Treatment on Properties of Roll-to-Roll Sputtered Sn-Doped In_2O_3 Films on Colorless Polyimide Substrate. *Thin Solid Films* **2014***, 559*, 27-30.

16. T. Choi, S. J. Kim, S. Park, T. Y. Hwang, Y. Jeon, B. H. Hong, Roll-to-Roll Continuous Patterning and Transfer of Graphene via Dispersive Adhesion. *Nanoscale* **2015***, 7*, 7138-7142.

17. X. Wang, L. Zhi, K. Müllen, Transparent, Conductive Graphene Electrodes for Dye-Sensitized Solar Cells. *Nano Lett.* **2008**, *8*, 323-327.

18. M. Vosgueritchian, D. J. Lipomi, Z. Bao, Highly Conductive and Transparent PEDOT:PSS Films with a Fluorosurfactant for Stretchable and Flexible Transparent Electrodes. *Adv. Funct. Mater.* **2012***, 22*, 421-428.

19. F. L. M. Sam, C. A.Mills, L. J. Rozanski, S. R. P. Silva, Thin Film Hexagonal Gold Grids as Transparent Conducting Electrodes In Organic Light Emitting Diodes. *Laser Photon. Rev.* **2014** 8, 172-179.

20. Z. Wu et al., Transparent, Conductive Carbon Nanotube Films. *Science* **2004**, *305*, 1273-1276.

21. J.-Y. Kim, J.-H. Jeon, M.-K. Kwon, Indium Tin Oxide-Free Transparent Conductive Electrode for GaN-Based Ultraviolet Light-Emitting Diodes. *ACS Appl. Mater. Interfaces,* **2015***,* 7, (15), 7945-7950.

22. D. Zhang, R.Wang, M. Wen, D. Weng, X. Cui, J. Sun, H. Li, Y. Lu, Synthesis of Ultralong Copper Nanowires for High-Performance Transparent Electrodes. *J. Am. Chem. Soc.* **2012***, 134*, 14283-14286.

23. Y. Ahn, Y. Jeong, D. Lee, Y. Lee, Copper Nanowire-Graphene Core-Shell Nanostructure for Highly Stable Transparent Conducting Electrodes. *ACS Nano* **2015***, 9*, 3125-3133.

24. B. Deng et al., Roll-to-Roll Encapsulation of Metal Nanowires between Graphene and Plastic Substrate for High-Performance Flexible Transparent Electrodes. *Nano Lett.* **2015***, 15*, 4206-4213.

25. S. Kim, S. Y. Kim, M. H.Chung, J. Kim, J. H. Kim, A One-Step Roll-to-Roll Process of Stable AgNw/PEDOT:PSS Solution Using Imidazole as a Mild Base for Highly Conductive and Transparent Films: Optimizations And Mechanisms. *J. Mater. Chem. C* **2015***, 3*, 5859-5868.

26. M.-S. Lee et al., High-Performance, Transparent, and Stretchable Electrodes Using Graphene-Metal Nanowire Hybrid Structures. *Nano Lett.* **2014***, 13*, 2814-2821.

27. T. Tokuno, M. Nogi, J. Jiu, T. Sugahara, K. Suganuma, Transparent Electrodes Fabricated via the Self-assembly of Silver Nanowires Using a Bubble Template. *Langmuir* **2012**, *28*, 9298–9302.

28. H. Wu, D. Kong, Z. Ruan, P-C. Hsu, S. Wang, Z. Yu, TJ. Carney, L. Hu, S. Fan, Y. A Cui, Transparent Electrode Based on a Metal Nanotrough Network. *Nat Nano* **2013**, *8*,421-425.

29. R. Gupta, K. D. M. Rao, K. Srivastava, A. Kumar, S. Kiruthika, G. U. Kulkarni, Spray Coating of Crack Templates for the Fabrication of Transparent Conductors and Heaters on Flat and Curved Surfaces. *ACS Appl. Mater. Interfaces* **2014,** *6*, 13688-13696.

30. K. D. M. Rao, R. Gupta, G. U. Kulkarni, Fabrication of Large Area, High-Performance, Transparent Conducting Electrodes Using a Spontaneously Formed Crackle Network as Template. *Adv. Mater. Interfaces* **2014***, 1*.

31. R. Gupta, M. Hösel, J. Jensen, F. C. Krebs, G. U. Kulkarni, Digital Grayscale Printing for Patterned Transparent Conducting Ag Electrodes and Their Applications In Flexible Electronics. *J. Mater. Chem. C* **2014***, 2*, 2112-2117.

32. C. Mayousse, C. Celle, A. Fraczkiewicz, J.-P. Simonato, Stability of Silver Nanowire Based Electrodes Under Environmental and Electrical Stresses. *Nanoscale* **2015***, 7*, 2107-2115.

33. A. R. Rathmell, M. Nguyen, M. Chi, B. J. Wiley, Synthesis of Oxidation-Resistant Cupronickel Nanowires for Transparent Conducting Nanowire Networks. *Nano Lett.* **2012***, 12*, 3193-3199.

34. J. L. Elechiguerra, L. Larios-Lopez, C. Liu, D. Garcia-Gutierrez, A. Camacho-Bragado, M. J. Yacaman, Corrosion at the Nanoscale: The Case of Silver Nanowires and Nanoparticles. *Chem. Mater.* **2005**, *17*, 6042-6052.

35. M. Rycenga, C. M. Cobley, J. Zeng, W. Li, C. H. Moran, Q. Zhang, D. Qin, Y. Xia, Controlling the Synthesis and Assembly of Silver Nanostructures for Plasmonic Applications. *Chem. Rev.* **2011***, 111*, 3669-3712.

36. Y. Ahn, Y. Jeong, Y. Lee, Improved Thermal Oxidation Stability of Solution-Processable Silver Nanowire Transparent Electrode by Reduced Graphene Oxide. *ACS Appl. Mater. Interfaces* **2012***, 4*, 6410-6414.

37. I. K. Moon, J. I. Kim, H. Lee, K. Hur, W. C. Kim, H. Lee, 2D Graphene Oxide Nanosheets as an Adhesive Over-Coating Layer for Flexible Transparent Conductive Electrodes. *Sci. Rep.* **2012,** *3*.

38. I. N. Kholmanov, S. H. Domingues, H. Chou, X. Wang, C. Tan, J.-Y. Kim, H. Li, R. Piner, A. J. G. Zarbin, R. S. Ruoff, Reduced Graphene Oxide/Copper Nanowire Hybrid Films as High-Performance Transparent Electrodes. *ACS Nano* **2013***, 7*, 1811-1816.

39. D. Lee, H. Lee, Y. Ahn, Y. Jeong, D.-Y. Lee, Y. Lee, Highly Stable and Flexible Silver Nanowire-Graphene Hybrid Transparent Conducting Electrodes for Emerging Optoelectronic Devices. *Nanoscale* **2013***, 5*, 7750-7755.

40. J. Chen, B. Wiley, J. McLellan, Y. Xiong, Z.-Y. Li, Y. Xia, Optical Properties of Pd-Ag and Pt-Ag Nanoboxes Synthesized via Galvanic Replacement Reactions. *Nano Lett.* **2005**, *5*, 2058-2062.

41. L. Zhou, Z. Liu, H. Zhang, S. Cheng, L.-J. Fan, W. Ma, Site-Specific Growth of AgPd Nanodendrites on Highly Purified Au Bipyramids with Remarkable Catalytic Performance. *Nanoscale* **2014,** *6*, 12971-12980.

42. L. Hu, H. S. Kim, J.-Y. Lee, P. Peumans, Y. Cui, Scalable Coating and Properties of Transparent, Flexible, Silver Nanowire Electrodes. *ACS Nano* **2010,** *4*, 2955-2963.

43. L. Liu, Y. Yu, C. Yan, K. Li, Z. Zheng, Wearable Energy-Dense and Power-Dense Supercapacitor Yarns Enabled by Scalable Graphene-Metallic Textile Composite Electrodes. *Nat Commun.* **2015***,* 6, 7260.

44. X. Liu, H. Chang, Y. Li, W. T. S. Huck, Z. Zheng, Polyelectrolyte-Bridged Metal/Cotton Hierarchical Structures for Highly Durable Conductive Yarns. *ACS Appl. Mater. Interfaces* **2010***,* 2, 529-535.

45. Y. Yu, C. Yan, Z. Zheng, Polymer-Assisted Metal Deposition (PAMD): A Full-Solution Strategy for Flexible, Stretchable, Compressible, and Wearable Metal Conductors. *Adv. Mater.* **2014***,* 26, 5508-5516.

46. Y. Yu, J. Zeng, C. Chen, Z. Xie, R. Guo, Z. Liu, X. Zhou, Y. Yang, Z. Zheng, Three-Dimensional Compressible and Stretchable Conductive Composites. *Adv. Mater.* **2014***,* 26, 810-815.

47. Y. Yu, Y. Zhang, K. Li, Yan, C. Z. Zheng, Bio-Inspired Chemical Fabrication of Stretchable Transparent Electrodes. *Small* **2015***,* 11, 3444-3449.

Chapter IIID

Fabrication of Hybrid Transparent Conducting Electrodes

Summary

Metal mesh-conducting oxide based hybrid transparent electrodes were fabricated, and its electrical uniformity and mechanical robustness were demonstrated with simple tests. Metal meshes were obtained using crackle templating method and oxides were deposited either by sol-gel or by RF sputtering process. The electrical conductivity of hybrid electrodes has been improved with minimal loss in optical transmittance.

IIID.1 Introduction

Most of the optoelectronic devices such as touch panels, OLEDs, LCDs, solar cells, *etc*. require transparent conducting electrode (TCE) for fabrication. As the name implies, TCEs have high electrical conductivity and optical transparency. The first transparent conducting oxide (TCO) reported was a thin film of CdO. However, due to the toxicity concern of the Cd, CdO is not widely used. Nowadays, the most commonly used and commercially available TCO, on which the current industry relies on includes indium tin oxide (ITO), fluorine-doped tin oxide (FTO) and aluminium doped zinc oxide (AZO) [1,2]. However, the next generation optoelectronic devices require conductive electrodes with low-cost, flexibility and compatibility with large scale manufacturing. Also, the other key parameters include thermal stability, process ability, chemical compatibility with other materials and work-function [3].

Although these conductive oxides are very well implemented in various applications, there are few limitations which prompted the researchers to investigate alternative materials that can replace the ITOs as discussed in Chapter I. For example, ITO which is commercially available, exhibits a transmittance of nearly 92% for visible wavelength and a sheet resistance, ~ 10 Ω/sq [4,5]. However, the less abundance of indium, the expensive fabrication processes and the brittle nature of oxides prevents its application in the flexible devices. This leads to the need for other alternative electrode materials. In the last decade, various transparent conducting

Paper based on this study: Manuscript under preparation

electrodes based on graphene films [6-8], CNTs [9,10], metal nanofibers, and nanowires [11,12] have been widely investigated. Even though carbon is available abundant in nature and inexpensive, the process of conversion of carbon into useful forms such as CNT and graphene are highly energy consuming. Also, a large number of grain boundaries and wrinkles formed during the growth process limit their usage in large area device fabrication [3].

The new generation electrodes which consist of percolative conducting networks of 1D nanomaterial such as metal nanowires, the CNT networks have been deposited on glass or PET. The light is transmitted through the bare area between the networks [13]. However, there is always a trade-off between the transmittance and the sheet resistance, mainly decided by percentage of loading. Also, to reduce the contact resistance caused due to the junctions of nanowires and the high surface roughness because of the redundant wires that remain unconnected to the network further processing conditions such as mechanical pressing, thermal annealing, etc. is indeed required. On the other hand, metal meshes fabricated through crackle template method are devoid of cross-bar junctions and redundant wires [14]. However, to obtain uniform conductivity throughout the substrate and to simultaneously attain higher transparency, SnO_2 has been coated as a thin film over the metal mesh.

SnO_2 is a wide band gap (3.7 eV) n-type semiconductor with low electrical resistance and high transparency in the visible region of the electromagnetic spectrum [15]. These properties of SnO_2 make it favourable for a wide range of applications such as electrode materials in solar cells, LEDs, transparent coatings, etc. numerous methods have been reported for the fabrication of SnO_2 thin films such as [16], spray pyrolysis [17], sputtering [18], pulsed laser deposition [19] and sol-gel methods. Among the various methods, sol-gel methods are simple, flexible and offer many advantages such as well-defined film thickness, excellent film homogeneity, low-cost processing and has ability to produce continuous thin films [20,21].

IIID.2 Scope of the present investigation

Metal mesh network obtained through crackle template method offers the most reliable transparent conductors for a broad range of applications including solar cells, transparent heaters, *etc.* due to its high transparency with very low sheet resistance

[14]. However, metal meshes have some inherent drawbacks such as non-uniform electrical conductivity on the surface with low fill-factor and ease of oxidation of metals by harsh environments such as electrolytes often from the active layer such as perovskite salts and dyes used in solar cells as well as humidity. To overcome such problems, protective coatings of transparent yet conducting metal oxides such as SnO_2 and AZO over metal mesh was explored, and stability of hybrid electrodes towards electrical uniformity and mechanical robustness is reported. In the present work, sol-gel derived SnO_2 was coated over the Au mesh by spin coating. The morphology, crystal structure, chemical composition, optical and electrical properties were characterized using FE-SEM, XRD, XPS, UV-visible spectroscopy, respectively. Furthermore, the coating of aluminium doped zinc oxide (AZO) over Cu mesh was also explored. The stability of AZO coating was confirmed through SEM and adhesion tests.

IIID.3 Experimental Details

Metal Mesh Fabrication

An acrylic resin based crackle precursor (Ming Ni Cosmetics Co., Guangzhou, China) diluted to 0.6 g mL^{-1} was spin coated (2000 rpm, Technoscience, Bangalore) on a glass substrate to obtain a crackle template. Metal such as Au and Cu was thermally evaporated (Hindvac, India) over the template at a base pressure of 10^{-6} Torr. In the later step, crackle template was removed by washing in chloroform.

SnO_2 coating

Stannous chloride (Ranbaxy, India) was dispersed in an ethanolic solution (0.5 M). The solution was stirred for 5 hours and left at room temperature for 24 h. The supernatant liquid (~ 2 mL) was spin coated (1200 rpm, 60 s) over Au mesh network and annealed at 80 °C for 10 minutes. This process is further continued for ten times to increase the thickness of the SnO_2 layer to ~ 300 nm with no crack. Finally, the samples were annealed at 500 °C for 2 h to improve the crystallinity.

AZO coating

Aluminium doped zinc oxide was coated over Cu wire mesh by RF sputtering process.

The substrate was annealed at ~ 250 °C while depositing AZO at 10^{-6} Torr vacuum. The thickness of AZO film coated was ~ 300 nm.

IIID.4 Results and Discussion

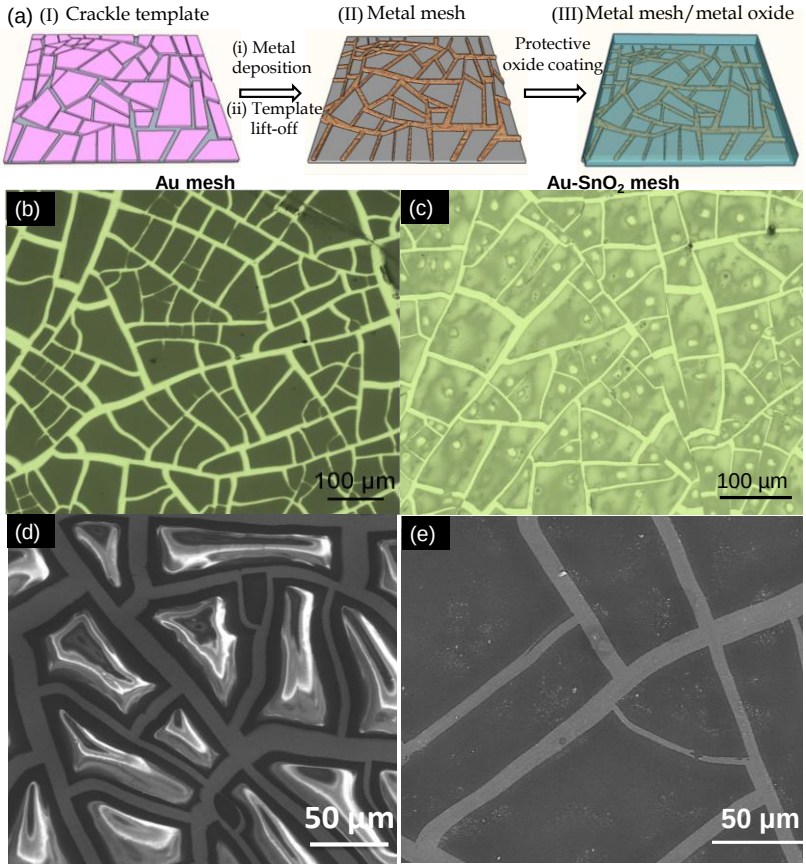

Figure IIID.1 (a) Schematic illustration of the metal mesh and metal oxide hybrid transparent electrodes. Top-view optical microscope and SEM images of metal mesh (b, d) and hybrid electrodes (c, e).

Figure IIID.1a shows the schematic structure of the fabrication of metal mesh and hybrid (metal mesh and metal oxide) transparent electrodes. The optical microscope images showed the interconnected Au network structure (Figure IIID.1b) and SnO_2 coated Au meshes (Figure IIID.1c). The wire widths were in the range of 5-20 µm. Even after annealing the sample at 500 °C for 2 h for SnO_2 preparation, the interconnectivity of the network was still preserved (Figure IIID.1c). In the FESEM image (Figure IIID.1d), the wires were clearly seen, but the polygonal areas in between exhibit varying shades indicating, local charging of the

insulating glass substrate induced by the e-beam which was absent in the case of conducting SnO_2 coated meshes (Figure IIID.1e).

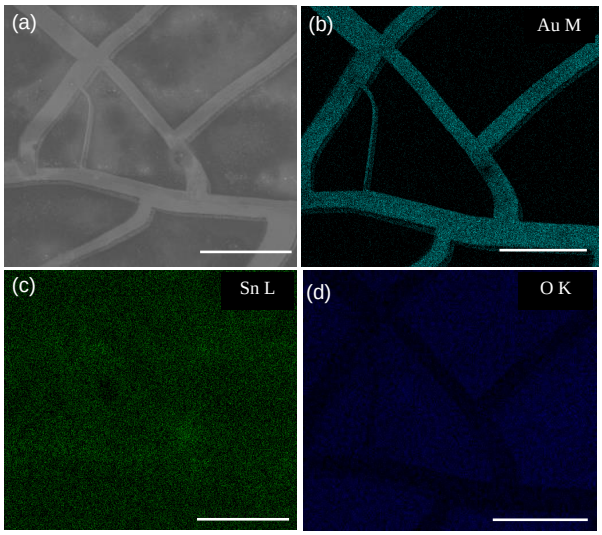

Figure IIID.2 (a) EDS mapping images of Au-SnO_2 meshes clearly showing the distribution of (b) Au, (c) Sn and (d) O components. Scale bar is 50 μm.

The elemental compositions of Au-SnO_2 meshes were analysed using energy-dispersive X-ray (EDX) spectroscopy measurements. The mapping of mesh areas clearly reveals the distribution of Au, Sn and O components (Figure IIID.2a-d). From the mapping images, it was understood that SnO_2 thin film uniformly embedded the Au mesh (see Figure IIID.2c and d).

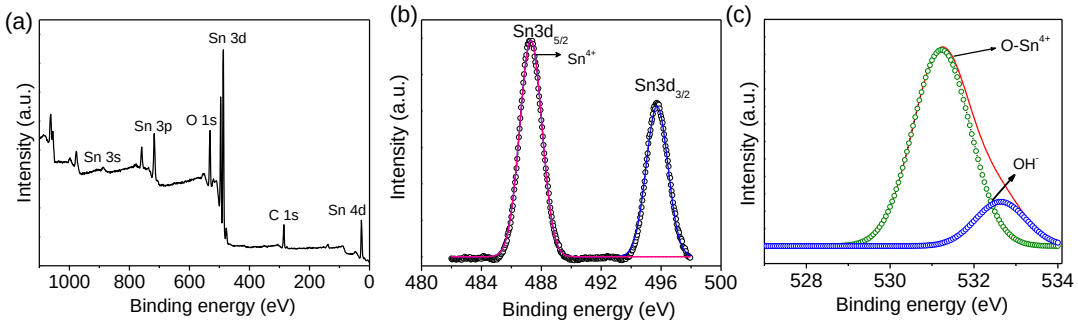

Figure IIID.3 (a) XPS survey spectrum and (b and c) spectra of individual lines of Sn 3d and oxygen peaks of 500 °C calcined SnO_2 coated Au mesh.

The semiconductive SnO_2 (resistivity of ~ 1 MΩ cm) thin film coated on Au mesh was analysed by XPS to gain insight about its chemical composition. Typical XPS survey spectrum and characteristic Sn 3d and O 1s peaks are shown in Figure IIID.3. Besides a weak C 1s peak centred around 285 eV, core levels of Sn and O were observed in survey spectrum (Figure IIID.3a). Sn 3d peaks clearly indicate the presence of single doublet at 487.3 eV for Sn $3d_{5/2}$ and 495.7 eV for Sn $3d_{3/2}$ which were in good agreement with literature reports. From the symmetry and position of Sn 3d peaks, it was clear that tin is present in its +4 oxidation state (Figure IIID.3b). Thus, XPS investigations indicate that the SnO_2 thin film formed by the sol-gel method was highly stoichiometric and chemically pure.

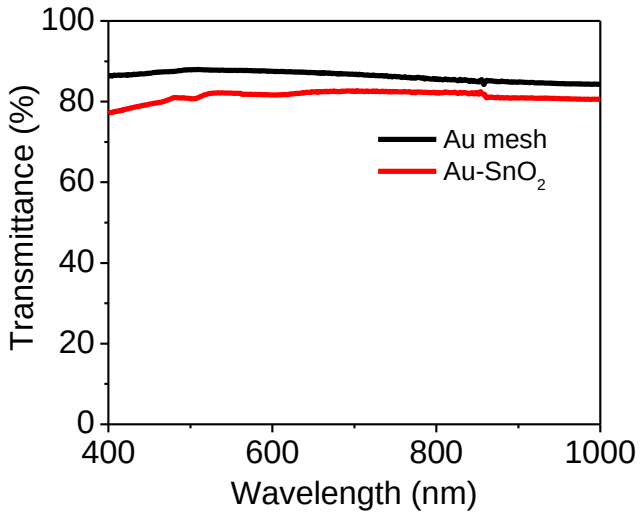

Figure IIID.4 Transmittance spectra of Au and Au-SnO_2 meshes in the wavelength range of 400- 1000 nm.

To investigate the optical and electrical properties of Au and Au-SnO_2 meshes, the optical transmittance was measured using UV-vis spectrophotometer (Figure IIID.4) whereas four-point probe was used to measure sheet resistance. The transmittance of bare Au mesh at 550 nm was 88% which was reduced to 82% after coating with the SnO_2 thin film. This result clearly indicates that SnO_2 is quite transparent. The sheet resistance of Au-SnO_2 hybrid electrode was slightly lesser than that of bare Au mesh (< 10 Ω/sq).

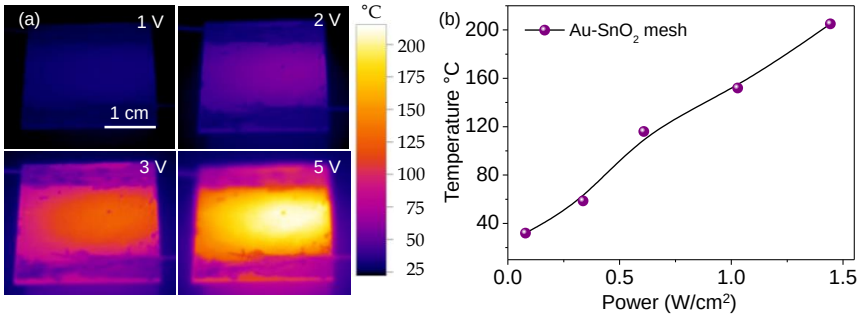

Figure IIID.5 (a) Infrared thermal image at different saturated temperatures and (b) temperature versus power plot of Au-SnO_2 hybrid mesh films.

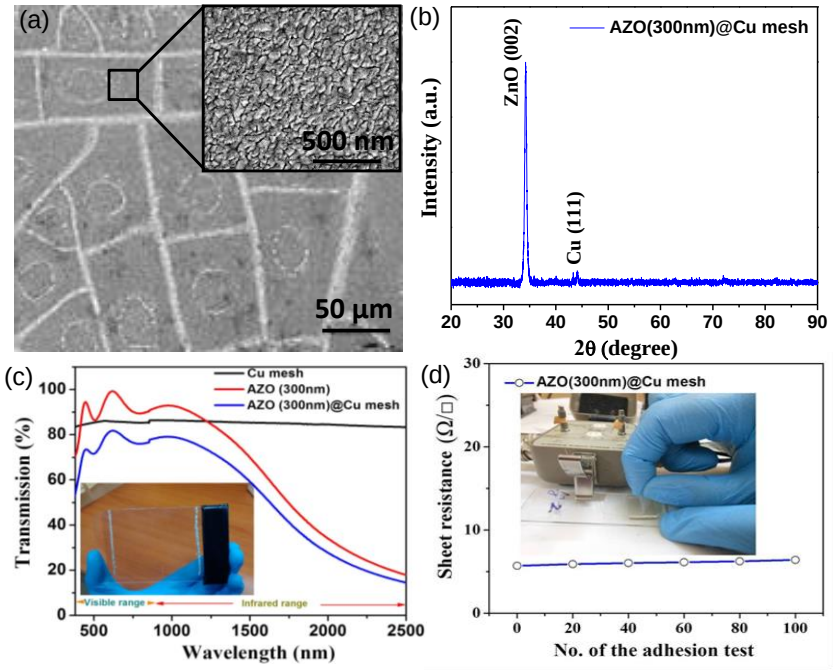

Figure IIID.6 (a) AZO-coated Cu mesh. Inset is magnified AZO granules. (b) XRD pattern, (c) transmittance spectra and (d) scotch tape adhesion test of hybrid TCEs.

Transparent heater finds enormous applications in various fields such as defroster or defogger windows, sensors, detectors, etc. The transparent Au-SnO_2 electrode while made to carry current with low input voltage, it acts as a transparent heater. From the IR images of the hybrid electrode at various input voltages (Figure IIID.5a), it was observed that temperature distribution was quite uniform which in turn confirms the uniformity of mesh and SnO_2 coating. In fact, with 1.5 W/cm^2, the temperature of the glass was raised to nearly 200 °C, in just 2

minutes (Figure IIID.5b). Also, electrodes were stable for many repetitive heating cycles.

To realize large-scale production with low materials cost, AZO coating by RF sputtering process was obtained over Cu mesh (10 × 10 cm^2). A 300 nm AZO sputter coated on the mesh eliminates the local charging effect in SEM (Figure IIID.6a). The nanogranular nature of the AZO film was shown in the inset. X-ray diffraction pattern of the hybrid electrode plate is given in Figure IIID.6b. From the Figure IIID.6c, it was evident that the electrodes exhibit appreciable transmittance in the IR regions as well. The inset is a photograph of the hybrid Cu-AZO electrode plate. Figure IIID.6d shown a variation in the resistance of the electrode in repeated adhesion tests. The sheet resistance was 6.4 Ω/sq even after 100 times peeling off the tape. In contrast, bare metal mesh on glass surface had shown several order increase in the resistance just after 10 cycles.

Table IIID.1 Comparing the optoelectrical performance of Cu mesh, AZO, and hybrid Cu-AZO mesh.

S. No.	Transparent Electrodes (on glass)	Transmittance (%) at 550 nm	Sheet Resistance, R_s (Ω/sq)
1	**Cu mesh** (150 nm)	88	9.5
2	**AZO** (~ 300 nm)	93	41.0
3	**Cu mesh coated with AZO** (Cu ~150 nm, AZO ~ 300 nm)	83	5.7

In the table shown above (Table IIID.1), it is observed that a slight loss in transmittance for the Cu mesh following AZO coating (from 88% to 83%) which may be acceptable given that local charging is completely avoided (see SEM image in Figure IIID.6a). The sheet resistance of the hybrid is less compared to that of the mesh (~ 3.2 Ω/sq) while compared to AZO, it is nearly 7 times less. It may be noted that an AZO film of comparable properties requires to be of much larger thickness (above 1500 nm) requiring several hours of deposition!

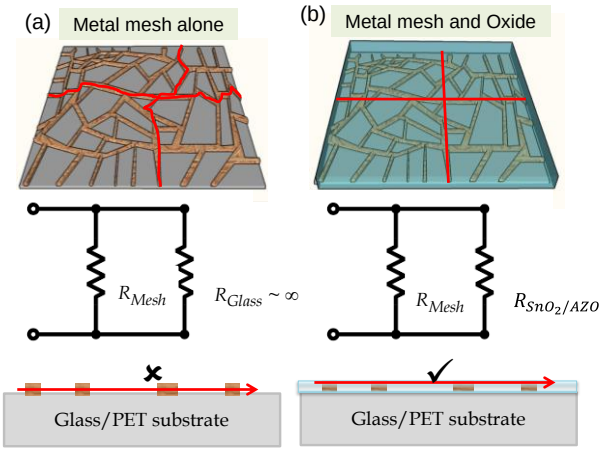

Figure IIID.7 Schematic representation of electrical non-uniformity and roughness in bare meshes (left) and the smooth electrically uniform surface of metal oxide coated mesh (right).

Metal mesh transparent electrode occupies less than 20% fill factor on the PET surface whereas about 80% is bare PET surface. This non-conducting PET surface fails to collect charge carriers from active materials in various applications such as solar cells, liquid crystal devices, etc. Between two metal lines, few tens of micron length bare PET region exists. Such non-conducting regions were made conducting by coating with a thin layer of oxides such as SnO_2 and AZO. These transparent oxides bridge the gaps between two metal wires and thus improve the electrical conductivity with minimal loss in transmittance. Figure IIID.7 shows the schematic illustration of these scenarios.

IIID.5 Conclusions

In summary, hybrid transparent conducting films were successfully realized by deposition of SnO_2 and AZO on metal mesh. The oxide coating of ~ 300 nm improved the conductivity of hybrid electrodes (~ 5 Ω/sq) without affecting the transparency (82%). To realize similar sheet resistance with metal oxide alone, not only the thickness of deposition has to be high (few microns) and hence the process cost, but also coloration of thick oxides obstructs the clarity of electrodes. Additionally, adhesion of metal mesh towards glass substrate was enhanced by these protective oxide coatings. The oxide coated meshes may find applications in non-ITO, non-FTO based solar cells and electrochromic devices.

References

1 M. Tadatsugu, *MRS Bulletin*, 2000, **25**, 38-44.

2 Ginley, David S, and C. Bright, *MRS Bulletin,* 2000, **25**, 15-18.

3 G. U. Kulkarni, S. Kiruthika, Ritu Gupta and KDM Rao, *Curr. Opin. Chem. Eng.,* 2015, **8**, 60.

4 K.L. Chopra, S. Major and D. K. Pandya, *Thin Solid Films*, **2983,** 1- 46.

5 C. S. Tao, J. Jiang and M. Tao, *Solar Energy Mater. Sol. cells*., 2011, **95**, 3176-3180.

6 I. Jung, D. A. Dikin, R. D. Piner and R. S. Ruoff, *NanoLett*, 2008, **8**, 4283-4287.

7 L. G. D. Arco, Y. Zhang, C. W. Schlenker, K. Ryu, M. E. Thompson and C. Zhou, *ACS Nano*, 2010, **4**, 2865-2873.

8 S. Gilje, S. Han, M. Wang, K. L. Wang and R. B. Kaner, *NanoLett*, 2007, **7**, 3394-3398.

9 Z. Wu, Z. Chen, X. Du, J. M. Logan, J. Sippel, M. Nikolou, K. Kamaras, J. R. Reynolds, D. B. Tanner, A. F. Hebard, A. G. Rinzler, *Science*, 2004, **305**, 1273-1276.

10 E. M. Doherty, S. De, P. E. Lyons, A. Shmeliov, P. N. Nirmalraj, V. Scardaci, J. Joimel, W. J. Blau, J. J. Boland, J. N. Coleman, *Carbon*, 2009, **47**, 2466-2473.

11 J. Y. Lee, S. T. Connor, Y. Cui and P. Peumans, *NanoLett*., 2008, **8**, 689-692.

12 A. Madaria, A. Kumar, F. Ishikawa and C. Zhou, *Nano Res*., 2010, **3**, 564-573.

13 R. Gupta and G. U. Kulkarni, *ACS Appl. Mater. Interfaces*., 2013, **5**, 730-736.

14 K. D. M. Rao, R. Gupta and G. U. Kulkarni, *Adv. Mater. Interfaces.,* 2014, **1**, 1400090.

15 J. C. Manifacier, M. De, Mureia, J. P. Fillarda, E. Vicario, *Thin Solid films*, 1997, **41**, 127-144.

16 S.Geetha, R. Rup, A. Mansingh, *J. Physics Review B*, 1991, **44**, 5672-5680.

17 K. S. Shamala, L.C.S. Murthy and K. N. Rao, *Bull. Mater Sci.,* 2004, **27**, 295-301.

18 S. Hamzaoui and M. Andnane, *Appl. Energy.* 2000, **65**, 19-28.

19 R. Poblec, M. A. El Khakani, A. M. Serventi, M. Trudeau, R. G. Saint Jacques, *Thin Solid films*, 2002, **419**, 230-236.

20 D. A. Popeseu, J. D. Hermann, A. Ensuque, F. B. Verduraz, *Phys. Chem. Chem. Phys*., 2001, **3**, 2522.

21 Y. C. Her J. Y. Wu, Y. R. Lin, Y. S. Tsai, *Appl. Phys. Lett.,* 2006, **89**, 043115.

22 R. G. Haverkamp, A. T. Marshall, B. C. C. Cowie, *Surf. Interface Analysis* 2011, **43**, 847–855.

Chapter IV

Fabrication of Transparent Functional Devices

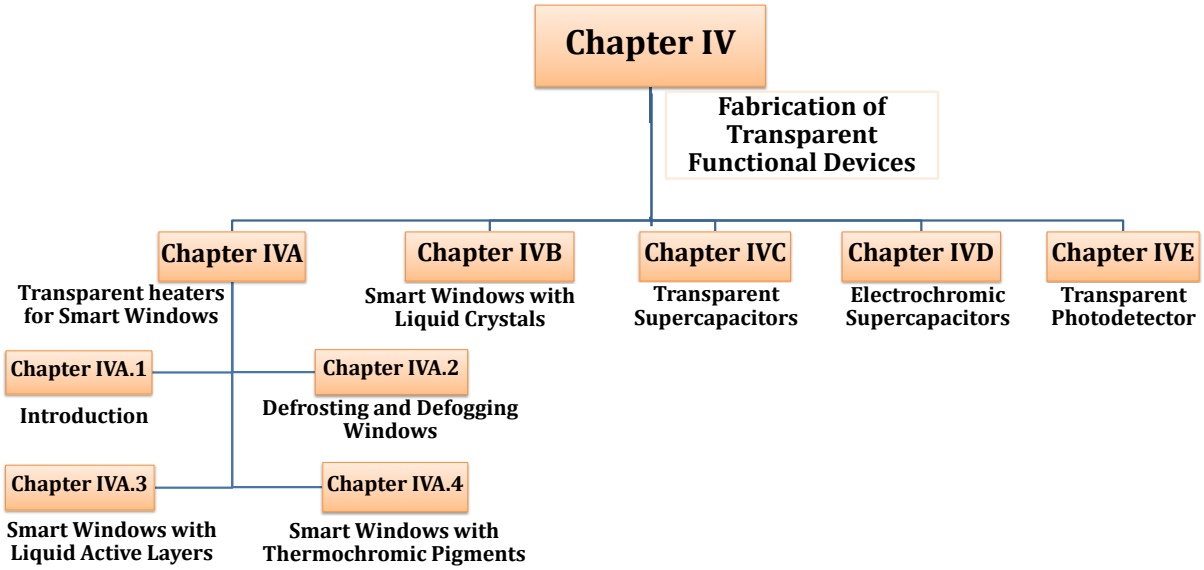

Chapter IV

Fabrication of Transparent Functional Devices

IV.1 General Introduction

Recently, there has been significant interest in making devices highly transparent not only for aesthetic appeal but also for integration of multi-functionality. Transparent devices find potential applications in various fields spanning from energy storage and conversion, displays, sensors, electronics and so on. There are a large number of interesting transparent devices designed and fabricated in the last few years which was mainly possible due to the development of alternative transparent electrodes. Although wide ranges of electrodes are available, achieving "all-see through" device was quite challenging due to the necessity of transparency of every component involved.

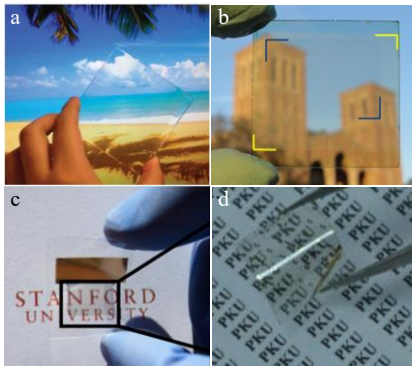

Figure IV.1 Photographs of various transparent devices (a) luminescent solar concentrator, (b) polymer solar cell, (c) battery and (d) photovoltaic detector [1-4].

Transparent energy conversion and storage devices are of high demand for integrating them into displays and windows of buildings and automobiles without compromising the aesthetic of the surfaces. Especially fabricating visibly transparent energy conversion systems using chromophores, whose absorption and emission are in the visible range was quite challenging. To overcome these hurdles, a thin film transparent luminescent solar concentrator (LSC) which is highly transparent in the visible spectrum was integrated onto solar windows, displays and smart glazing systems (Figure IV.1a) [1]. Alternatively, few attempts have been made to fabricate transparent polymer solar cells. A photograph of transparent polymer solar cells from literature is shown in Figure IV.1b. The thus fabricated device has shown 66% of visible light transmittance with 4% power conversion efficiency [2].

To bring transparency to portable personal electronics, not only the displays but also the power storage devices need to be transparent. In this context, efforts have been made to fabricate transparent supercapacitors and batteries. Transparency was achieved either by reducing the thickness of active materials or by patterning the electrodes whose dimensions are much smaller than the detection limit of the human eye. The transparent battery shown in Figure IV.1c provides the maximum energy density of 20 Wh/L [3]. Transparent ultrasound detector with 250 μm thick polymeric optical micro-ring resonator (MRR) is shown to provide sensitivity over wide receiving angles with high bandwidth [4]. CdSe nanobelt/graphene-based transparent self-powered photovoltaic detector (Figure IV.1d) has also been fabricated with high photosensitivity and responsivity [5]. On the other hand, fabrication of transparent gas sensor not only requires transparent detector but also the transparent heater to enhance the sensing performance. Graphene-based transparent electrodes served both as detector and heater, with high sensitivity for NO_2 gas even at very low concentrations [6]. Interestingly even transparent loudspeaker was recently fabricated with hydrogel TCEs and dielectric elastomers [7]. These are few examples of recently developed transparent devices with existing alternative electrodes. In this chapter, various functional devices fabricated with metal mesh network electrodes will be discussed, along with the insight into the low fabrication cost and stability for long term usage. They are classified as defrosting and defogging windows (Chapter IVA.2), smart windows with liquid active layers (Chapter IVA.3), thermochromic pigments (Chapter IVA.4) and liquid crystals (Chapter IVB), transparent and electrochromic supercapacitors (Chapter IVC and IVD) and transparent photodetectors (Chapter IVE).

References

1. Y.Zhao , G. A. Meek , B. G. Levine , R. R. Lunt, *Adv. Optical Mater*. 2014, **2**, 606–611.
2. C. C. Chen *et al*. *ACS Nano*, **6**, 7185-7190.
3. Y. Yang, S. Jeong, L. Hu, H. Wu, S. W. Lee and Y. Cui, *Proceedings of the National Academy of Sciences*, **108**, 13013-13018.
4. H. Li, B. Dong, Z. Zhang, H. F. Zhang, C. Sun, *Sci. Rep.,* **4**, 4496.
5. Z. Gao, W. Jin, Y. Zhou, Y. Dai, B. Yu, C. Liu, W. Xu, Y. Li, H. Peng, Z. Liu, L. Dai, *Nanoscale*, 2013, **5**, 5576- 5581.
6. H. Choi *et al*. *Small*, 2014, **10**, 3812-3812.
7. C. Keplinger, J. Y. Sun, C. C. Foo, P. Rothemund, G. M. Whitesides and Z. Suo, *Science*, 2013, **341**, 984-987.

Chapter IVA

Transparent Heaters for Smart Windows

IVA.1 Introduction to Transparent Heaters and Smart Windows

A transparent conductor, when made to carry current by applying voltage, acts as a transparent heater. Heater plates or sheets that are visibly transparent have many interesting applications in the field of optoelectronic devices such as displays, defrosting, defogging, gas sensing and point-of-care disposable devices etc. One such optoelectrical device is the defrosting and deicing window used typically in LCD panels, windows of vehicles, advertisement boards as well as in display screens of teller machines, avionics, etc. Indeed, these constitute a big fraction of the demand of transparent conductors. Transparent heaters tend to outscore hydrophobic coatings for defrosting and anti-icing applications [1], as the latter exhibit limited mechanical and chemical stability particularly in harsh weather conditions extending over long periods. The transparent heating systems available in the market to defog or deice windshields are ITO based heaters in general [2]. ITOs with sheet resistance ranging between 1 and 250 Ω/sq and power rating ranging from 0.05 to 20 W/sq. inch are available in the market today. ITO based commercial heaters have very low defect density (<5 μm/sq) over large areas with minimum roughness (R_{rms} < 2 nm) [3]. The ITO layer is usually sputtered under vacuum either on flat or on curved glass, because ITO is brittle and cannot be bent or flexed later for use. Typically, ITO films possess modest transmittance (~85%) and good adhesion with the substrate. ITO based heaters are usually laminated with protective layers for ruggedization, mechanical strength, and impact resistance. Additionally, optical coatings are applied on the surface of ITO heaters for index matching so as to reduce haze or reflection losses and to further improve the transmittance of the heater. Similarly, metallic wire or power line based heaters [4] embedded in the acrylic or glass are used to provide the required transparency in airbus cockpit windows [2] and large display boards [5,6]. However, the thickness of a metal wire being in the range of 10−500 μm obstructs the view and therefore, is not preferred in fine display and controls. This explains the growing demand for transparent heaters in recent years. The valuation of the smart glass market was $1581.4 million in 2013 with 20% growth predicted until 2020 [7].

Review based on this study: ACS Appl. Mater. Interfaces 2016, 8, 12559- 12575

In a transparent heater, a steady state temperature is achieved by controlled joule heating of the transparent conductor, and depending on its sheet resistance, the power gets dissipated as heat. The deciding parameter for a heater is its sheet resistance: lower the value better is its power efficiency. High degree of uniformity of the resistance is another important requirement. For a given applied voltage, the heating rate and the temperature attained, depends on the thermal properties of both the heating element and the substrate and also the interface being an additional entity. The temperature attained by the film is usually detected using a pyrometer, T-type thermocouple or a noncontact IR thermal camera, the latter being advantageous as it provides a macroscopic view of the heat distribution across the heater surface in the form of a surface temperature map. The thermal resolution of an IR camera is usually 10−20 mK and hence suitable for measuring temperature distribution over a narrow range of temperature while examining defects as well as hotspots across the active area of a transparent heater. During thermal imaging, the emissivity of the substrate is first calibrated for accurate measurement of temperature. The fabrication of a heater requires good Ohmic contacts with the electrode. The properties that make a transparent conducting electrode as an ideal transparent heater are its low sheet resistance and high thermal stability while not sacrificing the transmittance. Areal uniformity of these properties is also equally essential. In the chapter IVA.2, the current status of the field of transparent heaters is described, highlighting ongoing efforts worldwide in relation to next generation transparent heaters.

In order to maintain convenient indoor temperature, an enormous amount of energy is consumed in residence and much more in commercial buildings. Windows are important components of buildings for air ventilation, photo-protection, indoor lighting etc. [8,9]. Replacement of wooden windows with glass windows in modern days improved the light comforts but on the other hand, became the most vulnerable part of the building for heat loss and gain. In the report of Federal Office of England Efficiency, it is stated that nearly 10-25% of the heat loss in residence are through windows [10]. Furthermore, in another report, it has revealed that 40-50% of the winter heat loading in China is lost through windows [11]. Moreover, indoor artificial

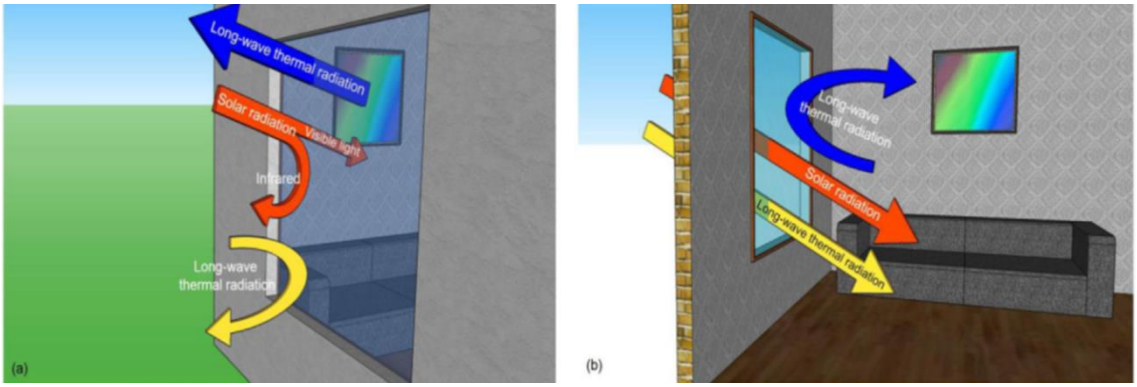

Figure IVA.1.1 Optical properties of an ideal window for (a) hot climate (b) cold climate.

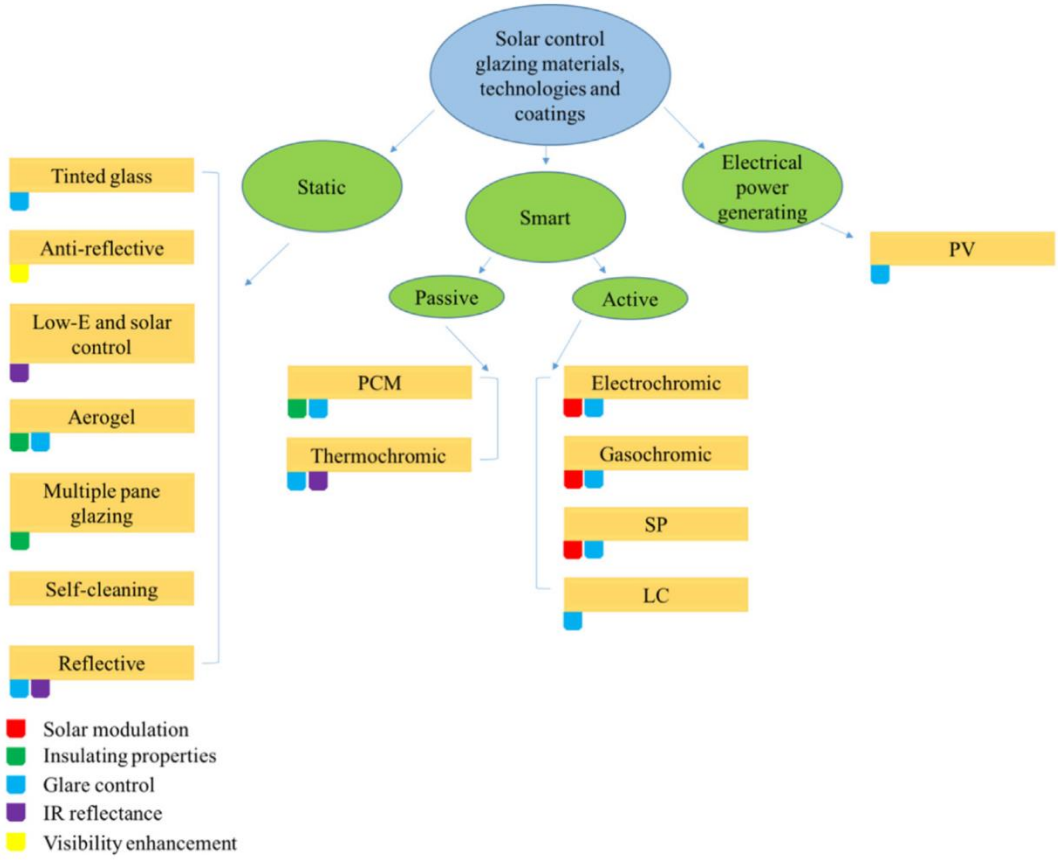

Figure IVA.1.2 Classification of solar control glazing materials, technologies, and coatings.

lighting increases 20% energy consumption worldwide [12]. The NIR transmittance of clear soda lime glass of 4 mm thick is 75-90% which is highly undesired for the summer season [13]. Although usage of curtains, blinds, roller shades, additional film coating, etc. helps to reduce the heat transfer but it is not ideal. An ideal glass window

should allow only visible light and reflect the IR and UV radiations in hot climate whereas it should permit visible and IR radiations and reflect UV light in winter seasons (Figure IVA.1.1) [14]. Realizing ideal glass for day-to-day use is practically difficult. With the advancement of glazing technology, replacing the plain glass with smart glass such as tinted glass, solar control coating, thermochromic, electrochromic, *etc.* reduces the heat loss (Figure IVA.1.2) [15].

Solar control glazing technologies are broadly classified to static, smart and electrical power generating based on its working principle (Figure IVA.1.2). Techniques listed under static are having fixed photo thermal control whereas properties of smart windows can be modulated by external stimuli. The photovoltaic system generates electricity upon exposure to sunlight. Among all these, few well-known technologies are discussed below.

Tinted Glass Windows

By adding metallic components to clear glass, color of the glass and thus the optical property of glass are modulated [16]. Thus, tinted glass considerably reduces the glare and solar light transmittance although it leads to the slight decrease in the color and visibility (See Figure IVA.1.3). For instance, green color glass (thickness, 8mm; visible transmittance, 68%) obtained by adding Co/Fe/Cr/V/Cu transfers only less than 50% of solar heat to indoor [8].

Figure IVA.1.3 Photographs of tinted glass.

Anti-reflective Coatings for Windows

Anti-reflective coating enhances the transmittance of solar light and energy inside the buildings. It can increase light transmittance up to 15% for a double pane window [17]. Two common approaches to achieve anti-reflective coatings are coating low refractive index materials (SiO_2 and MgF_2) with high refractive index (TiO_2) ones and employing patterned and porous structures on glass windows (Figure IVA.1.4) [18]. For metal oxide coatings various chemical (sol-gel, spin coating, and dip coating) and physical (CVD, PVD) method are used whereas nanoimprint lithography is used for patterning [19].

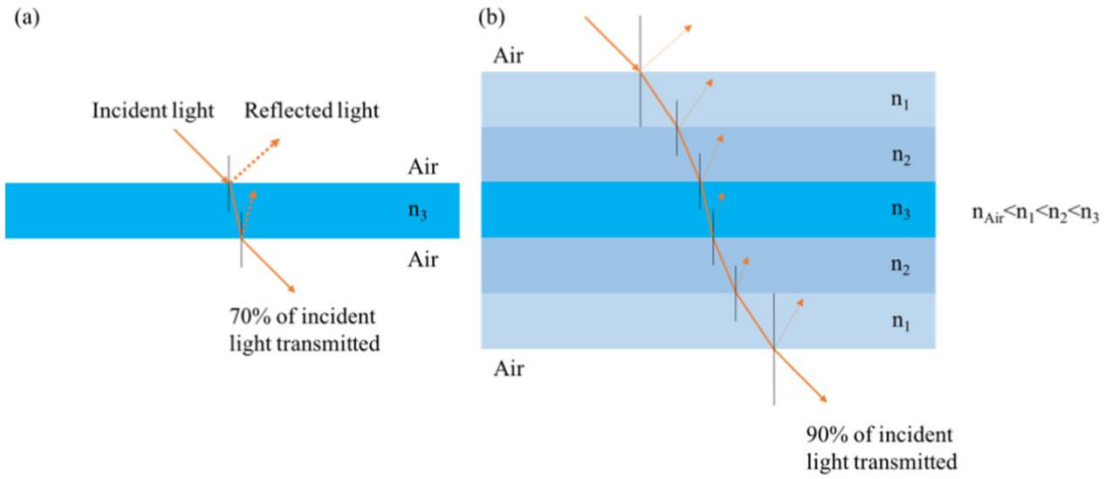

Figure IVA.1.4 (a) and (b) shows the schematic representation transmittance with plain and anti-reflective glasses.

Low-emissivity Glass coatings

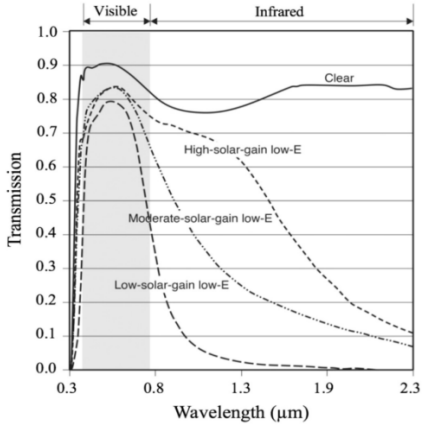

Figure IVA.1.5 Transmittance spectra of plain and low-E coated glasses.

Emissivity (E) is the measure of heat radiated by a material relative to the black body, for which emissivity is 1 [15]. Advantage of low-E coating is its spectral selectivity towards visible and IR radiations (see Figure IVA.1.5). While glass absorbs the solar energy, it exchanges heat with the environment. Thus, glass can reradiate solar heat inside the building and drastically affects the indoor temperature. Using low-E coating, this heat exchange can be avoided. Commonly doped metal oxides and metal films sandwiched between dielectric layer were used for low-E and solar control coatings [20].

Thermochromic Glazing Windows

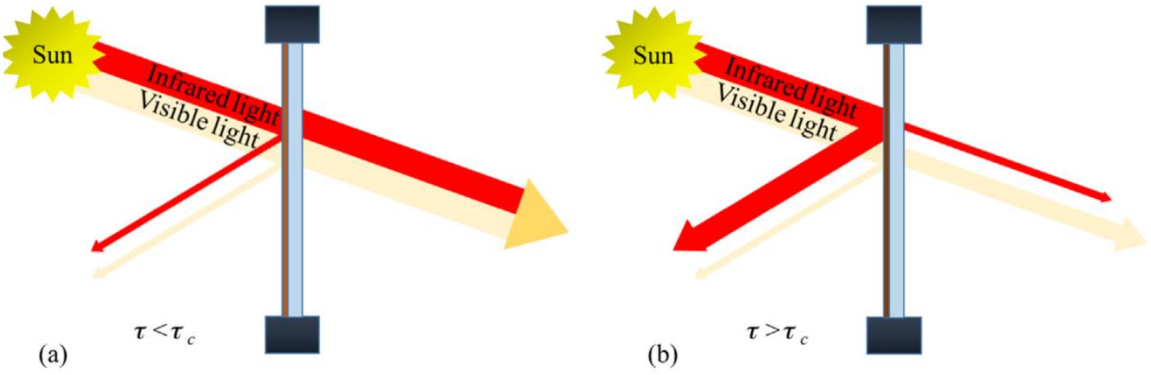

Figure IVA.1.6 Transmittance and reflectance of (a) plain soda-lime glass and (b) glass with a spectrally selective coating.

As the name suggests, the color and optical properties of these materials vary with respect to temperature [21]. Vanadium oxide (VO_2) is the most adept thermochromic material, but many polymer materials are also reported. At its transition temperature, semiconductor to metal transition of VO_2 occurs and it starts reflecting IR radiations (see schematic in Figure IVA.1.6) [15]. High transition temperatures (68 °C), low visible light transmittance, poor stability are few shortcomings of VO_2.

Phase Changing Materials (PCM) Based Windows

Phase changing materials possess high thermal energy storage and thus reduce the energy demand during winter by 50%. Organic components such as paraffin and non-paraffins (esters, glycols fatty acids, alcohols), inorganic compounds (salt hydrated metallic) and eutectic materials (both organic and inorganics) are used between glass

panes to realize PCM windows (see Figure IVA.1.7) [22]. Translucent PCM windows are commercially available, but the light transmittance quality has to be improved for better performance [23].

Figure IVB.1.7 PCM glazing windows in opaque solid (left), and transparent fluid state (right).

Liquid crystal (LC) windows

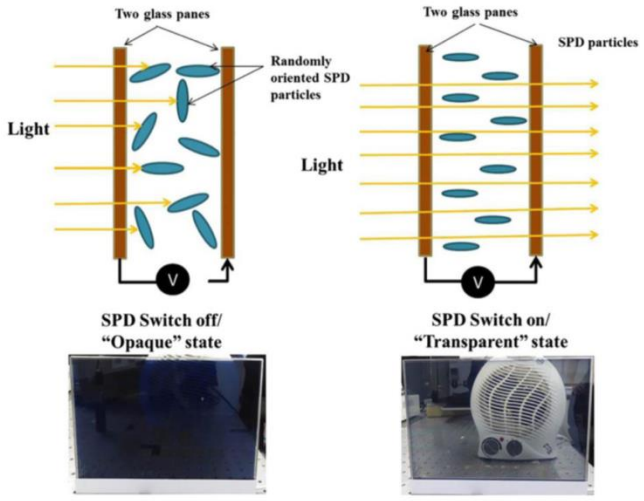

Figure IVA.1.8 Schematic and photographs of LC devices under V_{OFF} and V_{ON} state.

LC devices fall under the category of smart electroactive devices. The liquid crystals are made to disperse in polymers and are sandwiched between transparent conducting glasses. Under V_{OFF} state, the device looks translucent due to refractive index mismatch between the polymer matrix and LC droplets. Upon applying AC voltage, LC molecules which were randomly scattered will align and brings the transparency to the device (see Figure IVA.1.8) [24]. Unlike PCM based devices, light

transmittance can be tuned with the input voltage. Although LC windows are useful for privacy purposes, research is still going on to find reverse transition mode (transparent to opaque).

Electrochromic (EC) devices

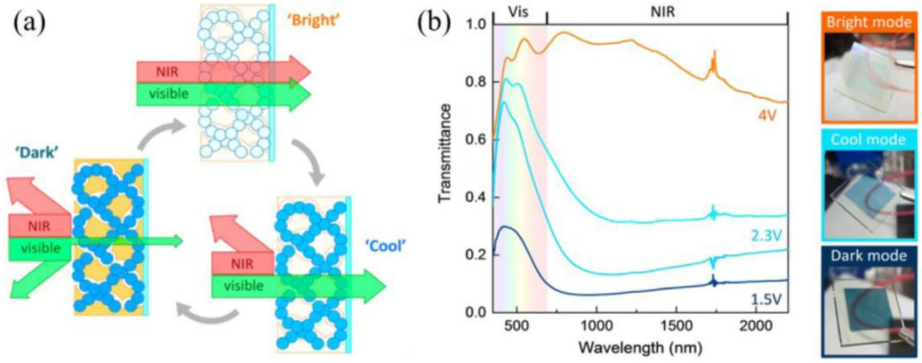

Figure IVA.1.9 (a) Schematic and (b) transmittance spectra of the spectrally selective electrochromic device.

Using an external stimulus (electric field), optical properties such as color and transmittance of EC material are modulated. Organic systems such as conducting polymers, quinones, terephthalates, phthalocyanines, bipyridilium system, cyanobiphenyls and tetrathiafulvalenes and inorganic metal oxides are widely used in EC device fabrication [25]. EC materials change color upon insertion or extraction of ions such as H^+ or Li^+ from them. High modulation of visible light and NIR transmittance occurs within few second switching time (see Figure IVA.1.9) [26]. Recent research suggests that NIR transmittance alone can be modulated without altering visible light transmittance [27-29]. Moreover, researchers are also developing self-powered EC devices for better energy conservation.

In this chapter, phase changing material based smart windows with low-cost metal mesh based transparent conductors have been demonstrated (Chapter IVA.3). Also, the thermochromic numeric display was designed and illustrated successfully (Chapter IVA.4). Furthermore, the fast switching liquid crystal based light modulation device has been fabricated using hybrid TCEs (Chapter IVB).

References

1. Lv, J. Y.; Song, Y. L.; Jiang, L.; Wang, J. J. Bio-Inspired Strategies for Anti-Icing. *ACS Nano* 8 (**2014**) 3152–3169.

2. http://www.saint-gobain-sully.com/aerospace_technologies_heating_systems.php (accessed April 1, **2016**).

3. http://www.vartechsystems.com/products/TransparentHeaters.asp (accessed April 1, **2016**).

4. Laforte, J. L.; Allaire, M. A.; Laflamme, J. State-of-the-Art on Power Line De-Icing. *Atmos. Res*. 46 **(1998)** 143–158.

5. http://www.frostfighter.com/clear-view-defrosters-about.htm (accessed April 1, **2016**).

6. https://www.plumbingsupply.com/clearmirrors.html (accessed April 1, **2016**).

7. http://www.marketsandmarkets.com/PressReleases/smartglass.asp (accessed April 1, **2016**).

8. H.K. Park, H. Kim, Acoustic insulation performance of improved airtight windows, *Constr. Build. Mater.* 93 (**2015**) 542–550.

9. C. Tuchinda, S. Srivannaboon, H.W. Lim, Photoprotection by window glass, automobile glass, and sunglasses, *J. Am. Acad. Dermatol.* 54 (**2006**) 845–854.

10. Tips: Windows, 2015. ⟨http://energy.gov/energysaver/articles/tips-windows⟩, **2014**.

11. S.Z. Wang, M. Guan, Windows—the key of building energy efficiency, *Constr. Glas. Glas. Ind.* 4 (**2005**) 3–8.

12. E.J. Gago, T. Muneer, M. Knez, H. Köster, Natural light controls and guides in buildings. Energy saving for electrical lighting, reduction of cooling load, *Renew. Sustain. Energy Rev.* 41 (**2015**) 1–13.

13. H. Pfaender, Flat glass, in: H.G. Pfaender (Ed.), *Schott Guide to Glass*, Springer, Netherlands, **1996**, pp. 51–83.

14. L. Long, H. Ye, How to be smart and energy efficient: a general discussion on thermochromic windows, *Sci. Rep.* 4 (**2014**).

15. S.D. Rezaei et al. *Sol. Energy Mater. Sol. Cells* 159 (**2017**) 26–51.

16. N.N. Shcherbakova, V.I. Kondrashov, I.A. Kupriyanova, V.A. Gorokhovskii, Regression equations for determining light transmission in tinted float glass, *Glass Ceram.* 58 (**2001**) 164–165.

17. T. Rosencrantz, H. Bülow-Hübe, B. Karlsson, A. Roos, Increased solar energy and daylight utilisation using anti-reflective coatings in energy-efficient windows, *Sol. Energy Mater. Sol. Cells* 89 (**2005**) 249–260.

18. H.K. Raut, S.S. Dinachali, K.K. Ansah-Antwi, V.A. Ganesh, S. Ramakrishna, Fabrication of highly uniform and porous MgF_2 anti-reflective coatings by polymer based sol-gel processing on large-area glass substrates, *Nanotechnology* 24 (**2013**) 505201.

19. H.K. Raut, V.A. Ganesh, A.S. Nair, S. Ramakrishna, Anti-reflective coatings: a critical, in-depth review, *Energy Environ. Sci.* 4 (**2011**) 3779–3804.

20. Commercial Windows, Window Technologies: Glass, Low-E Coatings, Commercial Windows, **2015** (n.d.). ⟨http://www.commercialwindows.org/lowe.php⟩.

21. I.P. Parkin, T.D. Manning, Intelligent thermochromic windows, *J. Chem. Educ.* 83 (**2006**) 393.

22. T. Silva, R. Vicente, F. Rodrigues, Literature review on the use of phase change materials in glazing and shading solutions, *Renew. Sustain. Energy Rev.* 53 (**2016**) 515–535.

23. S.E. Kalnæs, B.P. Jelle, Phase change materials and products for building applications: a state-of-the-art review and future research opportunities, *Energy Build.* 94 (**2015**) 150–176.

24. A. Ghosh, B. Norton, A. Duffy, Measured overall heat transfer coefficient of a suspended particle device switchable glazing, Appl. Energy 159 (**2015**) 362–369.

25. D. Cupelli, F.P. Nicoletta, S. Manfredi, G. De Filpo, G. Chidichimo, Electrically switchable chromogenic materials for external glazing, *Sol. Energy Mater. Sol. Cells* 93 (**2009**) 329–333.

26. H. Liu, Y. Chen, G. Tian, Z. Ren, C. Tian, H. Fu, Visible-light-induced self-cleaning property of $Bi_2Ti_2O_7$-TiO_2 composite nanowire arrays, *Langmuir* (**2015**).

27. J. Kim, G.K. Ong, Y. Wang, G. LeBlanc, T.E. Williams, T.M. Mattox, et al. Nanocomposite architecture for rapid, spectrally-selective electrochromic modulation of solar transmittance, *Nano Lett.* 15 (**2015**) 5574–5579.

28. G. Garcia, R. Buonsanti, A. Llordes, E.L. Runnerstrom, A. Bergerud, D.J. Milliron, Near-infrared spectrally selective plasmonic electrochromic thin films, *Adv. Opt. Mater.* 1 (**2013**) 215–220.

29. C.J. Dahlman, Y. Tan, M.A. Marcus, D.J. Milliron, Spectroelectrochemical signatures of capacitive charging and ion insertion in doped anatase titania nanocrystals, *J. Am. Chem. Soc.* 137 (**2015**) 9160–9166.

Chapter IVA.2

Large Area Defrosting and Defogging Windows

Summary

Highly interconnected crackles were obtained by spreading commercially available low cost crackle wall paint based precursor by the drop coating technique. An interconnected Ag mesh was fabricated by depositing metal over the crackle network followed by the removal of the template. The metal network is well conducting (1 Ω/sq) with transmittance of ~ 77% over the fabricated area, 18 × 15 cm^2. By joule heating using few volts, uniform temperatures up to 170 °C were achieved on the electrode area and a high thermal resistance of 255.2 °C cm^2 W^{-1} was obtained. The electrode was tested for defrosting application by exposing it to liquid nitrogen (LN_2) vapors at ~ -60 °C while applying 8.5 V for 2 min, when the frost disappeared making the display board below, visible. The transparent heater could successfully withstand an ultrasonication test, as well as many defrosting cycles.

IVA.2.1 Introduction

The changes in the climatic condition often result in frosting and icing that severely affect human life, especially in cold countries [1]. Frost formation and icing pose serious safety issues for aircrafts, telecommunication and road safety signals by blocking the displays, and thus leading to traffic failure and severe accidents [2,3]. Therefore, increasing efforts have been made towards designing anti-icing and defrosting surfaces by texturing, chemical coatings etc [4,5]. The patterning and structuring of a surface is usually performed to mimic lotus and rice leaf type nanostructures [6,7]. However, these methods need optimization in terms of processing and scalability for practical applications. The superhydrophobic chemical coatings, such as polymers and their nanocomposites, are used to prevent frost formation; however, not all superhydrophobic surfaces are icephobic in nature [7,8]. In this context, electrothermal or joule heating is considered to be one of the most efficient approaches [9]. The de-icing of conducting transmission lines by joule heating is universally adopted. Similarly, printed metal grids are highly efficient for

Paper based on this study: RSC Adv., 2014, 4, 49745

defrosting applications, but being visibly thick they obstruct ~ 50% of the total view, which is certainly undesired [10]. Several devices, such as outdoor displays, avionic displays, automobile windows, as well in periscopes, require clear visibility irrespective of the weather conditions, and thus the development of visibly transparent heaters is a necessity [11,12].

Transparent conducting oxide, tin doped indium oxide (ITO) has been the obvious choice as heating element because of its proven performance in optoelectronics, namely high transmittance in the visible region, low sheet resistance and stability in environmental conditions [13–15]. However, due to indium scarcity and the associated cost, ITO is considered prohibitive, particularly in large area applications [16–18]. Moreover, high power consumption and slow thermal response associated with ITO based heaters have limited its usage as discussed in Chapter IV.A. With major developments in optoelectronics in the last two decades, new alternative transparent conductors, such as graphene [19], carbon nanotube (CNT) network [20,21], metal nanowire [22,23], metal mesh network [24], PEDOT [25], as well as hybrid films [26–28], have been developed and there has been an increasing interest in using these non-ITO based alternatives in electrothermal applications. Thus, recently, attempts have been made to fabricate transparent heaters with graphene [11,29–31], CNT [12,32–36], nanocrystalline diamond [37], metallic nanowires [38], and sometimes involving their hybrids [39]. CNT and graphene based heaters have shown excellent heating performance with uniform heat distribution although the operating voltage and the power required for their operation are usually high [11,29,35], as in general, they possess high sheet resistance. A good heater should give uniform thermal distribution over the heating area and achieve higher temperatures with low power. Highly conducting metal nanostructures, on the other hand, can work with lower operating voltages with better response time, but the nanowire junctions are prone to oxidation and failure at temperatures typically above 50 °C [22]. To improve the junction resistance, and thus the overall performance of the heater, several post synthesis treatment and hybrid structuring methods have been reported [38]. While these remedies may bring down the sheet resistance to suit optoelectronic applications (typically few Ω/sq), the overall resistance for a large

area can be still high (a few tens or hundreds of Ω) requiring high power for electrothermal applications [41]. Further, the well-known trade-off between transmittance and sheet resistance in a transparent conductor is an added constraint [39,40]. Sheet resistance cannot be easily lowered without sacrificing the transmittance even with new generation alternatives. Extremely low sheet resistance (~1 Ω/sq) attained without disturbing transmittance is highly desirable, which is rather challenging.

The fabrication of transparent electrodes using template based methods is becoming demanding [40–42]. Recently, a crackle templating method of fabricating metal wire networks devoid of crossbar junctions have been developed and shown that their performance parameters are close to those of ITO [43,44]. In this templating method, the wire thickness could be increased to lower the sheet resistance without disturbing the transmittance. Because of low resistance, the wire mesh could be employed as a joule heater to reach annealing temperatures of a few hundred degrees Celsius over cm^2 areas [43]. In this study, their efficacy as transparent heaters was examined, especially in the context of defrosting over a large area.

IVA.2.2 Scope of the present investigation

In recent years, there have been many advances in this area with the advent of next generation transparent conducting electrodes (TCE) based on a wide range of materials such as oxide nanoparticles, CNTs, graphene, metal nanowires and their hybrids. The challenge has been to obtain uniform and stable temperature distribution over large areas, fast heating and cooling rates at low enough input power yet not sacrificing the visible transmittance. This chapter provides the details of fabrication of defrosting and defogging devices paying due attention to all the issues mentioned above. For this purpose, a simpler template formation method has been explored, unlike before, involving only a dropper or a brush, which requires minimal effort and no instrumentation. In this manner, the fabrication should be scalable to large areas with only a linear increase in cost. The prepared Ag mesh based transparent heaters have shown stability in defrosting even at sub-zero temperatures.

IVA.2.3 Experimental Details

Fabrication of Ag wire mesh

Commercially available crackle paint (Premium Coatings and Chemicals, India) was used as crackling precursor for these experiments. The crackle precursor was diluted with the diluter (0.65 to 1 g mL^{-1}) to get interconnected crackle network. The glass substrates (1.5 mm thickness) were cleaned with water, acetone and IPA prior to template formation. The crackle precursor was drop coated on the substrates and allowed to spread. The presence of film forming agents (ethyl acetate and pentyl acetate) in crackle precursor, enables the spreading and leveling leading to a uniform film coating over large area (vide infra). The wet film was allowed to dry under ambient conditions without any disturbance. Ag metal was physically deposited in the crackle grooves using a resistive thermal evaporator (Hind Hivac, India) at a base pressure of 10^{-6} torr and the template was lifted off neatly by gently rinsing it in acetone resulting in a chemically clean metal network. For surface modification, Ag mesh/glass was dipped in a 10 mM solution of 1-hexadecanethiol in ethanol for overnight.

IVA.2.4 Results and Discussion

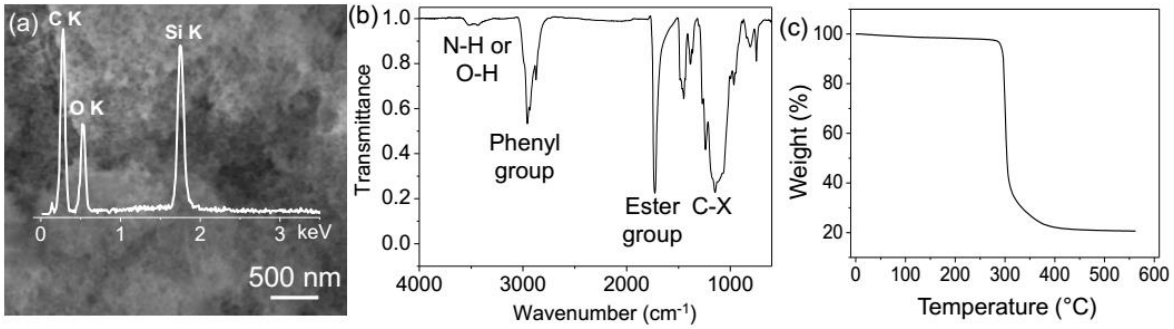

Figure IVA.2.1 (a) High magnification image of crackle paint and its EDS spectrum overlaid. (b) Infrared spectrum of crackle precursor. (c) TGA curve of crackling precursor shows that the decomposition starts around 300 °C and leaves behind SiO_2.

The crackle precursor is basically a colloidal dispersion of SiO_2 nanoparticles which is confirmed from EDS spectrum (Figure IVA.2.1a). IR spectrum shown in Figure IVA.2.1b confirms the presence of ester based component in crackle

precursor. Thermogravimetric analysis (TGA) shows that crackle precursor start decomposing at ~ 300 °C (Figure IVA.2.1c). Coating of the crackle template deserves some detailed mention. In the Chapter IIIB, the crackle precursor was spread over A4 sized substrates by the rod coating method to obtain the crackle template.

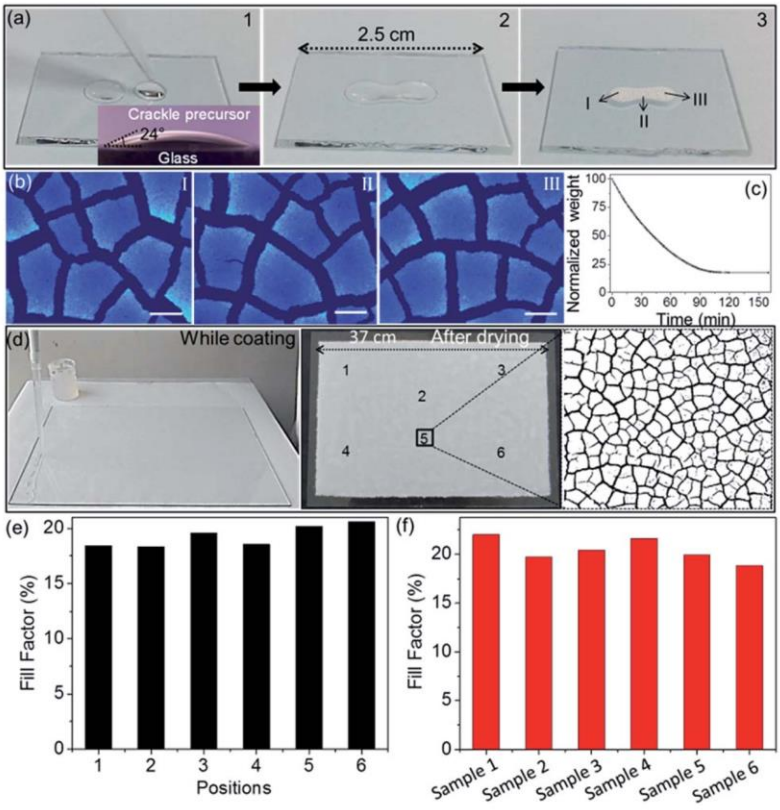

Figure IVA.2.2 (a) Shows spreading of the two drops of the crackle precursor leading to a uniform film. Inset is the contact angle measured between crackle precursor and glass substrate. The completely dried and crackled film was obtained after 20 min. (b) Optical profiler images taken at areas marked in (a) are shown in I, II and III. Scale bar is 200 μm and thickness of the crackle precursor is ~ 75 μm. (c) Change in the weight of the crackle precursor coated on glass substrate versus time. Images taken (d) while drop coating crackle precursor over a 37 × 25 cm^2 area glass substrate and after drying leading to crackle network formation. Fill factor of crackle network (the black trace refers to crackle network and white region corresponds to crackle precursor) from marked region in dried film. (e) Histogram of fill factor calculated from different positions of sample shown in (d). (f) The histogram representation of fill factor calculated from six samples.

Here in this study, the precursor after some optimization is examined for its ability to extend over even larger areas by a simple drop coating technique, which does not require any instrumentation or infrastructure. The primary requirement for drop coating a precursor is that the drops should effortlessly merge to form a uniformly thick wet layer all over. The uniformity in the layer thickness is important as it determines the properties of the crack network [45,46], namely the crack width, crack spacing and interconnectivity.

In order to examine this aspect, two drops of the crackle precursor were closely positioned, but separated (Figure IVA.2.2a). As the precursor wets the glass substrate with low contact angle (inset of Figure IVA.2.2a), the drops gradually spread and merge to form a dumbbell shaped layer as drying sets in. Optical profiler images from the different marked regions (see Figure IVA.2.2b) show cracks of similar widths indicating uniform thickness of the precursor layer.

The drying process is rather slow (Figure IVA.2.2c), which is clearly an advantage for extending drop coating to large areas. Under optimized conditions, the crackle precursor was drop coated over a big glass substrate as shown in Figure IVA.2.2d, which upon drying in air produced an interconnected crackle network (see Figure IVA.2.3).

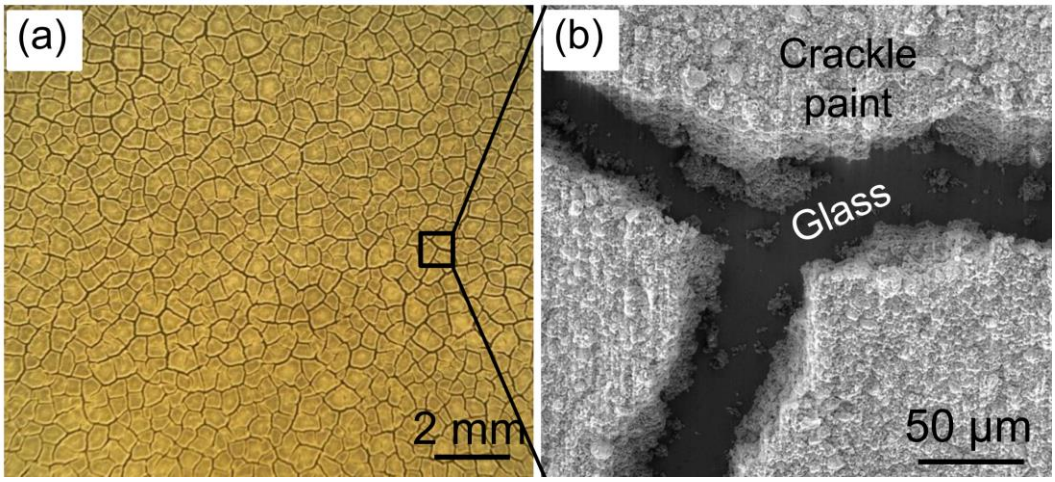

Fig. IVA.2.3 (a) Optical microscopic image of the crackle network. (b) SEM image of crackles formed by the crackle paint over glass substrate.

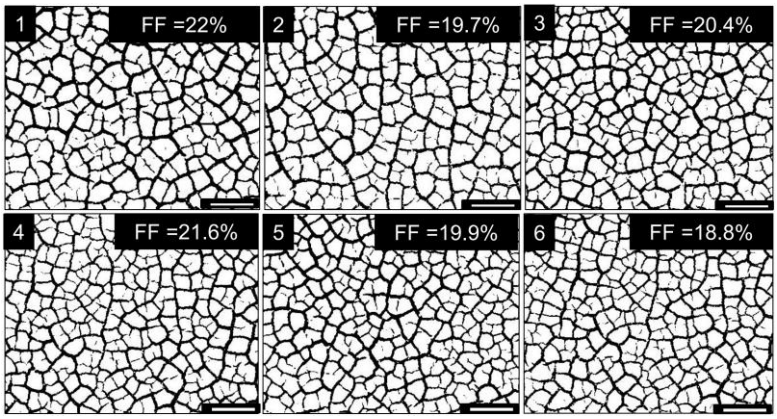

Figure IVA.2.4 The fill factor calculation on crackles formed at similar conditions over six different substrates. Scale bar is 1 mm.

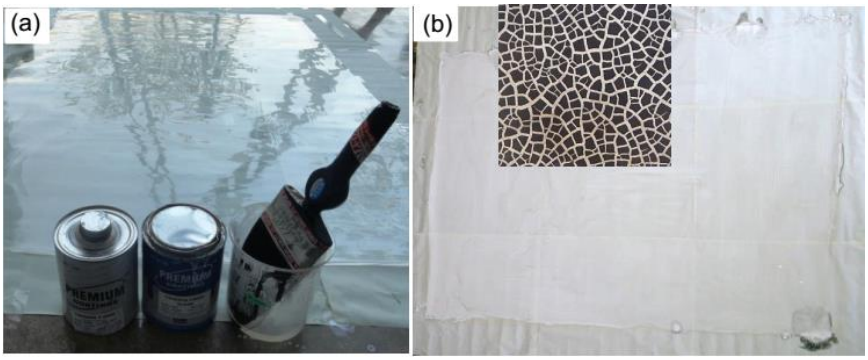

Figure IVA.2.5 (a) Developing crackle template by drop coating crackle precursor over 155 × 102 cm^2 PET substrate. The wet layer is left 2-3 h for self-drying. (b) The dried layer crackle itself and optical microscope image of crackled film is shown in the inset.

A magnified view of the crackle network is given in an SEM image (Figure IVA.2.3b) which indicates that crackles are ~ 40–50 μm wide and are deep down to the substrate except few little left over precursor in the grooves. The uniformity of the crackle network formed over large area glass substrate was evidenced from the fill factor analysis performed from various locations (see Figure IVA.2.2d). From the histogram shown in Figure IVA.2.2e, the fill factor of the network (black regions) is found to be nearly 20% from various locations, which is easily reproducible over many samples (Figure IVA.2.2f and Figure IVA.2.4). As is done during wall painting, a brush can aid to evenly spread the drying layer over ultra large areas (Figure IVA.2.5).

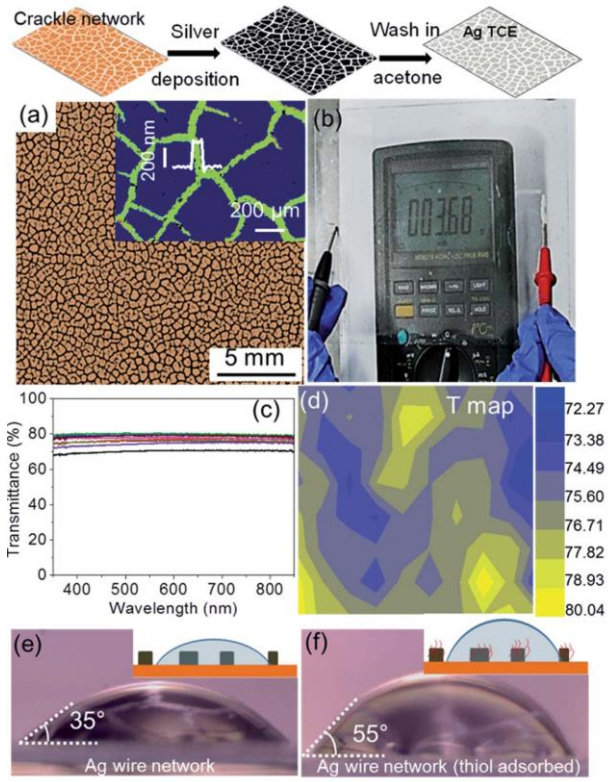

Figure IVA.2.6 Schematic for TCE fabrication is shown. (a) Optical image of the Ag mesh on glass. Inset is the optical profiler image (thickness ~ 300 nm). (b) The image of the transparent conductor connected to a multimeter. (c) Transmittance spectra measured from 10 different locations and (d) the transmittance map. The bright yellow and blue coloured regions correspond to 80% and 72% transmittance, respectively, with other intermediate colours representing transmittance in between 80% to 72%. Contact angle of water on Ag mesh/glass, (e) before and (f) after coating with 1-hexadecanethiol. The wire network is seen in reflection within the drop. Insets are schematic representations.

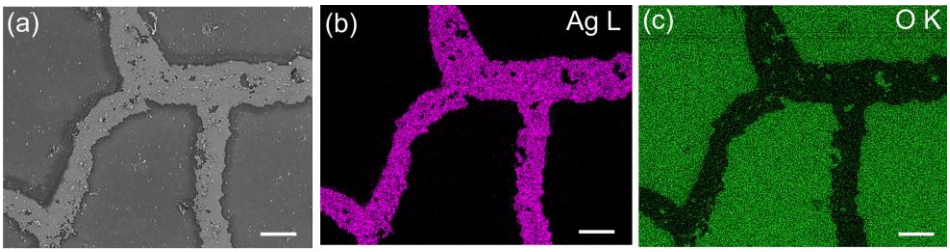

Figure IVA.2.7 (a) SEM image and EDS mapping of (b) Ag L and (c) O K signal from the patterned substrate. Scale bar is 50 μm.

Following Ag deposition by a physical evaporation method, the template layer was washed away in acetone leaving behind Ag mesh on the substrate (see schematic in Figure IVA.2.6). The optical image in Figure IVA.2.6a shows interconnected Ag wires in the network with ~ 300 nm thickness, as measured using an optical profiler (inset in Figure IVA.2.6a). A SEM image and EDS mapping of the Ag mesh (Figure IVA.2.7) show continuous Ag signal in the form of an interconnected junctionless wire with only slight defects because of the unwashed crack precursor. This crackle templating method is scalable as seen with the network formed over 18 × 15 cm^2 areas in Figure IVA.2.6b. A two probe measurement across 18 cm using a multimeter showed resistance of 3.68 Ω (Figure IVA.2.6b). The sheet resistance of Ag mesh is ~1 Ω/sq. Obviously, such low sheet resistance is achieved because of seamless junctions and high thickness (300 nm) of the mesh. The transmittance spectra measured from 10 different regions of the network are shown in Figure IVA.2.6c and an average transmittance value of ~ 77% ±2.1% was obtained over the entire spectrum. The transmittance mapping was performed by scanning the sample with a scanner (hp Scanjet 2400) and intensity distribution was analysed using ImageJ software. A typical transmission map over a 2.5 × 2.5 cm^2 area is shown in Figure IVA.2.6d. This value of transmittance is commendable given the low sheet resistance value. Thus, with this mesh structure, one can lower the resistance by increasing the thickness without affecting the transmittance. From transmittance and sheet resistance values, the figure of merit (FoM, σ_{DC}/σ_{OP}) was estimated for the transparent conductor, using the eqn (IVA.2.1)[10]

$$\sigma_{DC}/\sigma_{OP} = Z_o/2R_s(T^{-1/2} - 1) \quad \text{(IVA.2.1)}$$

The estimated FoM value is 1350, which is significant when compared to literature values [42]. Further, the surface property of the metal mesh can be exploited by chemically modifying it. By adsorbing a monolayer of 1-hexadecanethiol on the Ag mesh surface, the water contact angle was enhanced from 35° (Figure IVA.2.6e) to ~ 55° (Figure IVA.2.6f) [47]. Higher contact angle is beneficial in self-cleaning of the transparent electrode.

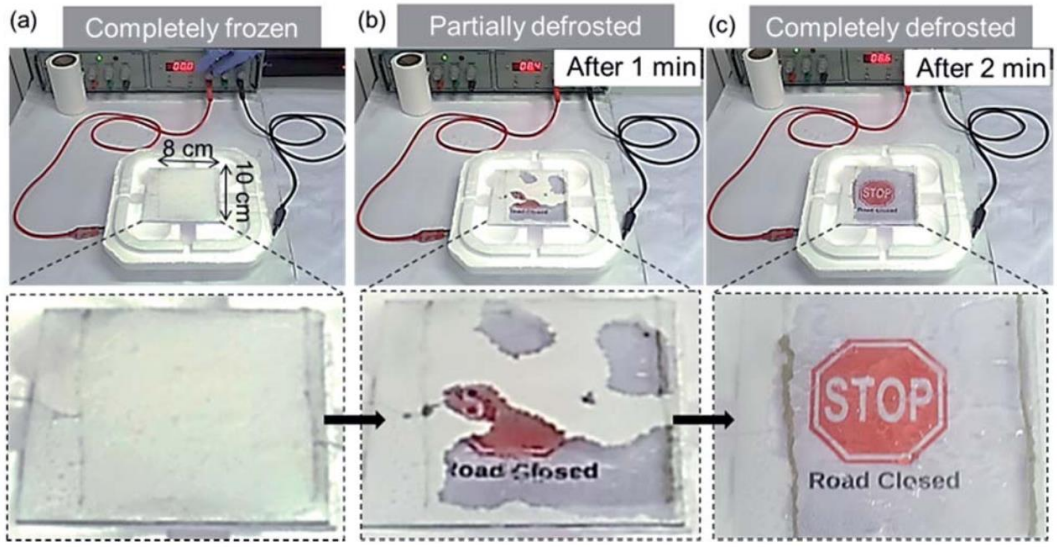

Figure IVA.2.8 Performance of Ag mesh/glass as defrosting window panel. (a) Transparent electrode was allowed to freeze by placing it over the LN_2 container. (b) After applying 8.5 V for 1 min, the bottom display board was partially visible, and at 2 min (c) the view becomes completely clear.

The performance of the Ag mesh as a transparent defrosting panel is demonstrated by joule-heating it under frosting conditions. First, the frost was allowed to form on the glass panel by placing it over a liquid nitrogen (LN_2) container. The panel appeared opaque as its temperature dropped to ~ -60 °C (measured using a thermocouple) because of the frost formation (Figure IVA.2.8a). Upon applying 8.5 V to the end terminals made of Ag epoxy, the frost began to melt leading to a clear view in ~ 2 min even in the presence of LN_2 vapors (Figure IVA.2.8b and c and Movie IVA.2.S1 in CD (speed, 6×)). A clear view of the display board from beneath was possible following defrosting (see bottom images in Figure IVA.2.8). Most literature results pertain to near zero degrees Celsius (see Table IVA.2.1). Importantly, in this study, the transparent heater was tested while it was kept in frosting conditions just like the real-life application. Other notable point is that it works at nominal power/voltage (see Table IVA.2.1), because of its low sheet resistance. The water droplets retaining over the Ag mesh could be avoided by holding the display board in vertical position rather than horizontal. Further, by

coating with thiol molecules, the contact angle can be increased to assist the water removal.

Table IVA.2.1 Literature comparison of TCE parameters, maximum temperature achieved, area of the heater, applied voltages and defrosting response time (NA – not available from manuscript)

Material	TCE		Temperature achieved (°C)	Area (cm^2)	Frost creating conditions	Voltage (V)	Time (s)	Ref.No.
	T (%)	R_s (Ω/□)						
SWCNT	91.3	1190	120	2.5 × 2.5	Freezer	12	60	12
MWCNT	85	669	37	2.5 × 2.1	Freezer	10	18	33
MWCNT	50	172	42	NA	Freezer	10	10	34
RGO	45	5370	NA	NA	Freezer	10	80	48
RGO	81	6079	45	2 × 1.4	Freezer	60	120	11
Graphene	85	750	55	NA	Freezer	30	30	31
AgNWs	92	11	NA	2.5 × 2.5	Freezer	10	40	49
AgNWs	>90	50	70	NA	Freezer	12	60	38
RGO/AgNWs	80	27	150	2.5 × 2.5	Freezer	10	40	50
ITO NPs	>90	2500	180	NA	Dry-ice	50	10	15
ITO NPs	>80	633	163	NA	Dry-ice	20	10	14
Patterned Ag	60-80	2	100	6 × 6	Freezer	0.8	>30	10
Ag mesh	**77**	**1**	**170**	**10 × 8**	**-60 °C, LN_2 vapors**	**8.5**	**120**	**Present study**

In the literature, defrosting transparent heaters have been fabricated using carbon derivatives (CNTs [12,33,34], graphene oxide (GO) [11,48], graphene [31]), Ag nanowires [38,49], composites of GO and Ag nanowires [50] and ITO [14,15]. Carbon based heaters with typically high sheet resistances require higher power to melt the frost [11,31], compared to the results shown above. Ag nanowire based heaters, although exhibiting lower sheet resistance and operating at relatively lower voltages [38,50], their outdoor stability is rather poor because of innumerable wire junctions. Zhang et al. used large sized graphene microsheets as protective layer for Ag nanowires [50]. Moreover, in most literature examples [11,12,31,33,34,38,48–50], the frost load on the heater is nominal with common refrigerator temperatures (~ -5 °C). Often, the frost load is taken off prior to heating, which makes it difficult to assess the efficacy of the heater. ITO based heaters; however, have been demonstrated live in dry ice conditions [14,15]. As evident, these issues were addressed in the present study. Other advantage of the present method is that the

thickness of the metal mesh can be tuned to enhance the performance of defrosting action.

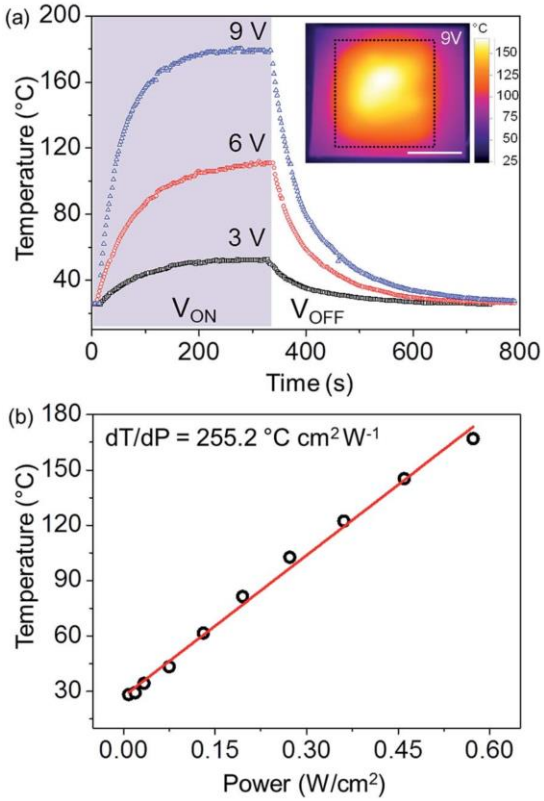

Figure IVA.2.9 Performance of Ag mesh/glass based transparent heater. (a) Temperature rise and fall curves for different applied voltages. Inset is the thermal image collected from backside of the TCE at 9 V. Scale bar is 1 cm. (b) Temperature versus power plot for the transparent heater.

The electrothermal performance of the Ag mesh/glass was quantitatively examined in detail using IR imaging under ambient conditions (Figure IVA.2.9). By applying a DC voltage across the two Ag epoxy contact pads, the mesh was heated and from the IR images the surface temperature was derived. The surface temperature was found to gradually increase to reach a steady state value, which increased with applied voltage. A thermal image obtained with 9 V (see inset of Figure IVA.2.9a) shows the temperature distribution in the heater area. The temperature uniformity as seen from the back of the glass substrate could have been better if a thinner substrate was used (in the present study, 1.5 mm). The edges of the substrate however, show lower temperatures because of radiative dissipation.

Leaving the contact lines and the edges, the active area as marked in inset of Figure IVA.2.9a shows 128 ± 43.5 °C (see marked rectangular region), which can be improved by reducing substrate thickness and also by defining the electrodes all around.

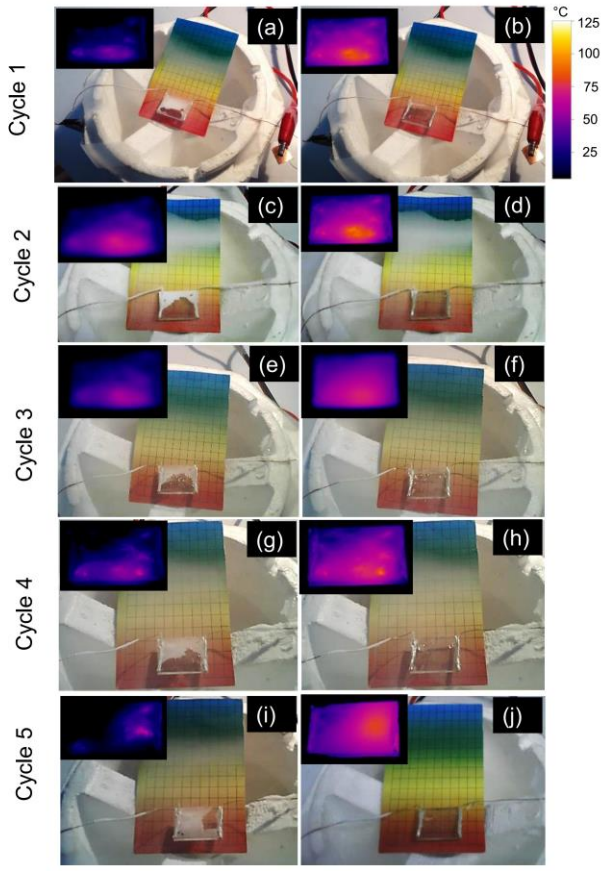

Figure IVA.2.10 Photographs on the left were taken while performing defrosting experiment and those on the right were captured after complete defrosting. The corresponding IR images are in the insets.

With increase in input voltage from 3 to 9 V, the temperature rise became as steep as shown in Figure IVA.2.9a. The response times can be further improved by the above considerations. The steady state temperature of the heater is found to linearly vary with applied power, as shown in Figure IVA.2.9b. The slope of this plot, which represents the thermal resistance of the heater, is estimated to be 255.2 °C cm^2 W^{-1}. Greater the thermal resistance value, superior is the performance of the heater. This value is indeed appreciable; for example, it is 53% higher than SWCNT

based heaters [35]. The thermal resistance value does depend on the mesh thickness; higher thickness will result in lower resistance of the heater; however, the thermal mass will increase [43]. Moderate thicknesses (~ 100 nm) exhibit high thermal resistance values favour the defrosting action.

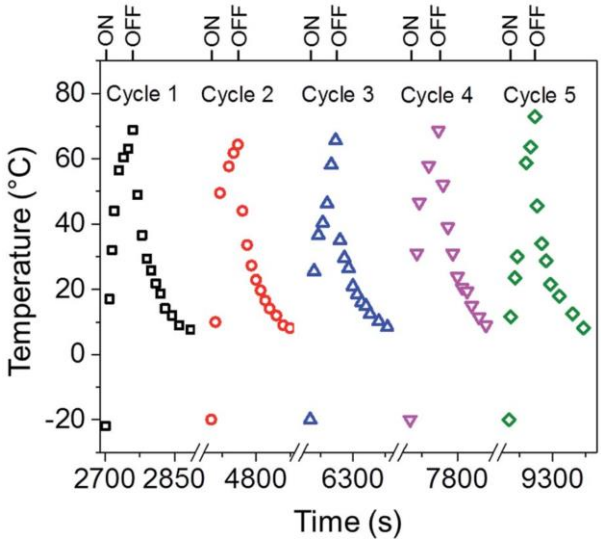

Figure IVA.2.11 Temperature vs. time plot of the frost and defrost cycles. Each time V_{ON} of 3 V was applied for nearly 60 s. The cycles were conducted by placing the transparent heater over a LN_2 container, such that the heater was constantly bathed in the cold vapors (see photographs and IR images in Figure IVA.2.10). The first cycle was started after 2700 s of placing the panel over LN_2 vapors.

The reliability of Ag mesh based defrosting window panel was examined by performing many frost cycles. The electrode (2.5 × 2 cm^2) was placed over a LN_2 container and allowed to form a thick frost (see Figure IVA.2.10). By applying 3 V for 60 s, the frost could be melted altogether to provide a clear view. The temperature of the electrode was measured using an IR camera. Once the frost disappeared, the voltage was turned off until a thick frost layer developed again. The electrode was tested for 5 cycles of frost-defrost conditions (see Figure IVA.2.10 and 11) and the performance were nearly reproducible. It may be noted that this test was performed without any encapsulation. After 6 h of exposure to LN_2 vapors for frost conditions and warming (defrosting) cycles, the Ag mesh showed no signs of change as determined by XRD (Figure IVA.2.12).

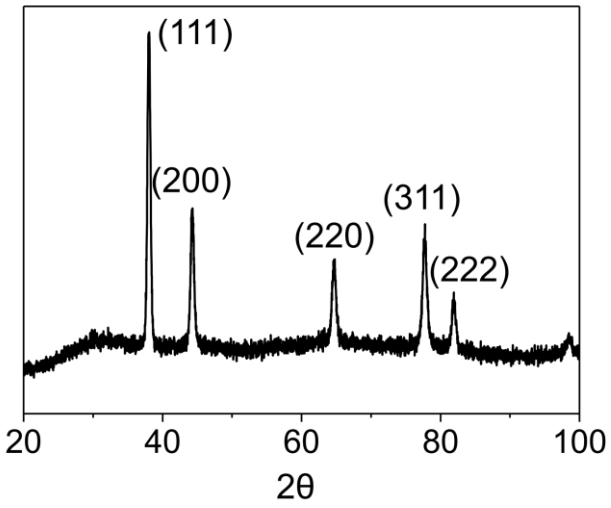

Figure IVA.2.12 X-ray diffraction pattern of Ag mesh after 6 h of exposure to LN_2 vapors and defrosting conditions. The peaks are matching well with Ag peak positions.

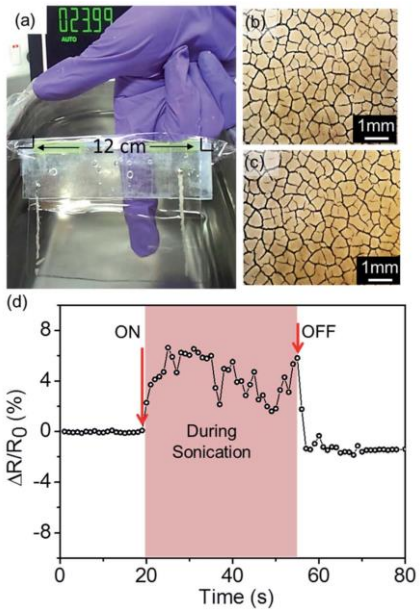

Figure IVA.2.13 Robustness of the Ag mesh on glass. (a) Image showing the ultrasonication set up to test the adhesion of the Ag mesh electrode. Optical microscope images of the fabricated Ag electrode (b) before and (c) after ultrasonication test. (d) Relative variation in resistance with time recorded during ultrasonication test.

The practical applicability of the electrodes is further established by examining the robustness of the electrodes. To mimic harsh weather conditions, a Ag mesh/glass electrode was immersed in an ultrasonic water bath (30 kHz), while the

resistance was continuously recorded (Figure IVA.2.13a). The mesh was hardly affected because of sonication (see Figure IVA.2.13b and c and Movie IVA.2.S2 in CD). As shown in Figure IVA.2.13d, the resistance change in the bath was irregular, but within 6%, which may have been because of the contribution from the electronic noise from the sonicator. As soon as sonication was turned off, the resistance reverted back to the normal value. Ag mesh adhesion on glass may be further enhanced by first depositing a few nm thick Ti/Cr layer prior to Ag, as it is conventionally done for thin films. Encapsulation is also expected to enhance its stability and make it scratch resistant.

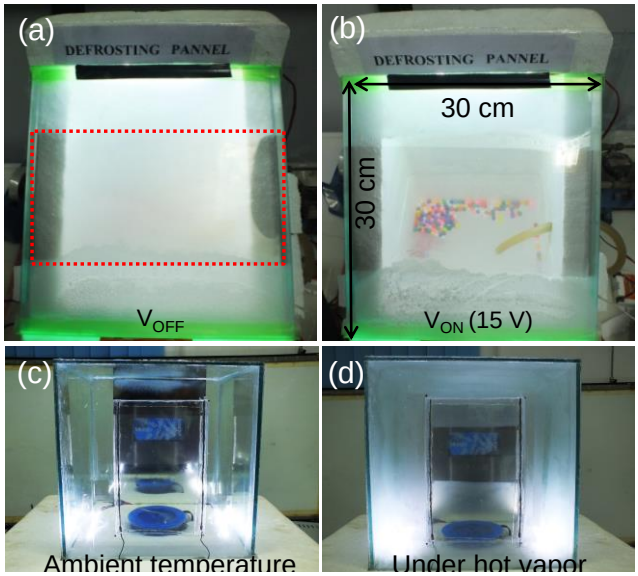

Figure IVA.2.14 (a) and (b) Prototype defrosting panel in fully frost (V_{OFF}) and defrosting (V_{ON}) conditions. Red dotted rectangle indicates the mesh coated area. (c) Prototype defogging panel consist of glass enclosure with Ag mesh adhered to front and rear windows and steamer in the middle. (d) When steamer is ON, the glass chamber became foggy and opaque except heater region and enables the user to see-through it.

Furthermore, a prototype defrosting panel of 1 ft^2 size (see Figure IVA.2.14a) has been fabricated and demonstrated its performance. The frost has formed all over the glass when kept over LN_2 container. Upon applying 15 V to the heater, it melts away the frost and enables the user to see the colored thermocol balls floating on the LN_2. In addition, defogging panels has also been fabricated by adhering mesh heaters to

glass enclosures. Hot vapors (using steamer) form fog on inner surface of the glass and obstruct the view. When mesh heaters were turned on, it avoids fogging as seen in Figure IVA.2.14b and improves the visibility.

IVA.2.5 Conclusions

In this study, transparent conducting electrodes were obtained by depositing metal (Ag) over spontaneously formed crackle network as a template made using commercially available crackle paint. The template was produced by a simple drop coating technique. Importantly, no external heating or power input was required; therefore, the method is suitable for low cost production. Thus, formed electrode is highly conducting (1 Ω/sq) over a large area with transmittance of ~ 77% which was used as a transparent heater. The thermal performance of the heater was examined by applying different voltages and a high thermal resistance of 255.2 °C cm^2 W^{-1} was obtained. The efficacy of the transparent heater (10×8 cm^2) was demonstrated by conducting a defrosting experiment, wherein the frost formed by exposing to LN_2 vapors could be completely removed by joule heating at 8.5 V for 2 min. Thus, the fabricated electrodes was used in practical applications as defrosting and defogging window panels even when the external temperature is close to polar temperatures (-60 °C) or near 80°C, respectively. The power required is nominal. The heater is highly robust as evidenced by the ultrasonication test. The efficacy of the transparent heater for outdoor stability was further demonstrated by continuously operating for many defrosting cycles.

References

1. J. Andrey, R. Olley, *Clim. Bull.,* 1990, **24,** 123–136.
2. S. K. Thomas, R. P. Cassoni, C. D. MacArthur, *J. Aircraft,* 1996, **33**, 841–854.
3. J. Laforte, M. Allaire, J. Laflamme, *Atmos. Res.,* 1998, **46**, 143–158.
4. P. Guo, Y. Zheng, M. Wen, C. Song, Y. Lin, and L. Jiang, *Adv. Mater.,* 2012, **24,** 2642-2648.
5. X. Chen, R. Ma, H. Zhou, X. Zhou, L.Che, S.Yao and Z.Wang *Sci. Rep.,* 2013, **3**, 2515.
6. J. Lv, Y. Song, L. Jiang and J. Wang, *ACS Nano,* 2014, **8**, 3152–3169.
7. B. Radha, S. H. Lim, M. S. M. Saifullah and G. U. Kulkarni, *Sci. Rep.,* 2013, **3,** 1078.
8. H. A. Stone, *ACS Nano,* 2012, **6,** 6536–6540.

9. D. S. Hecht , L. Hu and G. Irvin, *Adv. Mater.,* 2011, **23,** 1482–1513.

10. R. Gupta, S. Walia, M. Hösel, J. Jensen, D. Angmo, F. C. Krebs and G.U. Kulkarni, *J. Mater. Chem. A*, 2014, **2**, 10930-10937.

11. D. Sui, Y. Huang, L. Huang, J. Liang, Y. Ma and Y. Chen, *Small*, 2011, **7,** 3186-3192.

12. Y. H. Yoon, J. W. Song, D. Kim, J. Kim, J. K. Park, S. K. Oh and C. S. Han, *Adv Mater.,* 2007**, 19,** 4284-4287.

13. J. Ederth, G. A. Niklasson, A.Hultåker, P. Heszler, C. G. Granqvist, A. R. van Doorn, M. J. Jongerius and D. Burgard, *J. Appl. Phys.,* 2003, **93**, 984-988.

14. K. Im, K. Cho, J. Kim, and S. Kim, *Thin Solid Films,* 2010, **518,** 3960-3963.

15. K. Im, K. Cho, K. Kwak, J. Kim and S. Kim, *J. Nanosci. Nanotechnol.,* 2013, **13,** 3519-3521.

16. R. Po, C. Carbonera, A. Bernardi, F. Tinti and N. Camaioni, *Sol. Energy Mater. Sol. Cells,* 2012, **10,** 97–114.

17. A. Kumar and C. Zhou, *ACS Nano,* 2010, 4, 11-14.

18. S. Pang, Y. Hernandez, X. Feng and K. Müllen, *Adv. Mater.,* 2011, **23**, 2779-2795.

19. X. Wang , L. J. Zhi and K. Mullen, *Nano Lett.,* 2008 , **8,** 323-327.

20. R. M. Osuna, V. Hernández, J. T. López Navarrete, E. I. Kauppinen, and V. Ruiz, *J. Phys. Chem. Lett.,* 2010**, 1,** 1367–1371.

21. C. Feng, K. Liu, J.-S. Wu, L. Liu, J.-S. Cheng, Y. Zhang, Y.Sun, Q. Li, S. Fan, and K. Jiang, *Adv. Funct. Mater.,* 2010, **20,** 885–891.

22. H. Guo, N. Lin, Y. Chen, Z. Wang, Q. Xie, T. Zheng, N. Gao, S. Li, J. Kang, D. Cai and D.-L. Peng, *Sci. Rep.,* 2013**, 3,** 2323.

23. S. De, T. M. Higgins, P. E. Lyons, E. M. Doherty, P. N. Nirmalraj , W. J. Blau, J. J. Boland and J. N. Coleman, *ACS Nano,* 2009, **3**, 1767–1774.

24. M. G. Kang , L. J. Guo , *Adv. Mater.,* 2007, **19,** 1391-1396.

25. M. Vosgueritchian, D. J. Lipomi, and Z. Bao, *Adv. Funct. Mater.,* 2012, **22,** 421–428.

26. S. B. Yang, B.-S. Kong, D.-H. Jung, Y.-K. Baek, C.-S. Han, S.-K. Ohe and H.-T. Jung *Nanoscale,* 2011, **3,** 1361-1373.

27. M.-S. Lee, K. Lee, S.-Y. Kim, H. Lee, J. Park, K.-H. Choi, H.-K. Kim, D.-G. Kim, D.-Y. Lee, S. W. Nam, and J.-U. Park, *Nano Lett.,* 2013, **13**, 2814–2821.

28. H. Chang, G. Wang, A. Yang, X. Tao, X. Liu, Y. Shen, and Z. Zheng, *Adv. Funct. Mater.,* 2010**, 20,** 2893–2902.

29. J. J. Bae, S. C. Lim, G. H. Han, Y. W. Jo, D. L. Doung, E. S. Kim, S. J. Chae, T. Q. Huy, N. Van Luan and Y. H. Lee, *Adv. Funct. Mater.,* 2012, **22,** 4819-4826.

30. J. Kang, H. Kim, K. S. Kim, S.-K. Lee, S. Bae, J.-H. Ahn, Y.-J. Kim, J.-B. Choi and B. H. Hong, *Nano Lett.,* 2011, **11,** 5154-5158.

31. B.-J. Lee and G.-H. Jeong, *Curr. Appl Phys.* 2012**, 12,** S113-S117.

32. D. Janas, A. Cabrero-Vilatela, J. Bulmer, L. Kurzepa and K. K. Koziol, *Carbon,* 2013**, 64,** 305-314.

33. H.-S. Jang, S. K. Jeon and S. H. Nahm, Carbon, 2011, 49, 111-116.

34. D. Jung, D. Kim, K. H. Lee, L. J. Overzet and G. S. Lee, *Sens. Actuators, A,* 2013, **199,** 176-180.

35. T. J. Kang, T. Kim, S. M. Seo, Y. J. Park and Y. H. Kim, *Carbon*, 2011, **49,** 1087-1093.

36. Z. P. Wu and J. N. Wang, *Physica E,* 2009, **42,** 77-81.

37. T. H. Kim, W. M. Choi, D.H. Kim, M. A. Meitl, E. Menard, H. Jiang, J. A. Carlisle and J. A. Rogers, *Adv. Mater.,* 2008, **20,** 2171-2176.

38. T. Y. Kim, Y. W. Kim, H. S. Lee, H. Kim, W. S. Yang and K. S. Suh, *Adv. Funct. Mater.,* 2013, **23,** 1250-1255.

39. D. Kim, L. Zhu, D.-J. Jeong, K. Chun, Y.-Y. Bang, S.-R. Kim, J.-H. Kim and S.-K. Oh, *Carbon*, 2013, **63,** 530-536.

40. T. Tokuno, M. Nogi, J. Jiu, T. Sugahara and K. Suganuma, *Langmuir,* 2012**, 28,** 9298–9302.

41. D. E. Lee, S.J. Go, G. S. Hwang, B. D. Chin and D. H. Lee. *Langmuir,* 2013**, 29,** 12259−12265.

42. B. Han et al. *Adv. Mater.,* 2014, **26,** 873–877.

43. K. D. M. Rao and G. U. Kulkarni, *Nanoscale,* 2014, **6,** 5645-5651.

44 K. D. M. Rao, R. Gupta and G.U. Kulkarni, *Adv. Mater. Interface.,* 2014.

45. M. S. Tirumkudulu and W. B. Russel, *Langmuir,* 2005, **21**, 4938-4948.

46. W. P. Lee and A. F. Routh, *Langmuir*, 2004, **20**, 9885-9888.

47. J. C. Love, L. A. Estroff, J. K. Kriebel, R. G. Nuzzo and G. M. Whitesides, *Chem. Rev.,* 2005, **105**, 1103-1169.

48. J. Wang, Z. Fang, H. Zhu, B. Gao, S. Garner, P. Cimo, Z. Barcikowski, A. Mignerey and L. Hu, *Thin Solid Films*, 2014, **556,** 13-17.

49. S. Wang, X. Zhang and W. Zhao, *J. Nanomater.*, 2013, Article ID 456098.

50. X. Zhang, X. Yan, J. Chen and J. Zhao, *Carbon,* 2014**, 69**, 437-443.

Chapter IVA.3
Smart Windows with Liquid Active Layers

Summary

Indoor light control using thermotropic materials is an active area of research. While active materials are available to switch transmittance with temperature, large area heaters with desired transparency are not easily affordable. In this work, the fabrication of thermochromic devices using inexpensive Sn mesh electrodes (5 Ω/sq, transmission, 80%) produced by crackle lithography with hydroxypropyl methyl cellulose (HPMC) and hydrocarbons as active materials are reported. When laminated and coated on the inner surface of a PET window, the mesh served as a transparent heater to cause gelation in HPMC at ~40 °C to switch from water-clear transparency to paper-white opaqueness with 1 mm thickness of the active layer. The power consumption was only 0.2 W/cm^2. Few drops of a color ink produced interesting effects in this smart window prototype. Hydrocarbon device has shown transition from opaque to transition state upon joule heating.

IVA.3.1 Introduction

Maintaining a working temperature indoor irrespective of climate variations is challenging and towards this, many energy saving passive methods such as thermal insulation or reflective 'cool' wall coatings [1], solar protection films for windows [2], wet roofing [3] etc. have been developed. Although the latter ones significantly reduce the inflow of heat from roofs and walls in the hot season and thus, the air conditioning costs, they are inappropriate in winter as solar energy absorption is highly desired to avoid excessive energy consumption for room heating. Clearly, there is a demand for technologies to develop active materials and applications suitable for all weather conditions. 'Smart window' technology is one among them [4].

In contrast to traditional protection films with fixed optical properties [2], switchable solar control glazing coatings are highly desirable [5]. In this context, electrochromic [6] and thermochromic [7] materials are interesting due to their ability to modulate optical transparency with external stimuli, electrical field or temperature, respectively. In

Paper based on this study: Solar Energy Materials & Solar Cells 163 (2017) 231–236

general, thermochromic materials are relatively affordable and due to simplicity of the design, the resulting devices are usually less expensive. However, scouting for a thermochromic material with desired operating temperature window is not always easy. For example, now-a-days inorganic metal oxide (VO_2) based coatings [8,9] are used in windows for controlling IR transmission but its transition temperature is much higher (68 °C) compared to ambient temperatures. To address this issue, often doping with tungsten, niobium, molybdenum, iridium or tantalum oxide is done to bring down the transition temperature [10,11]. In this context, thermosensitive polymers are impressive as the transition from transparent to opaque takes place at near-room temperature [12–14]. Specifically, hydroxypropyl methyl cellulose (HPMC) mixed with NaCl features a lower critical solution temperature (LCST) of ~35 °C [15,16]. Gel bears a water-clear look at low temperatures and becomes paper-white at high temperatures due to molecular aggregation induced optical scattering. HPMC possesses many novel properties; it is aqueous and non-toxic and its transition is highly reversible with haze free opacity and no wonder, it finds widespread applications in smart displays/windows [15,17]. Large area thermotropic windows with hydrogels have been fabricated and shown reversible transition under sunlight in prolonged out-door testing [17]. Later, electrical controlling has been combined along with solar to obtain transition below LCST. Fisher et al. and Gyenes et al. have developed hydrogel devices with transparent heaters composed of tin-doped indium oxide (ITO) [4,15].

IVA.3.2 Scope of the present investigation

A pertinent issue on way to commercialization of thermochromic windows is related to the transparent heater, which is an important component of the device besides the thermochromic material itself. The heating is done by a joule heater which as the elegance demands, should remain essentially invisible when integrated into a window. Typically, ITO coated transparent conducting glass is used in order to achieve uniform heating across the large areas [4,15]. However, producing window size conducting glass with uniform areal heating is not trivial if one takes into account of cost effectiveness, else such designs are already in use in aviation industry [18,19]. The main objective of this work is to make affordable smart windows composed of inexpensive TCEs and thermotropic gels. The affordable aspects relates to the use of the earth abundant inexpensive

environmentally benign ingredients to produce transparent heaters which otherwise demand the expensive ITO. In this work, metal meshes produced by crackle lithography were used as affordable heaters for thermochromic windows [20]. For this purpose, metal mesh made of Sn (cost effective) was used which possessed sheet resistance of 5 Ω/sq and transmittance of ~80%. The specular transmittance of the hydrogel device could be switched from ~73% to less than 1% using 0.2 W/cm^2.

IVA.3.3 Experimental Details

Metal wire mesh fabrication

The process of fabricating Sn wire mesh is simple involving three steps as illustrated in Figure IVA.3.1. The PET substrates were cleaned in detergent, acetone, distilled water and isopropanol and purged with nitrogen before spin coating (2000 rpm) the acrylic resin based crackle precursor (0.5g/mL, Ming Ni Cosmetics Co., Guangzhou, China). Upon drying, it tends to form cracks due to the interfacial stresses. As these cracks are down to the substrate with no residual layer at the bottom substrate, it is termed as crackles (Figure IVA.3.2). The dried layer of the acrylic resin above the threshold thickness (~1 μm) produces highly interconnected crackle network with cracks of few micron widths [20]. The crack width and its density can be easily manipulated with the concentration of the crackle precursor. Here, the optimized concentration of 0.5g/mL was used [20]. Sn metal of ~400 nm was physical vapor deposited over the template at a base pressure of 10^{-6} Torr (Hindvac, India). Finally, the crackle layer was removed by dipping in chloroform. Thus produced Sn wire network showed a sheet resistance of ~5 Ω/sq with above 80% transmittance (Figure IVA.3.3).

Hydrogel preparation

Hydrogel prepared in this study is composed of hydroxypropyl methyl cellulose (HPMC, Sigma Aldrich), NaCl and water in the ratio of 2:5:100 (w). The solution was sonicated for 1 h to get homogenous dispersion. The hydrogel was stored in an air-tight bottle to minimize the evaporation of water.

PDMS spacer fabrication

Polydimethylsiloxane (PDMS) spacer was prepared by mixing Sylgard 184 curing agent and elastomer (Dow Corning) in the volume ratio 1:10 and mixed well followed by degassing. It was poured on a clean glass substrate upto the height of 1 mm thick Cu ring

and cured in the oven at 90 °C. The required mold was cut and adhered well between laminated TCE and PET using adhesives (Araldite, Huntsman Advanced Materials).

IVA.3.4 Results and Discussion

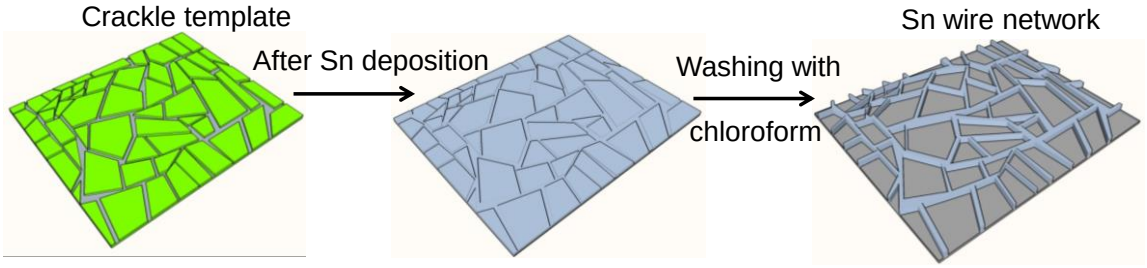

Figure IVA.3.1 Schematic illustration of the fabrication of Sn wire network.

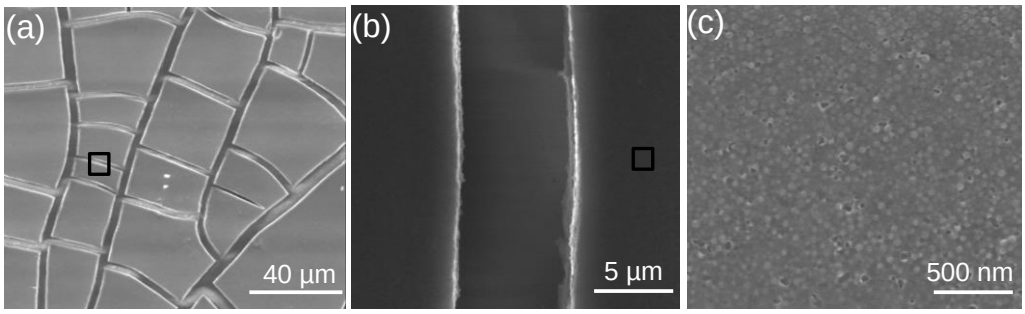

Figure IVA.3.2 (a) SEM images of crackle template network and enlarged image of a marked portion in (a) is shown in (b). (c) Morphology of acrylic resin particles.

Low-cost Sn wire network (see Figure IVA.3.1-3 for detailed fabrication and characterization) is used as a transparent conducting electrode, precisely as a transparent heater, to switch the hydrogel from its transparent to the opaque state. The uniqueness of crackle templating method is the high interconnectivity of the crack grooves from one end to the other, above the threshold crackle precursor thickness, as established in the earlier studies [20]. As crack widths are in the range of µms, the uniformity of the template can be easily validated using high magnification optical microscopes before metal deposition.

Sn metal was deposited over crackle template (shown in Figure IVA.3.2) by thermal evaporation and template was then washed away with chloroform. From the SEM images (Figure IVA.3.3a) the uniformly spread Sn wire network on PET substrate was observed with no template residues after neat lift-off. Importantly, the junctions in Sn wire network are seamless (see inset in Figure IVA.3.3a) due to crackle template method. Unlike metal

nanowire- based TCEs, where nanowires are randomly connected even leading to redundant nanowires (not part of conducting network), Sn meshes obtained here is basically a single wire network with the high degree of connectivity.

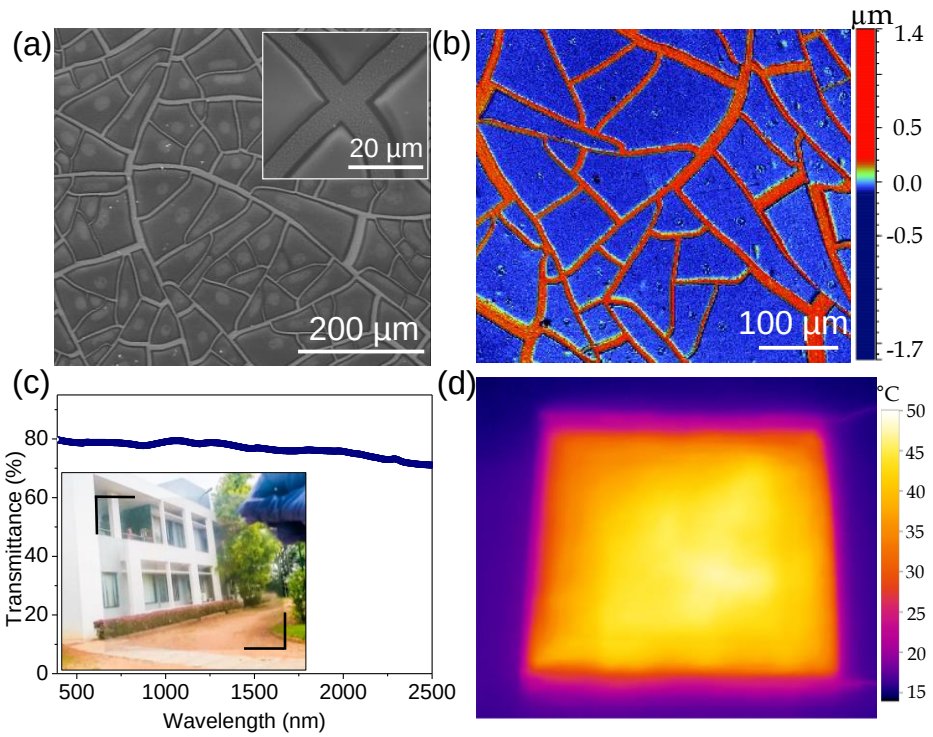

Figure IVA.3.3 (a) SEM images of Sn wire network. Inset is the magnified portion of a junction. (b) Optical profilometry of Sn wire mesh. (c) Transmittance spectrum of the Sn wire network from 380 – 2500 nm and inset is the photograph of a Sn wire network held against the building. (d) IR camera image of a large area Sn wire network (8 × 8 cm^2) while joule heating with 5 V.

The sheet resistance of the obtained Sn wire network of ~ 400 nm thickness (Figure IVA.3.3b) is 5 Ω/sq. These values are highly comparable or even better than those of nanowire or nanotube and ITO-based TCEs. Contradictory to the later, Sn wire network is inexpensive and prepared with simple processing conditions. The photograph of the prepared Sn TCE and its transmittance spectrum are shown in Figure IVA.3.3c. It is interesting to observe that Sn wire network is transparent not only in the visible region but also in the whole range of 380- 2500 nm. The Sn wire mesh/PET was further tested for its capability as a transparent resistive heater and moreover to confirm the uniformity of metal network across 8 × 8 cm^2 areas Furthermore, by analyzing the Sn

meshes with IR image (Testo 885-2), it is straightforward to confirm the interconnectivity and uniformity of meshes in the device region (Figure IVA.3.3d).

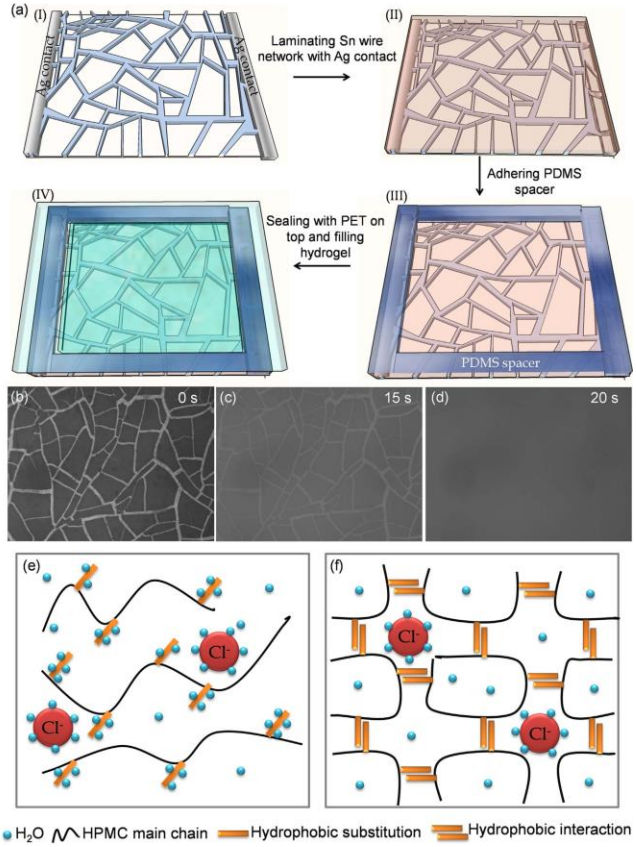

Figure IVA.3.4 (a) Schematic illustration of the fabrication steps of the hydrogel device. (b-d) Optical microscopic images of hydrogel device with a focus on Sn wire network. Images are captured with top light illumination. Pictorial representation of mechanism of hydrogel transition from transparent (e) to opaque state (f).

Figure IVA.3.4a shows the schematic of hydrogel based smart device fabrication. In order to avoid drying of the hydrogel, it was sealed between the laminated Sn wire network and PET. PDMS of ~1 mm thickness was used as a spacer and sealed with PETs using adhesive. The glass slides with silicone adhesive were also used as spacer for cost effectiveness. In order to enhance the durability of wire network towards scratch and other mishandlings, TCE was laminated after taking out Ag contacts. The thickness of the hydrogel was set to ~1 mm so as to achieve near-zero transmittance (paper white) in the gel state. The hydrogel switching was examined using optical microscopy (Figure IVA.3.4b–d) while focusing the Sn wire network. When the wire network was joule

heated with 10 V, the temperature of the device raised above 50 °C exceeding the LCST of the gel (~40 °C). Below its LCST (Figure IVA.3.4e), HMPC remained dissolved in water, forming a transparent solution whereas above LCST (Figure IVA.3.4f), HMPC chains collapse and separate out from the water leading to the observed opacity of the gel. Although this phenomenon is well-known in the literature, obtaining uniform transition over large area with high stability and reversibility has remained a difficult task. In this work, all these aspects have been studied while applying joule heat. It is interesting to note that the transition occurred in few seconds with a low input power (~0.2 W/cm^2).

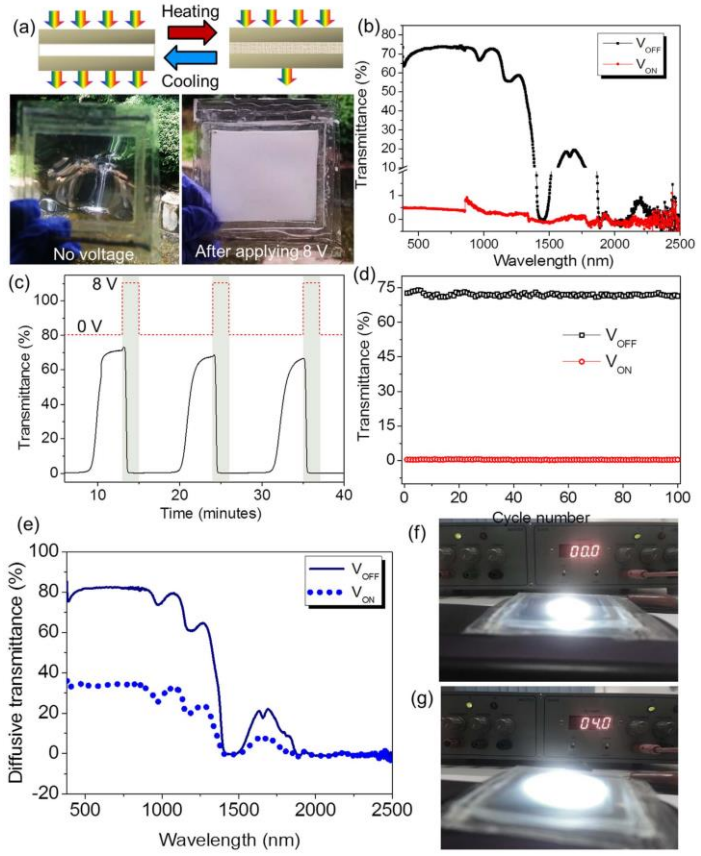

Figure IVA.3.5 (a) Photographs of the fabricated hydrogel device on Sn wire mesh before (left) and after (right) joule heating. The schematic above shows a sectional structure of the device with hydrogel sealed to illustrate the degree of transmittance at different temperatures. (b) Specular transmittance of the device in V_{ON} and V_{OFF} states. (c) and (d) illustrates the stability of the device for many cycles. (e) Diffusive transmittance spectra under V_{ON} and V_{OFF} states. (f) and (g) Photographs demonstrating the diffusive nature of hydrogel device under OFF and ON states, respectively.

The photographs of a large area hydrogel device under V_{ON} and V_{OFF} states are shown in Figure IVA.3.5a. The optical distortion in the device is due to usage of top PET to hold the hydrogel; it has been circumvented later by replacing PET with glass substrates (Figure IVA.3.6). As expected, the device is highly transparent under normal state (left image) whereas, at a higher temperature (above 40 °C), the scattering was high enough resulting in paper-white state with very low specular transmittance (< 1%) as seen in Figure IVA.3.5b (right image). The absorption features around 1400 and beyond 2000 nm are mainly due to the water present in the hydrogel (Figure IVA.3.5b) while the wire network itself is highly transparent at all wavelengths.

As regards cycling, the device is highly stable for many transition cycles at 550 nm (Figure IVA.3.5c and d). The response and recovery times of the device while joule heating with 8 V is 39 and 360 s, respectively (Figure IVA.3.5c). Recovery time could be brought down by lowering the applied voltage, but then the response time increases. However, the response and recovery time of the device is somewhat better than the PNIPAM and ITO based devices [4]. The modulation in the optical transparency over several cycles is shown in Figure IVA.3.5d. It was observed that the transparent-opaque transition of the hydrogel is highly reversible and could be repetitive without any significant variation. The device was found to be highly robust even at the end of 100th cycle with no measurable deterioration. In addition, the device is stable below 80 °C even for prolonged exposure but not above 100 °C as the hydrogel is mainly composed of water. Beyond its boiling temperature, the pressure created in the sealed device ruptures the spacer and hydrogel started leaking. Furthermore, the device will be highly stable towards extreme environmental conditions such as 60– 80 °C and 80% humidity. Transmittance spectra of the device under V_{ON} and V_{OFF} states measured using diffusive method (Figure IVA.3.5e) show that in V_{ON} state, there is nearly 30% increase in the diffusive transmittance with only ~1% transmission in specular mode (see Figure IVA.3.5b). This was further proven in the photographs as shown in Figure IVA.3.5f and g. When the device was kept close to a LED source, under V_{ON} (4 V) state (Figure IVA.3.5g), it is clearly evidenced that light is much more diffusive (although it is visibly opaque) than V_{OFF} state (Figure IVA.3.5f).

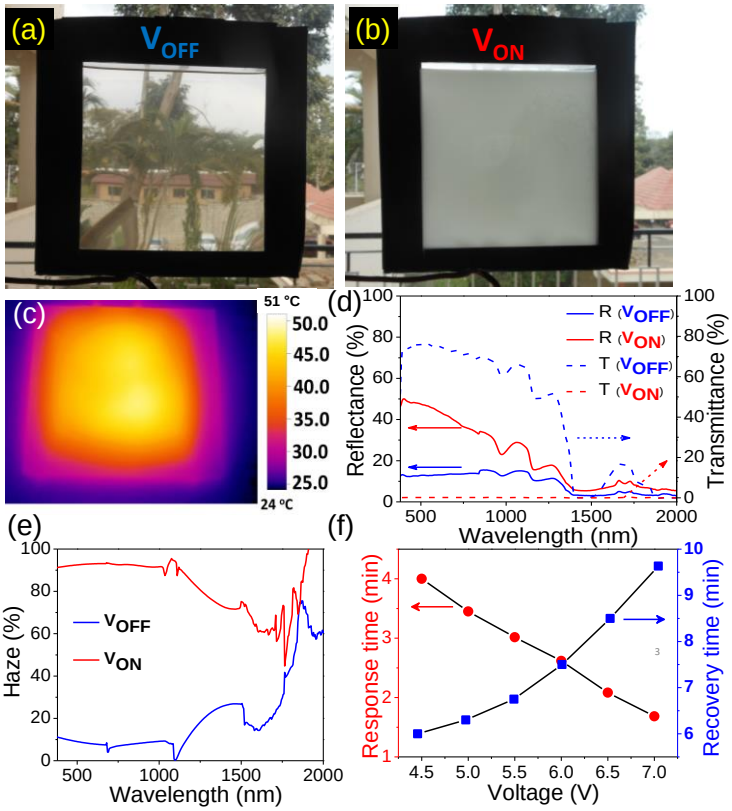

Figure IVA.3.6 (a) Photographs of the HPMC hydrogel device in its transparent (25 °C) (a) and opaque states (40 °C) (b). (c) Thermal image of the fabricated hydrogel device taken while joule heating (opaque state) with 4.5 V. (d) Reflectance and transmittance spectra of the device measured at normal (V_{OFF}) and under applied voltage (V_{ON}) circumstances. (e) Haze spectra of the device in its water-clear (V_{OFF}) and paper-white (V_{ON}) states. (f) Response and recovery times of the hydrogel device with respect to applied voltage.

Figure IVA.3.6a and b exhibit the as-fabricated (12 × 12 cm^2) hydrogel device in V_{OFF} and V_{ON} states, respectively. Upon applying 5 V to this device, the hydrogel temperature increased (> 40 °C) and thus the device became opaque due to its transition from transparent liquid to opaque gel state (see Figure IVA.3.6a and b). The infrared thermal image (Figure IVA.3.6c), in turn confirms that the transition occurs due to uniform joule heating of transparent heater. From the transmittance spectra in Figure IVA.3.6d, it is observed that ~ 79% difference is noticed between V_{OFF} to V_{ON} states at 550 nm. This difference is significant (50-70%) even in the infrared region. Moreover, unlike transmittance data, the reflectance and the haze at 550 nm is ~ 40 - 70% higher in the

V_{ON} states compared to V_{OFF} states (see Figure IVA.3.6e). However, this difference got suppressed in the far infrared region. As shown in Figure IVA.3.6f, the response time of the hydrogel device is just few minutes (~4 min) with 4.5 V even for 140 cm^2 area. The response times seem to drop to ~ 1 min for 7 V and also the recovery times are in the range of 5-10 min. These hydrogel based smart window is highly suitable for the low temperature tropical weather conditions as it remains transparent up to 40 °C.

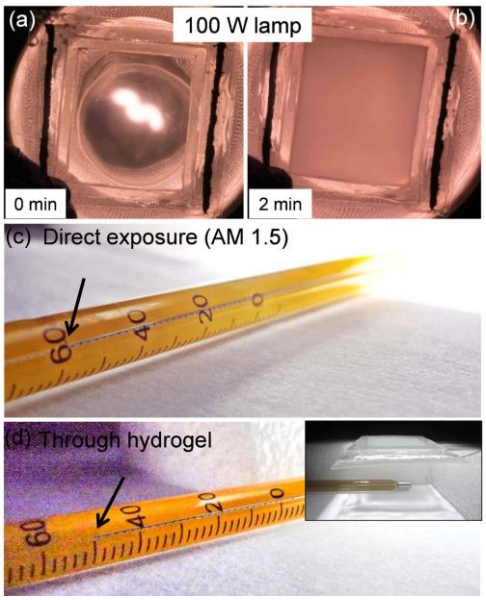

Figure IVA.3.7 The transformation from transparent (a) to opaque state (b) due to external heat from the lamp. Photographs showing the temperature variation in thermometer without (c) and with (d) hydrogel device while exposing to the bright sunlight (AM 1.5).

The thermochromic device is operable under external heat source as well. The photothermal effect of hydrogel device was monitored under light illumination (Figure IVA.3.7). When exposed to light in close proximity, the temperature of the device gradually increased above LCST of the hydrogel. Thus, the device turned opaque spontaneously (see Figure IVA.3.7a and b). It may be noted that the recovery time in this case is less compared to that obtained using internal heating by the TCE, as the latter has to cool from a temperature higher than the HPMC transition temperature. The effectiveness of the device in energy saving was examined via temperature variation in a confined space exposed to AM1.5 radiation, in the presence and absence of the hydrogel

device. In the absence of the device, the local temperature in the confined space reached ~60 °C as read by a thermometer (Figure IVA.3.7c), and with the device in its opaque state intercepting the light, the rise was limited to ~50 °C (see Figure IVA.3.7d). In the opaque state, the device seems to block IR and thus curtail the temperature rise.

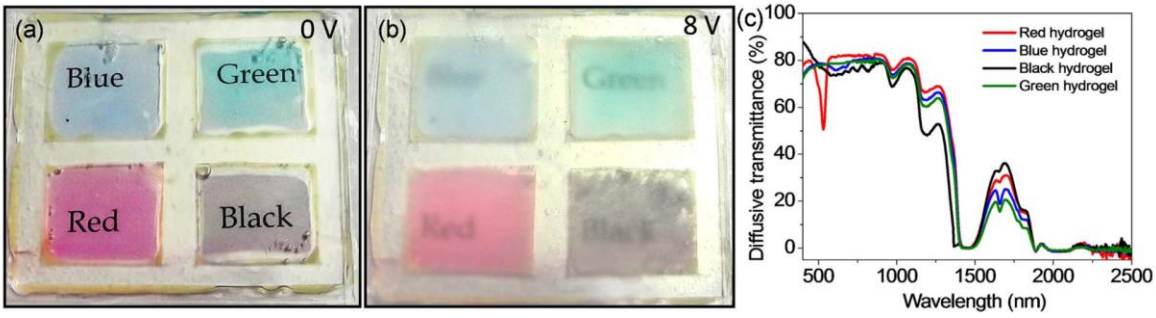

Figure IVA.3.8 Photographs of pixelated color pattern with blue, green, red and black color hydrogels on a TCE in V_{OFF} (a) and V_{ON} (b) states. The diffuse transmittance spectra of different colored hydrogels are shown in (c).

Usually, color windows impair the natural appearance of objects. On the other hand, color addition can bring aesthetic appeal and makes it ideal for buildings of art. The diluted common inks (Camel, India) were added to the hydrogel to attribute color, while still preserving the properties of the hydrogel. A pixelated color pattern was produced with 4 colors (red, blue, green and black) on a Sn TCE (Figure IVA.3.8a). The result is encouraging. This opens up the wide opportunity to choose colors of one's choice as part of interior designing. While joule heating the TCE, all colored hydrogels showed transition from transparent to opaque states evident from the difficulty in reading the text beneath (Figure IVA.3.8b). The transmittance of colored hydrogels shows slight absorption at particular wavelength characteristics of the individual color (Figure IVA.3.8c). The absorption coefficient depends on the concentration of the ink added to the hydrogel. For example with red ink, the absorption in the region, 470–550 nm was near 100% for increased concentration (see Figure IVA.3.9a). The diffused transmittance under opaque state is almost similar to that from the colorless device except for a kink (see Figure IVA.3.9b).

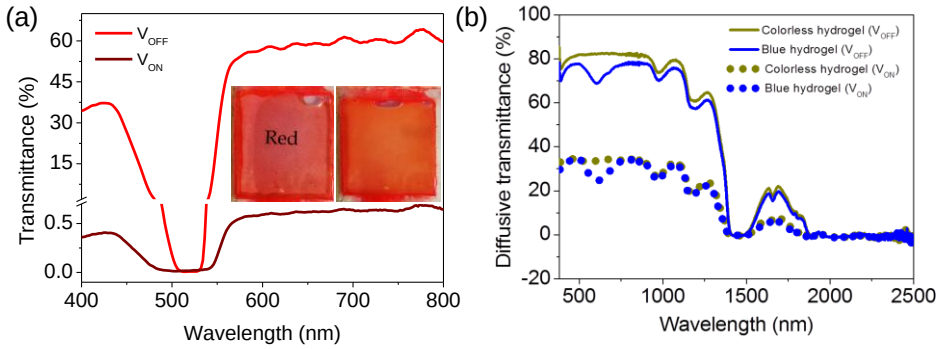

Figure IVA.3.9 Transmittance spectra of the red color hydrogel device under V_{OFF} (transparent) and V_{ON} (opaque) states. Inset left photograph corresponds to V_{OFF} whereas right one represents V_{ON} state. Diffusive transmittance spectra of colorless and blue color hydrogel device under V_{OFF} and V_{ON} states.

The hydrogel devices demonstrated in this work hold a great promise for smart window technology realization. As the crackle templating method is highly versatile for higher throughput processes as rod or roll coating processes [20], achieving large areas at affordable costs can be a near reality. Further, the transition temperature of HPMC can be manipulated by incorporating different anions or cations into the gel matrix. For an instance, by incorporating Na_3PO_4, the transition temperature may be brought down drastically whereas with NaBr or NaI, it can be increased [21].

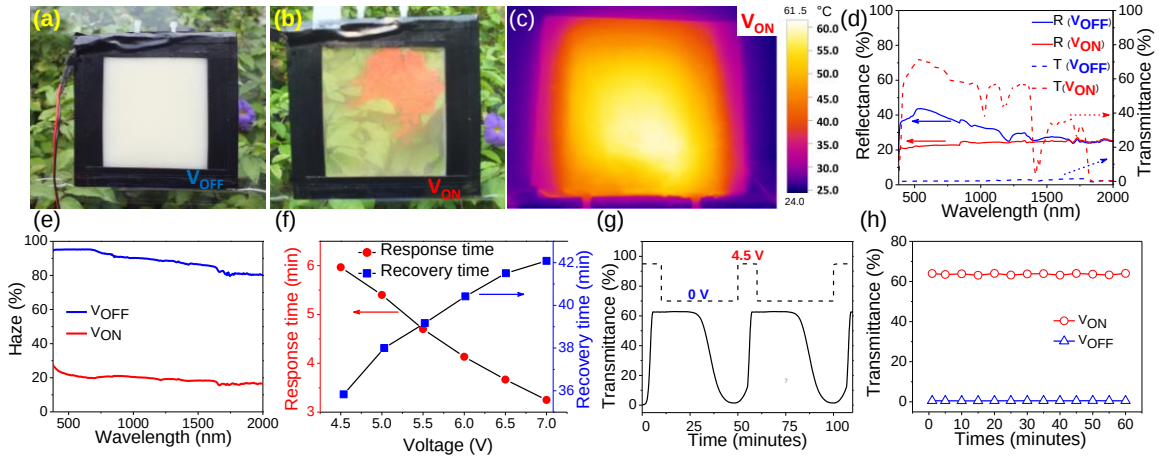

Figure IVA.3.10 Photographs of thermotropic devices (hydrocarbon layer) in its (a) V_{OFF} and (b) V_{ON} states. (c) IR-image of the device in V_{ON} state. (d) Reflectance, transmittance and haze (e) in V_{OFF} and V_{ON} states(f) Switching cycle test with respect to applied trigger voltage (g) Response and recovery time as a function of trigger voltage. (h) Transmittance values in V_{OFF} and V_{ON} states as a function of time.

A commonly available saturated hydrocarbon (Amul, India) which goes to transparent state from opaque at ~40 °C has also been used in this study to fabricate smart windows. Photographs of as-fabricated (12 × 10 cm^2) hydrocarbon are shown in Figure IVA.3.10a and b in the V_{OFF} and V_{ON} states, respectively. Upon applying 5 V to the device, the joule heat generated was slowly transferred to the hydrocarbon layer within the device. As the temperature increased beyond 40 °C, the device became transparent due to its transition from opaque solid to transparent liquid state. The IR image of the device in the V_{ON} state shown in Figure IVA.3.10c, confirming the uniformity of the temperature all over. From the reflectance and transmittance spectra in Figure IVA.3.10d, it is observed that the reflectance at 550 nm is ~ 25% higher in the V_{OFF} state compared to that in the V_{ON} state. Interestingly, more than 70% difference is observed in the transmittance spectra between V_{OFF} to V_{ON} states. This difference is significant (40-60%) even in the far infrared region. Unlike transmittance data, the haze difference between V_{OFF} to V_{ON} states is uniform (65-70%) across wide range of wavelengths (see Figure IVA.3.10e). As shown in Figure IVA.3.10f, the response time (time taken for heat induced color change) is of the order of minutes for this large area device (120 cm^2) and it tends to decrease with increasing V_{ON}, as expected. The recovery time on the other hand, can be much higher due to high thermal mass of the device. The cyclability and stability of the device under operation are shown in Figure IVA.3.10g and h, respectively. There is no degradation observed in the device performance even after long time usage. However, thermochromic and hydrocarbon based smart windows are not perfectly suitable for low temperature weather conditions as they remain opaque at lower temperatures.

IVA.3.5 Conclusions

In conclusion, an energy efficient light control device using hydroxypropyl methyl cellulose based hydrogel and saturated hydrocarbon have been demonstrated. The smart window fabricated in this study involves Sn wire mesh based transparent electrode which helps in switching the device efficiently by joule heating under demanding circumstances such as winter. Importantly, this new generation TCE used here is highly cost effective compared to commercial ITO electrodes. When the hydrogel device was subjected to strong sunlight or to joule heating, not only the visible light

through the device was significantly modulated but also the IR radiation was blocked. In a simple demonstration, it was shown that ~10 °C was reduced in a confined space when the hydrogel windows intercepted the hot sunlight. In order to enhance the aesthetic appeal, interesting color patterns may also be imparted to the hydrogel, not affecting the switching behaviour. These devices could be utilized in various present and futuristic energy efficient buildings to achieve their zero energy demand.

References

1. AH. Rosenfeld, H. Akbari, S. Bretz, B.L. Fishman, DM. Kurn, D. Sailor, H. Taha, *Energy Build*, 1995,**22** 255–265.

2. DHW. Li, JC. Lam, CCS. Lau, TW. Huan, *Renew. Energy*, 2004,**29**,921–937.

3. ACC. Rotzetter, CM. Schumacher, SB. Bubenhofer, RN. Grass, LC. Gerber, M. Zeltner, WJ. Stark, *Adv. Mater.,* 2012, **24**,5352–5356.

4. T. Gyenes, A. Szilágyi, T. Lohonyai, M. Zrínyi, *Polym. Adv. Technol.*, 2003, **14,**757–762.

5. D. Kim, E. Lee, H.S. Lee, J. Yoon, *Sci. Rep.,* 2015, **5**, 7646.

6. R. Baetens, BP. Jelle, A. Gustavsen, *Sol. Energy Mater. Sol. Cells*., 2010, **94**,87–105.

7. A. Seeboth, J. Kriwanek, D. Lötzsch, A. Patzak, Polym. Adv. Technol., 2002, **13,**507–512.

8. X. Cao, N. Wang, JY. Law, SCJ. Loo, S. Magdassi, Y. Long, *Langmuir,* 2014, **30**,1710–1715.

9. Y. Zhou, Y. Cai, X. Hu, Y. *J. Mater. Chem. A*., 2015,**3**,1121–1126.

10. TD. Manning, IP. Parkin, ME. Pemble, D. Sheel, D. Vernardou, *Chem. Mater.*, 2004,**16**,744–749.

11. GA. Niklasson, SY. Li, CG. Granqvist, *J. Phys.: Conf. Ser.*, 2014,**559**,012001.

12. M. Wang, Y. Gao, C. Cao, K. Chen, Y. Wen, D. Fang, L. Li, X. Guo, Ind. *Eng. Chem. Res.*, 2014, **53**, 18462 –18472.

13. X. Ye, Y. Luo, X. Gao, S. Zhu, *Energy Build.*, 2012,**48,** 175–179.

14. Y. Zhou, Y. Cai, X. Hu, Y. Long, *J. Mater. Chem. A*., 2014,**2**,13550–13555.

15. T. Fischer, R. Lange, A. Seeboth, *Sol. Energy Mater. Sol. Cells*. 2000,**64**,321–331.

16. J. Sun, Y. Chen, M.K. Priydarshi, Z. Chen, A. Bachmatiuk, Z. Zou, Z. Chen, X. Song, Y. Gao, M.H. Rümmeli, Y. Zhang, Z. Liu, *Nano Lett.,* 2015,**15**,5846–5854.

17. H. Watanabe, *Sol. Energy Mater. Sol. Cells*, 1998,**54**,203–211.

18. R. Gupta, KDM. Rao, S. Kiruthika, GU. Kulkarni, *ACS Appl. Mater. Interfaces,* 2016,**8**,12559–12575.

19. GU. Kulkarni, S. Kiruthika, R. Gupta, KDM. Rao, *Curr. Opin. Chem. Eng.,* 2015,**8**,60–68.

20. KDM. Rao, R. Gupta, GU. Kulkarni, *Adv. Mater. Interfaces.,* 2014,**1**,1400090.

21. SC. Joshi, *Materials*, 2011,**4**,1861–1905.

Chapter IVA.4

Smart Windows with Thermochromic Pigments as Active Layer

Summary

There is an increasing quest to develop smart glazing windows with tunable light and temperature to achieve zero-energy demands of modern buildings. The existing technologies using ITO heaters are unideal due to high cost and poor flexibility. In this study, thermochromic display has been fabricated with commercially available thermochromic pigment in combination with invisible mesh electrode as an alternative to ITO but with uncompromising optoelectronic properties. The chosen thermochromic material controls visible light transmission across this device.

IVA.4.1 Introduction

Buildings as living and working spaces, consume considerable energy for day-to-day operation. Glass panels being as part of windows, partitions or just as exterior wall finish behave sluggish with regard to heat and light transfer and therefore pose a big challenge to the energy management systems of buildings. A smart glass panel should work as wide area switchable gate for light and heat transaction with the external world, as briefly discussed in Chapter IVA.3.

In this framework, various energy saving active mode approaches have been tried out which include electrochromic [1], thermochromic [2], thermotropic [3], etc. Electrochromic windows offer the controlled transmission of light with the help of external power supply. Even though, electrochromic windows have good light control performance [4], it has various drawbacks such as high cost material involved, complicated manufacturing procedures, extra power consumption during the switching process. Certainly, this is not the supreme energy-efficient smart window technology. Besides electrochromic, thermochromic panels are more favourable technology due to their simple design, cost and power efficiency. These windows offer controlled optical switching (opaque to transparent/translucent) at a certain

Paper based on this study: J. Mater. Chem.C, Under Revision

threshold temperature. However, in these technologies achieving smart coating with near-room transition temperature with affordable cost is still quite challenging.

Although such solutions are somewhat appealing, there exists another big challenge towards its commercialization. It is related to the transparent heater, which is an essential element to support its user preference control. This transparent heater provides thermal heat to the thermochromic materials and simultaneously remains highly transparent when integrated with a glass window. So far, conventional ITO coated transparent heater has been utilized to achieve uniform heating across larger areas due to the lack of alternatives [5-7]. However, the cost of window panel size ITO based heaters can be formidable and may not match with consumer demands although such techniques are already in practice in aviation and space where cost effectiveness is not very important parameters [8,9]. In this context, many alternative heaters are designed and developed with active materials such as thin layer of metal nanowires, graphene and CNTs, patterned metal grids to name a few [10-17]. Above said alternatives are but compromising for large area affordable requirements.

IVA.4.2 Scope of the present investigation

For ideal transparent heaters, higher transmittance with lower sheet resistance is required for low operating energy with desired transmittance for window panels. In this work, a near ideal transparent heater using a recipe pioneered in the laboratory have been employed [18-20]. In the backdrop of the above discussion, it is important not only attempt to use inexpensive thermochromic active materials but also affordable large area transparent heaters. Specifically, a commercial thermochromic pigment with transition temperature around 48 °C going from opaque to translucent was used. Moreover, this thermochromic material is non-toxic with reversible phase transitions with low power/temperature requirement and minimal haze, which indeed make these devices ideal for smart display applications [5,6].

IVA.4.3 Experimental Details

Fabrication of Cu mesh

A commercially available crackle precursor (Ming Ni Cosmetics Co., Guangzhou, China) consisting of acrylic emulsion was dispersed in diluter (0.5 g/ml) and rigorously ultrasonicated for 15 minutes. The polyethylene terephthalate (PET)

substrates (100 μm) were cleaned with water and IPA prior to template formation. The suspended solution was spin coated at 700 - 1000 rpm on clean polyethylene terephthalate (PET) substrate for 120 s. Upon drying, a crack network formed spontaneously in the coated layer. Physical vapour deposition system (Hind High Vacuum Co., India) was used for Cu deposition. In the final step of lift-off, the crack layer was removed by rinsing with chloroform (see Figure IVA.4.1).

Fabrication of thermochromic device

Commercially available thermochromic pigment (Figure IVA.4.2) (Smarol Industry Co., Ltd., Zhejiang, China) was dispersed in transparent acrylic paint (Asian Paints Ltd. Mumbai, India) with the concentration of 0.2 g/ml and rigorously ultrasonicated for 20 minutes. The suspended solution was spin coated at 1000 rpm over the laminated Cu mesh to achieve the thickness of ~ 500 μm (Figure IVA.4.3). Further, for the fabrication of thermal display cell, two copper wires connected at the two edges of the sample with the help of silver paste, for providing external voltage to the sample, as shown in the schematic diagram (Figure IVA.4.4).

Fabrication of 13-segment flexible thermal display

13-segment design was printed on PET sheet with the help of laser printer. Laser printing was done on PET sheet in such a way that 13-segment design was kept clean and the rest of the area on PET sheet was coated with toner ink. The dimension of each cell segment was 3.5 × 0.3 cm^2. Further, the thermal display cells of same dimension have prepared and stuck over the space provided for the segment in the thermal display. Two wires coming out of each segment cell were connected to the programmable power supply, which is programmed in such a way that it has control over each segment to supply power. By doing manipulation over the power supply control to each segment cell of the thermal display, alphabets and numeric can be displayed on it. Portable power supply (mobile power bank-ASUS) used to supply power to the electrical circuit of the display.

IVA.4.4 Results and Discussion

As shown in the schematic in Figure IVA.4.1, a transparent conducting electrode (TCE) was produced using crackle lithography method (see experimental section). Thermochromic pigments used in this study are organic leucodyes based (carbon

coated) (see Figure IVA.4.2) as it can be easily scaled up by screen printing or by various coating techniques.

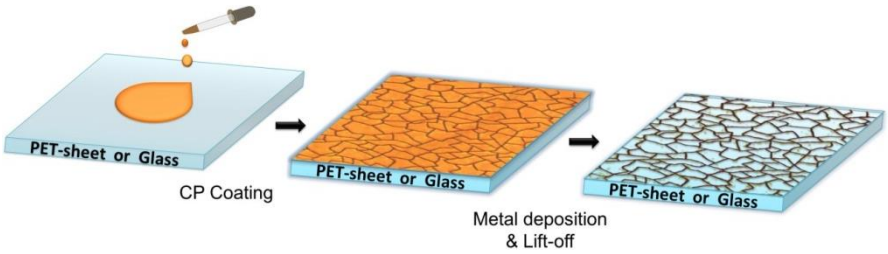

Figure IVA.4.1 Schematic illustration for the fabrication of metal mesh network.

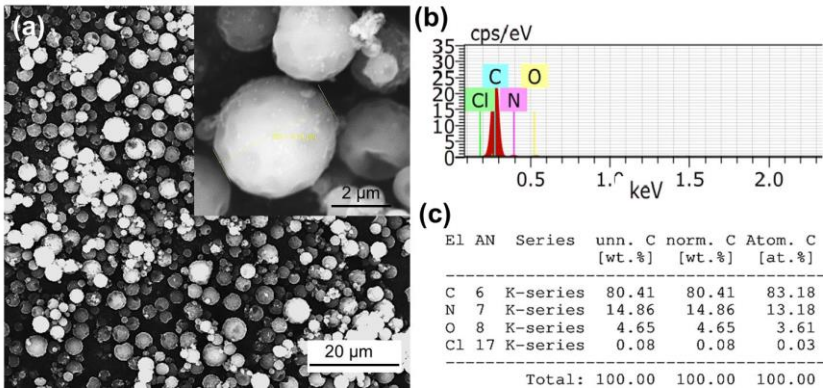

Figure IVA.4.2 (a) SEM image (b) EDS spectrum and (c) atomic composition of thermochromic pigment.

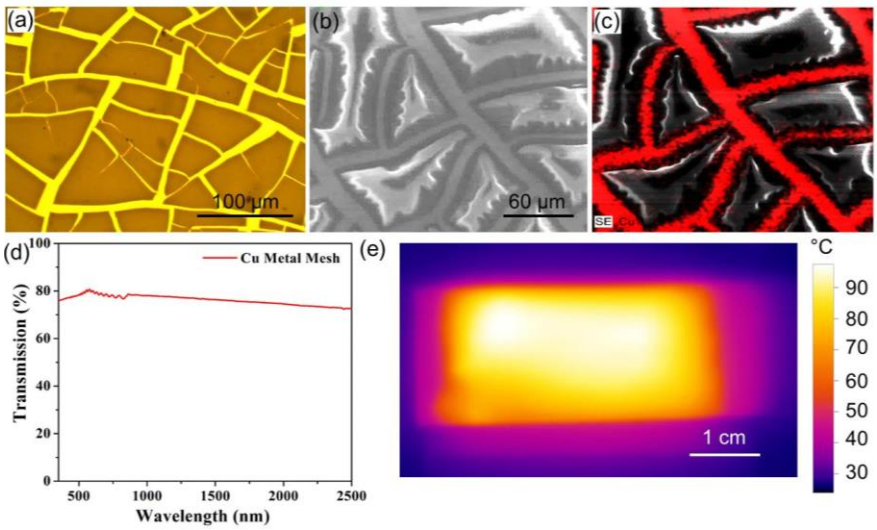

Figure IVA.4.3 (a) Optical microscopy and (b) SEM images of Cu mesh on PET substrate. (c) EDS mapping of Cu clearly indicates that Cu is present only in the network structure with no residues in between. (d) Transmittance spectrum and (e) IR image of the Cu mesh.

The Cu mesh obtained by crackle templating method is highly interconnected (Figure IVA.4.3a-c) with nearly 80% transparency (Figure IVA.4.3d) with ~ 5 Ω/sq sheet resistance. While applying few volts to TCE, temperature of the sample drastically increases and this in turn confirms the existence of metal mesh uniformly on the substrate. Infra-red imaging technique was adopted to measure the temperature variation (Figure IVA.4.3e). Thus, Cu mesh serves as the backbone of thermochromic display for providing user preference control. As shown in Figure IVA.4.4, a thermochromic pigment based light control device was made. Going by the design, the device is expected to change its color from opaque black to translucent white upon heating. The Cu mesh based transparent heaters are used in this study, to keep the low cost of the device under consideration. The active material was chosen such that transition was around 40 °C.

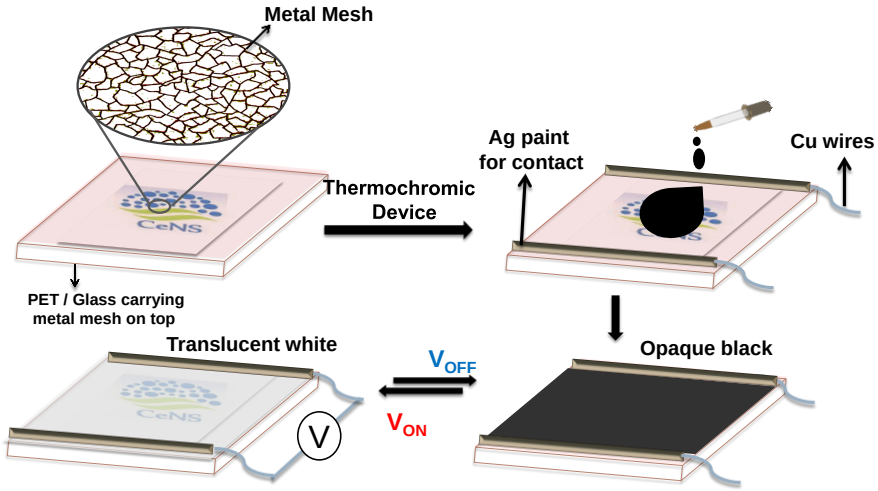

Figure IVA.4.4 Schematic diagram of the fabrication steps for thermochromic device. The CeNS logo beneath every sample in schematic provides the visual demonstration of various switching states in thermochromic device.

Figure IVA.4.5a shows as fabricated pitch black thermochromic device (4 × 3 cm^2) in its V_{OFF} state (when no external voltage applied to it). The fabrication process is highly versatile to extend the device dimension even beyond A4 size (see, Figure IVA.4.6). Upon applying an external voltage (V_{ON} ~ 3.5 V) to the device, its temperature raised above 50 °C in just 20 s due to the joule heating of Cu mesh wires. As a response, the opaque black thermochromic pigment layer changed its

color to translucent white making the CeNS logo beneath visible (see Figure IVA.4.5b); in other words, the proximal transparency increased significantly, while residual scattering continued to prevail.

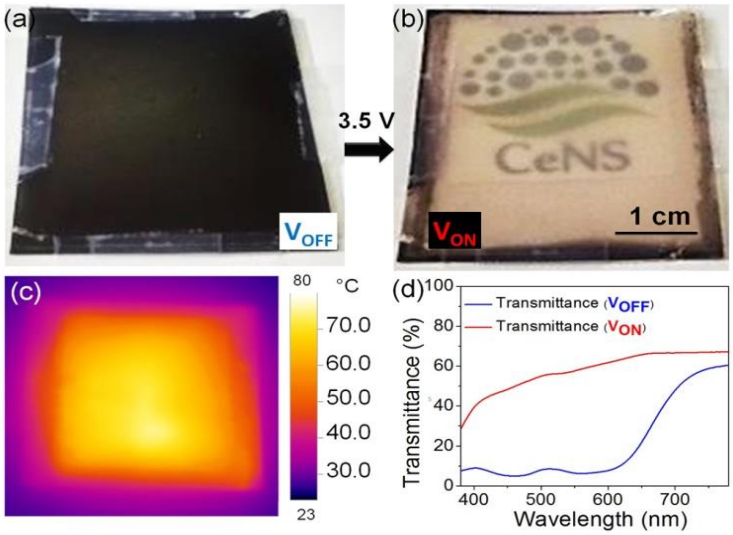

Figure IVA.4.5 Photographs of thermochromic device under V_{OFF} (a) and V_{ON} states (b). (c) IR-image of the device in V_{ON} state. (d) Transmittance of the device in its V_{OFF} and V_{ON} states.

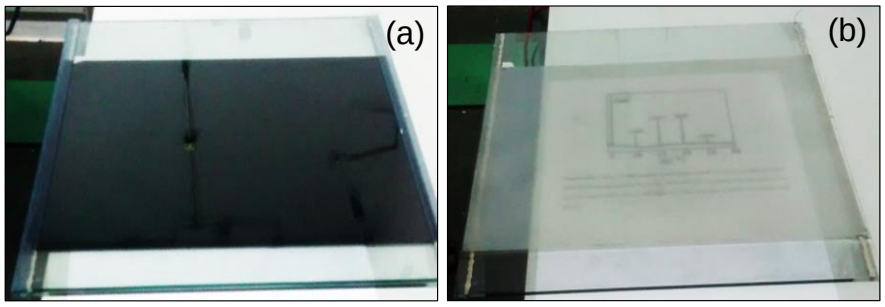

Figure IVA.4.6 Photographs of A4 size thermochromic device fabricated with Cu mesh in its V_{OFF} (a) and V_{ON} states (b).

The IR image of the device in its V_{ON} state shown in Figure IVA.4.5c confirmed the uniformity of the heater temperature all across. The specular transmittance of the device in its V_{OFF} and V_{ON} states are ~ 5% and 60% at 550 nm (see Figure IVA.4.5d). The device is highly reversible in nature; when external voltage was turned off, the transparent heater cooled to ambient temperature and thus the display colour returned to opaque black.

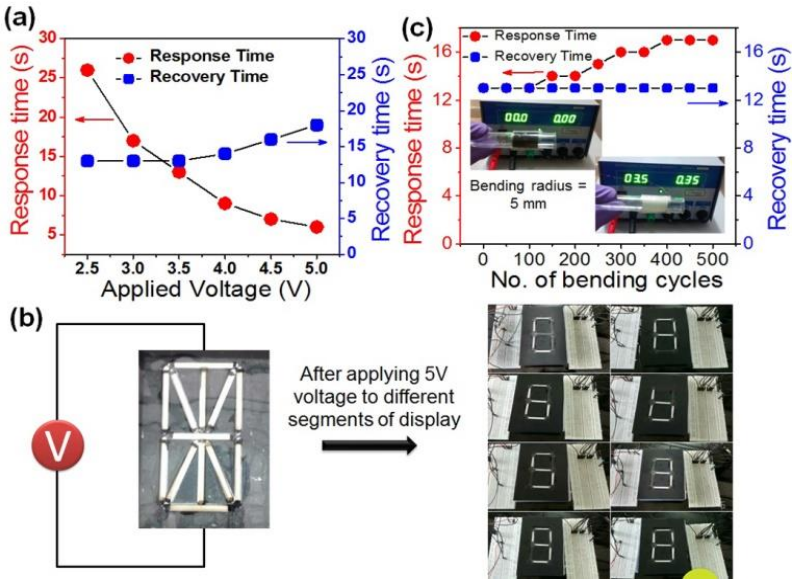

Figure IVA.4.7 Response and recovery times of thermochromic device as a function of (a) applied voltage and (c) number of device bending cycles (data points are taken after every 50th bending cycle at 3.5 V). (b) Demonstration of 13-segment thermochromic display connected to a bread board.

As the thermochromic device functioning depends on the heat flow to the active material, higher the applied voltage faster is the device response (Figure IVA.4.7a). For instance, with 3.5 V the response and recovery times were 12 and 13 s, respectively. On increasing the input voltage (upto 5 V), the color as well as transmittance of the device (opaque black to translucent white) changed within 6 s. On the other hand, with higher input voltage, the recovery time of the device increased by 5 s (from 13 s to 18 s). Having examined the thermal response of films, a 13-segment thermochromic display was fabricated for information display application (see Figure IVA.4.7b). By controlling the power of each segment, alphabets and numerics could be displayed on the display board as shown in Figure IVA.4.7b.

In order to demonstrate the mechanical robustness of both active material and Cu mesh heater in the fabricated thermochromic device, it was subjected to repetitive bending cycles (5 mm). Even after 100 bending cycles, no change in response and recovery times were observed (see Figure IVA.4.7c). However, after 500 bending cycles, the response time to reach the steady state temperature started increasing

due to a slight increase in the sheet resistance while the recovery time remained unaltered. Nonetheless, the increase in the former was only 4 s.

IVA.4.5 Conclusions

In conclusion, large area smart thermochromic devices have been realized with affordable Cu mesh based transparent heaters while using commonly available pigments as thermoactive layers requiring minimal input power (~ 0.2 W/cm^2) for activation. A thermal display fabricated using this recipe has shown fast switching from opaque to translucent within few seconds. These devices could be utilized in various present and futuristic smart display applications.

References

1. R. Baetens, B. R. P. Jelle and A. Gustavsen, *Sol. Energy Mater. Sol. Cells*, **2010**, *94*, 87.
2. A. Seeboth, J. Kriwanek, D. Lötzsch and A. Patzak, Polym. *Adv. Technol*. **2002**, *13*, 507.
3. T. Gyenes, A. Szilágyi, T. Lohonyai and M. Zrínyi, Polym. *Adv. Technol*., **2003**, *14*, 757.
4. E. S. Lee, D. L. DiBartolomeo and S. E. Selkowitz. *Energ. Buildings*., **2006**, *38*(1), 44.
5. T. Fischer, R. Lange and A. Seebot, *Sol. Energy Mater. Sol. Cells,* **2000**, *64,* 321.
6. H. Watanabe, *Sol. Energy Mater. Sol. Cells*, **1998**, *54*, 203.
7. M. Wang, Y. Gao, C. Cao, K. Chen, Y. Wen, D. Fang, L. Li and X. Guo, *Ind. Eng. Chem. Res*., **2014**, *53*, 18462.
8. G. U. Kulkarni, S. Kiruthika, R. Gupta and K. D. M. Rao, *Curr. Opin. Chem. Eng*., **2015**, *8*, 60.
9. KDM. Rao, R. Gupta, GU. Kulkarni, Adv. Mater. Interfaces., 2014, 1, 1400090.
10. R.R. Nair, P. Blake, A.N. Grigorenko, K.S. Novoselov, T.J. Booth, T. Stauber, N.M.R. Peres and A.K. Geim. *Science*, **2008**, *320*, 1308.
11. J. Liang, L. Li, K. Tong, Z. Ren, W. Hu, X. Niu, Y. Chen and Q. Pei, *ACS Nano*, **2014**, *8*, 1590.
12. A.R. Rathmell and B.J. Wiley, *Adv. Mater.,* **2011**, *23*, 4798.
13. D. Zhang, R. Wang, M. Wen, D. Weng, X. Cui, J. Sun, H. Li and Y. Lu, *J. Am. Chem. Soc.,* **2012**, *134*, 14283.
14. D.S. Hecht, L. Hu and G. Irvin, *Adv. Mater.,* **2011**, *23*, 1482.
15. M. Zhang, S. Fang, A.A. Zakhidov, S.B. Lee, A.E. Aliev, C.D. Williams, K.R. Atkinson and R.H. Baughman, *Science*, **2005**, *309*, 1215.
16. S. Hong, J. Yeo, G. Kim, D. Kim, H. Lee, J. Kwon, H. Lee, P. Lee and S.H. Ko, *ACS Nano,* **2013**, *7*, 5024.
17. B.Y. Ahn, D.J. Lorang and J.A. Lewis, *Nanoscale,* **2011**, *3*, 2700.
18. R. Gupta, K.D.M. Rao, K.Srivastava, A. Kumar, S. Kiruthika and G.U. Kulkarni, *ACS Appl. Mater. Inter.,* **2014**, *6*(16), 13688.
19. R Gupta, KDM Rao, S Kiruthika, GU Kulkarni, Visibly transparent heaters, *ACS Appl. Mater. Inter*., **2016**, *8* (20), 12559.
20. K. D. M. Rao and G. U. Kulkarni, *Nanoscale*, **2014**, *6*, 5645.

Chapter IVB

Smart Windows with Liquid Crystals as Active Layer

Summary

A hybrid (Au-SnO_2) electrode with good optoelectronic properties has been used as the transparent conducting electrode (TCE) for polymer dispersed liquid crystal device (PDLC) fabrications. The Au mesh electrodes were obtained through crackle templating process whereas SnO_2 was deposited by sol-gel solution process. The performances of these devices are highly comparable to that of ITO electrodes. With this alternative electrode, it is demonstrated that PDLC devices can have transmittance modulation with only 25 V.

IVB.1 Introduction

Smart windows, especially electronically switchable devices alter the optical properties (opaque or translucent to transparent or vice versa) with an applied input voltage [1,2]. Among many smart window technologies such as electrochromic, thermochromic to name a few, polymer dispersed liquid crystals (PDLC) find enormous applications in automobiles and architectural fields as energy saving windows mainly because of its simple fabrication process, fast switching speed, durability and minimal transparency of device in its 'off' state [3].

PDLC device basically has liquid crystals embedded in polymers sandwiched between two TCE [4]. With no external electric field applied to the TCE, liquid crystals are randomly oriented in polymer matrix giving rise to a milky white appearance due to scattering of light passing through the device. Upon supplying few volts to the device, the liquid crystals tend to align in a direction due to their intrinsic dipole moments allowing light to pass through thus, making the device appear transparent. By tuning the external electric field, the degree of device transparency can be altered [5]. Not only the liquid crystal durability but also strong mechanical robustness and high optoelectronic properties of TCEs are necessary for the excellent performance of PDLC devices [5,6].

Paper based on this study: Manuscript under Preparation

In general ITO electrodes are used in PDLC devices due to its outstanding optoelectronic performance as discussed in earlier section (Chapter I). Recently, researchers have tried to replace ITOs with alternative electrodes in PDLC devices. Khaligh *et al* have shown the PDLC device fabrication using Ag nanowire network electrodes. Although the device has shown transmittance modulation with an external voltage, the device in its 'on' state has shown non-uniform specular transmittance mainly because of non-uniform electric field provided by nanowire network [1]. Later, organic polymers, Ag meshes, and its hybrids have been used to fabricate PDLC devices [7,8]. Among them, Ag mesh coated with thin metal oxide has shown promising response [8].

IVB.2 Scope of the present investigation

An attempt to address the above pertinent issues, a hybrid transparent conductor was fabricated consisting of a SnO_2 layer deposited over a metal nanomesh. The latter was typically made of Au and can be obtained over virtually unlimited areas using crackle lithography [9,10]. It involves simple process steps using low-cost ingredients, yet produces transparent conductors of superior properties (T~ 85%, R_S ~ 5-10 Ω/sq). A novel feature of a metal mesh in comparison to CNT/nanowire networks is its assured wire connectivity all over the electrode surface and high degree of planarity even at junctions. This is clearly an advantage if one plans to submerge the mesh under a thin overlayer. Here, SnO_2 coating by the sol-gel process was tried out. The above recipe seems attractive as the hybrid- Au mesh coated with the SnO_2 layer, will possess the excellent conductive property of the metal mesh while offering oxide surface finish for the uniform conductive glass. In this hybrid structure, SnO_2 not only fills the perforated polygonal areas (bare glass) but also renders them somewhat conducting, making it ideal electrode for liquid crystal devices.

IVB.3 Experimental Details

Fabrication of Au mesh

The fabrication process involves three simple steps. Initially, an acrylic resin based precursor (0.6 g/mL, Ming Ni Cosmetics Co., Guangzhou, China) was spin coated over a pre-cleaned and dried glass substrate to create a crackle template. By depositing Au over the template through physical evaporation process, followed by removal of the

template yields highly interconnected Au wire mesh on the substrate (see Figure IVB.1 (i)-(ii)).

SnO_2 coating

Stannous chloride (Ranbaxy, India) was dispersed in an ethanolic solution (0.5 M). The solution was stirred for 5 hours and left at room temperature for 24 h. The supernatant liquid (~ 2 mL) was spin coated (1200 rpm, 60 s) over Au mesh network and annealed at 80 °C for 10 minutes. This process is continued for ten more times to increase the thickness of the SnO_2 layer to ~ 300 nm with no crack. Finally, the samples were annealed at 500 °C for 2 h to improve the crystallinity.

IVB.4 Results and Discussion

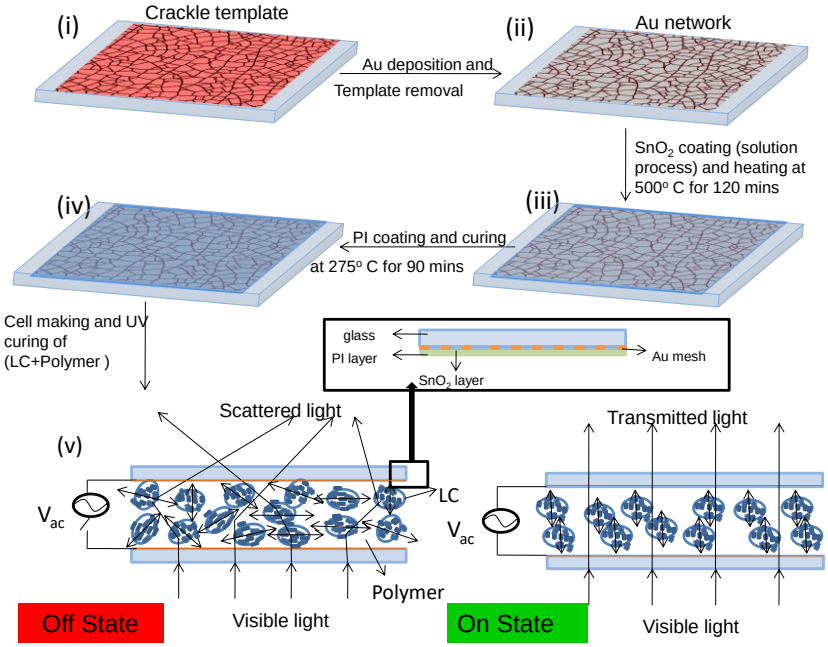

Figure IVB.1 Schematic of PDLC liquid crystal device fabrications using Au-SnO_2 mesh based transparent electrodes.

Figure IVB.1 (i)-(iii) shows the schematic diagram for the fabrication of Au-SnO_2 mesh. Firstly, Au mesh was obtained by crackle templating method as discussed in experimental details. Secondly, SnO_2 thin film was coated over Au mesh through a simple solution process (see Chapter IIID for more details). Thus obtained Au-SnO_2 mesh was employed for fabrication of PDLC device. A few nm thick polyimide films were coated upon Au-SnO_2 mesh electrodes for facilitating the alignment of liquid

crystals (Figure IVB.1 (iv)). PDLC was obtained by mixing NOA 65 (Norland products) and nematic LC E8 in the ratio of 2:3 wt%. PET of ~ 25 microns was used as spacers to hold two TCEs and also control the thickness of PDLC layer. The mixture of LC/NOA65 was filled between two TCE by capillary action while holding the device at 258 °C. As shown in Figure IVB.1 (v) and (vi), light modulation across the device was controlled by external AC voltage.

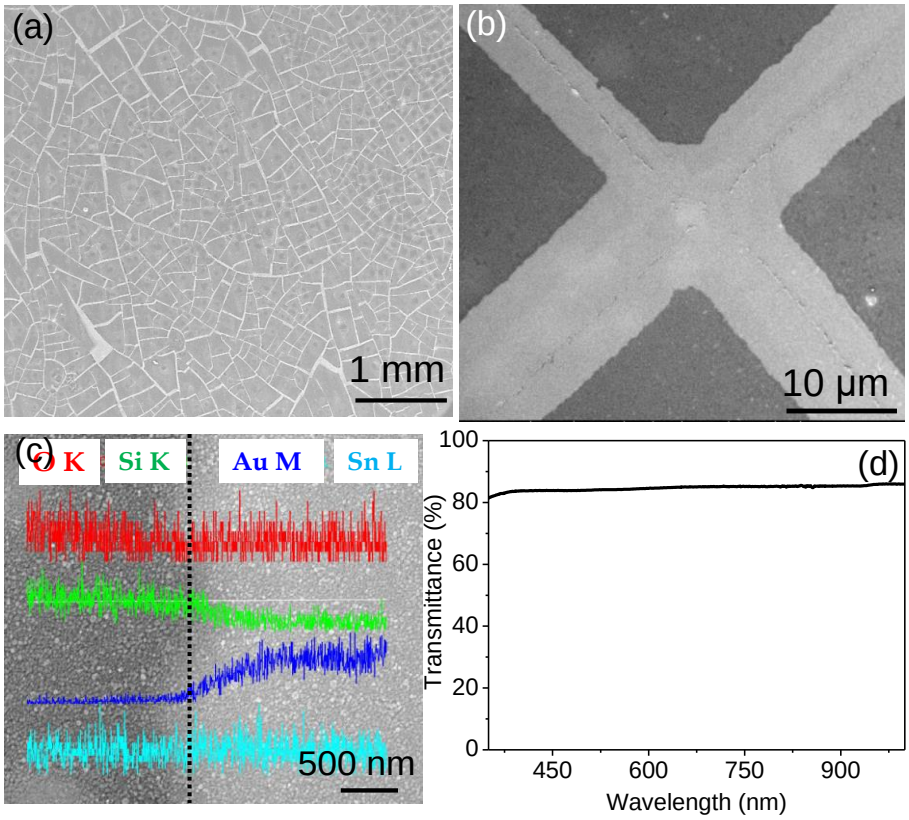

Figure IVB.2 (a and b) SEM images of the obtained Au-SnO_2 mesh on a glass substrate at different magnifications. (c) SEM line mapping indicating the uniform coating of SnO_2 nanoparticles across the bare glass and Au mesh coated regions. (d) Transmittance spectrum of fabricated Au-SnO_2 mesh.

Figure IVB.2a confirms the uniform SnO_2 coating across large area of interconnected Au mesh and the enlarged image in Figure IVB.2b further proves the smooth SnO_2 surface with no defects and seamless junction of Au mesh. The Au wire widths vary in the range of 5-20 µm. Uniform distribution of SnO_2 coating over Au mesh was further proven from the EDS line mapping clearly indicating the

compactness of SnO_2 nanoparticles (Figure IVB.2c). Figure IVB.2d shows the optical transmittance spectrum of Au-SnO_2 mesh. The average transmittance of the mesh electrode in the entire visible region (400-800 nm) is ~ 84% with the sheet resistance of ~ 8-10 Ω/sq.

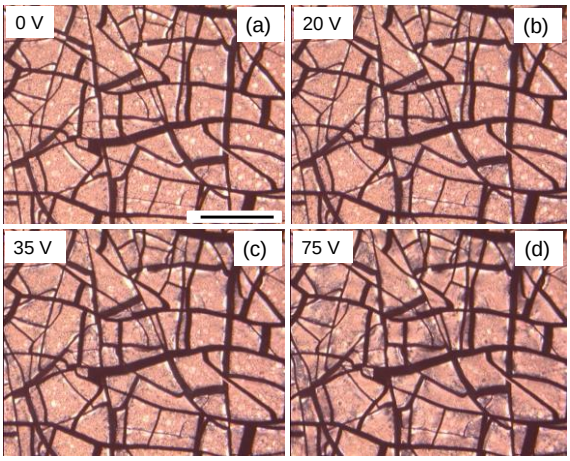

Figure IVB.3 (a-d) Polarized optical microscopic images of PDLC devices fabricated using Au mesh as TCEs. Scale bar is 100 μm.

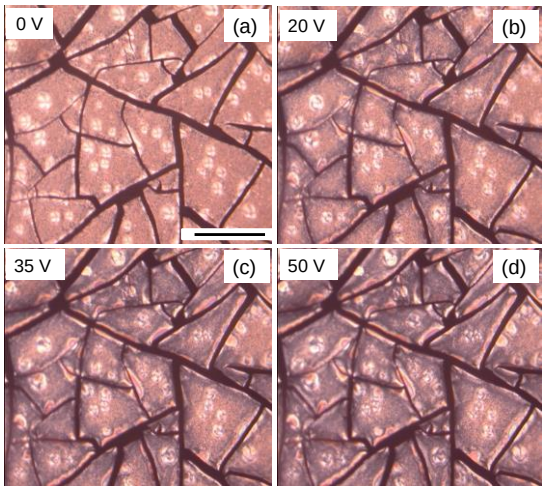

Figure IVB.4 (a-d) Polarized optical microscopic images of PDLC devices fabricated using Au mesh and ITO. Scale bar is 50 μm.

A SnO_2 film deposited on the Au mesh not only protects the mesh electrode but also ensures the uniform electrical conductivity on the TCE surface. While using bare Au mesh electrode for PDLC device fabrication (Au mesh/PDLC/Au mesh), it

was observed that even with the high input voltage (75 V) the liquid crystals alignment occurred only near mesh regions (black contrast in Figure IVB.3d) whereas in the bare glass regimes there is no alignment (Figure IVB.3a-d). To understand further, one of the Au mesh TCE was replaced with ITO electrode (ITO/PDLC/Au mesh). Now upon supplying external field, the liquid crystal aligned all-across and thus contrast was noticeable in Figures IVB.4. These two experiments clearly depicted the vital importance of electrically uniform transparent electrodes for LC devices.

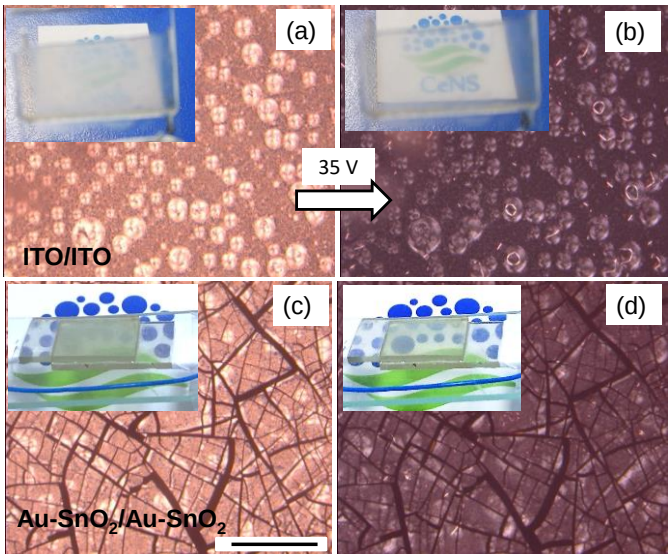

Figure IVB.5 Polarized optical microscopic images of PDLC devices fabricated using ITO (a-b) and Au-SnO_2 mesh (c-d) in its V_{OFF} and V_{ON} states. Scale bar is 50 μm. Insets are photographs of the device.

Figure IVB.5a presents the optical microscopic image of PDLC device with ITO electrodes in its V_{OFF} state. Due to the random alignment of liquid crystals in the polymer matrix, the device appears milky white opaque (inset in Figure IVB.5a). While applying 35 V to the device, liquid crystals tend to align towards a direction and became transparent (see Figure IVB.5b). Before replacing both ITOs with alternative Au-SnO_2 electrodes in LC device, initially an attempt was made to replace one of the ITO electrodes (ITO/PDLC/Au-SnO_2). The device has shown uniform contrast similar to that with ITO-based electrodes (Figure IVB.6). Latter both the

ITO electrodes were replaced with Au-SnO_2 electrodes and its optical microscopic images and photographs are shown in Figure IVB.5c and d. Unlike bare Au mesh based device, Au-SnO_2 electrodes offer uniform electric field surface and thus liquid crystals alignment resulting in the modulation of transmittance of the device as noticed from the inset photographs (Figure IVB.5c and d).

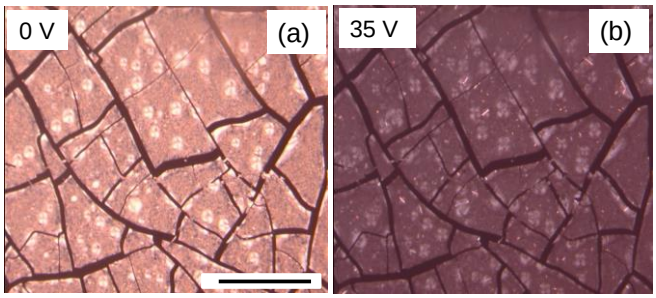

Figure IVB.6 Optical microscopic images of PDLC devices fabricated using an ITO and an Au-SnO_2 mesh in its V_{OFF} (a) and V_{ON} (b) states. Scale bar is 100 µm.

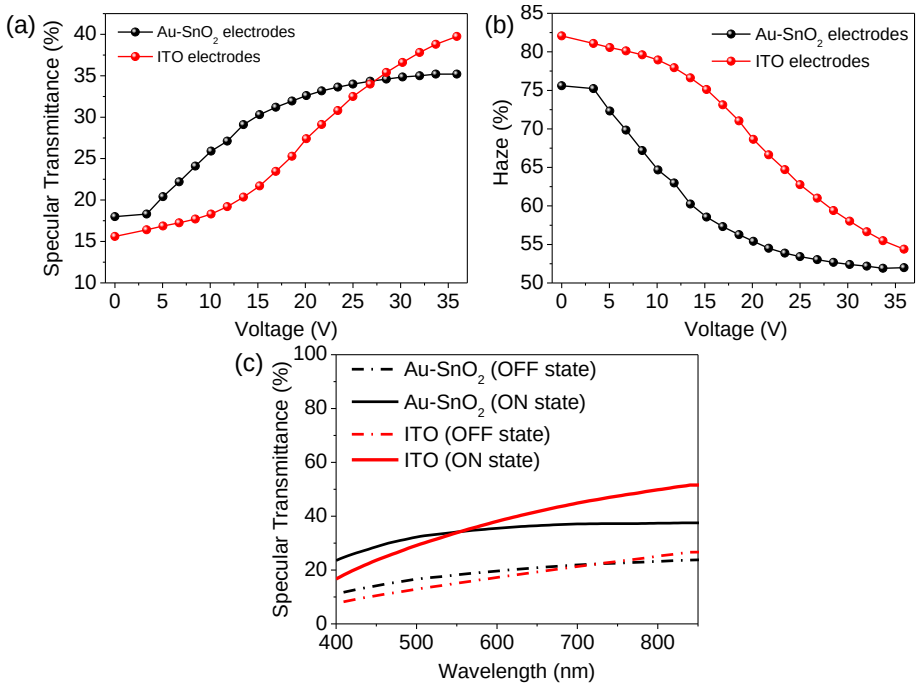

Figure IVB.7 (a) Specular transmittance and (b) haze variations at 550 nm with various input voltages to ITO and Au-SnO_2 PDLC devices. (c) The specular transmittance of ITO and Au-SnO_2 based PDLC devices in the 'ON' and 'OFF' states in the visible region.

The variation in specular transmittance (light transmitting through the device without scattering) and haze (transmitted light which is scattered) of PDLC device

fabricated using ITO and alternative Au-SnO_2 mesh electrodes are shown in Figure IVB.7a and b, respectively. At 0V, light falling over the device was either reflected or forward scattered. While increasing the input voltage, incident light was transmitted with less scattering and the transmittance of the Au-SnO_2 mesh-based device was saturated around 35% (air as reference) while the ITO device reaches the maximum transmittance of ~ 40% at 35 V. Thus, the hybrid electrode not only reaches the saturation transmittance with low input voltage (~ 20 V) but also provides lower energy consumption than ITO electrodes. Furthermore, the haze of the Au-SnO_2 mesh-based devices is lower than that of ITO electrodes (Figure IVB.7b). Figure IVB.7c shows the specular transmittance of both the devices in the on and off states in the visible region wavelength. According to Figure IVB.7a, 25 V was selected as ON state voltage to study the transmittance and reflectance. The transmittance difference (ΔT_{ON-OFF}) at 550 nm between ON (34.2%) and OFF (18%) state for the hybrid Au-SnO_2 electrode device is 16.2% whereas that of ITO electrode is 19%. However, the transmittance of both hybrid and ITO-based devices at 550 nm are almost same (34%).

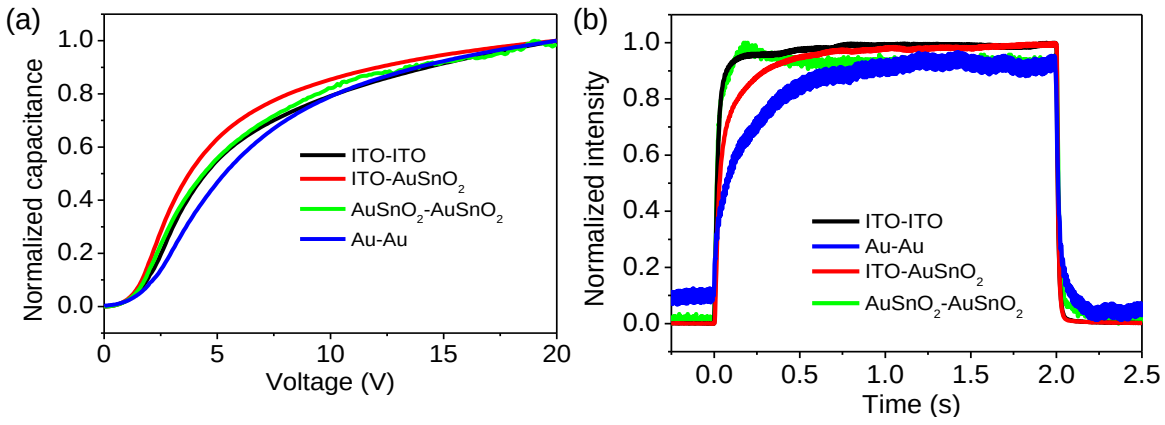

Figure IVB.8 (a) Normalized capacitance versus applied voltage profiles for various LC devices at 30 °C exhibiting the Freedericksz transformation behaviour. (b) Electro-optic (EO) response and recovery times for the on (τ_{ON}) and the off (τ_{OFF}) states when the voltage (1 kHz sine) is applied and subsequently.

The profiles of the voltage dependence of the normalized capacitance for various PDLC devices based on ITO-ITO, Au mesh-Au mesh, ITO-$AuSnO_2$, and $AuSnO_2$-

$AuSnO_2$ electrodes are shown in Figure IVB.8a. With respect to ITO electrodes, ITO-$AuSnO_2$ and $AuSnO_2$ -$AuSnO_2$ electrodes have shown a gentle decrement in threshold voltage (V_{th}) (see Table IVB.1). More conspicuous is the performance immediately above V_{th} where ITO-$AuSnO_2$ and $AuSnO_2$ have a sharp rise in the capacitance compared to ITO-based and Au mesh-based devices. The electro-optic response and recovery times of these devices were measured by simultaneously monitoring the light transmittance through the device using photodetector while the device was turned on and off with the applied input voltage (Figure IVB.8b). The response and recovery times of $AuSnO_2$ based devices are slightly higher than that of ITO-based ones whereas these values are lower than that of Au mesh-based devices (Table IVB.1).

Table IVB.1 Switching speed and threshold voltage comparison of various devices.

S. No	System	τ_{ON} (ms)	τ_{OFF} (ms)	Threshold voltage (V)
1	ITO/ITO	44	80	1.45
2	Au-Au	69	320	1.91
3	ITO/Au-SnO_2 mesh	49	270	1.23
4	Au-SnO_2/Au-SnO_2 mesh	62	170	1.28

IVB.5 Conclusions

Oxide coated Au mesh TCE for PDLC smart window device is demonstrated as an alternative to ITO electrodes. With the combination of crackle templating method and the sol-gel method, the Au-SnO_2 electrodes were realized through an environmentally friendly process. The PDLC smart device based on Au-SnO_2 electrodes exhibiting the maximum transmittance of 35% with ~ 20 V input voltage. A lower voltage supply is sufficient to work with Au-SnO_2 based device since it's on state can be reached at 15V which is much lower than the ITO-based device. Furthermore, this result encourages the use of hybrid metal mesh electrodes for a range of other LC and smart window devices.

References

1. H. Hosseinzadeh Khaligh, K. Liew, Y. Han, N. M. Abukhdeir, I. A. Goldthorpe, Silver nanowire transparent electrodes for liquid crystal-based smart windows, *Solar Energy Materials and Solar Cells*, **132**,337-41.

2. S. D. Rezaei, S. Shannigrahi, S. Ramakrishna, A review of conventional, advanced, and smart glazing technologies and materials for improving indoor environment, *Solar Energy Materials and Solar Cells*, **159**,26-51.

3. S. Park, J. W. Hong, Polymer dispersed liquid crystal film for variable-transparency glazing, *Thin Solid Films*, 2009,**517(10)**,3183-6.

4. Y. Kim, D. Jung, S. Jeong, K. Kim, W. Choi, Y. Seo, Optical properties and optimized conditions for polymer dispersed liquid crystal containing UV curable polymer and nematic liquid crystal, *Current Applied Physics*, **15(3)**,292-7.

5. R. Baetens, BrP. Jelle, A. Gustavsen, Properties, requirements and possibilities of smart windows for dynamic daylight and solar energy control in buildings: A state-of-the-art review, Solar Energy Materials and Solar Cells, **94(2)**,87-105.

6. Y. Liu, S. Shen, J. Hu, L. Chen, Embedded Ag mesh electrodes for polymer dispersed liquid crystal devices on flexible substrate, *Optics Express*, **24(22)**,25774-84.

7. K. Jin-Yeol, W. Hak-Yong, B. Ji-Woong, K. Tae-Wook, S. Eun-Ah, P. Su-Cheol, *et al*., Polymer-dispersed liquid crystal devices using highly conducting polymers as electrodes. *Applied Physics Letters*, 2008,**92(18)**,183301.

8. L. Qi, J. Li, C. Zhu, Y. Yang, S. Zhao, W. Song, Realization of a flexible and mechanically robust Ag mesh transparent electrode and its application in a PDLC device, *RSC Advances*, **6(16)**,13531-6.

9. R. Gupta, K. D. M. Rao, K. Srivastava, A. Kumar, S. Kiruthika, G. U. Kulkarni, Spray Coating of Crack Templates for the Fabrication of Transparent Conductors and Heaters on Flat and Curved Surfaces, *ACS Applied Materials & Interfaces*, **6(16)**,13688-96.

10. K. D. M. Rao, R. Gupta, GU. Kulkarni, Fabrication of Large Area, High-Performance, Transparent Conducting Electrodes Using a Spontaneously Formed Crackle Network as Template, *Advanced Materials Interfaces*, **1(6)**,1400090-n/a.

Chapter IVC

Transparent Supercapacitors for Smart Devices

Summary

Transparent and flexible energy storage devices have received immense attention due to their suitability for innovative electronics and displays. However, it remains a great challenge to fabricate devices with high storage capacity and high degree of transmittance. This study describes a simple process for fabrication of supercapacitors with ~ 75% of visible transparency and areal capacitance of ~ 3 mF cm^{-2} with high stability tested over 5000 cycles of charging and discharging. The electrodes consist of Au networks obtained by a simple crackle template method which were coated with MnO_2 nanostructures by electrodeposition process. Importantly, the membrane separator itself has been employed as substrate to bring in the desired transparency and light weight while additional exploiting its porous nature in enhancing the interaction of electrolyte with active material from both sides of the substrate, thereby enhancing the storage capacity. This method opens the door for fabricating transparent devices and provides the choice of active materials.

IVC.1 Introduction

Lightweight and flexible energy storage devices have attracted a great attention mainly due to the increasing demand for integration in devices such as portable personal electronics. Among them, supercapacitors have become increasingly popular as they provide higher power densities than the lithium ion batteries and higher energy densities than electrolytic capacitors with many additional advantages such as long cycle life, fast charging-discharging rates as well as enhanced safety [1]. The application area is wide- from pulse power systems to electric vehicles, where rapid energy release on demand, is crucial [2,3]. Typically, a supercapacitor is composed of a set of current collectors made of a chosen electrode material, an electrolyte and a separator. In contrast to metal strips current collectors such as copper, stainless steel, and nickel foils, conducting thin films deposited on polymer (PET) or paper substrates afford light weight [4]. Light weight supercapacitors have

Paper based on this study: Submitted May 2017

been fabricated on various paper substrates including photocopier paper, commercial separator membrane, lens wiping papers, etc. [5-10]. Thus fabricated devices possess an integrated structure, in which the separator membrane is made to host the two electrodes on both sides. Besides being light weight, these devices provide high areal capacitance and are usually stable towards many charge storage cycles [5]. However while integrating device on a sheet of paper, the micron-sized pores present in the cellulose matrix may lead to short circuiting. This issue can be resolved by coating PVDF or graphene from pencil trace on both sides of porous paper membranes before loading active materials [7-9]. This work focuses on the fabrication of a light weight supercapacitor from quite a different approach.

IVC.2 Scope of the present investigation

Extensive research is being done to incorporate aesthetic properties such as transparency, flexibility, and wearability to the intrinsic performance of the futuristic supercapacitors [11,12]. The supercapacitors reported in the literature are largely opaque mainly due to non-transparency of either the substrate or of the active material [5,7,8]. Recent efforts have been focused on developing entirely transparent devices by incorporating transparent current collectors and thin layers of active materials. Due to several drawbacks of traditional indium tin oxide (ITO) transparent electrodes such as scarcity, high processing cost, limited chemical resistance as well as lack of flexibility, alternative electrodes consisting of graphene, CNTs, metal nanowires or metal meshes are being pursued [13-18]. As regards the transparency of the active layer, reducing the thickness alone may not be helpful; the areal capacitance may get hindered [11]. Recently, there have been significant efforts dedicated towards the fabrication of transparent supercapacitors with creative new designs to enable some transparency in the device [19-21]. In an instance, Zhi *et al.* employing nanosphere lithography process produced Au/MnO_2 core-shell mesh electrodes which yielded 48% transparency in the device with the areal capacitance of 4.7 mF cm^{-2} (at a current density of 5 μA cm^{-2}) [22]. However, the lithography method is inherently unsuitable for large area device fabrication and mass production. In another report, free-standing transparent graphene paper was used as an effective active material for energy storage [23]. Despite their flexibility and high

efficiency for charge storage (3 mF cm^{-2}), the obtained transparency of the device was < 50%. On the other hand, the supercapacitor with the transparency of 75% has been achieved with ~ 2 nm thick graphene as an active layer. However, the areal-specific capacitance of the device is only 0.1 mF cm^{-2} [11]. Thus, there appears to be a trade-off between the transparency and energy storing capability of the device. In this work, a light-weight flexible device has been fabricated with an additional attribute of visible transparency without in any way compromising the device performance.

Here, over Au mesh transparent current collector pseudo-capacitive MnO_2 flakes were grown. The fabricated energy storage device was highly flexible, light-weight and transparent (~75%) with the areal capacitance of ~ 3 mF cm^{-2}. The simple fabrication process with environmentally benign materials is the added advantages.

IVC.3 Experimental Details

Fabrication of Au mesh

The fabrication process involves three simple steps. Initially, an acrylic resin based precursor (0.6 g/mL, Ming Ni Cosmetics Co., Guangzhou, China) was spin coated over a pre-cleaned and dried separator substrate (BOPP films from Mirwec Film, Inc) to create a crackle template. By depositing Au over the template through physical evaporation process, followed by removal of the template yields highly interconnected Au wire mesh on the separator substrate.

Fabrication of Au/MnO_2 mesh

MnO_2 was electrodeposited over Au mesh by immersing the electrode into plating solution composed of 1:1 mixture of 50 mM Na_2SO_4 and 50 mM of $Mn(Ac)_2$ under steady potential of 0.45 V *vs* Ag/AgCl electrode and Pt as reference electrode. MnO_2 loading was varied with time of deposition (8 – 90 min).

Fabrication of solid-state supercapacitor

PVA-H_2SO_4 gel was used as an electrolyte as well as a spacer between two Au/MnO_2(60min) electrodes. The gel electrolyte was prepared by dissolving 1 g of H_2SO_4 and 1 g PVA in 10 mL of DI water at 80 °C under vigorous stirring till it dissolves completely to form a clear solution.

IVC.4 Results and Discussion

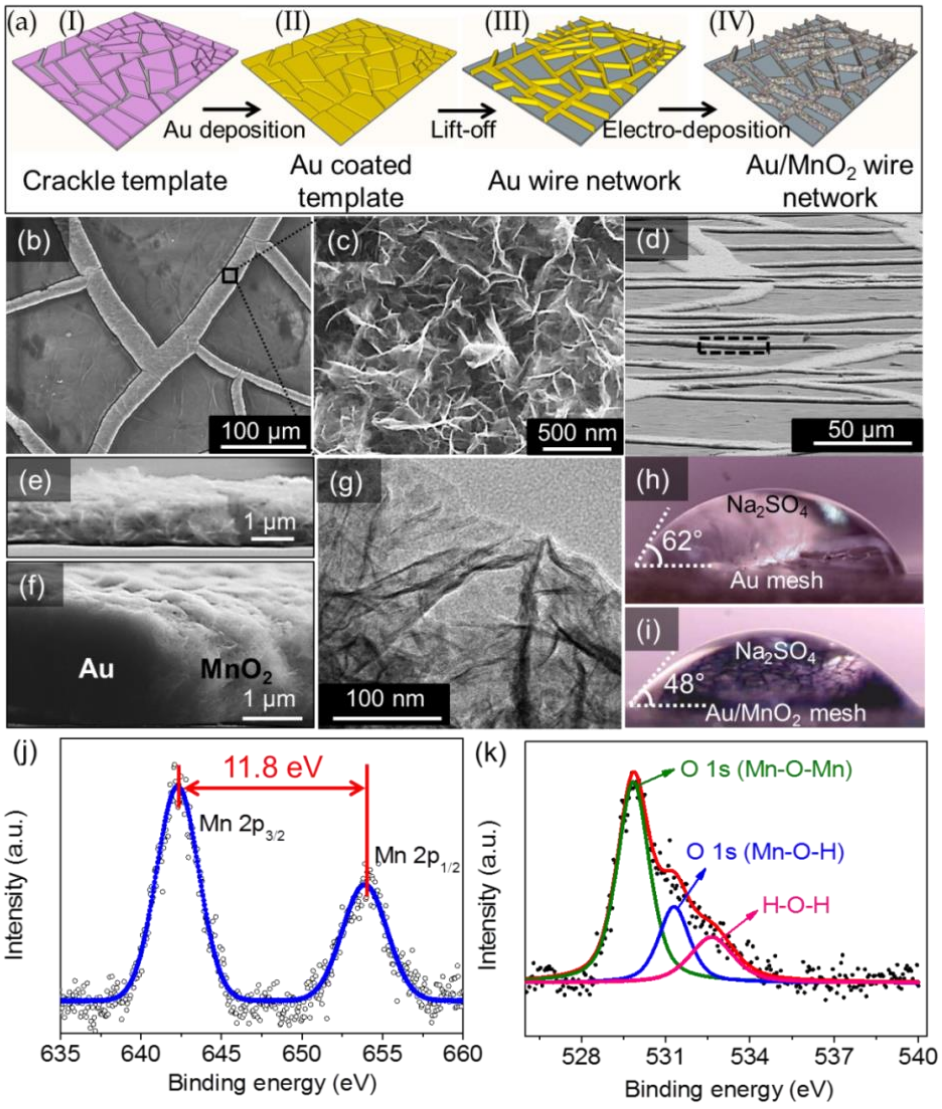

Figure IVC.1 (a) Schematic illustration for the fabrication of Au/MnO_2 wire network on the separator. In step I, the crackle template was prepared on the separator by spin coating acrylic resin based precursor. Upon the template, Au metal was deposited by a physical evaporation method (II) followed by removal of the template to obtain highly interconnected Au wire network (III). Later, Au was decorated with MnO_2 flakes by an electrodeposition process (IV). SEM images of the fabricated Au/MnO_2 wire meshes are shown in (b-f). (b) and (c) Top views and (d-f) the cross-sectional views of the Au/MnO_2 (60 min) network. The marked region in (d) is shown in (e). (g) TEM image of MnO_2 flakes. Photographs of Na_2SO_4 droplets on (h) Au and (i) Au/MnO_2 mesh surfaces. XPS survey spectrum of (j) Mn 2p and (k) O 1s of Au-MnO_2 mesh on the separator substrate.

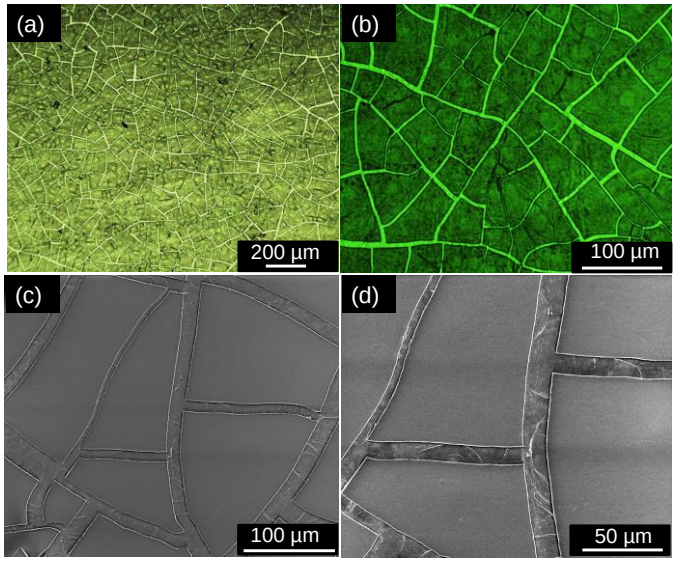

Figure IVC.2 (a) and (b) Optical microscope, (c) and (d) SEM images of the crackle network on separator.

Schematic of the fabrication process to prepare Au/MnO_2 core-shell wire network is presented in Figure IVC.1a. The transparent Au wire network based current collector was obtained using the crackle template method pioneered in the laboratory [24-30]. Initially, a highly interconnected crackle template with crack widths in the range of 10 - 20 µm (see Figure IVC.2) was obtained over the separator substrate. The networks are highly interconnected over large area and down to the substrate as seen in optical micrographs (Figure IVC.2a and b). From the SEM images Figure IVC.2c and d, the width of crackle networks are found to be ~10 - 20 µm. The crackles were down to the separator and devoid of any crackle precursor and can be readily used as a template for metal deposition.

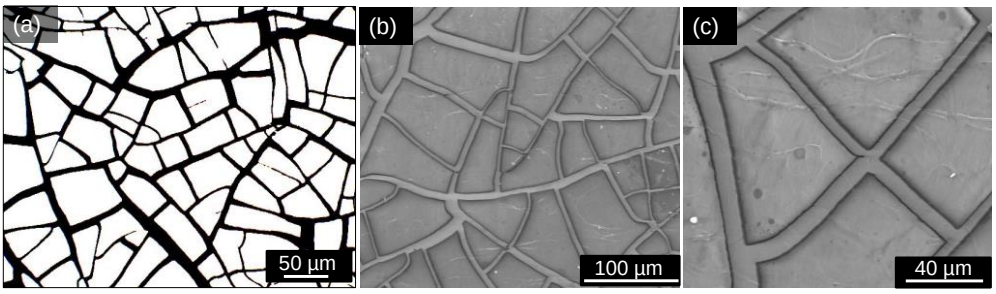

Figure IVC.3 (a) Optical microscopic and SEM images of the Au network over separator (b) and (c).

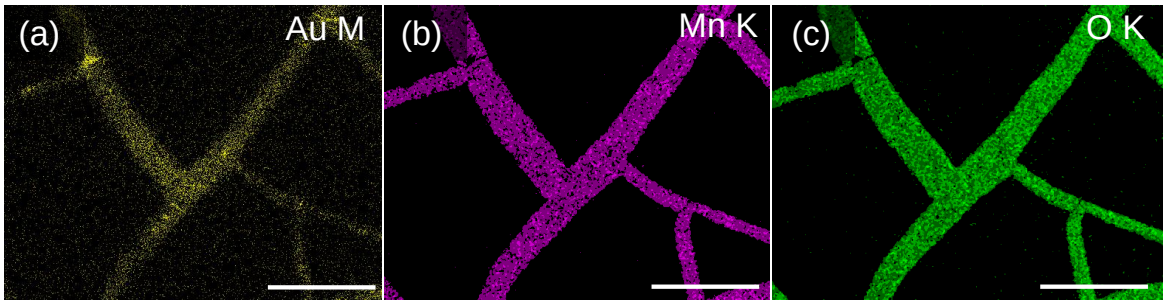

Figure IVC.4 (a-c) Energy-dispersive spectroscopy (EDS) mapping confirms the presence of Au and MnO_2 in the form of interconnected network. Scale bar is 100 μm.

After Au deposition and removal of template, Au wire mesh (< 5 Ω $\square^{-1}$, 86% transmittance) with seamless junctions was obtained on the substrate (see Figure IVC.3). The optoelectronic properties of the Au mesh electrode could be further varied by modulating the density, width, and thickness of the metal mesh. The Au wire networks were coated with high surface area MnO_2 flakes by an electrodeposition process. The low and high-resolution SEM images of the Au/MnO_2 deposited for 60 min (henceforth, Au/MnO_2(60 min)) core-shell networks are shown in Figure IVC.1b and c, respectively. From the elemental mapping, it is clear that the Au wire mesh is uniformly coated with MnO_2 shell (see Figure IVC.4). Unlike metal nanowire networks, where the complications of cross-bar junctions and agglomerations are highly troublesome for devices, Au/MnO_2 network has a low surface roughness due to its in-plane arrangement as shown in Figure IVC.1d. Complete encapsulation of the Au core by MnO_2 is evidenced from the side view SEM images in Figure IVC.1e and f. The highly porous and spiky nature of MnO_2 is supported from the SEM and TEM images in Figure IVC.1f and g, respectively. Furthermore, MnO_2 deposition improves the wettability of Na_2SO_4 (an electrolyte) and reduces the contact angle (48°) (Figure IVC.1h and i). The hydrophilic nature of the electrode is highly desirable in this context for the fast access of the ions to the interface between electrode and electrolyte.

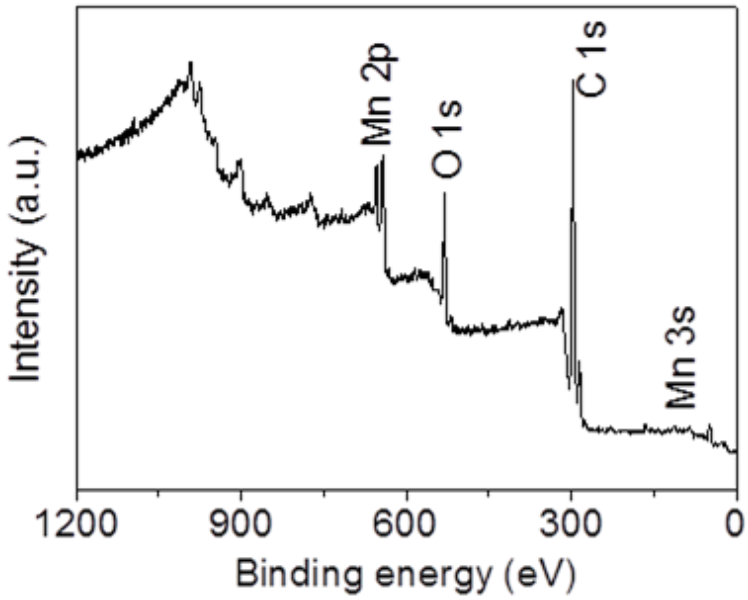

Figure IVC.5 XPS wide survey scan of Au/MnO_2 on separator showing Mn 2p, O 1s, C 1s and Mn 3s core level peaks.

The chemical compositions and the oxidation states of Mn in Au/MnO_2 wire network were analyzed using XPS studies. The major peaks in survey XPS spectrum (see Figure IVC.5) shows the presence of Mn, O, and C elements. The core-level XPS spectrum of Mn 2p is shown in Figure IVC.1j. The two peaks located at 642.2 and 653.9 eV are corresponding to binding energies of Mn $2p_{3/2}$ and Mn $2P_{1/2}$ electrons, respectively, suggesting the existence of Mn^{4+} oxidation state in the obtained MnO_2 flakes. In addition, spin energy separation of 11.8 eV between the binding energies of Mn 2p levels matches well with that reported for MnO_2 [31]. The O 1s deconvolution leads to three features at ~529.8, 531.2 and 533 eV corresponding to Mn-O-Mn of oxides, Mn-O-H of hydroxides and H-O-H of residual water, respectively (Figure IVC.1k) [32].

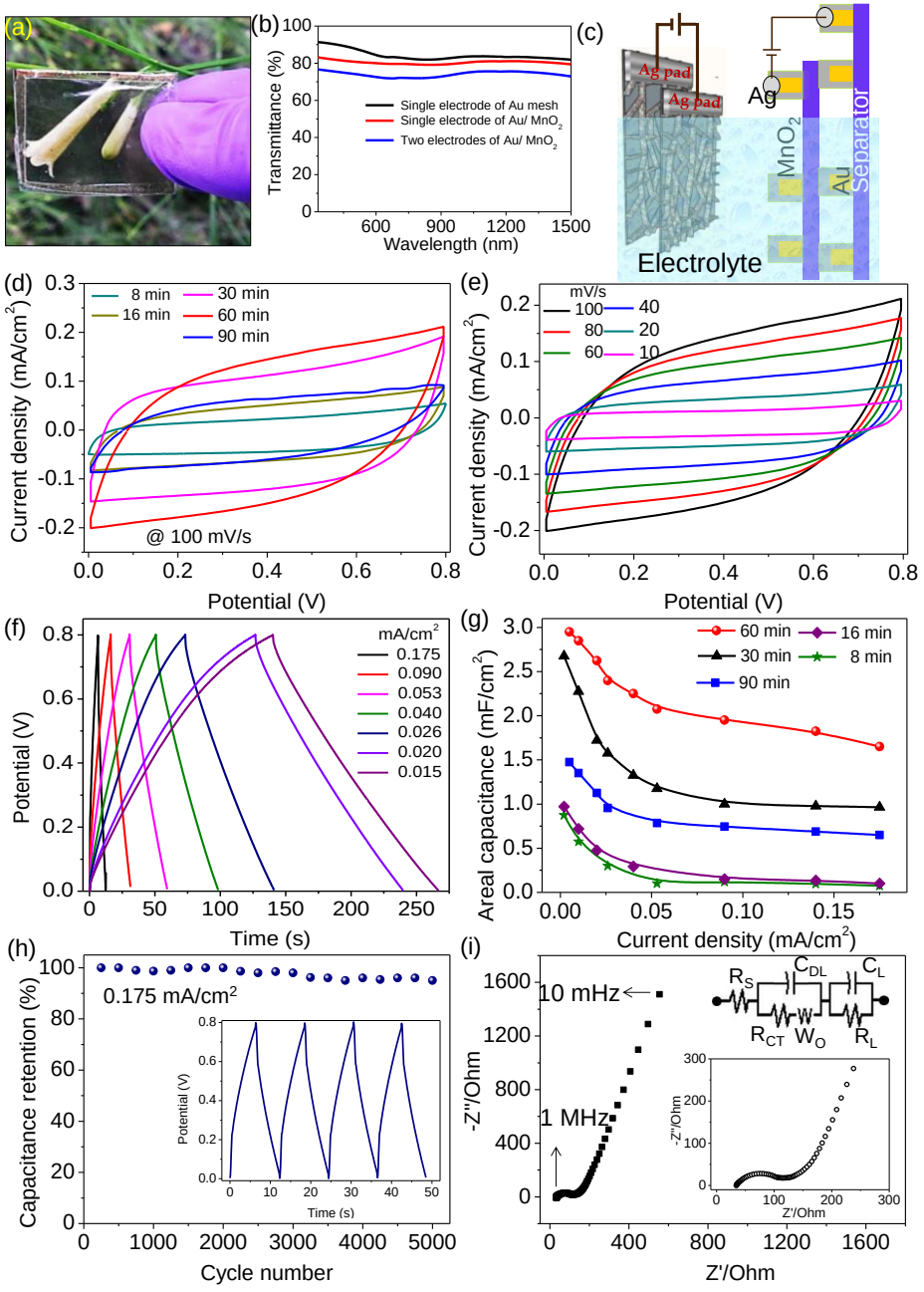

Figure IVC.6 (a) Photograph of resultant single Au/MnO_2 mesh on the separator (border laminated for stiffness). (b) Transmittance spectra of Au mesh, Au/MnO_2 (60 min) mesh and assembled two Au/MnO_2 (60 min) meshes. (c) Schematics of Au/MnO_2 electrode assembly/configuration. (d) Cyclic voltammograms (CV) of Au/MnO_2 with different MnO_2 loading at the scan rate of 100 mV s^{-1} in 1 M Na_2SO_4 electrolyte. CV curves at different scan rates and galvanostatic charge-discharge (CD) profile at different current densities of Au/MnO_2 (60 min) MnO_2 devices are shown in (e) and (f), respectively. (g) Dependence of areal capacitance of Au/MnO_2 meshes with different MnO_2 loading on the discharging current

density. (h) Stability of supercapacitor for 5000 charging and discharging cycles at a current density of 0.175 mA cm^{-2}. Inset is the CD profile at 0.175 mA cm^{-2}. (i) Nyquist impedance plot of Au/MnO_2 (60 min) supercapacitor. Insets are the magnified high-frequency region of impedance plot and fitted equivalent circuit where R_S is the series resistance, C_{DL} is the double layer capacitance, R_{CT} is the charge transfer resistance, W_O is the Warburg impedance, C_L denotes the pseudocapacitance and R_L is the leakage resistance.

A photograph of the fabricated Au/MnO_2 electrode on the separator is shown in Figure IVC.6a with the transmittance spectrum in Figure IVC.6b. As seen from the spectrum, the transparency is ~ 81% at 550 nm, which is not significantly less compared to that of bare Au mesh (~ 86%) in spite of the growth of MnO_2 on top. The optical transmittance of the assembled two electrode supercapacitor is nearly 72% (see Figure IVC.6b), which is commendable. Electrochemical performances of Au/MnO_2 wire meshes on flexible separator were measured in the two-electrode configuration in 1 M Na_2SO_4 (aq.) electrolyte. As supercapacitor separator was used as the substrate in this study, the two electrodes have been placed one over the other (see schematic in Figure IVC.6c) than the typical alignment (facing each other with a separator in-between). This new strategy not only avoided the additional usage of separator but also worked effectively (see Figure IVC.7).

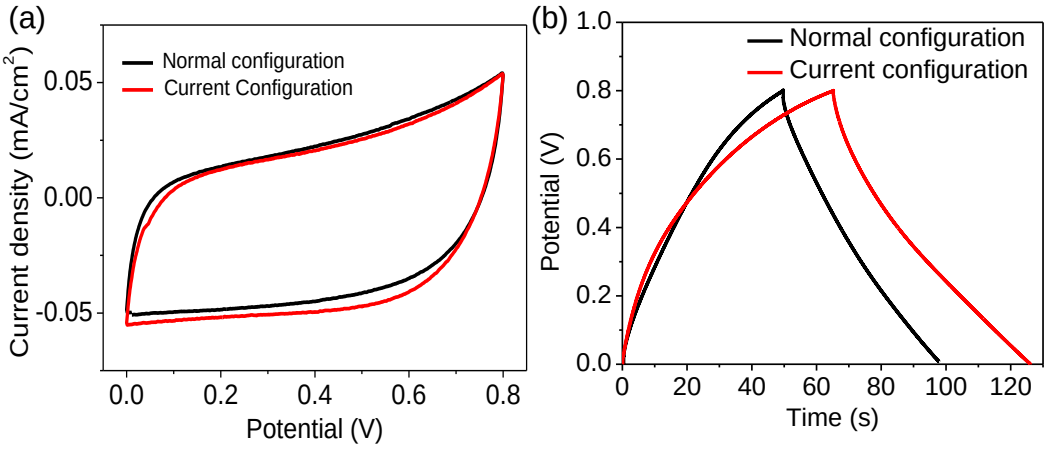

Figure IVC.7 (a) Cyclic voltammograms and (b) charge-discharge profile of two supercapacitor electrodes with different configurations. In the current configuration, electrode is arranged one over the other rather than facing each other with thin separator in between (normal) mainly because of separator as the substrate.

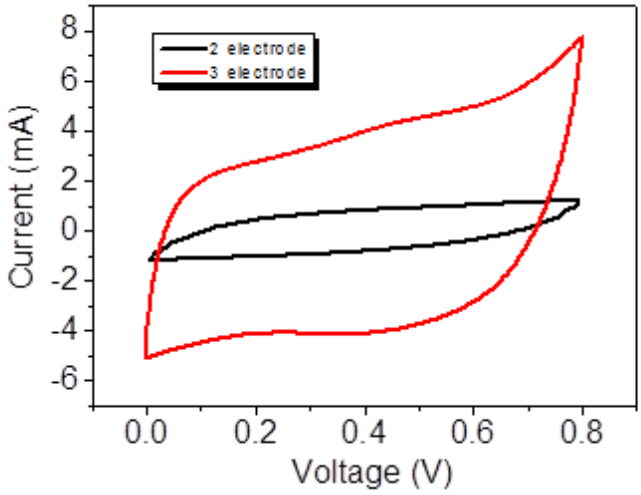

Figure IVC.8. Cyclic voltammogram of two and three electrode configurations.

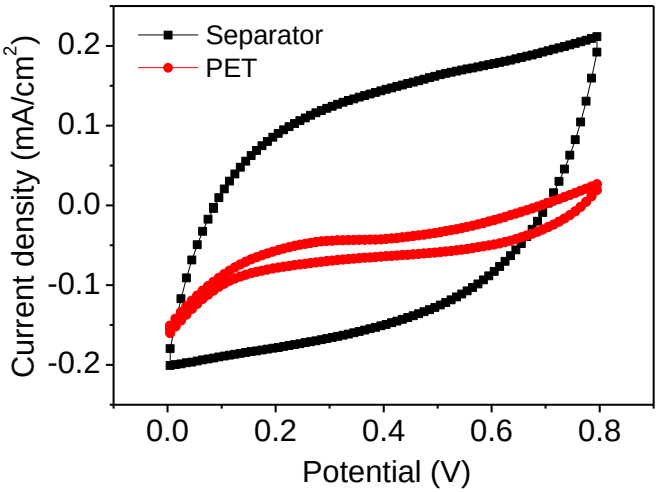

Figure IVC.9 Cyclic voltammograms (CV) of device fabricated on PET substrate (Au/MnO_2(PET)/ separator/Au/MnO_2(PET)) and separator substrate.

The comparison of the cyclic voltammograms (CV) measured in three electrode configuration with the data from two electrode configuration is shown in Figure IVC.8. The former values are quite higher as expected. Figure IVC.6d shows the CV data for Au/MnO_2 wire meshes with different MnO_2 loadings at a scan rate of 100 mV s^{-1}, where it is observed that the Au/MnO_2(60 min) electrodes exhibit the highest current density. It is important to note that capacitance from current collecting Au mesh alone is negligible. Also, the current density obtained from the device fabricated on PET substrate (Au/MnO_2(PET)/separator/Au/MnO_2 (PET)) is an order less than

the device fabricated with the separator as the substrate (see Figure IVC.9). The CV curves of Au/MnO_2(60 min) measured at various scan rates from 10 to 100 mV s^{-1} exhibited nearly rectangular shaped curves indicating the ideal capacitive behaviour of the device (Figure IVC.6e).

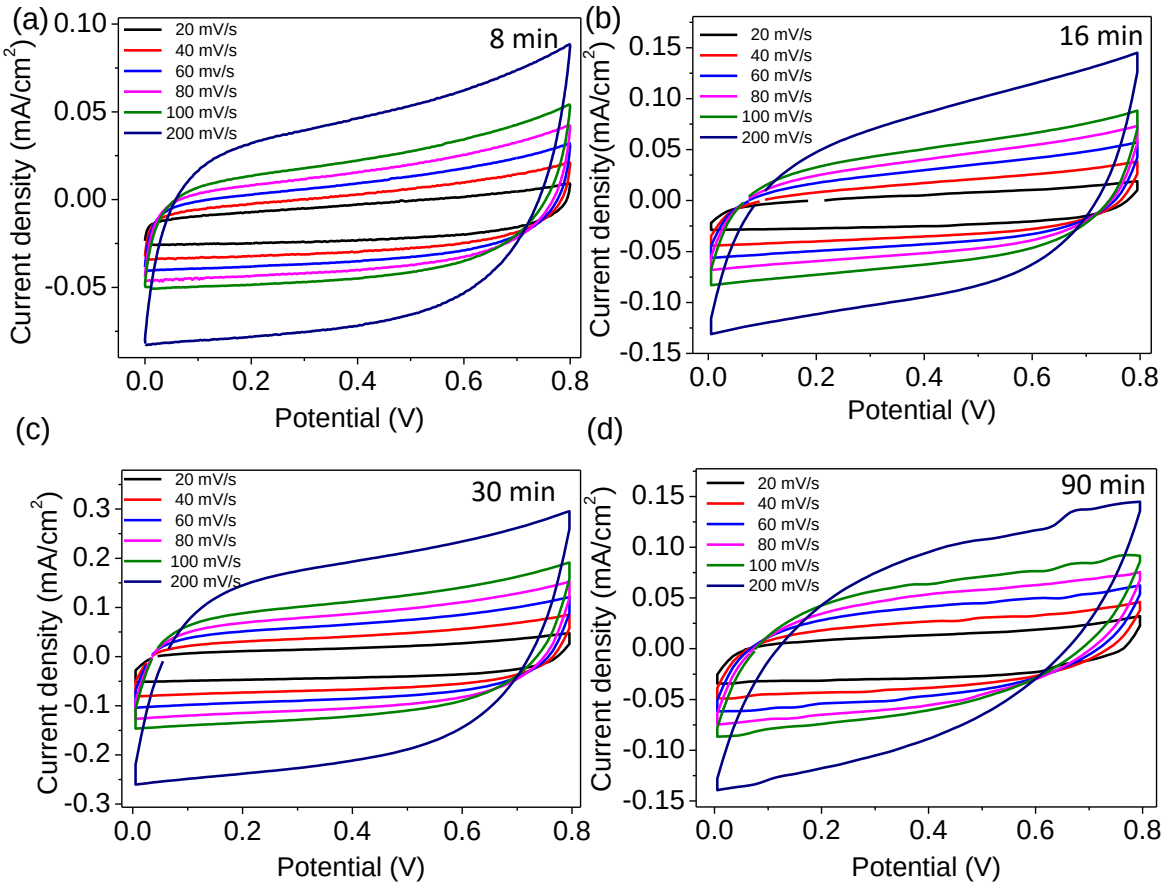

Figure IVC.10 Cyclic voltammograms (CV) of transparent supercapacitors with various MnO_2 electrodeposition timings such as (a) 8 min, (b) 16 min, (c) 30 min and (d) 90 min at different scan rate in 1 M Na_2SO_4 electrolyte.

Figure IVC.10a-d display the CV curves of Au/MnO_2 with different MnO_2 electrodeposition times varying from 8 min to 90 min. Galvanostatic charge-discharge (CD) curves of Au/MnO_2(60 min) transparent supercapacitors were acquired between 0 - 0.8 V potential window with various current densities ranging from 0.015 to 0.175 mA cm^{-2} (Figure IVC.6f). CD curves are nearly triangular in shape confirming the formation of the electrochemical double layer and efficient charge propagation across the two electrodes. The areal capacitance of these devices was

calculated from both the discharging slope of CD curves (equation IVC.1) measured at various current densities (Figure IVC.6g) and from the CV curves (equation IVC.2) as a function of scan rate (Figure IVC.11) [22].

$$C_{areal} = I/[-(\Delta V/\Delta t)A] \ldots\ldots\ldots\ldots\ldots \text{(IVC.1)}$$

$$C_{areal} = I/s.A \ldots\ldots\ldots\ldots\ldots\ldots\ldots \text{(IVC.2)}$$

where C_{areal} is the areal capacitance, I is the current applied, $-(\Delta V/\Delta t)$ is the slope of the discharging curves after IR drop, A is the area of the device, s is the scan rate in mV s^{-1} (s= dV/dt). Figure IVC.6g displays the areal capacitance calculated from the charge-discharge curves. The highest areal capacitance of ~ 3 mF cm^{-2} was achieved at 0.005 mA cm^{-2} current density for Au/MnO_2(60 min) device. It preserves 56% of the areal capacitance when the current density increases from 0.005 to 0.175 mA cm^{-2}. The areal capacitance value was found to linearly increase with MnO_2 loading up to deposition of 60 min beyond which it began to decrease.

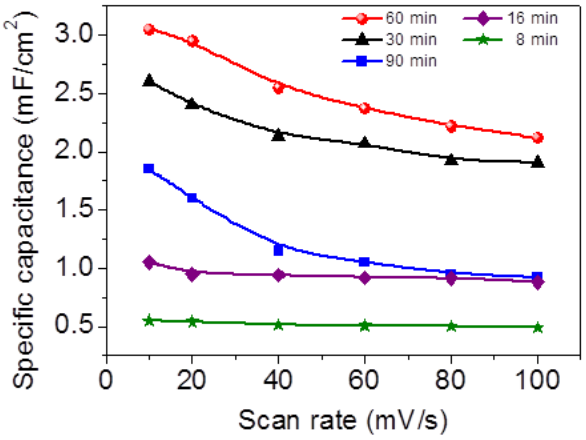

Figure IVC.11 Dependence of specific capacitance of Au/MnO_2 meshes with different MnO_2 loading on the CV scan rate.

Similar trend was observed for areal capacitance values calculated from the CV curves (Figure IVC.11). From Figure IVC.11, it has been noticed that with increasing the MnO_2 loading specific capacitance seems to increase up to 60 min and decreases further, probably because of the restricted movement of ions between current collector (Au) and active material (MnO_2).

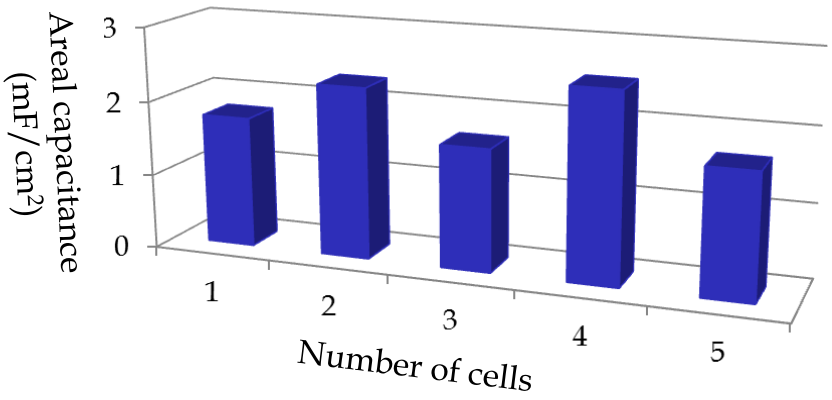

Figure IVC.12 Areal capacitance (at 100 mV s^{-1}) of 5 cells fabricated with 60 min electro-deposition.

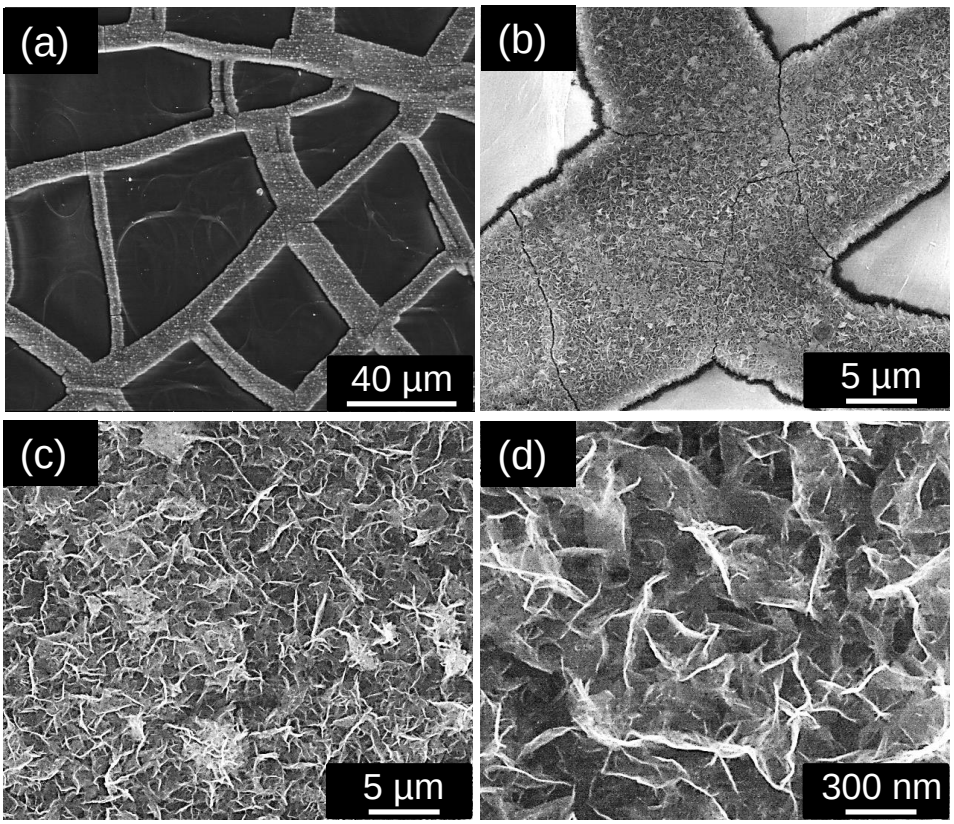

Figure IVC.13 High magnified SEM images of Au/MnO_2 on separator after 5000 cycles of charge-discharge test (a) - (d).

The areal capacitance of 1.98 ± 0.35 mF cm^{-2} (100 mV s^{-1}) was obtained from 5 cells fabricated with 60 min electrodeposition (see Figure IVC.12), evidencing the

reproducibility of obtained results. The supercapacitor device (Au/MnO_2(60 min)) shows less than 5% degradation in performance after testing for 5000 charge-discharge cycles (Figure IVC.6h). Inset in Figure IVC.6h shows the CD profile at a current density of 0.175 mA cm^{-2}. Even after 5000 cycling test, no change in the morphology of Au/MnO_2 network was observable (see Figure IVC.13).

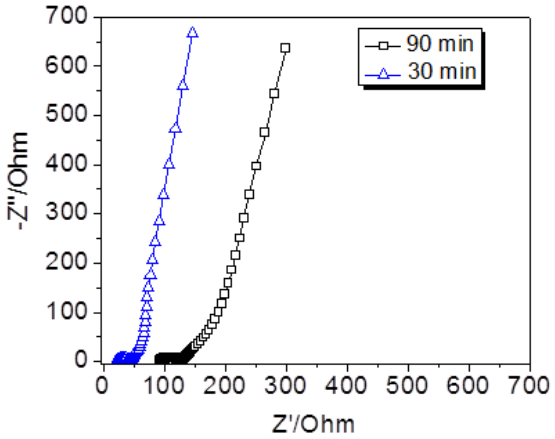

Figure IVC.14 Nyquist plot of Au/MnO_2 meshes with 30 min and 90 min of MnO_2 deposition showing ESR of 23 Ω and 96 Ω, respectively.

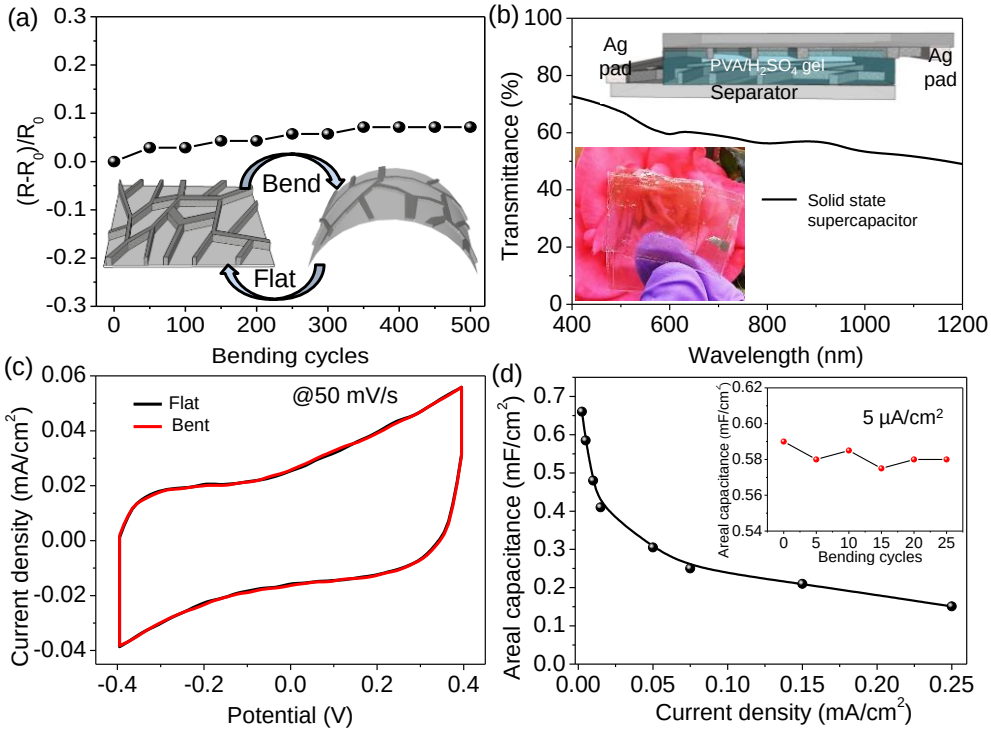

Figure IVC.15 (a) Relative change in resistance of Au/MnO_2(60 min) electrode while bent to 2.5 mm bending radius. (b) Transmittance spectrum of cross assembled solid-state

supercapacitor device. Schematic of electrode alignment (top) and the photograph of the device (bottom) are shown in the inset. (c) CV curves of Au-MnO_2(60 min) solid state supercapacitor with PVA/H_2SO_4 gel electrolyte in flat and while bent to 2.5 mm radius. (d) Areal capacitance as a function of current densities and inset is a change in areal capacitance as a function of bending cycles.

Electrochemical impedance spectroscopy (EIS) (Figure IVC.6i and Figure IVC.14) has been used as a powerful tool to understand the fundamental behaviour at the electrode-electrolyte interface. Figure IVC.6i shows the Nyquist impedance plot of Au/MnO_2(60 min), in the frequency range, 10^{-2} to 10^6 Hz with the fitted equivalent circuit in the inset. The nearly vertical shape at low frequencies is indicative of the capacitive behaviour of the device and the estimated R_S is 34.3 Ω denoted from the intersection point on the real axis. Such low series resistance owes much to the highly conducting Au mesh as well as effective charge transfer between Au and MnO_2.

Besides being highly transparent and conducting, Au/MnO_2 electrodes exhibit high flexibility and stability towards bending. Figure IVC.15a shows the normalized resistance of Au/MnO_2(60 min) as a function of bending cycles. The bending test was performed using a custom designed setup in which one side was kept movable using a screw gauge with the other end fixed. Even after few hundred bending cycles (bending radius, 2.5 mm), it showed only ~ 7% rise in electrode resistance.

Solid-state flexible supercapacitor was fabricated by sandwiching two Au/MnO_2(60 min) electrodes with PVA/H_2SO_4 gel electrolyte. The transmittance of an assembled device is nearly 64% at 550 nm (see inset in Figure IVC.15b), which is only ~ 7% less with the introduction of the electrolyte (see Figure IVC.6b). Furthermore, the device stability towards deformations (see Figure IVC.15c and d inset) is almost as good as bare electrodes shown in Figure IVC.15a. The electrochemical behaviour of the solid state device (Figure IVC.15c) is quite comparable to that of the aq. electrolyte device (Figure IVC.6d). However, the specific areal capacitance of the device seems to decrease faster with increasing current density values (Figure IVC.15d) which may be due to the restricted motion of ions in gel matrix.

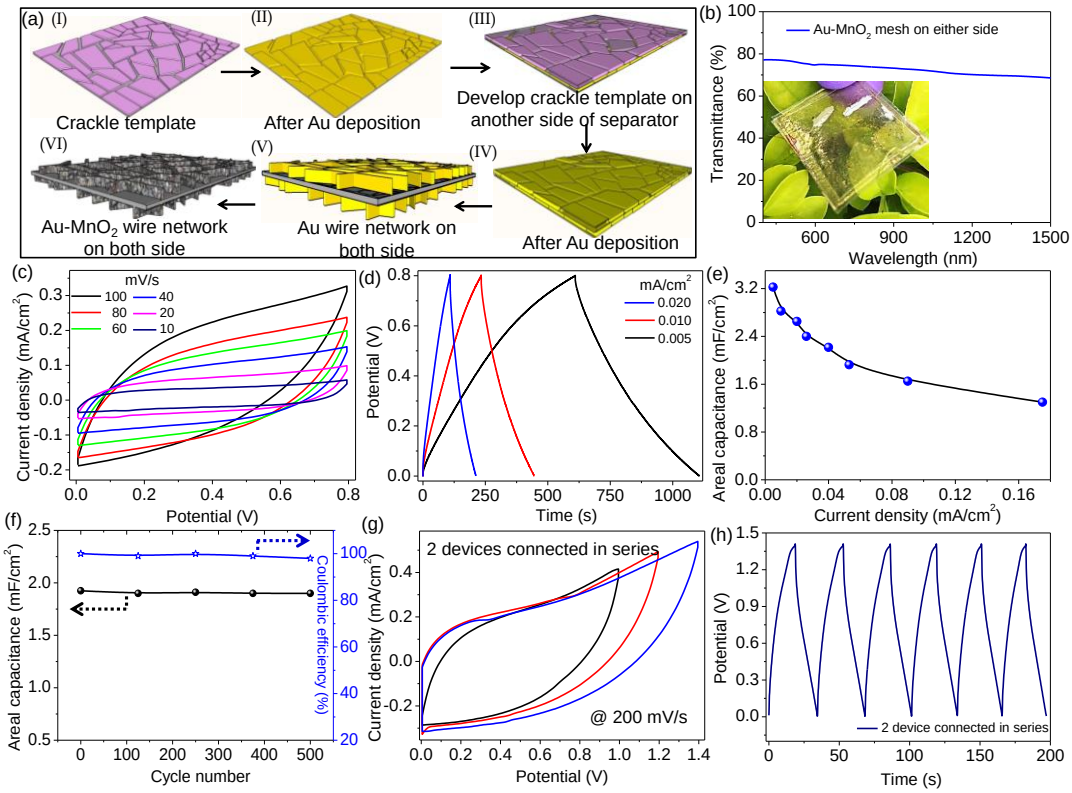

Figure IVC.16 (a) Schematic illustration of various steps to fabricate Au/MnO_2 on both side of the separator. (b) Transmittance spectrum of supercapacitor electrodes fabricated of both side of separator and inset is the photograph of the device. (c) CV curves at different scan rates and (d) CD curves of Au/MnO_2(60 min) at various discharge current densities. Dependence of areal capacitance on discharging current densities is shown in (e). (f) Cycle stability and coulombic efficiency of supercapacitor at a current density of 0.05 mA cm^{-2}. (g) CV curves of two devices connected in series at scan rate of 200 mVs^{-1}. (h) CD curves of two series connected devices at 0.27 mA cm^{-2}.

In order to achieve light weight supercapacitors with no loss in capacitance and transmittance, fabrication of Au/MnO_2 (optimized 60 min deposition) on both sides of a separator was executed. Figure IVC.16a (i-iv) schematically shows the fabrication process of Au/MnO_2(60 min) . Initially, crackle template was created on a separator (i) followed by Au deposition (ii). These process steps were repeated on another side of the separator as well (iii and iv). The Au wire networks obtained after the removal of the templates were taken further for MnO_2 deposition on both sides, in consecutive steps. Here, a separator membrane besides being a substrate to hold Au/MnO_2 on both sides, it is acting as the electrical insulator between two electrodes while

simultaneously allowing ion diffusion across the membrane. Thus fabricated device is highly transparent (78%) and flexible. The clear visibility of the plant beneath the electrode illustrates its transmittance (inset of Figure IVC.16b). The electrochemical property and resistive behaviour of the fabricated devices were examined by CV, CD, and EIS measurements. The CV curves were measured with different scan rates in the range of 10 - 100 mV s^{-1} as shown in Figure IVC.16c. The galvanostatic CD curves at various current densities are presented in Figure IVC.16d. Typical triangular shape of these CD curves with high symmetry indicating the high reversibility and high coulombic efficiency of these electrodes. The areal capacitance was calculated from CD curve measured from the slope of discharge curve (Figure IVC.16e). The maximum areal capacitance of 3.23 mF cm^{-2} was obtained at a current density of 0.005 mA cm^{-2}. As a comparison, areal capacitance calculated from two separate electrode configuration (Figure IVC.6g) was plotted with device developed on both side of the separator in Figure IVC.17. Capacitance values retained almost same in both configurations except the slight differences at higher current densities (Figure IVC.17). Furthermore, these transparent supercapacitors exhibited high stability as their areal capacitance and coulombic efficiency (ratio of discharging and charging times) did not change over 500 cycles of charge-discharge at 0.05 mA cm^{-2} (Figure IVC.16f). Finally, to demonstrate the potential of Au/MnO_2 based transparent supercapacitor, two devices were connected in series and examined their CV and CD performances. A CV scan and CD curves clearly show that the potential window of the device was extended up to 1.4 V (Figure IVC.16g and h).

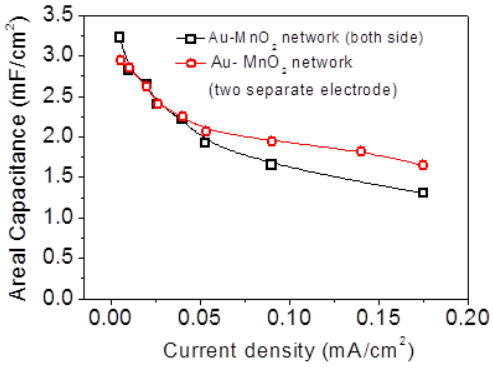

Figure IVC.17 Dependence of specific capacitance of Au/MnO_2 (60 min) networks on the discharging current density for both side and two separate electrode configurations.

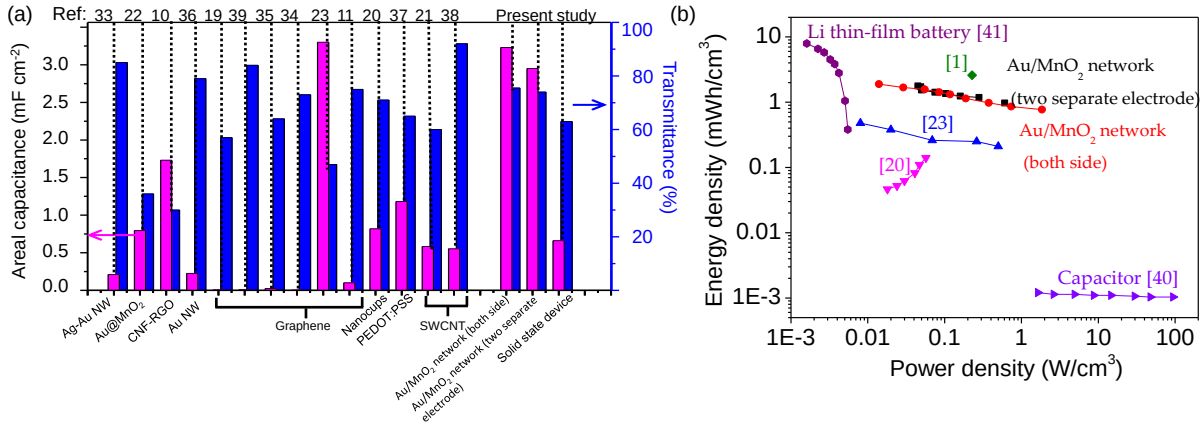

Figure IVC.18 (a) Comparing the areal capacitance and transparency (at 550 nm) of present devices with recent transparent supercapacitor devices. (b) Ragone plot comparing the volumetric energy and power densities of devices fabricated in this study with other transparent supercapacitors [1,20,23], thin-film batteries [41] and capacitors [40] from the literature.

The transparency and electrochemical performance of the present supercapacitors are compared with literature data in Figure IVC.18a. It is important to note that the current device besides providing higher transmittance offers higher capacitance as well when compared to literature values (Figure IVC.18a and Table IVC.1) [10,11,19-23,33-39]. The energy storage properties of transparent supercapacitor have been evaluated through Ragone plot, in which volumetric energy density was plotted versus power density (Figure IVC.18b). These values were obtained by using the following equations (IVC.3 and 4) [23].

$$E = (\tfrac{1}{2} \times C \times (\Delta V)^2)/ 3600 \ldots\ldots\ldots\ldots \text{(IVC.3)}$$

$$P = (E/\Delta t) \times 3600 \ldots\ldots\ldots\ldots\ldots\ldots \text{(IVC.4)}$$

where E is the energy density (Wh cm^{-3}), C is the volumetric areal capacitance (F cm^{-3}), ΔV is the discharge voltage range (V), P is the power density (W cm^{-3}) and Δt is the discharge time (s). The data from the present study is compared with high-power electrolytic capacitor (3V/300 μF) [40], thin-film lithium ion batteries[41] and transparent supercapacitors from literature [1,20,23] as shown in the Ragone plot (Figure IVC.18b). In comparison to two electrodes separated by separator, the

electrode on both side of the separator has shown slightly higher values. The obtained density values are an order of magnitude higher than that of the transparent carbon film based supercapacitors [20]. Particularly, the obtained energy and power densities of transparent supercapacitor fabricated in this study are highly comparable with those of other transparent supercapacitors [1,20,23]and Li thin-film batteries [41].

Table IVC.1. Transparency and areal capacitance comparison of devices fabricated in this work with various transparent supercapacitors reported in the literature.

Material	Transmittance at 550 nm (%)	Areal capacitance (mF/cm^2)	Reference
Ag-Au NW	~ 85	0.21	[33]
Au@MnO_2	36	0.76	[22]
CNF-RGO	30	1.73	[10]
Au NW	79	0.23	[36]
Graphene	57	0.006	[19]
Graphene	84	0.008	[39]
Graphene	64	0.025	[35]
Graphene	73	0.005	[34]
Graphene	~47	3.3	[23]
Graphene	~75	0.101	[11]
Nanocups	71	0.818	[20]
PEDOT:PSS	65	1.18	[37]
SWCNT	60	0.584	[21]
SWCNT	92	0.552	[38]
Au/MnO_2 network (both side)	75.5	3.2	This work
Au/MnO_2 network (two separate electrode)	74	3.0	This work
Solid-state device	63	0.660	This work

In this study although Au metal is expensive, it was chosen as current collecting electrode mainly due to its stability towards electrochemical environment where metals such as Ag, Cu, etc. fail. As regards MnO_2, abundance, low-cost, environmental

benignity as well as high theoretical capacitance (1370 F g^{-1}) makes it ideal for pseudocapacitive active material. A supercapacitor separator itself was used as substrate because it is transparent, flexible, thin light-weight, porous and furthermore it is highly stable towards mesh fabrication processes. Furthermore, electrodeposition of MnO_2 on Au mesh transparent current collector not only retains the transparency but also improves its contact resistance. It may be noted that the Au/MnO_2 meshes are highly transparent even in the near-IR regions (Figure IVC.6b), unlike ITO or oxide based devices where electrodes are effectively transparent only in visible region due to electronic absorption of oxides [4].

IVC.5 Conclusions

In conclusion, highly transparent and flexible supercapacitors employing metal network structure have been fabricated. A core-shell network of Au/MnO_2 with high transmittance was fabricated through the crackle template process developed in this laboratory followed by electrodeposition technique. Using the novel approach of fabricating the electrodes on the separator itself, the interaction of electrolyte with active material (MnO_2) was improved which further enhanced the storage capacity along with cycling stability. The resulting supercapacitor yielded the areal capacitance of ~ 3 mF cm^{-2} with nearly 75% transmittance at 550 nm. The obtained values are highly comparable with transparent supercapacitors devices fabricated in the recent literature. Further investigation revealed that both the electrodes can be fabricated on either sides of a separator with no loss in transmittance and capacitance. In addition, fabrication cost of the device could be reduced further by using Ag/Au core-shell mesh structures. These fabrication methods can be generalized for the production of large area transparent devices with networked metal or material of one's desire.

References

1. ZS. Wu, K. Parvez, X. Feng, K. Müllen, *Nat. Commun.,* 2013,**4**, 2487.

2. R. Yuksel, Z. Sarioba, A. Cirpan, P. Hiralal, H. E. Unalan, *ACS Appl. Mater. Interfaces,* 2014, **6,** 15434.

3. C. Liu, L. Feng, Ma. Lai-Peng, C. Hui-Ming, *Adv. Mater.,*2010, **22**.

4. Y. Hu, H. Zhu, J. Wang, Z. Chen, *J. Alloys Compd.,* 2011, **509**, 10234**.**

5. P. Tang, L. Han, L. Zhang, *ACS Appl. Mater. Interfaces,* 2014, **6,** 10506.

6. S. Li, D. Huang, B. Zhang, X. Xu, M. Wang, G. Yang, Y. Shen, *Adv. Energy Mater.,*2014, **4**.

7. L. Hu, H. Wu, Y. Cui, *Appl. Phys. Lett.,* 2010, **96**, 183502.

8. S. Hu, R. Rajamani, X. Yu, *Appl. Phys. Lett.,* 2012, **100**, 104103.

9. G. Zheng, L. Hu, H. Wu, X. Xie, Y. Cui, *Energy Environ. Sci,* 2011, **4**, 3368.

10. K. Gao, Z. Shao, X. Wu, X. Wang, Y. Zhang, W. Wang, F. Wang, *Nanoscale,*2013, **5**, 5307.

11. K. Jo, S. Lee, S. M. Kim, JB. In, S. M. Lee, JH. Kim, HJ. Lee, KS. Kim, *Chem. Mater.,* 2015, **27,** 3621.

12. R. Gupta, KDM. Rao, GU. Kulkarni, *RSC Adv.,* 2015, **8**, 60.

13. G. Cai, P. Darmawan, M. Cui, J. Wang, J. Chen, S. Magdassi and P. S. Lee, *Adv. Energy Mater*., 2016, **6.**

14. D. S. Hecht, L. Hu, G. Irvin, *Adv. Mater.,* 2011*,* **23**, 1482.

15. G. U. Kulkarni, S. Kiruthika, R. Gupta, K. D. M. Rao, *Curr. Opin. Chem. Eng.,* 2015, **8**, 60.

16. T. Sannicolo, M. Lagrange, A. Cabos, C. Celle, J. P. Simonato, D. Bellet, *Small,* 2016, **12**,6052.

17. S. Ye, A. R. Rathmell, Z. Chen, I. E. Stewart, B. J. Wiley, *Adv. Mater.,* 2014,**26**,6670.

18. Z. Yin, J. Zhu, Q. He, X. Cao, C. Tan, H. Chen, Q. Yan, H. Zhang, *Adv. Energy Mater.,* 2014,**4**.

19. T. Chen, Y. Xue, AK. Roy, L. Dai, *ACS Nano,* 2013, **8**,1039.

20. HY. Jung, MB. Karimi, MG. Hahm, PM. Ajayan, YJ. Jung, *Sci. Rep.,* 2012,**2**, 773.

21. Z. Niu, W. Zhou, J. Chen, G. Feng, H. Li, Y. Hu, W. Ma, H. Dong, J. Li, S. Xie, *Small,* 2013,**9**, 518.

22. T. Qiu, B. Luo, M. Giersig, E. M. Akinoglu, L. Hao, X. Wang, L. Shi, M. Jin, L. Zhi, *Small,* 2014, **10**, 4136.

23. N. Li, G. Yang, Y. Sun, H. Song, H. Cui, G. Yang, C. Wang, *Nano Letters,* 2015,**15**, 3195.

24. R. Gupta, KDM. Rao, K. Srivastava, A. Kumar, S. Kiruthika, GU. Kulkarni, *ACS Appl. Mater. Interfaces,* 2014, **6**, 13688.

25. S. Walia, R. Gupta, K. D. M. Rao and G. U. Kulkarni, *ACS Appl. Mater. Interfaces*, 2016, **8**, 23419.

26. C. Hunger, K. D. M. Rao, R. Gupta, C. R. Singh, G. U. Kulkarni and M. Thelakkat, *Energy Technology*, 2015, **3**, 638.

27. KDM. Rao, R. Gupta, GU. Kulkarni, *Adv. Mater. Interfaces,* 2014,**1**.

28. R. Gupta, KDM. Rao, S. Kiruthika, GU. Kulkarni, *ACS Appl. Mater. Interfaces,* 2016, 8, 23419.

29. K. D. M. Rao, C. Hunger, R. Gupta, G. U. Kulkarni and M. Thelakkat, *Phys. Chem. Chem. Phys*, 2014, **16**, 15107.

30. KDM. Rao, GU. Kulkarni, *Nanoscale,* 2014, **6**, 5645.

31. RB. Rakhi, W. Chen, D. Cha, HN. Alshareef, *Adv. Energy Mater.,* 2012, **2**, 381.

32. P. Lv, P. Zhang, Y. Feng, Y. Li, W. Feng, *Electrochim. Acta.,*2012,**78**, 515.

33. H. Lee, S. Hong, J. Lee, YD. Suh, J. Kwon, H. Moon, H. Kim, J. Yeo, SH. Ko, *ACS Appl. Mater. Interfaces,* 2016,**8**,18516.

34. P. Xu, J. Kang, JB. Choi, J. Suhr, J. Yu, F. Li, J. H. Byun, BS. Kim, TW. Chou, *ACS Nano,* 2014,**8**, 9437.

35. Y. Gao, YS. Zhou, W. Xiong, LJ. Jiang, M. Mahjouri-samani, P. Thirugnanam, X. Huang, MM. Wang, L. Jiang, YF. Lu, *APL Mat.,* 2013,**1**,012101.

36. S. Gong, Y. Zhao, Q. Shi, Y. Wang, L. W. Yap, W. Cheng, *Electroanalysis,*2013,**1**,012101.

37. T. Cheng, YZ. Zhang, JD. Zhang, WY. Lai, W. Huang, *J. Mater. Chem. A.,* 2016,**4**, 10493.

38. K. Petri, L. Nguyen Dang, S. Le Hoang, VA. Ilya, T. Alexey, Sl. Jukka, GN. Albert, K. Tanja, *Nanotechnology*, **27**, 235403.

39. X. Fan, T. Chen, L. Dai, *RSC Adv.,* 2014,**4**, 36996.

40. MF. El-Kady, V. Strong, S. Dubin, RB. Kaner, *Science,* 2012, **335**, 1326.

41. D. Pech, M. Brunet, H. Durou, P. Huang, V. Mochalin, Y. Gogotsi, PL. Taberna, P. Simon, *Nat. Nano,* 2010, **5**, 651.

Chapter IVD

Smart Electrochromic Supercapacitors

Summary

In this chapter, the design and fabrication of a smart electrochromic supercapacitor employing novel Au mesh and polyaniline (PANI) electrodes are reported. The Au mesh was obtained through crackle templating method whereas PANI was brought in by electrodeposition process. The device exhibited a high capacitance of ~ 15 mF cm^{-2} with good charge-discharge cycling stability. What is attractive about this device is that it could switch its color rapidly yellow, green or blue with increasing applied voltages which also serves to indicate the level of energy stored in the supercapacitor visually.

IVD.1 Introduction

Supercapacitors as energy storage devices are highly promising due to its long cycle life, stability, high energy and power densities [1, 2]. Incorporating additional novel features such as flexibility, wearability, energy level indicators, etc. in the supercapacitors bring them closer to the realistic applications [3-6]. Supercapacitors combined with other functionalities are gaining much attention as the energy stored locally can be utilized in running proximal applications. For example, fiber-shaped supercapacitors have offered high output voltage even up to 1000 V which was successfully utilized to power an electronic watch and to lit series of light emitting diodes (LEDs) [7]. The same group has fabricated woven textile supercapacitors which can supply stand-by power to various electronic devices including wristbands, earphones, and mobile phones [4]. The capacitance of semiconducting material based supercapacitor has been enhanced by solar light illumination due to its photoconductivity. Furthermore, self-powered photodetector supercapacitor device was also demonstrated [8]. In this context, electrochromic supercapacitors have gained great attention due to its ability to indicate energy storage levels [9]. These intelligent and interactive features make the device functioning more convenient to the end users.

Paper based on this study: Submitted May 2017

Electrochromic or color changing devices are basically a light modulating device composed of an active material and electrodes. In order to illustrate the electrochemical energy storage and electrochromic switching in a device, the active material should satisfy certain demands such as high surface area, stable towards harsh electrolytes, light modulation upon applied voltage and so on [10]. Typically, carbon composites, transition metal oxides, and conducting polymers have been utilized as active storage materials for supercapacitors whereas organic dyes, conducting polymers and inorganic metal oxides have been used for electrochromic devices. Inorganic materials/metal oxides such as tungsten oxide, Prussian blue, nickel oxide and vanadium oxide and, organic conducting polymers like Poly(3,4-ethylenedioxythiophene) (PEDOT), polypyrrole (Ppy) and polyaniline (PANI) have been widely used as active materials for smart electrochromic supercapacitors [1, 5, 9, 10]. Unlike inorganic materials, which are brittle and difficult to coat uniformly over a large area, conducting polymers form smooth thin films. Conducting organic polymers were widely known for its color modulation in response to various external stimuli such as the ion/ligand interaction, solvent, pH and so on. Due to its high theoretical capacitance, low cost, ease of synthesis and high stability towards deformations, PANI is recognised as the precise active material for the flexible electrochromic supercapacitor device. While using as active material, PANI stores charge via redox reactions due to its transition between various oxidation states.

IVD.2 Scope of the present investigation

For the fabrication of electrochromic displays, apart from the active electrochromic material, another vitally important component used is the transparent conducting electrode which serves as a current collector. In general, highly expensive ITO based transparent electrodes are used as current collector [11]. Recently, carbon nanowire networks, metal grids, organic polymer based alternative electrodes etc. have been used to replace ITO in such devices [5, 9, 12,13]. In the past couple of years, metal wire network based electrodes developed from crackle lithography process, with good optoelectronic properties has emerged as a potential candidate for replacing ITO in various functional devices including high temperature joule heaters [14], solar cells [15], capacitors [16], hydrogen sensors [17], etc. Wei et

al have fabricated an energy storage smart window with PEDOT:PSS and PANI as TCE and active materials respectively, and shown its efficacy as the smart window [6]. In another study, aligned CNT sheet served as TCE for smart supercapacitors [3]. In the light of above discussion, the performance of metal network electrodes replacing the expensive ITO as TCE for electrochromic supercapacitors with cost effective PANI active material is investigated in this study.

IVD.3 Experimental Details

Fabrication of Au mesh

The Au mesh fabrication process involves three simple steps. Initially, an acrylic resin based precursor (0.6 g/mL, Ming Ni Cosmetics Co., Guangzhou, China) was spin coated over a pre-cleaned and dried separator substrate (BOPP films from Mirwec Film, Inc) to create a crackle template. Depositing Au over the template through physical evaporation process, followed by removal of the template yields highly interconnected Au wire mesh on the separator substrate.

Electrodeposition of PANI

PANI was electrodeposited over Au mesh (working electrode) with Pt wire and Ag/AgCl as counter and the reference electrode, respectively. Aniline (0.1 M) was polymerized using 1 M HCl. At a potential of 0.8 V for 1 min (at ambient temperature) versus reference electrode, PANI seed layer was formed. The growth of the nanowire was continued with a constant current density of 2 mA/cm^2. Electrochemical measurements were performed with 1 M H_2SO_4 and PVA/H_2SO_4 gel electrolytes.

Fabrication of solid-state supercapacitor

The PVA/H_2SO_4 gel was used as an electrolyte as well as a spacer between two Au/PANI electrodes. The gel electrolyte was prepared by dissolving 1 g of H_2SO_4 and 1 g PVA in 10 mL of DI water at 80 °C under vigorous stirring till it dissolves completely to form a clear solution.

IVD.4 Results and Discussion

Figure IVD.1 illustrates the procedure for the fabrication of Au-PANI mesh electrode. The Au mesh was fabricated through crackle templating method as discussed in earlier chapters. It is a simple three-step process involving the spin

coating of commercially available crackle precursor followed by metal deposition and crackle template lift-off.

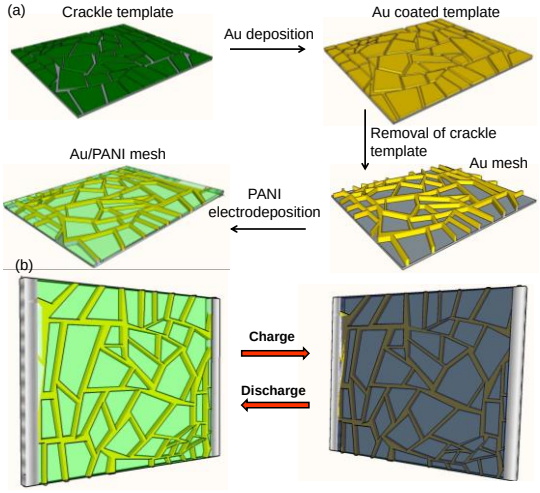

Figure IVD.1 Schematics for Au/PANI mesh fabrication process (a) and a working principle of an energy storage smart supercapacitors (b).

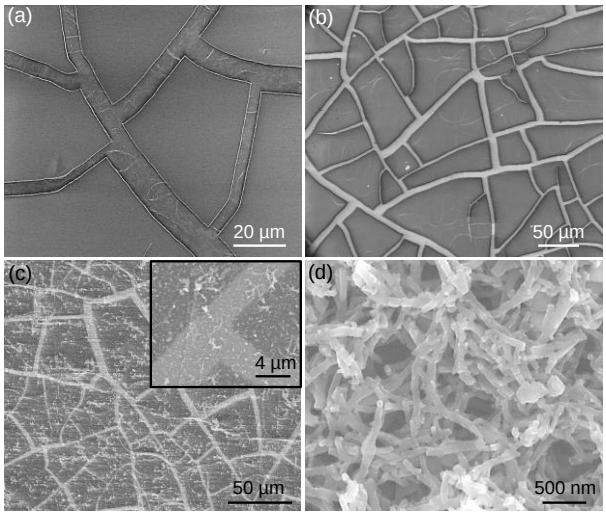

Figure IVD.2 Schematics for Au/PANI mesh fabrication process (a) and a working principle of an energy storage smart supercapacitors (b).

This templating method is highly versatile and can be created on any chosen substrate. In this study, crackle template was fabricated on BOPP film, which is commonly used as separator substrate. The advantages are it is transparent, flexible and light-weight. After spin-coating the crackle precursor of optimized concentration on the substrate [14], it was allowed to dry to form the highly

interconnected crackles (down to substrate) which serve as the template for metal deposition (Figure IVD.2a). In order to gain high stability towards electrochemical oxidation and reduction environment, Au (~ 150 nm) has been chosen to deposit in the crackle grooves followed by rinsing the samples in chloroform solution to remove crackle precursors. Thus obtained Au wire network is highly interconnected (see Figure IVD.2b) with a transparency of ~ 82% and a sheet resistance of ~ 8 Ω/sq. The uniform growth of PANI nanowires over Au mesh was obtained by electrodeposition technique which is evidenced from the visible change in color of the electrode from colorless to light green (Figure IVD.1a). While serving as a potential electrode for supercapacitor and electrochromism, PANI changes its color between the green oxidized state (emeraldine), the light yellow reduced state (leucoemeraldine) and completely oxidized blue state (pernigraniline). Although the morphology of PANI is confined to nanofibers or nanogranulars by electro polymerization technique, it is a much faster process and free from additives and oxidants. The growth of PANI nanowires over Au mesh was further confirmed from SEM images (Figure IVD.2c). The magnified view of PANI growth over mesh is shown as an inset in Figure IVD.2c. The PANI nanowires are typically in the range of 100 – 120 nm in diameter (Figure IVD.2d).

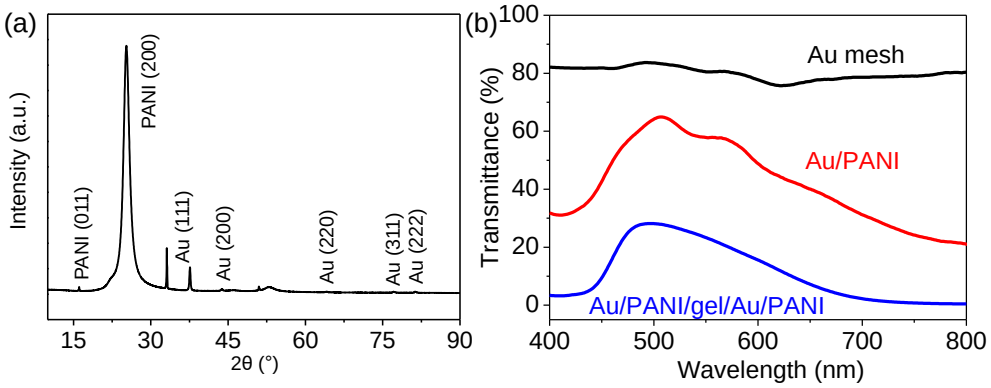

Figure IVD.3 (a) XRD pattern of Au/PANI. (b) The optical spectra of Au mesh, Au mesh/PANI, and the device.

The crystal structure and optical properties of the Au-PANI mesh electrodes were characterized by X-ray diffraction pattern (XRD) and UV-vis spectroscopy. As shown in Figure IVD.3a, there is essentially an intense peak at 2θ = 25.8° corresponding to

(200) crystal planes of PANI indicating the single phase nature of PANI nanowires. Moreover, the diffraction intensity of Au mesh is much lower than PANI peaks. The Au mesh exhibited an optical transmittance of ~ 80% at the wavelength of 550 nm whereas the transmittance of Au mesh coated with PANI has reduced to 60% due to the deposition of PANI in the voids between the meshes. The light transmittance of the device comprising of Au/PANI//gel electrolyte//Au/PANI has further dropped down to ~ 23% as seen in Figure IVD.3b.

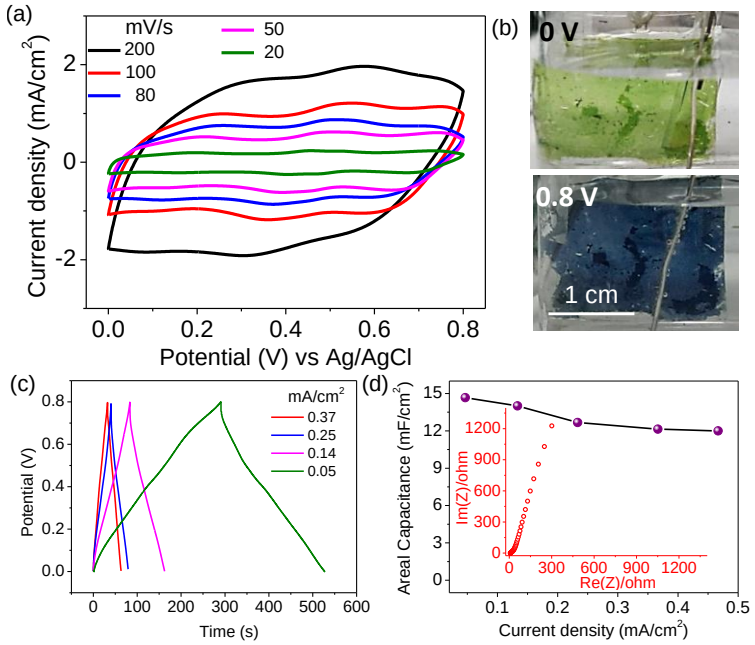

Figure IVD.4 (a) Cyclic voltammogram (CV) curves of Au mesh/PANI tested in aqueous three electrode configuration at different scan rates. (b) The photographs the change in color of supercapacitor under different charging conditions such as discharged (green state) fully charged (blue state). (c) Charge-discharge (CD) profiles of the sample at different current densities. (d) The areal capacitance of supercapacitor based on Au/PANI electrodes at different current densities. Inset is the Nyquist plot.

The energy storing capability of fabricated electrodes was electrochemically characterized in detail. Figure IVD.4a shows typical CV curves of PANI nanofibers grown on Au mesh in 1 M H_2SO_4 aqueous electrolyte at various scan rates ranging from 20 to 200 mV s^{-1} between voltage windows of 0 to 0.8 V. As shown in the CV curve, the device showed two pairs of redox peaks corresponding to the transformation of PANI from leucoemeraldine to emeraldine and emeraldine to

pernigraniline, typically indicating the pseudocapacitive nature of the active electrode material (PANI) [5]. Photographs of the device under different potentials are shown in Figure IVD.4b. When the device was charged to 0.8 V, the electrode color changed from green (discharged) to blue. It is to be noted that the color intensity of the device at charging and discharging states could be controlled by modulating the PANI deposition duration. However, it was observed that the 400 s deposition is optimal for both optical modulations and capacitance. Galvanostatic charge-discharge profiles of PANI supercapacitor at different current densities are shown in Figure IVD.4c. The near-linear CD slopes are indicating the high reversibility of charging and discharging processes of the supercapacitor device. Furthermore, the shapes of the CD curves are maintained for various current densities implying the sustainability of the device for the broad range of current densities. The charge storing capability of the device was evaluated using areal units (mF cm^{-2}) both from CV and CD curves, as the active material weight was negligible. Using the equation C = I/A.s (I is the current, A is the area of the electrode and s is the scan rate), the areal capacitance was calculated from CV curves. The capacitance was gradually reduced from 12 to 9 mF cm^{-2} with the increasing scan rate (20 – 200 mV s^{-1}). Even at a fast scan rate (200 mV s^{-1}), nearly 75% of the capacitance was retained. These values are highly comparable with supercapacitors fabricated with Ag nanowires (TCE) and WO_3 hybrid active material (13 mF cm^{-2} at 10 mV s^{-1}) [12]. The areal capacitance can also be calculated from CD curves as well using the equation C = (I.Δt/ΔV.A) (where I is the discharge current, Δt is the discharge time, ΔV is the voltage window and A is the area of the electrode). At lower current density (0.05 mA cm^{-2}), the device could deliver an areal capacitance of ~ 15 mF cm^{-2} whereas at the higher current density (0.5 mF cm^{-2}), it decreases to 12 mF cm^{-2}. Although this decrease in capacitance with increasing current density is common, the relatively flat plateau in the capacitance plot is achieved with just 20% loss in capacitance (Figure IVD.4d). The fundamental behaviour of supercapacitor has been analysed through electrochemical impedance spectroscopy (EIS). The impedance of the device was measured in the frequency range of 0.01 Hz to 1 MHz with an AC perturbation of 10 mV at the open circuit voltage (inset in Figure IVD.4d). The straight line almost parallel to imaginary axis

indicates the capacitive behaviour of the device. The intercept at real part (x axis) in the high-frequency region is about 8 Ω which refers to the combination of internal resistance of electrode, electrolyte and its interface. This resistance value is quite low comparable to other PANI -based electrochemical supercapacitors manifesting the low resistance of the electrode and high ionic conductivity of the electrolyte in this device.

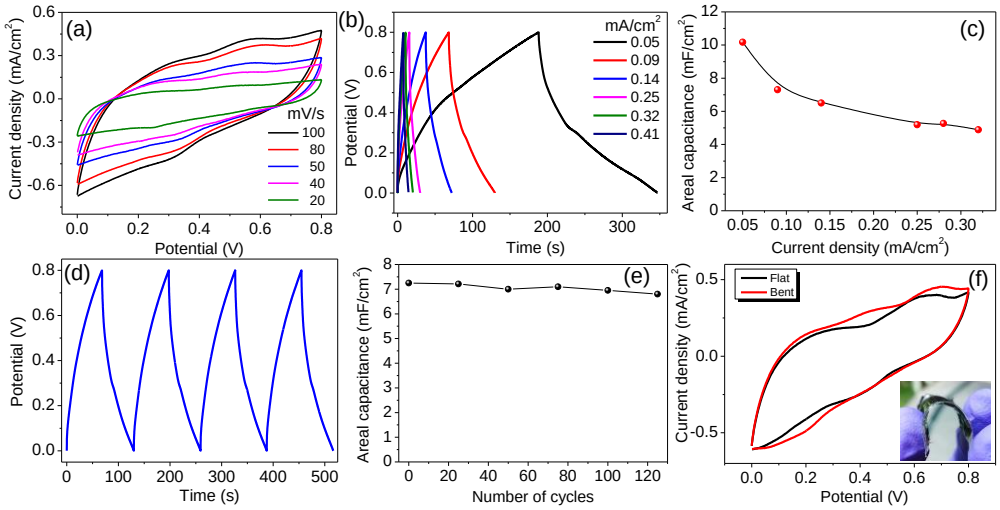

Figure IVD.5 CV and CD curves of Au/PANI supercapacitor fabricated on separator substrate with gel electrolyte in between two electrodes at different scan rates and current densities are shown in (a) and (b), respectively. (c) Areal capacitance at different current density. (d) CD profile of few cycles with 0.09 mA cm^{-2}. (e) Cycling performance of two electrode device with 0.09 mA cm^{-2} current density. (f) CV curves of the device in normal and bent state at a scan rate of 100 mV s^{-1}. Inset is an illustration of the bending test.

Symmetrical supercapacitor composed of Au/PANI on separator substrate was fabricated and their electrochemical characteristics in a PVA/H_2SO_4 gel electrolyte were investigated. Gel electrolyte has been used to replace aqueous electrolyte for the fabrication of solid-state supercapacitors. Cyclic voltammogram gives information about the redox response of PANI on both the electrodes. The CV curves of the two electrode device collected at various scan rates are shown in Figure IVD.5a. As expected, the current density increases with increase in sweep rates ranging from 20 – 100 mV s^{-1}. The reversible Faradaic reactions on electrode surface have been observed from redox peaks in CV. Two pairs of redox peaks indicate the transition of

PANI to different phases at different applied potentials. The areal capacitance calculated from CV curves varies from 7 – 5 mF cm^{-2} for 20 -100 mV s^{-1} scan rates. The capacitance values of the current device are similar to the capacitance obtained from PEDOT:PSS/PANI device [9]. Galvanostatic charge-discharge profiles of Au/PANI electrodes with gel electrolyte at different current densities are shown in Figure IVD.5b. The non-linearity in discharging profiles indicates the energy storage contribution from pseudocapacitance nature of PANI. Figure IVD.5c shows the areal capacitance calculation from the discharge profiles. At low current density (0.05 mA cm^{-2}), areal capacitance of the device is ~ 10 mF cm^{-2} whereas the capacitance dropped to ~ 5 mF cm^{-2} for higher current density (0.25 mA cm^{-2}). The charge-discharge cycling stability of device was tested for long life stability (Figure IVD.5d). There is only negligible loss in capacitance after 125 cycles at 0.09 mA cm^{-2} (Figure IVD.5e). As for the flexibility of the device is concerned, the electrochemical performance of the device under bent state was evaluated by bending to 5 mm radius. Figure IVD.5f represents the CV curves of the device under flat and bent state. In comparison to the flat device, the bent device has shown better performance, may be due to increased area of interaction between the electrode and electrolyte.

IVD.5 Conclusions

Electrochromic supercapacitors with Au mesh and polyaniline were fabricated by a simple crackle template method and electrodeposition process, respectively. Electrochemical investigations clearly indicated that as-prepared device showed excellent capacitance (~ 15 mF cm^{-2}) with high cycling capability. Furthermore, the color of the device changed from green to blue while charging and it reverts to green color while discharged. This smart electrochromic supercapacitor which shows the reversible change in color of the device is highly helpful for visual modnitoring of energy storage level. This design strategy can be extended to various device fabrications.

References

1. K. Gopalakrishnan, S. Sultan, A. Govindaraj, C.N.R. Rao, Supercapacitors based on composites of PANI with nanosheets of nitrogen-doped RGO, $BC_{1.5}N$, MoS_2 and WS_2, *Nano Energy,* **12**, 52-8.

2. N. Kurra, S. Kiruthika, G.U Kulkarni, Solution processed sun baked electrode material for flexible supercapacitors, *RSC Advances*, **4(39)**, 20281-9.

3. X. Chen, H. Lin, P. Chen, G. Guan, J. Deng, H. Peng, Smart Stretchable Supercapacitors, *Advanced Materials*, **26(26)**, 4444-9.

4. H. Sun, S. Xie, Y. Li, Y. Jiang, X. Sun, B. Wang, *et al*., Large-Area Supercapacitor Textiles with Novel Hierarchical Conducting Structures, *Advanced Materials*, **28(38)**, 8431-8.

5. Y. Tian, S. Cong, W. Su, H. Chen, Q. Li, F. Geng, *et al*., Synergy of $W_{18}O_{49}$ and Polyaniline for Smart Supercapacitor Electrode Integrated with Energy Level Indicating Functionality, *Nano Letters*, **14(4)**, 2150-6.

6. D. Wei, MRJ. Scherer, C. Bower, P. Andrew, T. RyhÃonen, U. Steiner, A Nanostructured Electrochromic Supercapacitor, *Nano Letters*, **12(4)**, 1857-62.

7. H. Sun, X. Fu, S. Xie, Y. Jiang, H. Peng, Electrochemical Capacitors with High Output Voltages that Mimic Electric Eels, *Advanced Materials*, **28(10)**, 2070-6.

8. M. Zhu, Y. Huang, Y. Huang, Z. Pei, Q. Xue, H. Li, *et al*., Capacitance Enhancement in a Semiconductor Nanostructure-Based Supercapacitor by Solar Light and a Self-Powered Supercapacitor–Photodetector System, *Advanced Functional Materials*, **26(25)**, 4481-90.

9. K. Wang, H. Wu, Y. Meng, Y. Zhang, Z. Wei, Integrated energy storage and electrochromic function in one flexible device: an energy storage smart window, *Energy & Environmental Science*, **5(8)**,8384-9.

10. G. Cai, X. Wang, M. Cui, P. Darmawan, J. Wang, AL-S. Eh, *et al*., Electrochromo supercapacitor based on direct growth of NiO nanoparticles, *Nano Energy*, **12**, 258-67.

11. G.U. Kulkarni, S. Kiruthika, R. Gupta, K.D.M Rao, Towards low cost materials and methods for transparent electrodes, *Current Opinion in Chemical Engineering*, **8**, 60-8.

12. L. Shen, L. Du, S. Tan, Z. Zang, C. Zhao, W. Mai, Flexible electrochromic supercapacitor hybrid electrodes based on tungsten oxide films and silver nanowires, *Chemical Communications*, **52(37)**, 6296-9.

13. An. CalifÃrnia, AS. Silva, J. GonÃ§alves, A. Branco, C. Pinheiro, Cu. Costa. Silver grid electrodes for faster switching ITO free electrochromic devices. *Solar Energy Materials and Solar Cells*, **153**, 61-7.

14. K.D.M. Rao, G.U Kulkarni. A highly crystalline single Au wire network as a high temperature transparent heater, *Nanoscale*, **6(11)**, 5645-51.

15. K.D.M. Rao, C. Hunger, R. Gupta, G.U. Kulkarni, M. Thelakkat. A cracked polymer templated metal network as a transparent conducting electrode for ITO-free organic solar cells, *Physical Chemistry Chemical Physics*, **16(29)**, 15107-10.

16. R. Gupta, K.D.M Rao, G.U. Kulkarni. Transparent and flexible capacitor fabricated using a metal wire network as a transparent conducting electrode, *RSC Advances*, **4(59)**, 31108-12.

17. Sunil Walia, Ritu Gupta, K.D.M. Rao, G.U. Kulkarni. Transparent Pd Wire Network based Areal Hydrogen Sensor with Inherent Joule Heater, *ACS Appl. Mater. Interfaces,* 2016, **8 (35)**, 23419–23424.

Chapter IVE
A smart window based UV-photodetector

Summary

Transparent electronics as a futuristic technology are fast growing and expanding beyond conventional optoelectronics. The fabrication of a large area, visibly transparent ultraviolet (UV) photodetector employing a laser deposited ZnO active layer in between branched Au wire networks was reported, with the latter serving as electrodes due to being transparent in UV as well as visible regions. The Au wire networks were prepared using a crack templating method which is not only cost effective but also enables heterostructuring with simple processes. When compared to Ag contact pads, these wire network electrodes seem to enhance photocurrent collection efficiency resulting in high UV sensitivity at low response times. Importantly, the visible light transparency was as high as 80%.

IVE.1 Introduction

Emerging transparent functional devices such as organic light-emitting diodes [1], thin film loudspeakers [2], capacitors [3], batteries [4], solar cells [5], etc. have paved the way for next generation "see-through" devices. Transparent devices have become increasingly attractive due to their high impact in various areas such as displays, sensors, photodetectors, etc [6,7]. Transparency is not just meant for visual appeal but also to gain crucial visual space, in much the same way that glass partitions do in lieu of opaque walls. Taking photodetectors as an example, a "visible blind" photodetector will have an extended practical usage when combined with the variety of devices which require exposure to visible light [8]. In this work, the fabrication of a transparent UV detector was explored.

UV photodetectors play important roles in day-to-day lives, from pollution monitoring to water purification [9–11]. Most commercially available photodetectors are based on semiconducting materials such as Si, GaN, InGaAs, etc. which are opaque and brittle, thus restricting their possible usage in flexible transparent detectors [12]. Further, such conventional detectors possess an active area of ~1 mm^2, which serves

Paper based on this study: RSC Adv., 2016, 6, 44668

essentially as a point detector. On the other hand, for large area detection, the active material should be relatively inexpensive yet maintain higher efficiencies. In other words, the material should be optically transparent with high photoconductivity in the UV region. In this direction, a few attempts have been made in recent literature to fabricate transparent photodetectors with materials such as SnO_2, TiO_2, and InGaZnO as well as their hybrids [13–18]. However, the demonstrated device areas are rather small.

IVE.2 Scope of the present investigation

This work aimed at producing large area photodetectors using a ZnO layer as the active material as it exhibits high transparency in the visible region and high absorbance in the UV region while being amenable for easy fabrication [19]. Although the active materials for UV detection may be visibly transparent, the contact electrodes in the device obstruct visibility, which is yet another challenge. Consequently, a transparent UV detector cannot be realized as the electrodes occupy a considerable area in these devices. Thus, it is important that the electrodes themselves are made of a transparent conductor. ITO is a well-known transparent conducting material widely employed in optoelectronic devices. Yu et al. made use of ITO as the contact electrode for a ZnO nanowire photodetector [8]. However, the shortcomings associated with ITO such as its brittleness, high price, and instability under high-temperature processing conditions have led to the usage of alternative transparent electrodes such as graphene, Ag nanowires etc [20]. The latter, however, pose other issues such as high surface roughness and contact resistance and demand further remedial steps such as mechanical pressing and thermal annealing [21,22]. In this work, fine Au wire meshes [23,24] with seamless junctions have been employed as transparent electrodes in an UV photodetector.

IVE.3 Experimental Details

The Au/ZnO/Au based UV photodetector was fabricated on glass substrates (2 × 2 cm^2) after stepwise cleaning via ultrasonication in detergent, acetone, distilled water, and isopropanol. A schematic of the different steps involved in the fabrication of the photodetector is presented in Figure IVE.1a. An acrylic resin based crackle

precursor (Ming Ni Cosmetics Co., Guangzhou, China) diluted to 0.5 g mL^{-1} was spin coated (2000 rpm, Technoscience, Bangalore) on a glass substrate to obtain a crackle template as discussed earlier chapters. Over the template, Au was thermally evaporated (Hindvac, India) at a base pressure of 10^{-6} Torr, which was followed by template lift-off using chloroform. The formed Au wire network was highly transparent and conducting. Later, a ZnO layer was deposited using the pulsed laser deposition (PLD) technique at an oxygen partial pressure of 2×10^{-5} Torr over the Au wire network. A frequency tripled pulsed Nd: YAG laser (Quanta-Ray GCR-170, Spectra-Physics, USA) was used to ablate the zinc oxide target (obtained via thermal decomposition of zinc acetate at 1200 °C), which was fixed at 45° to the laser beam, with a pulse width of ~5 ns and a repetition rate of 10 Hz. The laser beam having ~180 mJ of energy per pulse was focused onto the target using a convex lens that had a 50 cm focal length through a quartz window. To increase the width of the plasma plume and also to avoid ablation at a point, the target holder was driven by a linear-rotary motion controlled by the stepper motor. The Au wire network/glass was held at ~ 4 cm from the target and deposition was carried out at room temperature.

IVE.4 Results and Discussion

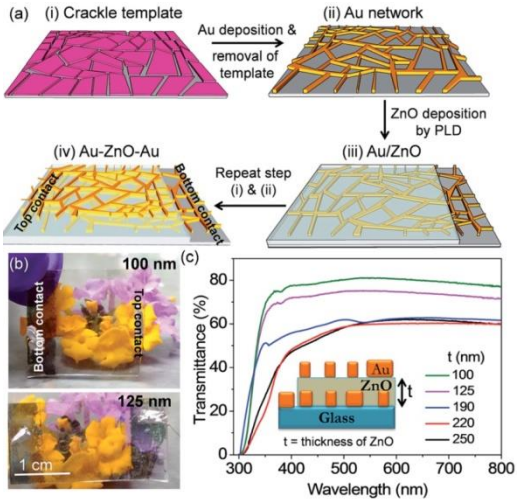

Figure IVE.1 (a) Schematic illustration of the fabrication steps for the UV photodetector. (b) Photographic images of the obtained photodetectors. (c) Transmittance spectra of the photodetecting device, along with the Au top and bottom layers, with a varying ZnO thickness (in nm). The inset shows the schematic of the photodetector.

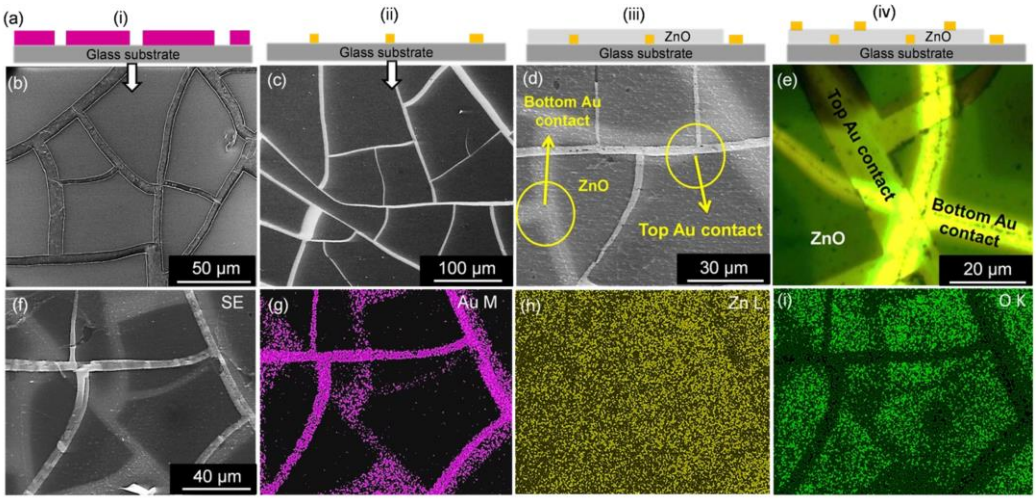

Figure IVE.2 (a) Schematic depiction of fabrication of Au /ZnO/Au photodetector. (b) and (c) SEM images of crackle network and Au network fabricated on the glass substrate, respectively. (d) SEM and (e) optical microscopic image of a complete device clearly showing the presence of ZnO layer sandwiched between top and bottom Au networks. (f) - (i) represents the elemental mapping of a device where the presence of Au in network structure and ZnO as a thin film is evident.

The fabrication steps are shown in Figure IVE.1a and Figure IVE.2a. An acrylic resin based crackle precursor (CP) was spin coated on glass substrate resulting in a dried layer of an interconnected crackle network with widths in the range of 5–15 μm (Figure IVE.1a(i) and Figure IVE.2b). Using a physical vapor deposition process, Au was deposited on the crackle template. The CP layer was then removed via washing with chloroform, resulting in a fine interconnected Au network on the glass substrate (Figure IVE.1a(ii) and Figure IVE.2c). The sheet resistance of the formed Au network was found to be ~8 Ω/sq, and it had a transmittance of ~ 90% in the entire range, 200–3000 nm (Figure IVE.3). A part of the Au network was then masked for use as the bottom electrical contact, and the remaining part was coated with ZnO via pulsed laser deposition (PLD) with the glass substrate held at room temperature (Figure IVE.1a(iii)). ZnO layers of varying thickness, ~ 100–250 nm, were then deposited on Au mesh coated substrates.

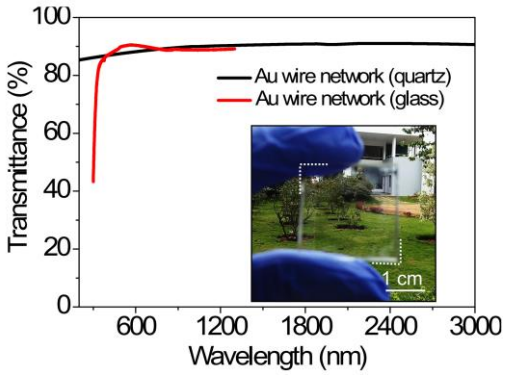

Figure IVE.3 Transmittance spectrum of Au wire network on a glass substrate (300-1300 nm) and a quartz substrate (200 to 3000 nm). The inset is the photograph of Au wire network on a quartz substrate.

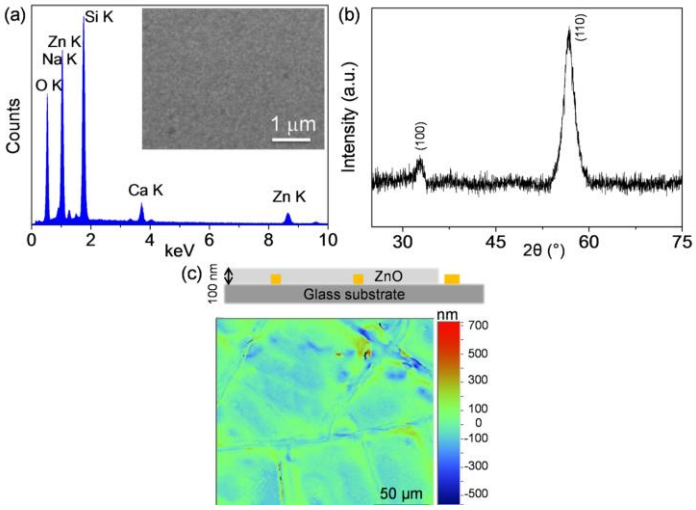

Figure IVE.4 (a) EDAX spectrum of ZnO layer; Inset shows the SEM image of ZnO film of 100 nm thickness without the Au network. (b) XRD patterns of ZnO film deposited on glass substrate exhibits diffraction peaks characteristic to (100) and (110) of ZnO. (c) Optical profiler image of ZnO thin film deposited over Au wire mesh. Above is the schematic illustration denoted with a thickness of ZnO.

The top Au network was then deposited using similar steps detailed in Figure IVE.1a(iv). SEM micrographs of the assembled device, (Figure IVE.2d) along with optical micrographs (Figure IVE.2e) and EDS elemental mapping (Figure IVE.2f–i), clearly reveal the presence of top and bottom Au mesh electrodes. The ZnO layer being transparent is not discernible, but the EDS spectrum confirms the presence of

a uniform ZnO layer (Figure IVE.2 and Figure IVE.4a). An XRD pattern of the as-deposited ZnO film on the glass substrate is shown in Figure IVE.4b. The optical profilometric image in Figure IVE.4c demonstrates that the as-deposited ZnO layer submerges the bottom Au wire mesh uniformly at a layer thickness of 100 nm. This fabricated Au mesh/ZnO/Au mesh (henceforth Au/ZnO/Au) photodetector is found to be highly transparent in the visible range as is evident from the photographs and the transmittance spectra shown in Figure IVE.1b and c. The presence of the fine Au wire network makes the device transparent in both the UV and visible regions and enables the illumination to fall upon the entire ZnO layer from both sides, as appropriate to the context. The transmittance spectrum of the device on the quartz substrate clearly indicates that absorption below 400 nm is mainly due to the ZnO layer (Figure IVE.5) as the metal mesh and quartz are transparent at this wavelength (see Figure IVE.3).

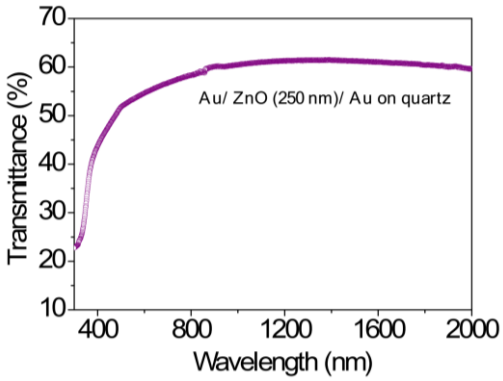

Figure IVE.5 Transmittance spectrum of the device fabricated on the quartz substrate. The transmittance spectrum of the device on the quartz substrate clearly indicates that absorption below 400 nm is mainly due to ZnO layer as metal mesh and quartz is transparent at this wavelength (see Figure IVE.3).

I–V measurements have been performed on the fabricated device in the presence and absence of UV-light (365 nm), as shown in Figure IVE.6. A typical I–V curve for a photodetector with 100 nm of ZnO (see Figure IVE.6a) shows that, upon UV illumination, the photocurrent increases by ~ 6.5 times that of the dark current. The I–V curves are symmetrical and quite linear [25], indicating that the carrier density

in ZnO is high and the Au–ZnO contacts are ohmic. The photoinduced change in the current that is observed is in line with the known behaviour of ZnO [26]. The ZnO layer absorbs the incident photons and generates electron–hole pairs (Figure IVE.6b).

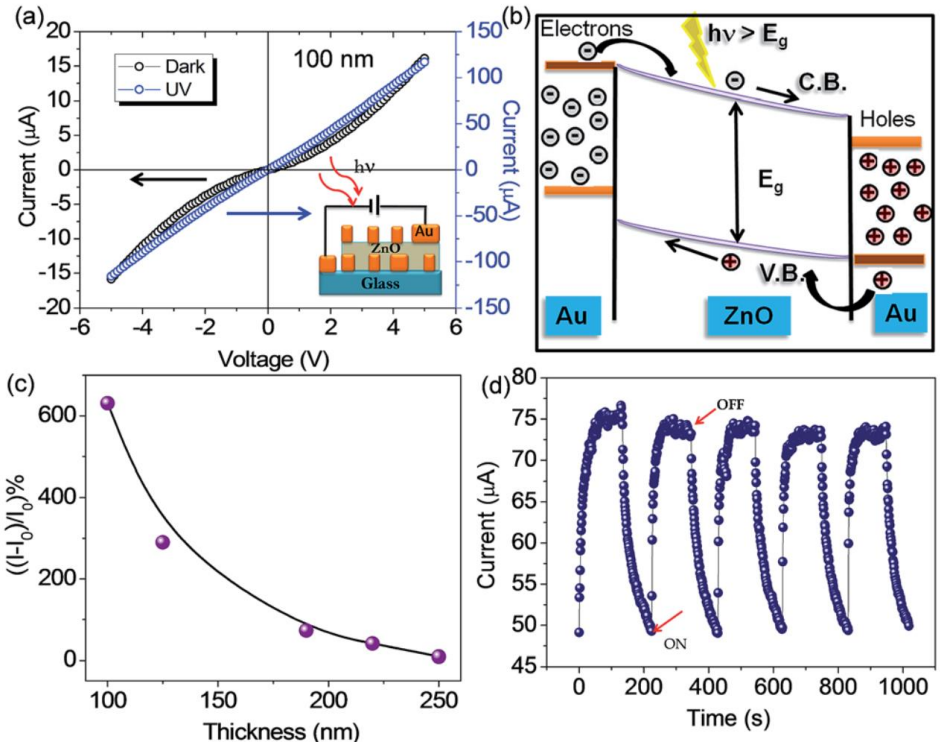

Figure IVE.6 (a) Typical I–V characteristics measured in the dark and under UV light illumination; the inset shows a schematic of the photodetection process. (b) Schematic of the band diagram. (c) Percentage change in the current with illumination on the different thicknesses of the ZnO film in the photodetector. (d) Current vs. time plot for various ON and OFF positions for the photoconductive device with 125 nm thick ZnO at an applied bias of 1 V.

The band bending at the heterojunction suppresses exciton recombination in the presence of light, thereby encouraging discharge as well as the acceleration of trapped electrons [27]. The photocurrent response of the detectors was also found to scale linearly with the applied bias. The barrier height for Au/ZnO (100 nm)/Au was calculated to be 0.77 eV (see note IVE.1). Detectivity is one of the important photodetector characteristics of merit and is given by the expression IVE.1 [27]

$$D = (J_{ph}/AE_i)/(2qJ_d)^{1/2} \text{ ……..(IVE.1)}$$

where J_{ph} and J_d are the photocurrent (125 mA) and dark current (10 mA), respectively, E_i is the light intensity (250 mW), q is the coulombic charge (1.6×10^{-19} coulomb) and A is the active area exposed to UV light (0.5×2 cm^2). Another important parameter is responsivity. Responsivity (A W^{-1}) is defined by

$$R = J_{ph}/AE_i \text{ …… (IVE.2)}$$

For the given device, a detectivity of $\sim 10^{10}$ Jones (cm $Hz^{1/2}$ W^{-1}) and responsivity of $\sim 10^{-2}$ A W^{-1} were estimated. The obtained responsivity value is comparable to the literature value (0.0013 A W^{-1}) obtained with a ZnO nanoparticle/RGO composite with an active area of 10×5 mm^2 [28].

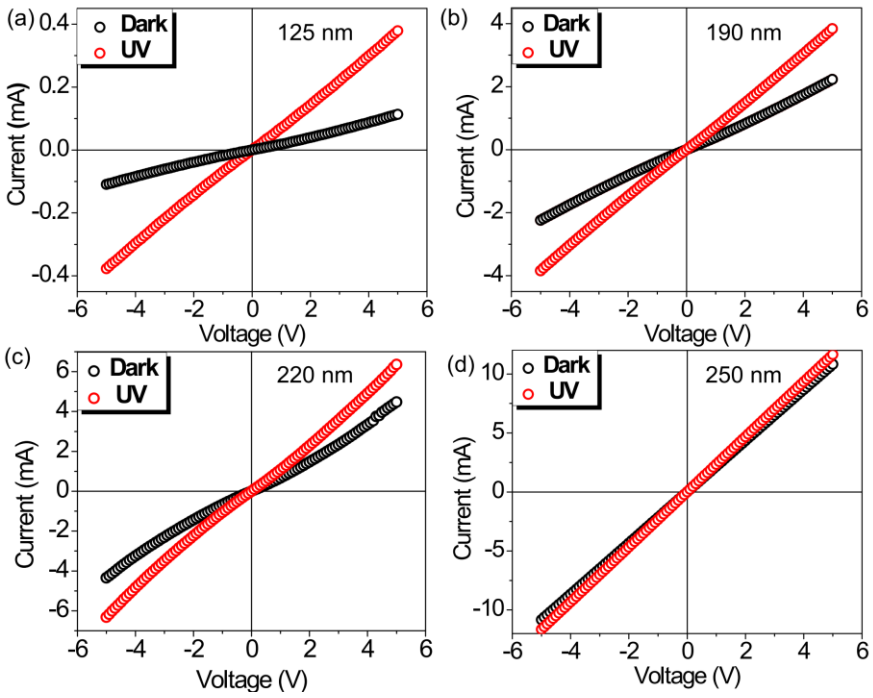

Figure IVE.7 (a-d) I-V characteristics of Au mesh/ZnO/Au mesh with different ZnO layer thickness.

Similar I–V characteristics were measured for different thicknesses of the ZnO active layer, as shown in Figure IVE.7, and the percentage change in photocurrent (also known as sensitivity), $(I-I_0)/I_0\%$ where I_0 is the forward current in the dark at

a forward bias of 5 V, and I is the current under illumination at 5 V, is presented in Figure IVE.6c. This also gives the photoconductive gain (G, calculated from the ratio of the photocurrent to the dark current at the same bias voltage) value as 7. An Au electrode in the form of a network facilitates a reduced gap between the two electrodes shortening the carrier transit time (Figure IVE.8).

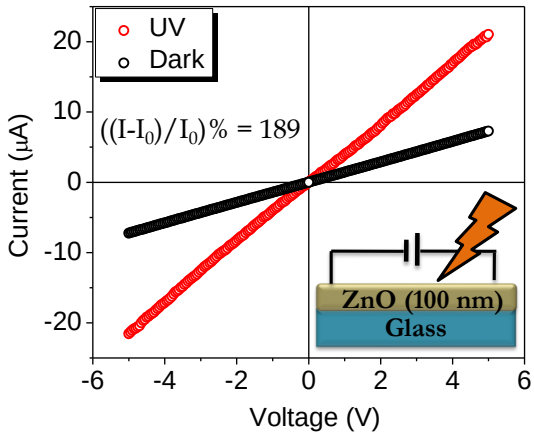

Figure IVE.8 I-V characteristics of PLD deposited 100 nm ZnO films on a glass substrate with Ag paint contact. The inset shows the schematic of measurements.

Consequently, a long lifetime and short transit time of photogenerated carriers can cause a photoconductive gain. For the device with a ZnO layer thickness of 100 and 125 nm, the percentage change value was as high as 630 and 290, respectively, whereas the value decreased to 73, 41 and 9, for increasing thicknesses of 190, 220 and 250 nm respectively (Figure IVE.6b). These sensitivity values are nearly 3 times higher compared to the values obtained with Ag paint contacts (Figure IVE.8). The thickness of the ZnO film is known to influence the overall properties significantly [29] accompanied by morphological changes as well. The defect states also increase with increasing film thickness, while the optical band gap is known to decrease only marginally [30,31]. With an increased thickness the higher energy photons are absorbed in or near the surface of the semiconductor, where the photogenerated electron–hole pairs recombine at a much higher rate than in the bulk region. This leads to a lower contribution of photogenerated electrons and holes to the

photocurrent. Hence, the performance of the photodetector device decreases with increasing film thickness.

Another important parameter of photodetectors is their response speed. Hence, time-dependent studies of photoresponse were recorded to study the response as well as recovery times. The transient response of the present photodetectors was measured by turning on and off an UV LED with a centre peak wavelength at 365 nm, as shown in Figure IVE.6d. The response time, τ_r, (the time required to reach 63% of the maximum photocurrent) and recovery time (the time required to fall to 37% of the maximum photocurrent) [32] were measured to be around 3.3 s and 20 s, respectively. These response and recovery times for the present device are much smaller compared to those based on polycrystalline ZnO photodetectors, where the response times range between minutes to hours [33–35]. It is worth mentioning that the time constant for the rise time is always faster than the fall time, again suggesting the involvement of traps and other defect states in this process. Such a transient response is expected for large area UV photodetectors that are fabricated from wide band gap metal oxides such as ZnO and is very desirable for their practical applications in devices such as light-wave communications or optoelectronic switches. The increase in light-induced conductivity is extremely sensitive to ultraviolet light and is also a reversible phenomenon (Figure IVE.6d). The reproducible response observed implies the excellent stability of the device.

Flexibility is an attractive feature of a device. Using similar design principles, to fabricate a transparent and flexible photodetector, PET was used as the substrate in place of glass (both exhibit similar absorption for 365 nm) (Figure IVE.9). Although the net photodetection effect was minimal even with 100 nm ZnO thin film (~10% change) perhaps due to different interfacial phenomena between PET and the ZnO heterostructures, it does give way to a new possibility of these materials being used as large area transparent and flexible photodetectors with optimized thickness. These devices can be employed as transparent windows for atop devices which need visible light. The nature of the ZnO active material makes the device transparent in the entire range of 350 nm and beyond. Further optimization of the ZnO morphology may lead to transparent strain sensors as the film does show a

small change in resistance during bending to different radii, as shown in Figure IVE.9b.

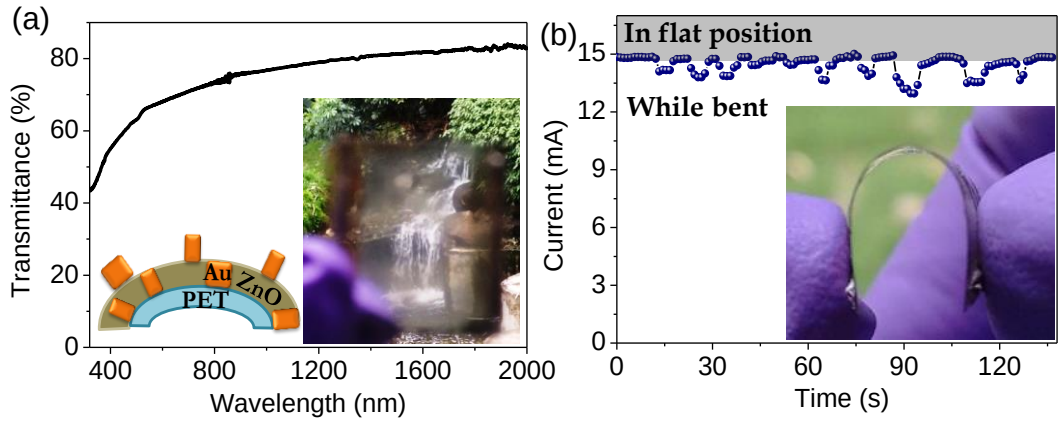

Figure IVE.9 (a) Optical transmittance characteristics of the photodetector device on a PET substrate. The insets are a schematic of the fabricated photodetector (left) and a real photographic image of the device (right). (b) The change in current of the flexible detector on a PET substrate when bent to various radii under a fixed bias of 5 V.

Note IVE.1

The barrier height for Au mesh/ZnO (100 nm)/Au mesh was calculated using following equation.

Barrier height formula and calculation

$$\Phi_{Bo} = \frac{kT}{q} \ln\left(\frac{AA^{*}T^{2}}{I_o}\right)$$

where,

k → Boltzmann constant = 1.3806 x 10^{-23} J K^{-1}

T → Temperature in Kelvin = 298 K

Q → The elementary charge = 1.602x10^{-19} C

A → Area of the contact = 0.6 cm^2

A* → Richardson constant for ZnO= 32 A cm^{-2} K^{-2}

I_s → Saturation current = Intercept ($\ln I_s$) → I_s = 129 nA

Thus, Φ_b = 0.776 eV

The obtained barrier height is comparable to the barrier height of interdigitated configuration of Au/ZnO/Au (0.8 eV) [36] and higher (0.735 eV) than the planar asymmetric electrode configuration (Au/Cr/ZnO/Al) [37].

IVE.5 Conclusions

In this work, UV photodetectors with a 2 cm^2 active area have been successfully fabricated with a visible light transparency of 80%. The fabrication involved depositing Au wire networks sandwiching a laser ablated ZnO film in between, while using glass as a substrate. Such heterostructuring has been possible thanks to the crackle template method pioneered in this laboratory. The main advantage of using metal wire networks as electrodes has been their high degree of transparency, from UV to beyond the visible range, as well as the enhanced electrical contact with the active layer. The fabricated devices showed typically a sensitivity of 630%, detectivity of $\sim 10^{10}$ Jones and responsivity of $\sim 10^{-2}$ A W^{-1}. Using PET as a substrate in place of glass, a flexible photodetector was also made and demonstrated. It is noteworthy that the devices fabricated in this study do not require a complex lithography process for electrode fabrication and the resulting electrodes exhibit transparency in spite of being on the top and bottom of the active layer.

References

1. G. Gu, V. BuloviÄ, P. E. Burrows, S. R. Forrest and M. E. Thompson, *Appl. Phys. Lett.*, 1996, **68**, 2606-2608.
2. C. Keplinger, J.-Y. Sun, C. C. Foo, P. Rothemund, G. M. Whitesides and Z. Suo, *Science*, 2013, **341**, 984-987.
3. R. Gupta, K. D. M. Rao and G. U. Kulkarni, *RSC Adv.*, 2014, **4**, 31108-31112.
4. Y. Yang, S. Jeong, L. Hu, H. Wu, S. W. Lee and Y. Cui, *Proc. Natl. Acad. Sci.,*, 2011, **108**, 13013-13018.
5. Y. Zhao, G. A. Meek, B. G. Levine and R. R. Lunt, *Adv. Opt. Mater.*, 2014, **2**, 606-611.
6. A. Facchetti , T. J. Marks, *Transparent Electronics*, John Wiley & Sons, Ltd, Editon edn., 2011 pp. 443-448.
7. D. Chen, Z. Liu, B. Liang, X. Wang and G. Shen, *Nanoscale*, 2012, **4**, 3001-3012.
8. H. Yu, E. Ali Azhar, T. Belagodu, S. Lim and S. Dey, *J. Appl. Phys.*, 2012, **111**, 102806.
9. T. V. Blank and Y. A. Gol'dberg, *Semiconductors*, 2003 **37**, 999-1030.

10. S. Dali, Y. Mingpeng, L. Jie and S. Shayla, *Nanotechnology*, 2013 **24**, 295701.

11. H.-G. Li, G. Wu, M.-M. Shi, L.-G. Yang, H.-Z. Chen and M. Wang, *Appl. Phys. Lett.*, 2008, **93**, 153309.

12. Y.-L. Liu, C.-C. Yu, K.-T. Lin, T.-C. Yang, E.-Y. Wang, H.-L. Chen, L.-C. Chen and K.-H. Chen, *ACS Nano*, 2015, **9**, 5093-5103.

13. C. Gao, X. Li, X. Zhu, L. Chen, Y. Wang, F. Teng, Z. Zhang, H. Duan and E. Xie, *J. Alloys Compd.*, 2014, **616**, 510-515.

14. S. Huang, C. F. Guo, X. Zhang, W. Pan, X. Luo, C. Zhao, J. Gong, X. Li, Z. F. Ren and H. Wu, *Small*, 2015 **11**, 5712-5718.

15. H. K. Li, T. P. Chen, S. G. Hu, X. D. Li, Y. Liu, P. S. Lee, X. P. Wang, H. Y. Li and G. Q. Lo, *Opt. Express*, 2015, **23**, 27683-27689.

16. X. Liu, X. Liu, J. Wang, C. Liao, X. Xiao, S. Guo, C. Jiang, Z. Fan, T. Wang, X. Chen, W. Lu, W. Hu and L. Liao, *Adv. Mater.*, 2014, **26**, 7399-7404.

17. M. Patel, H.-S. Kim and J. Kim, *Adv. Electron. Mater.*, 2015, **1**, n/a-n/a.

18. S. W. Shin, K.-H. Lee, J.-S. Park and S. J. Kang, *ACS Appl. Mater. Interfaces*, 2015, **7**, 19666-19671.

19. S. J. Young, L. W. Ji, S. J. Chang and Y. K. Su, *J. Cryst. Growth*, 2006, **293**, 43-47.

20. W. Tian, T. Zhai, C. Zhang, S.-L. Li, X. Wang, F. Liu, D. Liu, X. Cai, K. Tsukagoshi, D. Golberg and Y. Bando, *Adv. Mater.*, 2013, **25**, 4625-4630.

21. H. Lu, D. Zhang, X. Ren, J. Liu and W. C. H. Choy, *ACS Nano*, 2014, **8**, 10980-10987.

22. Z. Siwei, G. Yuan, H. Bin, L. Jia, S. Jun, F. Zhiyong and Z. Jun, *Nanotechnology*, 2013, **24**, 335202.

23. K. D. M. Rao, R. Gupta and G.U. Kulkarni, *Adv. Mater. Interface.,* 2014, **1**, 1400090.

24. K. D. M. Rao and G. U. Kulkarni, *Nanoscale*, 2014, **6**, 5645-5651.

25. K. K. Manga, J. Wang, M. Lin, J. Zhang, M. Nesladek, V. Nalla, W. Ji and K. P. Loh, *Adv. Mater.*, 2012, **24**, 1697-1702.

26. W. Dai, X. Pan, S. Chen, C. Chen, W. Chen, H. Zhang and Z. Ye, *RSC Adv.*, 2015, **5**, 6311-6314.

27. Z. Yang, M. Wang, X. Song, G. Yan, Y. Ding and J. Bai, *J. Mater. Chem. C*, 2014 **2**, 4312-4319.

28. K. Liu, M. Sakurai, M. Liao and M. Aono, *J. Phys. Chem. C*, 2010, **114**, 19835-19839.

29. V. Kumar, N. Singh, R. M. Mehra, A. Kapoor, L. P. Purohit and H. C. Swart, *Thin Solid Films*, 2013, **539**, 161-165.

30. R. Ghosh, D. Basak and S. Fujihara, *J. Appl. Phys.*, 2004, **96**, 2689-2692.

31. Y. C. Lin, B. L. Wang, W. T. Yen, C. T. Ha and C. Peng, *Thin Solid Films*, 2010 **518**, 4928-4934.

32. Z. Wang, X. Zhan, Y. Wang, S. Muhammad, Y. Huang and J. He, *Nanoscale*, 2012, **4**, 2678-2684.

33. J. Liu, R. Lu, G. Xu, J. Wu, P. Thapa and D. Moore, *Adv. Funct. Mater.*, 2013, **23**, 4941-4948.

34. P. Sharma, K. Sreenivas and K. V. Rao, *J. Appl. Phys.*, 2003, **93**, 3963-3970.

35. K. Liu, M. Sakurai and M. Aono, *Sensors*, 2010, **10**, 8604-8634.

36. H. Y. Chen, K- W. Liu, X. Chen, Z- Z. Zhang, M- M. Fan, M- M. Jiang, X- H. Xie, H- F. Zhao and D- Z. Shen*, J. Mater. Chem. C*, 2014, **2**, 9689-9694.

37. G. M. Ali and P. Chakrabarti, *IEEE Photonics J.* 2010, **2**, 784-793.

Chapter V

Miscellaneous work

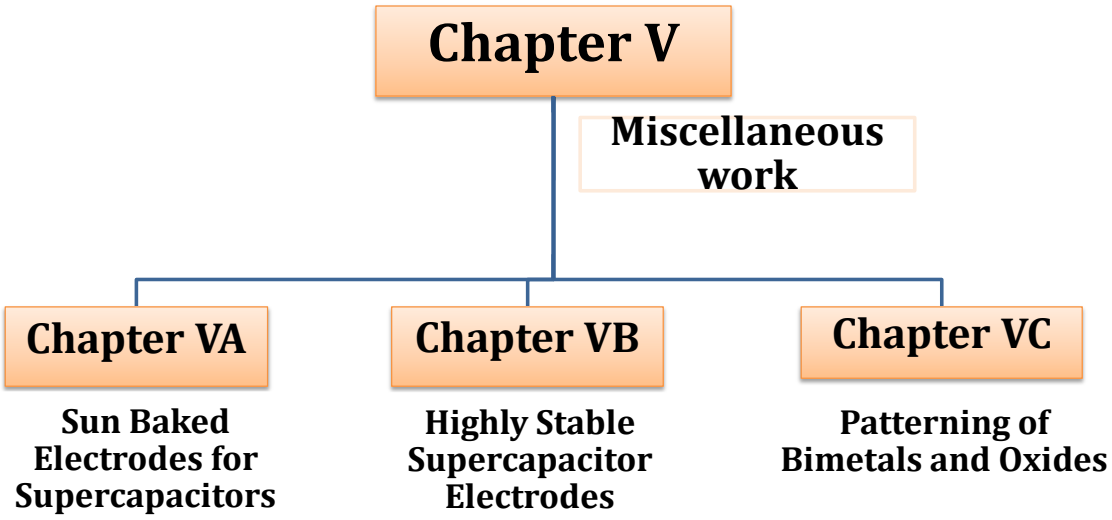

Chapter VA

Sun Baked Electrodes for Supercapacitors

Summary

A new strategy for making electrode materials for supercapacitors is reported here based on a nanocrystalline Pd/carbon (nc-Pd/C) composite obtained by thermolyzing a thin film of Pd hexadecylthiolate under sunlight. Thus obtained nc-Pd/C composite is porous (BET specific surface area, 67 m^2 g^{-1}), hydrophilic (contact angle, 49°) and of excellent electrical conductivity (resistivity ~2 μΩ m), all these properties being highly suitable for supercapacitor electrodes. The autocatalytic nature of the nc-Pd/C composite was exploited for electrolessly depositing MnO_2 bearing a nanowall morphology to serve as a pseudocapacitive material. Using MnO_2/nc-Pd/C electrodes in 1 M Na_2SO_4, a specific capacitance of ~450 F g^{-1} was obtained at 10 mV s^{-1}. The electrode precursor being a direct write lithography resist allowed fabrication of a planar micro-supercapacitor with an ionic liquid as an electrolyte, exhibiting a cell capacitance of 8 mF cm^{-2}. As this recipe does not make use of an additional charge collecting layer and binder, nor does it use any external energy during fabrication, the only cost consideration is related to Pd; however, given the extremely small amount of Pd consumed per device (~0.18 mg), it is highly cost effective.

VA.1 Introduction

There is a great deal of interest worldwide in developing electrochemical energy storage devices with the aim of achieving high energy and power densities [1–3]. Conventionally, batteries and fuel cells work based on Faradaic processes [4] with high energy density (~10 to 200 Wh kg^{-1}), but suffer from low power densities, low cyclability and discharge rates [3–6]. To circumvent these problems, alternative energy storage devices with higher power densities are being developed in the form of electrochemical capacitors or supercapacitors [6–9]. Besides power density, long cycle life and fast discharge rates have made supercapacitors quite attractive in recent times [1,7–9]. Basic designs of supercapacitors typically employ electrodes made of highly porous carbon-based materials sometimes with pseudocapacitive

Paper based on this study: RSC Adv., 2014, 4, 20281

coatings, with aqueous, organic or ionic liquids as electrolytes in a two or a three electrode configuration. The capacitance of a supercapacitor is superior to that of the conventional capacitor due to the formation of electrical double layer (EDL) where the ions from the electrolyte get accumulated at the electrode–electrolyte interface on applying potential [3,10,11]. The electrode material used in a supercapacitor should therefore be electrically well conducting and possess high specific surface area. These properties make an electrode accumulate a large amount of charge in the EDL which can be harnessed in an external circuit [1,3,10,11]. In this context, carbon-based materials have been explored extensively due to their tunable surface area, high electrical conductivity and excellent electrochemical stability, essential for a supercapacitor electrode [12–15]. Carbon materials can be activated through chemical, thermal and plasma methods [16–19] to enhance porosity and tune the morphology. Thus, activated carbon in the form of nano-onions [20], nanoparticles [21], fibres [22] and nanotubes [23] have been employed as electrode materials for building supercapacitors. Similarly, graphene and its derivatives like curved [24], activated [25], solvated [26], doped graphene [27] as well as three-dimensional graphene networks [28], have been utilized as an electrode material in supercapacitors. It was found that the graphene layers tend to restack themselves with increasing number of cycles and this issue has been addressed by mixing spacers such as carbon nanotubes (CNTs) and Au nanoparticles [29,30].

VA.2 Scope of the present investigation

Supercapacitors based on carbon materials and pseudocapacitive coatings involve high temperature treatments, activation by chemicals, multi-step complex solution processing and chemical vapor deposition techniques [16–39]. Due to its low cost and nontoxicity, MnO_2 (theoretical specific capacitance ~1370 F g^{-1}) has been widely employed as a pseudocapacitive material in combination with high surface area electrodes [40–43]. Implementation with additives such as polymer binders and conductive adhesives may increase the mechanical stability of the electrode materials but often cause degradation of the electrochemical performance [30–35]. Addressing these issues, recently, Wei et al., have fabricated thin activated carbon film electrode based supercapacitor obtained through carbonization and activation using

temperatures above 700 °C [44]. Processing of highly conducting carbon-based thin films at lower temperatures could offer new capabilities in making on-chip energy storage devices. Thus, the quest is to arrive at an optimized electrode material involving simple and solution processable chemical recipes in a binder-free manner. Here, using novel metal–organic precursor Pd nanoparticles embedded in conducting carbon films were obtained through a solution processable route combined with thermolysis at just about 220 °C, using sunlight. The autocatalytic nature of this composite was realised through the spontaneous reduction of permanganate ions into insoluble MnO_2 with nanowall morphology, confirmed through Raman and SEM analysis. This synthesis protocol eludes processing involving high temperatures, multistep solution processing as well as the use of binders without compromising the electrochemical performance. Using direct write e-beam lithography, the fabrication was extended to realise planar micro-supercapacitors.

VA.3 Experimental Details

Synthesis of nc-Pd/C composite

The synthesis procedure for the precursor, Pd hexadecylthiolate, $Pd(SC_{16}H_{33})_2$, is reported elsewhere [45-49]. Briefly, 100 mM of 1-hexadecylthiol (Sigma Aldrich) was added to 100 mM of $Pd(OAc)_2$ (Sigma Aldrich) in toluene solution under stirring. The solution became viscous, and color changed from orange to reddish orange. The glass substrates used for film formation were cleaned with deionized water, IPA and, acetone followed by drying under N_2 flow. A 100 µl of 100 mM Pd hexadecylthiolate precursor solution was drop casted on a cleaned glass substrate (1 × 2.5 cm^2) resulting in an orange colored film. A convex lens with a diameter of 20 cm and a focal length of 50 cm was used for concentrating the sunlight to a spot diameter of 1 cm to reach a temperature of ~ 220 °C on the film, measured using a thermometer. During the heat treatment, the precursor decomposes leading to the formation of conducting nc-Pd/C composite within 30 minutes. Alternatively, nc-Pd/C was also obtained through heating on a hot plate (temperature ~ 220 °C) for 3 h.

MnO_2 deposition

Neutral aqueous solution (pH =7) of $KMnO_4$ (6 mM) was employed as a precursor solution for depositing MnO_2 nanoscale petals in an electroless manner on the

autocatalytic nc-Pd/ C surfaces for dipping times of 30 seconds, 1, 2, 5 and 10 minutes. The samples were thoroughly washed with distilled water in order to remove the unreacted permanganate solution followed by drying using N_2. The mass of the coated MnO_2 was calculated from the weight difference before and after the coating process. The loading amount of MnO_2 in this study is approximately 20 to 140 mg depending on the plating time, which was measured using a microbalance.

Fabrication of micro-supercapacitors

50 µL of Pd hexadecylthiolate (500 mM, filtered through 200 nm Millipore filter) was spin coated on SiO_2/Si substrates followed by drying of toluene solvent in air. Electron beam lithography was performed using a field-emission SEM (Nova NanoSEM 600 instrument, FEI Co., The Netherlands) at a chamber pressure of 1×10^{-6} Torr, at a working distance of 5 mm. Selected regions on the substrate were exposed to e-beam dosages of 50 µC cm^{-2} at 10 kV (beam current ~ 0.64 nA) in the patterning mode. After patterning, the substrate was developed in toluene for 10 seconds followed by thermolysis at 220 °C for 3 h which results in the formation of interdigitated nc-Pd/C electrodes.

Electrochemical measurements

The electrochemical properties of the nc-Pd/C films were investigated in two electrode configuration using 1 M Na_2SO_4 aqueous solution. The PVA/H_2SO_4 gel electrolyte was prepared as follows: 1 g of H_2SO_4 was added into 10 mL of deionized water, followed by 1 g of PVA powder. The whole mixture was heated to 85 °C while stirring until the solution became clear. Whatmann filter paper (pore size of 220 nm, NKK TF40, 40 µm) was used as a separator, sandwiched between two nc-Pd/C electrodes. An ionic liquid such as 1-butyl-3-methylimidazolium methylsulfate was employed as an electrolyte in the microsupercapacitors. Cyclic voltammetry and galvanostatic charge–discharge experiments were performed on the potentiostat equipment from Technoscience Instruments (Model PG 16250) and CH Instruments 650 Electrochemical Station (Austin, TX, USA).

Electrochemical characterization

Electrochemical double layer capacitor

Supercapacitor is a commonly used term to a versatile class of energy storage devices that rely on the physical adsorption of ions at an electrode/electrolyte interface to form an electric double layer with a typical charge separation distance of ~ 1 nm. The geometry of the supercapacitors includes two identical porous carbon based electrodes separated by an ion permeable separator and electrolyte. The performance of supercapacitors can be investigated through cyclic voltammetry, charge-discharge and impedance measurements.

Cyclic voltammetry gives a voltammogram which is a measure of charge response with respect to changing voltage, estimating capacitance of a supercapacitor. The voltammogram records the current change with respect to the changing voltages at constant scan rate (dV/dt). The capacitance can be related to current (I) and scan rate (s) by the following equation VA.1.

$$C = I/s \quad \text{.....(VA.1)}$$

The specific capacitance was calculated from the equation VA.2.

$$C_s = 2(1/m_t)(I/s) \quad \text{.....(VA.2)}$$

where m_t is the total mass of the electrodes (0.4-0.45 mg), I is the current in mA and s is the sweep rate in mV/sec (s = dV/dt).

The voltammogram for an ideal capacitor with no resistance would be of rectangular shape, but most real EDLC voltammograms would have the shape of parallelogram with irregular peaks. Prominent peaks at particular voltages are usually due to Faradaic processes (pseudocapacitive behavior). Higher scan rates correspond to charging and discharging of the supercapacitor at higher power levels. Typically, a set of cyclic voltammograms will be displayed at different scan rates in the same graph to determine the impact on charging characteristics at different power levels. The degree of reversibility of an electrode reaction can also be inferred from the voltammogram in which the reversible and irreversible processes would have mirror image and two separate charge and discharge profiles respectively.

Electrical impedance spectroscopy (EIS) is a powerful method for evaluating the supercapacitor performance in the frequency domain. After applying a small AC voltage, the changes in magnitude and phase over a range of frequencies will be measured. The impedance can then be plotted on a Nyquist diagram where the imaginary part of impedance (-Z''(ohm)) is plotted against the real part (Z'(ohm)). For an ideal capacitor, vertical straight line shifted on the real axis by its ESR is seen.

VA.4 Results and Discussion

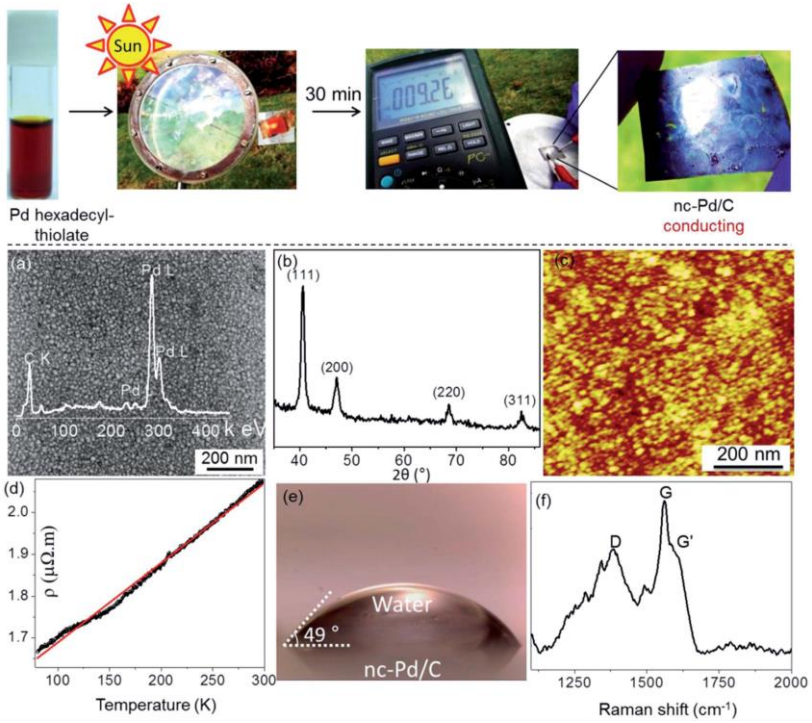

Figure VA.1 Photograph showing solution processable metal–organic precursor, Pd hexadecyl-thiolate. Thermolysis of Pd hexadecylthiolate (orange color) into nc-Pd/C (black color) after annealing under sunlight. A focussed spot of sunlight on the sample surface along with the lens is shown. Multimeter displaying the resistance value of the nc-Pd/C composite film which is conducting following thermolysis. (a) FESEM image showing the densely packed Pd nanoparticles, inset is the energy dispersive spectrum (EDS) showing Pd L and C K signals. (b) XRD of nc-Pd/C composite film. The indexed peaks are matching well with metallic Pd. (c) AFM topography of the nc-Pd/C film. (d) Temperature dependent resistivity of the film showing near metallic behavior. (e) Water contact angle of the nc-Pd/C film, indicating hydrophilic nature of the surface. (f) Raman spectrum of the nc-Pd/C film showing the presence of functionalized amorphous carbon.

Pd hexadecylthiolate is a novel precursor which upon mild thermolysis, produces nanocrystalline Pd in carbon matrix (nc-Pd/C) with the desirable conducting property [45]. The precursor is amenable for patterning by various lithography techniques to achieve fine features of the nc-Pd/C [46–49]. This composite was previously employed in this laboratory as an active material in fabricating hydrogen [47] and strain sensors [45]. In this study, supercapacitors were fabricated by employing nc-Pd/C composite as conducting electrode, importantly, by carrying out the thermolysis of the precursor under sunlight. Pd hexadecylthiolate precursor was drop coated on a glass or quartz substrate and allowed to dry in air to give rise to an orange colored film which was poorly conducting. The dried film was brought under a lens focusing the sunlight such that the local temperature reached ~ 220 °C when the film began to release volatile carbonaceous species and turned into a dark colored film (see Movie VA.S1 in the CD). It became highly conducting as shown on the right side of the schematic in Figure VA.1. The film has been characterized in detail (Figure VA.1a–e). It is essentially a nanocrystalline film with particle size of 15–20 nm as seen from the FESEM image in Figure VA.1a. The EDS spectrum showed the presence of Pd and C in the ratio ~40 : 60 at%. It is evident that the Pd hexadecylthiolate underwent decomposition leading to the formation of the Pd nanoparticles along with the carbonaceous species. The XRD pattern of the film showed peaks corresponding to metallic Pd with the estimated particle size of ~16 nm (Figure VA.1b). The measured roughness from AFM image in Figure VA.1c was 1.13 nm, which is in the acceptable range for a planar electrode. The room temperature resistivity of the film was found to be ~ 2 μΩ m, which decreased nearly linearly with temperature exhibiting metallic type behavior (Figure VA.1d). Thus, the sun baked nc-Pd/C composite film exhibited essential requisites of an electrode. Further, the water contact angle was only 49° (Figure VA.1e), an important property for use with the aqueous electrolyte. The Raman spectrum showed the presence of a broad D (position, 1377 cm^{-1}, width, 185 cm^{-1}) and G bands (1564 cm^{-1}, 38 cm^{-1}) with a shoulder at 1620 cm^{-1}corresponding to the G' band (width ~55 cm^{-1}), implying the presence of functionalized amorphous carbon (see Figure VA.1f) [45]. The latter may be expected to enhance water wettability.

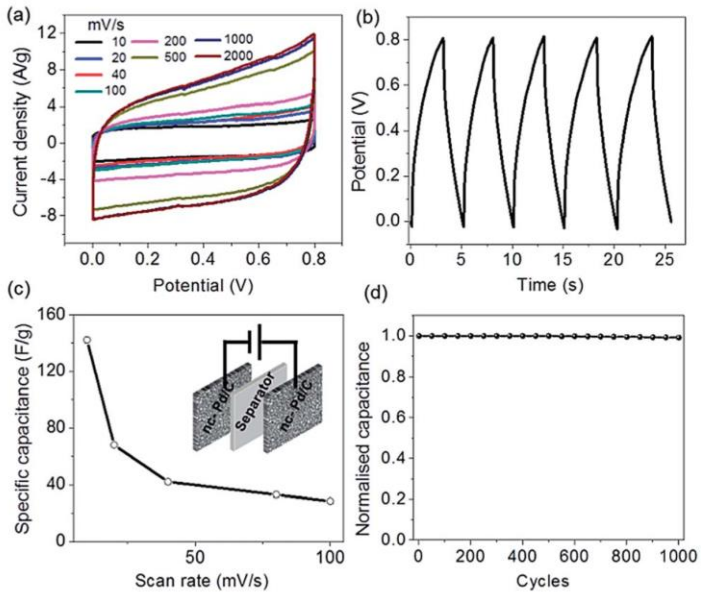

Figure VA.2 The performance of the symmetric nc-Pd/C electrochemical capacitor in aqueous 1 M Na_2SO_4 solution. (a) Cyclic voltammograms (CV) at different scan rates, from 10 to 2000 mV s^{-1}. (b) Galvanostatic charge–discharge (CD) curves at a current density of 5 A g^{-1}. (c) Specific capacitance as a function of scan rate, the inset shows the two electrode configuration of the symmetric nc-Pd/C electrodes along with the separator. (d) Normalized capacitance vs. a number of cycles showing the electrochemical stability of nc-Pd/C electrodes over 1000 cycles (data points corresponding to every 50th cycle, are shown).

A symmetric supercapacitor was assembled using two nc-Pd/C electrodes separated by a filter paper and in 1 M Na_2SO_4 as aqueous electrolyte. The electrochemical performance of the device was examined by cyclic voltammetry (CV) and galvanostatic charge–discharge (CD) measurements (Figure VA.2). The CV curves are nearly rectangular in shape over scan rates of 10–2000 mV s^{-1} in the potential window of 0–0.8 V, indicating clearly the formation of EDL (Figure VA.2a). The CD curves measured in the potential window of 0–0.8 V at a current density of 5 A g^{-1} (Figure VA.2b), showed nearly triangular shape reflecting efficient EDL at the electrode–electrolyte interface. The specific capacitance of ~140 F g^{-1} (areal capacitance of 56 mF cm^{-2}) was estimated at a low scan rate of 10 mV s^{-1}which was found to decrease with increasing scan rate (Figure VA.2c). The drop of specific capacitance at higher scan rates is due to mesoporous nature of the sample with

limited diffusion rate of ions. Using the typical value for EDL capacitance as ~0.3 F m^{-2}[10], the electrochemical active specific surface area was estimated to be 466 m^2 g^{-1}. Compared to BET value, the latter may be more appropriate particularly for thin film supercapacitors [50]. The capacitance retention test conducted over 1000 cycles demonstrated the excellent electrochemical stability of the device and hence the nc-Pd/C electrodes (Figure VA.2d).

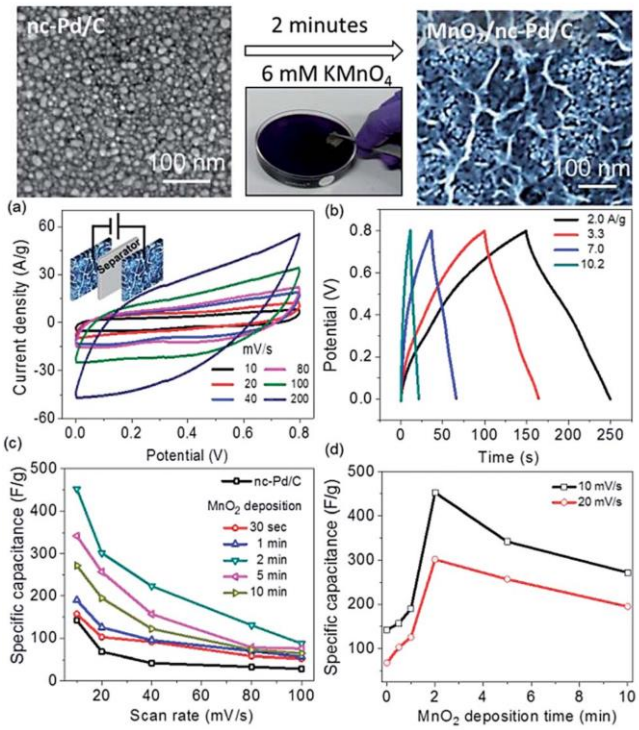

Figure VA.3 The process of depositing MnO_2 on the nc-Pd/C electrode is shown in the top schematic. (a) Cyclic voltammetry curves for (2 minutes) MnO_2/nc-Pd/C symmetric supercapacitor at different scan rates ranging from 10 to 200 mV s^{-1} (electrolyte used, 1 M Na_2SO_4). Inset shows the schematic of the supercapacitor cell. (b) Galvanostatic charging–discharging curves at different current densities. (c) Specific capacitance versus scan rates for varied mass loadings of MnO_2 in comparison to nc-Pd/C. (d) The plot of specific capacitance with respect to MnO_2 deposition times at scan rates of 10 and 20 mV s^{-1}.

The autocatalytic nature of the nc-Pd/C composite was exploited for spontaneous deposition of MnO_2 by dipping in neutral permanganate solution. MnO_4^- ions could be reduced to MnO_2 on functionalized nc-Pd/C surfaces based on reaction (VA.3) [51,52].

$$4MnO_4^- + 3C + H_2O \rightarrow 4MnO_2 + CO_3^{2-} + 2HCO_3^- \quad \text{VA.3}$$

$$MnO4^- + 4H^+ + 3e^- \rightarrow MnO_2 + 2H_2O \quad \text{VA.4}$$

Reduction of permanganate ion (MnO_4^-) to MnO_2 on carbon surfaces is pH dependent. Typically, protons and electrons are required for the reduction of permanganate into MnO_2 according to the equation VA.4. In the case of graphitic materials such as carbon nanotubes and graphene, the surfaces have to be treated with acid solutions in order to functionalize for reduction of permanganate into MnO_2. As nc-Pd/C composite is conducting and contains functionalized carbon, the surface offers plenty of reduction sites for the permanganate ions to get reduced to MnO_2. Earlier, it has been shown that the nc-Pd/C surface exhibits autocatalytic property which could assist the spontaneous growth of Cu, ZnO and polyaniline [53,54].

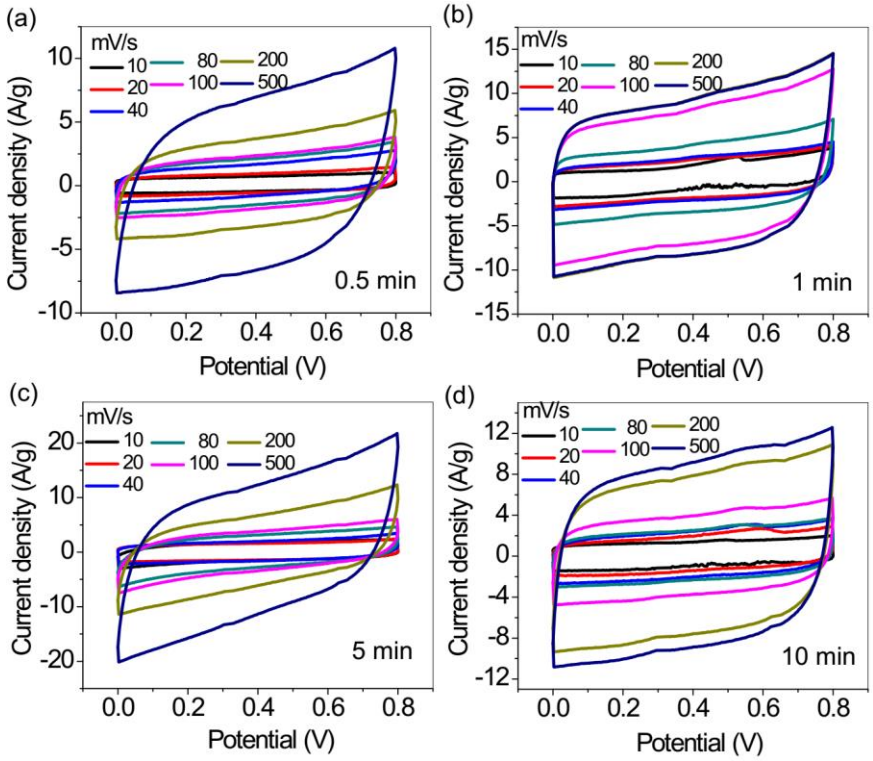

Figure VA.4 (a-d) Cyclic voltammetry curves for MnO_2/nc-Pd/C symmetric electrodes at different scan rates (10-500 mV/s) with different MnO_2 deposition times of 0.5, 1, 5 and 10 minutes, respectively.

The amount of MnO_2 deposited on the nc-Pd/C surface was controlled by the dipping time (30 seconds to 10 minutes) in permanganate solution. Figure VA.3a

shows the scan rate dependent CVs for a symmetric supercapacitor with 2 minutes deposited MnO_2 (scan rates of 10–200 mV s^{-1} and potential window, 0–0.8 V). The electrochemical performance of the MnO_2/nc-Pd/C electrodes with different loadings of MnO_2 (dipping times of 0.5, 1, 5 and 10 minutes) was investigated using cyclic voltammetry (Figure VA.4). It was found that the mass loading of MnO_2 obtained with 2 minutes deposition produced high current density and hence high specific capacitance compared to other loadings. The galvanostatic charge–discharge curves at different current densities (2 to 10.2 A g^{-1}) are shown in Figure VA.3b. The triangular nature of the charge and discharge curves reveals the capacitive characteristics of the MnO_2/nc-Pd/C electrodes. The specific capacitance of the different loadings of MnO_2 on nc-Pd/C was plotted against the scan rate (Figure VA.3c). It was found that the 2 minutes deposition showed a maximum specific capacitance of 450 F g^{-1} at a scan rate of 10 mV s^{-1}. The specific capacitance was found to increase from 140 F g^{-1} for the pristine nc-Pd/C to 450 F g^{-1} after MnO_2 deposition (2 minutes). The electrochemical active surface area for the MnO_2/nc-Pd/C architecture is found to be 1500 m^2 g^{-1} which is 3 times higher compared to planar nc-Pd/C composite film. For higher loading of MnO_2, however, the specific capacitance decreased (Figure VA.3d). As MnO_2 is an insulating material, thicker deposits increase the resistivity in the film, leading to the decreased specific capacitance. An optimal coverage of MnO_2 over the nc-Pd/C is required for obtaining better performance which under the conditions employed was found to be ~2 minutes.

Micro-supercapacitors is an emerging area of research with potential applications as micropower devices in many fields such as RFID tags, ac-line filtering and as often such devices are realized in planar geometry [55–58]. As Pd hexadecylthiolate is amenable for patterning [45–48], electron beam lithography has been employed to fabricate interdigitated nc-Pd/C electrodes on a SiO_2/Si substrate. Patterning of interdigitated planar electrodes could be useful for improved kinetic performance due to a shortened diffusion length [17,20]. Interdigitated electrodes (width, 65 μm; length ~ 350 μm with a spacing of ~10 μm) were fabricated by exposing a thin film of Pd hexadecylthiolate (~500 nm) at an e-dosage of 50 μC cm^{-2} followed by developing

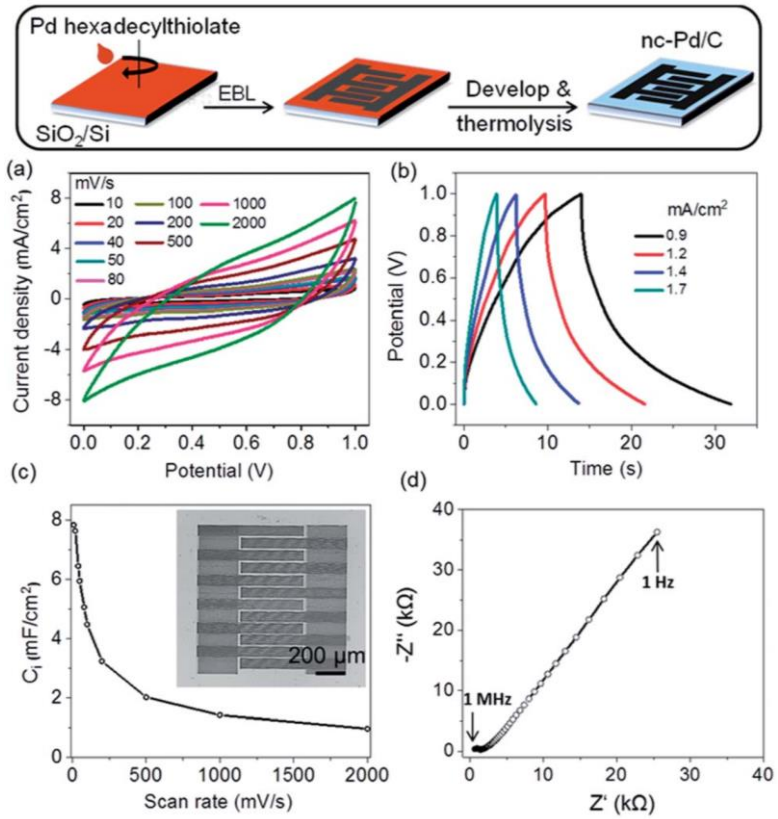

Figure VA.5 Micro-supercapacitors based on nc-Pd/C composite. Schematic shows the fabrication of micro electrodes of nc-Pd/C through electron beam lithography of Pd hexadecylthiolate. (a) CV curves of the nc-Pd/C micro-supercapacitor at different scan rates. (b) Charge– discharge cycles at different current densities. (c) Specific capacitance vs. scan rate of the micro-supercapacitor. Inset shows the optical micrograph of interdigitated nc-Pd/C electrodes. (d) Nyquist plot for the micro-supercapacitor recorded from 1 Hz to 1 MHz.

in toluene for 10 seconds. Thus obtained patterns were thermolysed at 220 °C for 3 h which resulted in the formation of conducting nc-Pd/C electrodes in a planar geometry (schematic Figure VA.5). An ionic liquid (1-butyl-3-methylimidazolium methylsulfate) was employed as an electrolyte due to its low vapor pressure. The CV curves were nearly rectangular even at a high scan rate of 2000 mV s^{-1} (see Figure VA.5a). The charge–discharge cycles were recorded at different current densities (0.9–1.7 mA cm^{-2}) which were triangular in shape due to efficient EDLs that were formed in the micro nc-Pd/C electrodes (Figure VA.5b). The cell capacitance, calculated based on the total area of the electrode pads, found to be 8 mF cm^{-2} at a

scan rate of 10 mV s^{-1} (Figure VA.5c). Microsupercapacitors based on carbon materials have shown typical values of 0.4–2 mF cm^{-2} [20]. The inset in Figure VA.5c shows SEM image of the fabricated interdigitated electrode, while optical microscopy image of the device with the contacts is given in Figure VA.6. The ESR value for the fabricated micro-supercapacitor was found to be ~ 600 Ω. The Nyquist plot showed a small semicircle in the high-frequency region which is due to charge transfer resistance [10] and linear behavior in the low-frequency range, indicative of the capacitive behavior of the micro-supercapacitor (Figure VA.5d).

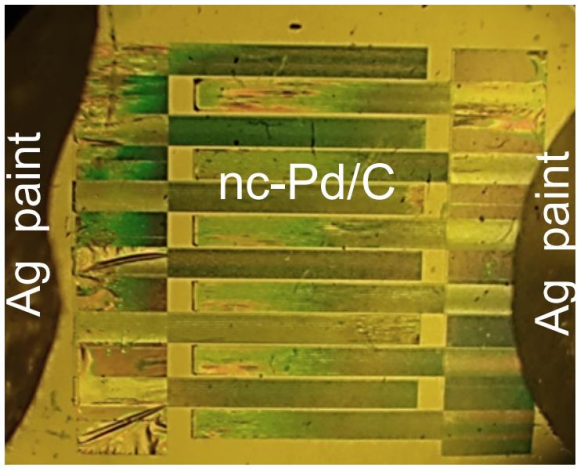

Figure VA.6 Optical micrograph showing the micro-supercapacitor of nc-Pd/C electrode on SiO_2/Si substrate with silver paint contact. Ionic liquid electrolyte was coated over the electrode surface.

VA.5 Conclusions

In conclusion, a new strategy for making electrode material in the form of conducting nc-Pd/C composite has been developed by thermolyzing Pd hexadecylthiolate film under sunlight. The autocatalytic nature of nc-Pd/C enabled electroless deposition of pseudocapacitive MnO_2 layer within minutes. Maximum specific capacitance of 450 F g^{-1} was achieved with an optimal thickness of MnO_2. As Pd is present only in tiny amount (~ 0.18 mg) and as the fabrication involves no significant energy or material input, these are essentially low-cost devices. By patterning the Pd precursor, planar micro-supercapacitors were also realised exhibiting cell capacitance of 8 mF cm^{-2}.

References

1. M. F. El-Kady, V. Strong, S. Dubin and R. B. Kaner, *Science*, 2012, **335**, 1326–1330.

2. C. Largeot, C. Portet, J. Chmiola, P.-L. Taberna, Y. Gogotsi and P. Simon, *J. Am. Chem. Soc.,* 2008, **130**, 2730–2731.

3. P. Simon and Y. Gogotsi, *Nat. Mater*., 2008, **7**, 845–854.

4. M. Winter and R. J. Brodd, *Chem. Rev.,* 2004, **104,** 4245–4270.

5. Y. Zhu, S. Murali, M. D. Stoller, K. J. Ganesh, W. Cai, P. J. Ferreira, A. Pirkle, R. M. Wallace, K. A. Cychosz, M. Thommes, D. Su, E. A. Stach and R. S. Ruoff, *Science*, 2011, **332**, 1537–1541.

6. Y. Zhai, Y. Dou, D. Zhao, P. F. Fulvio, R. T. Mayes and S. Dai, Adv. Mater., 2011, 23, 4828–4850.

7. C. Meng, C. Liu, L. Chen, C. Hu and S. Fan, Nano Lett., 2010, 10, 4025–4031.

8. B. G. Choi, J. Hong, W. H. Hong, P. T. Hammond and H. Park, ACS Nano, 2011, 5, 7205–7213.

9. J. J. Yoo, K. Balakrishnan, J. Huang, V. Meunier, B. G. Sumpter, A. Srivastava, M. Conway, A. L. Mohana Reddy, J. Yu, R. Vajtai and P. M. Ajayan, Nano Lett., 2011, 11, 1423–1427.

10. B. E. Conway, Electrochemical Supercapacitors, Scienti□c, Fundamentals and Technological Applications, Plenum, New York, 1999.

11. J. R. Miller and P. Simon, Science, 2008, 321, 651–652.

12. Y. Huang, J. Liang and Y. Chen, Small, 2012, 8, 1805–1834.

13. H. Nishihara and T. Kyotani, Adv. Mater., 2012, 24, 4473– 4498.

14. S. L. Candelaria, Y. Shao, W. Zhou, X. Li, J. Xiao, J. G. Zhang, Y. Wang, J. Liu, J. Li and G. Cao, Nano Energy, 2012, 1, 195– 220.

15. G. Wang, L. Zhang and J. Zhang, Chem. Soc. Rev., 2012, 41, 797–828.

16. L. L. Zhang, X. Zhao, M. D. Stoller, Y. Zhu, H. Ji, S. Murali, Y. Wu, S. Perales, B. Clevenger and R. S. Ruoff, Nano Lett., 2012, 12, 1806–1812.

17. J. Chmiola, C. Largeot, P. L. Taberna, P. Simon and Y. Gogotsi, Science, 2010, 328, 480–483.

18. L. Hu, J. W. Choi, Y. Yang, S. Jeong, F. La Mantia, L.-F. Cui and Y. Cui, Proc. Natl. Acad. Sci. U. S. A., 2009, 106, 21490– 21494.

19. V. L. Pushparaj, M. M. Shaijumon, A. Kumar, S. Murugesan, L. Ci, R. Vajtai, R. J. Linhardt, O. Nalamasu and P. M. Ajayan, Proc. Natl. Acad. Sci. U. S. A., 2007, 104, 13574–13577.

20. D. Pech, M. Brunet, H. Durou, P. Huang, V. Mochalin, Y. Gogotsi, P. L. Taberna and P. Simon, Nat. Nanotechnol., 2010, 5, 651–654.

21. A. G. Pandolfo and A. F. Hollenkamp, J. Power Sources, 2006, 157, 11–27.

22. E. Frackowiak and F. B´ eguin, Carbon, 2001, 39, 937–950.

23. E. Frackowiak and F. B´ eguin, Carbon, 2002, 40, 1775–1787.

24. C. G. Liu, Z. Yu, D. Neff, A. Zhamu and B. Z. Jang, Nano Lett., 2010, 10, 4863–4868.

25. Y. Zhu, S. Murali, M. D. Stoller, K. J. Ganesh, W. Cai, P. J. Ferreira, A. Pirkle, R. M. Wallace, K. A. Cychosz, M. Thommes, D. Su, E. A. Stach and R. S. Ruoff, Science, 2011, 332, 1537–1541.

26. X. Yang, J. Zhu, L. Qiu and D. Li, Adv. Mater., 2011, 23, 2833– 2838.

27. H. M. Jeong, J. W. Lee, W. H. Shin, Y. J. Choi, H. J. Shin, J. K. Kang and J. W. Choi, Nano Lett., 2011, 11, 2472–2477.

28. X. Cao, Y. Shi, W. Shi, G. Lu, X. Huang, Q. Yan, Q. Zhan and H. Zhang, Small, 2011, 7, 3163–3168.

29. V. Sridhar, H.-J. Kim, J.-H. Jung, C. Lee, S. Park and I.-K. Oh, ACS Nano, 2012, 6, 10562–10570.

30. Z. Niu, J. Du, X. Cao, Y. Sun, W. Zhou, H. H. Hng, J. Ma, X. Chen and S. Xie, Small, 2012, 8, 3201–3208.

31. M. G. Hahm, A. Leela Mohana Reddy, D. P. Cole, M. Rivera, J. A. Vento, J. Nam, H. Y. Jung, Y. L. Kim, N. T. Narayanan, D. P. Hashim, C. Galande, Y. J. Jung, M. Bundy, S. Karna, P. M. Ajayan and R. Vajtai, Nano Lett., 2012, 12, 5616–5621.

32. J. M. Miller, B. Dunn, T. D. Tran and R. W. Pekala, J. Electrochem. Soc., 1997, 144, L309–L311.

33. G. Yu, L. Hu, M. Vosgueritchian, H. Wang, X. Xie, J. R. McDonough, X. Cui, Y. Cui and Z. Bao, Nano Lett., 2011, 11, 2905–2911.

34. L. Yuan, X.-H. Lu, X. Xiao, T. Zhai, J. Dai, F. Zhang, B. Hu, X. Wang, L. Gong, J. Chen, C. Hu, Y. Tong, J. Zhou and Z. L. Wang, ACS Nano, 2012, 6, 656–661.

35. C. Yuan, X. Zhang, L. Su, B. Gao and L. Shen, J. Mater. Chem., 2009, 19, 5772–5777.

36. Q. Wu, Y. Xu, Z. Yao, A. Liu and G. Shi, ACS Nano, 2010, 4, 1963–1970.

37. L. Yuan, X. Xiao, T. Ding, J. Zhong, X. Zhang, Y. Shen, B. Hu, Y. Huang, J. Zhou and Z. L. Wang, Angew. Chem., Int. Ed., 2012, 51, 4934–4938.

38. H. Jiang, C. Li, T. Sun and J. Ma, Nanoscale, 2012, 4, 807–812.

39. J. Zhang, J. Jiang, H. Li and X. S. Zhao, Energy Environ. Sci., 2011, 4, 4009–4015.

40. J. Jiang, Y. Li, J. Liu, X. Huang, C. Yuan and X. W. Lou, Adv. Mater., 2012, 24, 5166–5180.

41. M. Zhi, C. Xiang, J. Li, M. Li and N. Wu, Nanoscale, 2013, 5, 72–88.

42. G. Xiong, K. P. S. S. Hembram, R. G. Reifenberger and T. S. Fisher, J. Power Sources, 2013, 227, 254–259.

43. X. Lang, A. Hirata, T. Fujita and M. Chen, Nat. Nanotechnol., 2011, 6, 232–236.

44. L. Wei, N. Nitta and G. Yushin, ACS Nano, 2013, 7, 6498– 6506.

45. B. Radha, A. A. Sagade and G. U. Kulkarni, ACS Appl. Mater. Interfaces, 2011, 3, 2173–2178.

46. T. Bhuvana and G. U. Kulkarni, ACS Nano, 2008, 2, 457–462.

47. A. A. Sagade, B. Radha and G. U. Kulkarni, Sens. Actuators, B, 2010, 149, 345–351.

48. B. Radha and G. U. Kulkarni, Small, 2009, 5, 2271–2275.

49. B. Radha, S. H. Lim, M. S. M. Saifullah and G. U. Kulkarni, Sci. Rep., 2013, 3, 1078.

50. H. Nakanishi and B. A. Grzybowski, J. Phys. Chem. Lett., 2010, 1, 1428–1431.

51. S. W. Lee, J. Kim, S. Chen, P. T. Hammond and Y. S. Horn, ACS Nano, 2010, 4, 3889–3896.

52. X. Jin, W. Zhou, S. Zhang and G. Z. Chen, Small, 2007, 3, 1513–1517.

53. B. Radha, G. Liu, D. J. Eichelsdoerfer, G. U. Kulkarni and C. A. Mirkin, ACS Nano, 2013, 7, 2602–2609.

54. T. Bhuvana and G. U. Kulkarni, Int. J. Nanosci., 2011, 10, 699– 705.

55. M. Armand and J. M. Tarascon, Nature, 2008, 451, 652–657.

56. S. D. Jones and J. R. Akridge, Solid State Ionics, 1996, 86–8, 1291.

57. J. Lin, C. G. Zhang, Z. Yan, Y. Zhu, Z. W. Peng, R. H. Hauge, D. Natelson and J. M. Tour, Nano Lett., 2013, 13, 72–78.

58. C. Z. Meng, J. Maeng, S. W. M. John and P. P. Irazoqui, Adv. Energy Mater., 2013, DOI: 10.1002/aenm.201301269.

Chapter VB

Highly Stable Supercapacitor Electrodes for Harsh Electrolytes

Summary

In this chapter, supercapacitors have been fabricated by employing Pd_4S as the electrode material which is highly conducting and chemically robust to the acid and alkali media. The synthesis strategy is simple and involves a single step thermolysis of palladium octanethiolate film in the H_2 atmosphere at 250 °C for 1 h. Besides its conducting nature, its porous morphology makes it a suitable electrode material for supercapacitors. The electrochemical properties of the Pd_4S were examined in harsh alkali media (30 M KOH). Typically in the literature, only lower concentration of the electrolyte (6 M KOH) is preferred as the electrode may not stand higher concentrations. With this device, a specific capacitance of 570 F/g with energy and power densities of 28 Wh/kg and 1.5 kW/kg respectively, were achieved with 30 M KOH electrolyte. After 1500 cycles of charging and discharging with a constant current density of 1.75 A/g, more than 98% capacitance retention was observed.

VB.1 Introduction

It is of great importance to achieve high power energy resources with excellent cyclic stability, safety and low-cost [1,2]. Among many energy storage devices, supercapacitors attract great attention due to its high energy and power densities with long-cycle life and safe mode of operation [3]. There have been many efforts to improve the storage efficiencies of supercapacitors by various strategies such as introducing oxides and sulfides as pseudocapacitive materials [4-6], improving the surface area by nanostructures [7], increasing the potential working window [8], etc. The former increases the storage capacity by introducing the Faradic reactions in the active materials. Recently, some metal sulfides such as CoS_x, CuS_x, Ni_xS_y are gaining much interest as the electrode material for batteries and supercapacitors due to their exciting intrinsic properties and high electrochemical performance [9-15]. Furthermore, nanostructures of metal sulfides on carbon matrices such as graphene

Paper based on this study: Manuscript Submitted

and CNTs improve the capacitance and cycling stability of the devices [9-12]. However, maintaining high cycling capability and stability of metal sulfide based devices remains a great challenge till date due to their poor conductivity and chemical instability in electrolytic environment [13]. Hence, there is a necessity to develop electrodes with enhanced stability and conductivity.

VB.2 Scope of the present investigation

Here, a new strategy was introduced to fabricate supercapacitors with Pd_4S plates serving both as current collector and active material owing to its stability towards harsh acidic and alkaline environments [16]. In this study, the electrochemical performance of Pd_4S based supercapacitor device was demonstrated in higher KOH electrolyte concentrations (6 M and 30 M). The capacitance seems to increase with the increase in the electrolyte concentration, possibly due to the stability of electrode in such alkali environment. Furthermore, an organic electrolyte (1 M tetrabutylammonium bromide (TBABr)) was employed to enhance the potential window of supercapacitor beyond 1 V.

VB.3 Experimental Details

Synthesis of nc-Pd/C composite

The synthesis procedure for the precursor, Pd octanethiolate, $Pd(SC_8H_{17})_2$, is reported elsewhere.[16] Briefly, 5 mM of 1-octanethiol (Sigma Aldrich) was added to 5 mM of $Pd(OAc)_2$ (Sigma Aldrich) in toluene solution while stirring. The obtained octanethiolate was washed with methanol and acetonitrile and dispersed in toluene. The glass substrates used for film formation were cleaned with deionized water, IPA and, acetone followed by drying under N_2 flow. A 100 μL of 10 mM Pd octanethiolate precursor solution was drop casted on a cleaned glass substrate (1 × 2.5 cm^2) resulting in an orange colored film. Pd_4S film was obtained by annealing thiolate in a tube furnace in the H_2 atmosphere (temperature ~ 250 °C) for 1 h.

VB.4 Results and Discussion

The Pd_4S thin film was obtained by annealing palladium octanethiolate solution on the glass substrate in the H_2 atmosphere at 250 °C for 1 h (Figure VB.1a). The obtained films were highly conducting with the resistance of few Ohms for ~ 300 nm film and the sharp peaks in XRD identifiable for Pd_4S phase (JCPDS PDF No. 731387)

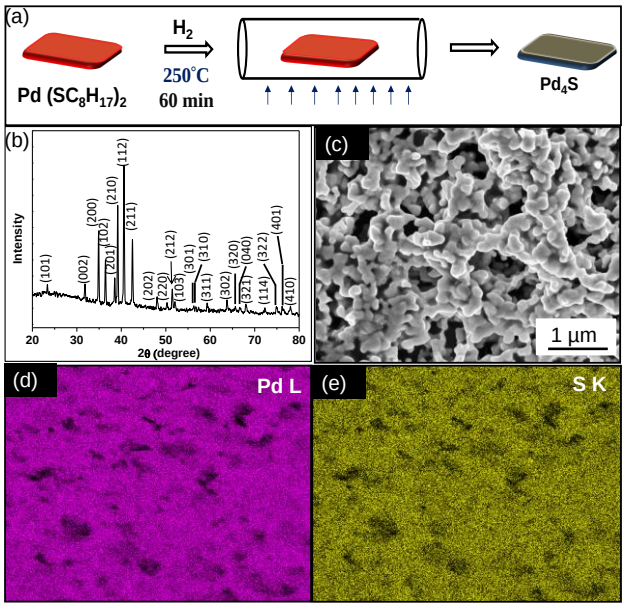

Figure VB.1 (a) Schematic illustration of the synthesis procedure for Pd_4S electrodes fabrication. (b) XRD pattern of the prepared Pd_4S thin film. (c) SEM image and EDS mapping (d) and (e) of the Pd_4S film.

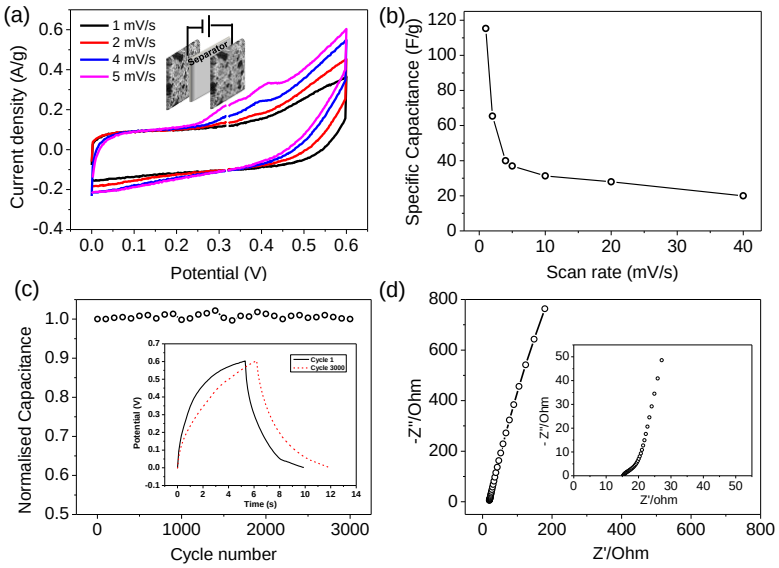

Figure VB.2 (a) Cyclic voltammetry (CV) curves of the Pd_4S supercapacitor in 6 M KOH electrolyte. Inset is the schematic of two electrode configuration of the symmetric Pd_4S electrodes along with the separator. (b) The plot of specific capacitance of the device as a function of various scan rates. (c) Cycling performance of the Pd_4S electrodes at a current density of 0.5 A/g. Inset is the charge-discharge (CD) curves of 1st and 3000th cycles. (d) Impedance Nyquist plot at open circuit potential. Inset is the magnified portion of the high-frequency region.

confirms the high crystallinity of the film with no impurity peaks (Figure VB.1b). The microscopy results are shown in Figure VB.1c-e. SEM image shows the highly porous Pd_4S surface (see Figure VB.1c). The uniform distribution of Pd and S elements throughout the thin film surface was evidenced from the EDS mapping shown in Figure VB.1d-e.

The stability of Pd_4S electrode in 6 M KOH electrolyte was checked before the supercapacitor fabrication. The resistance of the electrodes as well as its adhesion to the glass substrate was remained unaltered even after 5 h of dipping in KOH solution. A supercapacitor was fabricated by assembling two Pd_4S electrodes separated by a filter paper. The CV curve was recorded at different scan rates in the potential range of 0 to 0.6 V (Figure VB.2a). All the CV curves were shown a deviation from the ideal rectangular behaviour signifying the pseudocapacitive characteristics of Pd_4S. The specific capacitance from the voltammetric response was calculated using the following equation VB.1

$$C_S = 2(1/m_t)(I/s) \quad \text{(VB.1)}$$

where m_t is the total mass of the electrodes (~ 0.5 mg), I is the current in mA and s is the sweep rate in mV/s (s = dV/dt). A maximum specific capacitance of 115 F/g was obtained for 1 mV/s scan rate at potential of 0.3 V (see Figure VB.2b). The capacitance dropped down to 20 F/g at higher scan rates (40 mV/s). The cycle life and coulombic efficiency (ratio of discharging and charging durations) of the supercapacitor were tested by performing 3000 cycles of continuous charging and discharging at a current density of 0.5 A/g. As shown in Figure VB.2c, the device exhibited nearly 100% capacitance retention as well as coulombic efficiency (ratio of discharging and charging times) confirming the excellent reversibility of Pd_4S electrodes. The electrochemical impedance spectrum (Figure VB.2d) showed a small semi-circle in the higher frequency region indicating the high interfacial charge-transfer resistance (~ 15 Ω) probably due to the poor electrical conductivity of the Pd_4S electrodes. At lower frequencies, curves were parallel to the y-axis representing the capacitance nature of the electrode.

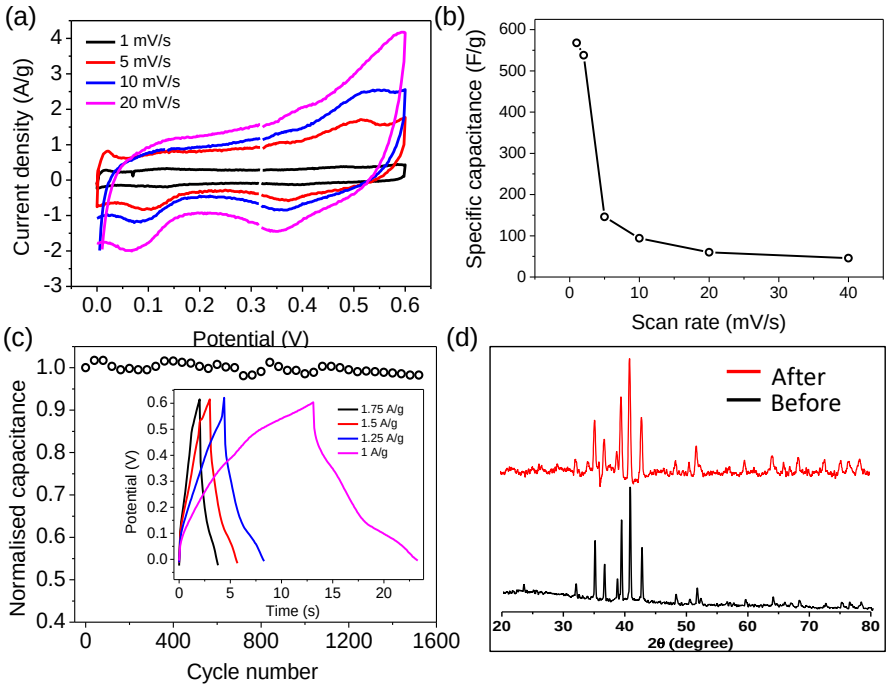

Figure VB.3 (a) CV curves of the Pd_4S supercapacitor in 30 M KOH electrolyte at different scan rates and its corresponding specific capacitance (b). (c) Cycling performance of the Pd_4S electrodes at 1 A/g current density. Inset is the CD curves of various current densities. (d) XRD patterns of the Pd_4S electrode before and after testing its energy storage performance.

Figure VB.3a shows the CV profiles of Pd_4S supercapacitor in the potential range of 0 – 0.6 V. The CV curves indicate the pronounced pseudocapacitive nature of Pd_4S electrodes. The capacitance of the device increased to 570 F/g from 115 F/g by increasing the concentration of the KOH electrolyte from 6 M to 30 M. It is merely possible due to the robustness of the electrodes towards such harsh conditions. By increasing the scan rate (10 mV/s), the capacitance dropped down to 100 F/g (Figure VB.3b). Another important parameter for supercapacitor is its cycling stability. Therefore, CD measurement was performed for 1500 cycles at 1.75 A/g current density. Nearly 98% retention was observed. The galvanostatic charge-discharge profiles at different current densities are provided as the inset in Figure VB.3c. Furthermore, the electrodes were analyzed to detect any possible oxidations due to their exposure to concentrated KOH electrolyte. More importantly, XRD patterns of the electrode did not show any peaks corresponding to the impurities (Figure VB.3d).

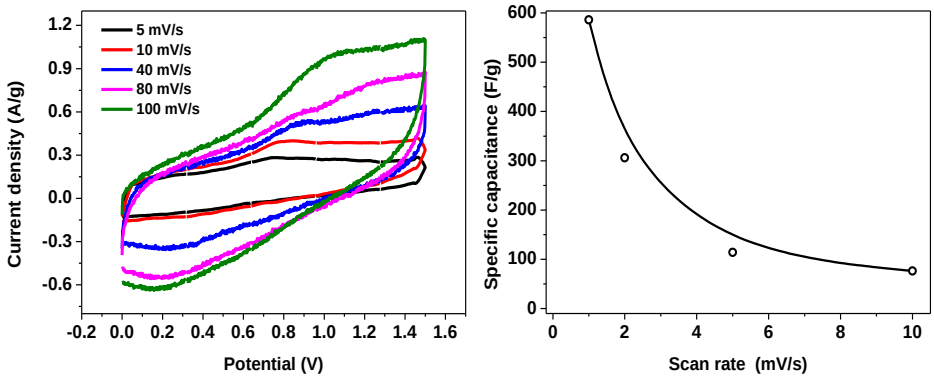

Figure VB.4 (a) CV curves of the Pd_4S supercapacitor in 1 M TBABr organic electrolyte at different scan rates and its corresponding specific capacitance (b).

Instead of increasing the energy storage using the higher concentration alkali electrolyte, one can use organic electrolytes and thus can improve the operating voltage window beyond 1 V. The restriction of voltage window in the aqueous electrolyte is mainly due to the thermodynamic decomposition of water (1.23 V). Here, 1 M TBABr dissolved in acetonitrile was used as an electrolyte due to which the device working potential increased up to 1.6 V as shown in Figure VB.4a. The maximum specific capacitance obtained was ~ 590 F/g at 1 mV/s which dropped to 100 F/g while increasing the scan rate (10 mV/s) (Figure VB.4b).

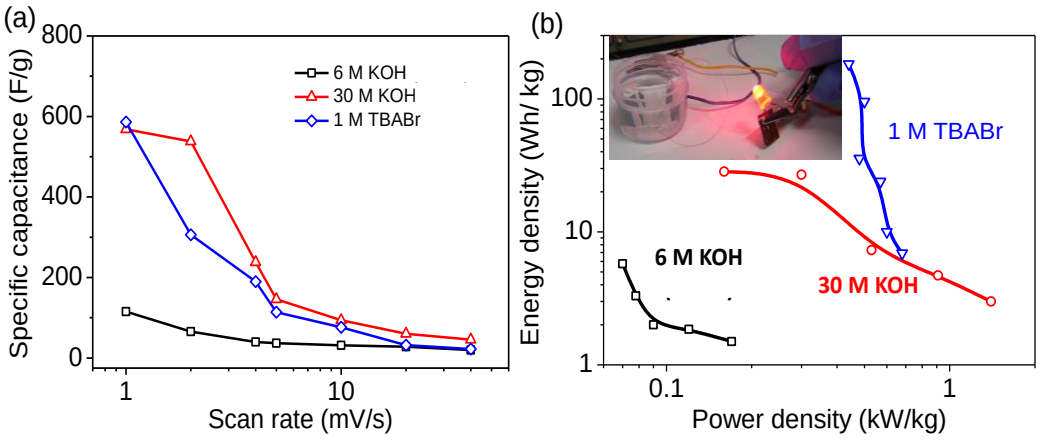

Figure VB.5 (a) Comparison of specific capacitance and (b) Ragone plot showing the estimated energy and power densities obtained for Pd_4S supercapacitors using various electrolytes.

The specific capacitance *vs* scan rates of Pd_4S supercapacitors in different electrolytes is compared in Figure VB.5a. It is clearly noticeable that the specific capacitance slowly decreased with the increase in scan rate for all electrolytes. Both 30 M KOH and 1 M TBABr electrolytes provide the higher capacitance value. The energy and power densities of a supercapacitor can be estimated from the equation VB.2 and VB.3.

$$E = (1/2)C_S(V)^2 \text{.....(VB.2)}$$

where V is the working potential window of an electrolyte.

$$\text{Power (P)} = I \times V \text{ .....(VB.3)}$$

Figure VB.5b shows the Ragone plot of calculated energy and power densities. High energy (28.4 Wh/kg) and power (1.4 kW/kg) densities were obtained with slow and fast charging and discharging rates for 30 M KOH electrolytes. On the other hand, for 1 M TBABr organic electrolyte, maximum energy and power densities of 183 Wh/kg and 0.69 kW/kg, respectively, were obtained. The obtained values are quite comparable to other metal sulfides based supercapacitors supported on the graphene or CNTs [11,12].

VB.5 Conclusions

In summary, a highly conducting Pd_4S thin film (~ 300 nm) was prepared on glass plates by a simple thermolysis (250 °C) of Pd octanethiolate in the H_2 atmosphere. The as-formed Pd_4S film serves as an electrode for supercapacitor energy storage device. The electrochemical performance was investigated in 6 M and 30 M KOH electrolytes which gave a maximum specific capacitance of 570 F/g at a scan rate of 1 mV/s. Further, an organic electrolyte (1 M TBABr) was used which showed the maximum capacitance, energy, and power densities of 590 F/g, 183 Wh/kg, and 0.69 kW/kg, respectively. Also, the precursor is amenable for patterning by e-beam and soft lithography, and it can be taken forward to fabricate in-plane or micro-supercapacitor for miniaturization in power source on a chip. Unlike many other electrode materials, Pd_4S can withstand harsh environments; it can become a suitable electrode material in the energy storage devices such as supercapacitors and batteries.

References

1. J. M. Tarascon and M. Armand, *Nature*, 2001, **414**, 359.
2. M. Winter and R. J. Brodd, *Chem. Rev*., 2004, **104**, 4245
3. C. Liu, F. Li, L. P. Ma and H. M. Cheng, *Adv. Mater.*, 2010, **22**, 28.
4. J. Zhang, J. Jiang, H. Li and X. S. Zhao, *Energy Environ. Sci*., 2011, **4,** 4009.
5. W. Sugimoto, H. Iwata, Y. Yasunaga, Y. Murakami and Y. Takasu, *Angew. Chem., Int. Ed*., 2003, **42**, 4092.
6. Q.Wang, L. Jiao, H. Du, J. Yang, Q. huan, W. Peng, Y. Si, Y. Wang and H. Yuan *Crys. Eng. Comm.*, 2011, **13,** 6960.
7. C. W. Cheng , B. Liu , H. Y. Yang , W. W. Zhou , L. Sun , R. Chen , S. F. Yu , J. X. Zhang , H. Gong , H. D. Sun , H. J. Fan , *ACS Nano* 2009, **3**, 3069.
8. J. Y. Hwang, M. Li, M. F. El-Kady, and R. B. Kaner, *Adv. Funct. Mater*. 2017, **27**, 1605745.
9. T. Zhu, H. B. Wu, Y. Wang, R. Xu and X. Wen Lou, *Adv. Energy Mater*. 2012, **2**, 1497.
10. B. Wang, J. park, D. Su, C. Wang, H. Ahn and G. Wang, *J. Mater. Chem*., 2012, **22**, 15750.
11. B. Qu, Y. Chen, M. Zhang, L. Hu, D. Lei, B. Lu, Q. Li, Y. Wang, L. Chen and T. Wang, *Nanoscale*, 2012, **4**, 7810.
12. T. Zhu, B. Xia, L. Zhou and X. Wen Lou*, J. Mater. Chem.,* 2012, **22**, 7851.
13. Q. Wang, L. Jiao, H. Du, Y. Si, Y. Wang and H. Yuan, *J. Mater. Chem*., 2012, **22**, 21387.
14. T. Zhu, Z. Wang, S. Ding, J. S. Chen, X. Wen Lou, *RSC Advances*, 2011, **1**, 397.
15. L. Zhang, H. B. Wu and X. Wen Lou, *Chem. Commun*., 2012, **48**, 6912.
16. B. Radha and G. U. Kulkarni, *Adv. Funct. Mater.*, 2010, **20,** 879.

Chapter VC

Patterning of Bimetals and Oxides Using Single Source Precursors

Summary

Patterning of materials such as metals, alloys as well as compounds such as oxides is important for industrial applications. Among the several existing methods, patterning through micromolding using PDMS stamps is a quite simple process giving rise to large throughputs. A method proposed here uses metal anion alkyl ammonium complex precursor (M-ToABr) which can be easily molded and converted to the desired material in a single step known as direct patterning. In this work, patterning of bimetals such as PtPd, PdAu, AuCu and PtAu and oxides such as ITO were obtained by soft lithography method.

VC.1 Introduction

Alloys and bimetals of noble metals are immensely useful for various applications including catalysis [1], optics [2], magnetism [3], owing to their improved performance and stability [4] over simple metals. Especially nanoparticles of bimetals and alloys with the high surface area have been most sought after, due to the synergy of metal combinations. For, e.g., AuCu nanoparticles have been used for Cu nanoparticles alone due to its enhanced oxidation stability [4].

Most of the applications such as catalysis, require supporting these bimetal/alloy particles on a solid support. Conventionally drop casting, or spin-coating of pre-made nanoparticle solutions are used for this purpose which leads to aggregation and reduction of the available surface. Also, the capping agents required for stabilizing the nanoparticles in solution, are hard to get rid off, after the deposition of nanoparticles onto solid supports. It would be ideal to grow the nanoparticles on the support substrate so as to fix them firmly without contamination from capping agents, as well as to avoid the aggregation [5]. Thus, it leads to the emergence of a need for a simple method to make such alloy and bimetallic nanoparticles on substrates.

Paper based on this study: Manuscript under preparation

VC.2 Scope of the present investigation

Achieving the patterning of active materials into size and shape controlled structures are important as well as difficult because, in nanotechnology, properties mainly depend on size and shape of materials [6]. Noble metals, such as Au, Pd, and Pt which are widely used in microelectronics, are ideal candidates for these processes due to their stability versus oxidation combined with a high conductivity. Transparent conducting oxides are essential for making optoelectronic devices such as displays, organic light-emitting diodes (OLEDs), thin-film transistors (TFTs), and solar cells as it combines optical transparency with controllable electrical conductivity [7]. Among the several existing methods, obtaining a pattern of metal or combination of different metals through micromolding using PDMS stamps are quite simple and gives large throughput. A method proposed here uses the precursor which can be easily converted to desired material in a single step known as direct patterning [8,9]. Through this method alloys (AuPd), bimetals (PtAu, PtPd, AuPd) and oxide (ITO) have been prepared.

VC.3 Experimental Details

The metal precursors like K_2PtCl_4, $PdCl_2$, In_2O_3, $SnCl_2.2H_2O$ and $Pd(OAc)_2$ were purchased from Sigma Aldrich and $CuCl_2$, $HAuCl_4$ and tetraoctylammonium bromide (ToABr) from Spectrochem, India. They were used without further purification. Double distilled and deionized water was used in this study. To 50 mM bimetal solutions in water, 50 mM ToABr solution in toluene was added and stirred to aid the phase transfer. In certain cases (ITO, AuCu), conc. HCl was added to the aqueous solution to support the effective phase transfer of metal ions to organic medium.

Direct Micromolding

Glass substrate and Si substrates were cleaned with DI water, acetone, and IPA solutions and dried under N_2 atm. An Elastomeric PDMS stamp was obtained by mixing Sylgard 184 curing agent (Dow Corning) and its elastomer in the ratio of 1:10 and mixed thoroughly. After degassing the mixture under vacuum for 30 min, PDMS was coated onto the polycarbonate backing of the master (CD) and then cured at 90 °C for 5 h. The stamp was peeled off from the master contained protruding line feature of ~ 505 nm width separated by ~ 950 nm channels. The thickness of the

stamp was ~ 3 mm. The stamp was cleaned in hexane and ethanol subsequently and dried in the N_2 atmosphere.

VC.4 Results and Discussion

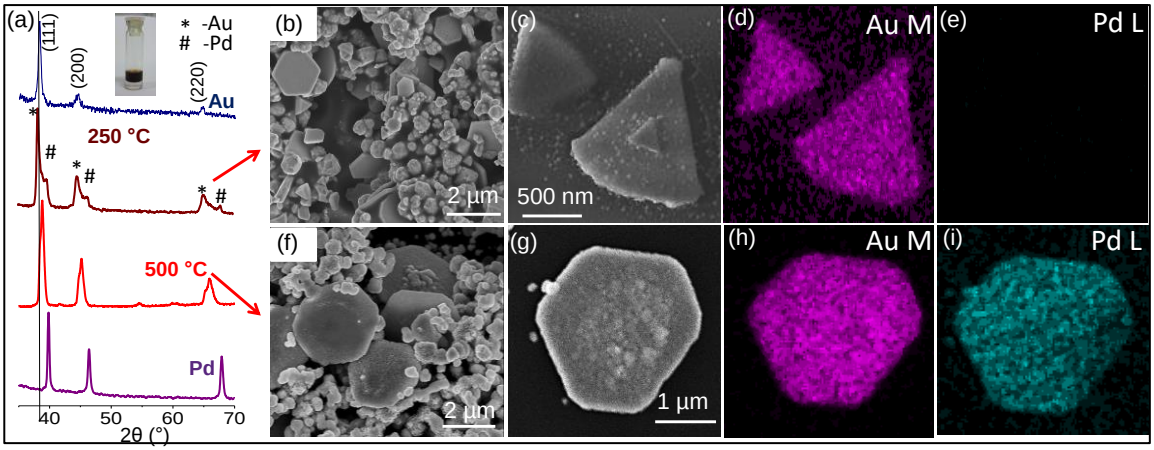

Figure VC.1 (a) XRD and SEM images of Au-Pd bimetal and alloy. The peaks are indexed by reference to the standard pattern in JCPDS PDF files indicated in parentheses (a) (Au (65-2870), Au-Pd bimetal, $Au_{0.52}Pd_{0.48}$ alloy and Pd (88-2335)). Inset shown is phase transferred AuPd-ToABr complex. (b) & (c) and (f) & (g) are the low and high magnification SEM images of Au- Pd bimetal and Au-Pd alloy, respectively. EDS mapping to confirm the distribution of Au and Pd on triangular and hexagonal shaped micro crystallites of bimetal and alloy compositions are shown in (d) & (e) and (h) & (i), respectively.

Using this modified Brust method [10], not only metals but also bimetals and alloys of different metal combinations were quite possible by direct thermolysis. The bimetals of Pd-Au, Pd-Pt, Au-Pt and Cu-Au was synthesized using metal-ToABr complex. By subjecting the AuPdToABr complex to different thermolysis temperature (250 °C or 500 °C) in air, AuPd bimetal or the alloy composed of triangle- and hexagonal-shaped and submicron-sized particles were obtained (Figure VC.1). Figure VC.1b is the SEM image of Pd-Au bimetals and EDS mapping in Figure VC.1c-e clearly indicate the presence of only Au over triangle shaped particles and the absence of Pd. However, thermolysis at 500 °C leads to homogenous mixing of metal ions and formation of hexagonal and triangular shaped particles with an uniform distribution of Au and Pd as seen from the SEM and EDS mapping shown in Figure VC.1f-i. The resistance and resistivity of PdAu film are 12.3 Ω and 65.23 µΩ.cm, respectively.

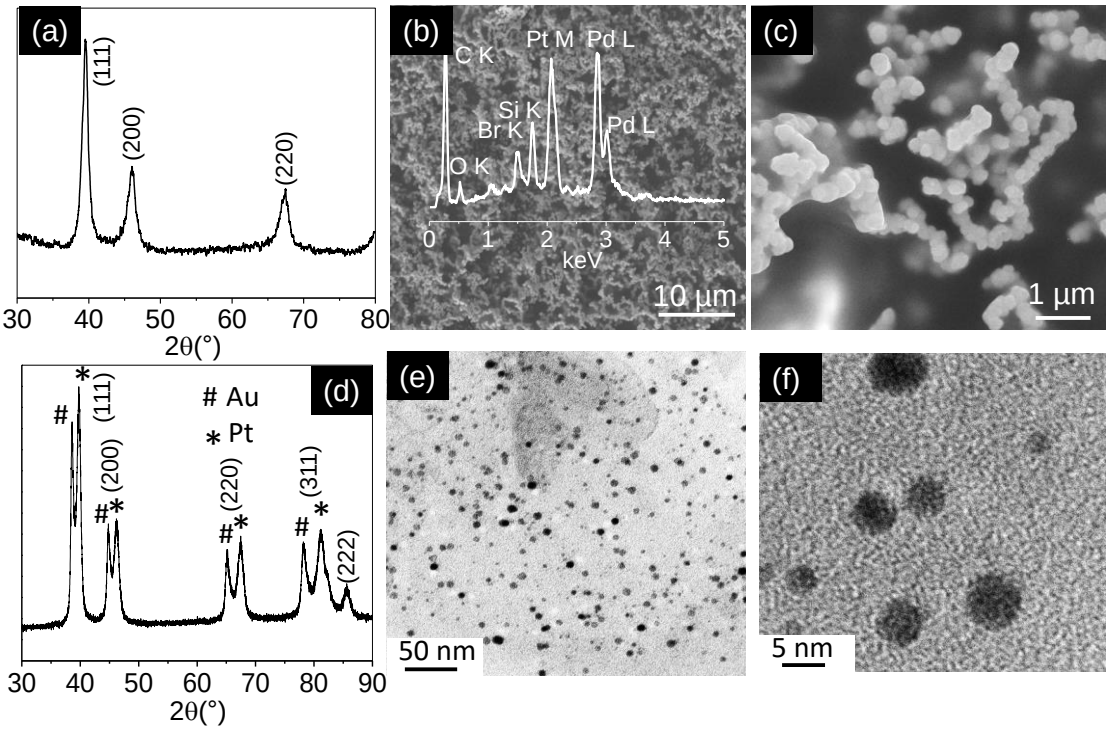

Figure VC.2 XRD (a) and SEM images of (b & c) PtPd alloy. ED spectrum is overlaid on the SEM image in (b). (d) XRD and (e & f) TEM images of Au-Pt bimetal at different magnifications.

Similarly, by mixing different metal anion precursors while phase transferring, the bimetals like Pt-Pd was obtained by simple thermolysis at 250 °C for 1h in air (Figure VC.2a-c). The obtained thin film was analysed using XRD, SEM, and EDS confirming the presence of Pt and Pd in the ratio of 57:43. The resistance and resistivity of the obtained film are 2.58 Ω and 86.69 µΩ.cm. By annealing the AuPt-ToABr precursor at 375 °C for 3h in air leads to the formation of Au-Pt (54:46) bimetal (as shown in Figure VC.2d) with low resistivity 73.02 µΩ.cm. The obtained particles are of few nanometer dimensions as shown in Figure VC.2e and f.

The direct micromolding involves a soft PDMS stamp as mold, replica from the polycarbonate backing of the master (CD). The precursor solution of ~ 60 µL (Metal-ToABr complex) was dropped on a Si/glass substrate on which a patterned PDMS was kept. The solution fills the microchannels exist between stamp and substrate due to

capillary action. The temperature was raised to 250 °C at the ramp rate of 2 °C/min and dwelled at that temperature for 30 min. After cooled down to room temperature,

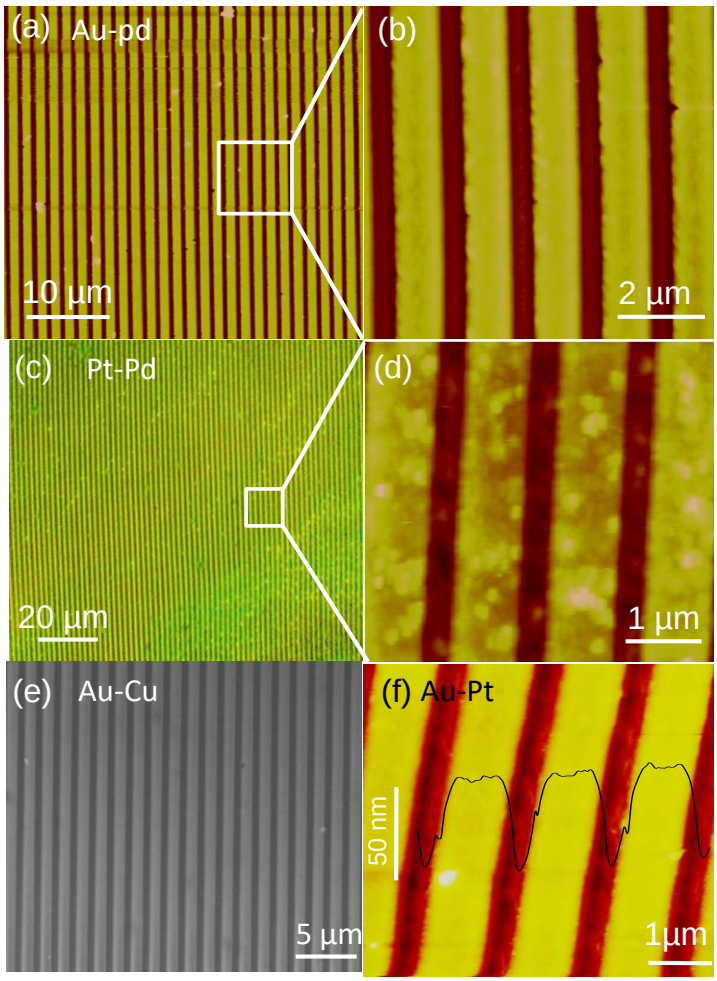

Figure VC.3 Patterning of different bimetal and alloys. (a) AFM image showing nanowires of Au-Pd over the large area and an enlarged portion is shown in (b). (c) Optical microscopic image of Pt-Pd µ-stripe grating and AFM image of the same in (d). (e) SEM image of Au-Cu µ-stripe grating. (f) AFM image of the formed Au-Pt lines with the z-profile overlaid.

the stamp was removed to realize the periodic lines of bimetals. AFM and SEM images of metal grating patterns are shown in Figure VC.3a-f.

The thermolysis of the InSn-ToABr precursor at 500 °C in air leads to the fabrication of ITO thin film. This precursor ratio gives ~ 10 % Sn-doped In_2O_3. By changing the ratio of Sn, one can tune the properties of the obtained ITO. The SEM image in the Figure VC.4a shows particulate nature of the film which is further evidenced by the powder XRD pattern (Figure VC.4d). As this organic precursor ink

gives the ITO by direct heating, the ITO gratings were obtained by micromolding. The Figure VC.4b shows the large area pattern of ITO on a silicon surface. It can be extended to other substrates like mica, kapton, etc. which will offer flexible transparent conducting electrode. The Figure VC.4c shows the AFM image of the patterned ITO. The resistance of the film across 2 cm is 73.2 Ω, calculated from I-V curve shown in Figure VC.4e and the transmittance of the film is around 80% (Figure VC.4f).

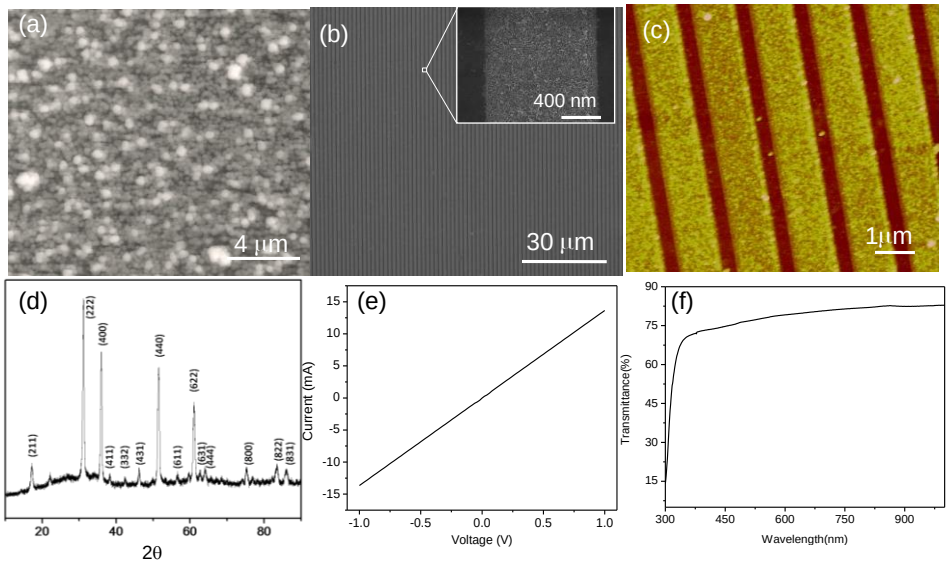

Figure VC.4 SEM images of ITO thin film (a) and μ-stripe grating pattern (b). (c) AFM image of the ITO pattern. (d) XRD pattern, (e) I-V characteristics, and (f) transmittance measurement of the prepared ITO film.

VC.5 Conclusions

In summary, the possibility of making thin films and micropatterns of various bimetals (AuPd, AuPt, PtPd, AuCu) and oxides (ITO) were explored using metal organic precursor. The metal organic complex was obtained by the simple process of transferring metal anions to the organic medium using tetraoctylammonium bromide as phase transferring agent. An organic precursor is highly feasible to make thin films and amenable for the soft lithography process to obtain periodic metal gratings across 0.25 cm^2 area. By controlling the ratio of metals and thermolysis temperature,

products with the desired composition could be achieved. This method can be generalized to various materials.

References

1. J. Llorca, A. Casanovas, M. Domínguez et al., *J. Nanopart. Res.,* 2008, **10**, 537–542.
2. B. Rodriguez-Gonzalez, A. Burrows, M. Watanabe et al., *J. Mater. Chem.,* 2005, **15**, 1755–1759.
3. H. She, Y. Chen, X. Chen et al., *J. Mater. Chem*., 2012, **22**, 2757–2765.
4. Y. Yoshida, K. Uto, M. Hattori, and M. Tsuji, *CrystEngComm*, 2014, **16**, 5672–5680.
5. T.C. Deivaraj and J.Y. Lee, *J. Electrochem. Soc.,* 2004, **151**, A1832–A1835.
6. M.Cavallini, P. Stoliar, J. F. Moulin, M. Surin, P. Lecle`re, R. Lazzaroni, D. W. Breiby, J. W. Andreasen, M. M.Nielsen, P. Sonar, A. C. Grimsdale, K. Mu¨llen, F. Biscarini, *Nano Lett.* 2005, **5**, 2422-2425.
7. T. Minami, *Thin Solid Films*, 2008, **516**, 5822-5828.
8. B. Radha, G. U. Kulkarni, *Small*, 2009, **5**, 2271-2275.
9. B. Radha , S. Kiruthika, G. U. Kulkarni, *J. Am. Chem. Soc*, 2011, **133**, 12706–12713.
10. M. Brust, M. Walker, D. Bethell et al., *J. Chem. Soc. Chem. Commun.,* 1994, **7**, 801–802.

Summary and Outlook

In this thesis, the crackle templating method developed in this laboratory was taken to next level by incorporating into many applications to produce various devices. Prior to device fabrications, the potential of the template method for large area electrodes was established by rod coating (**Chapter IIIB**) and roll and spray coating (**Chapter IIIC**) techniques. Functional devices, particularly in the context of smart windows (**Chapter IV**) were then fabricated using mesh as transparent electrode. The usage was extended to other devices such as defrosting and defogging windows (**Chapter IVA.2**), transparent supercapacitors (**Chapter IVC**), electro-chromic supercapacitors (**Chapter IVD**) and transparent photodetectors (**Chapter IVE**). Thus, the thesis clearly demonstrates how metal mesh serves as inexpensive alternative for ITO films while having additional advantages such as high temperature attainability (600 °C) and flexible or curved heaters with few second response times. Mesh does suffer from shortcomings such as non-uniformity of the electric field due to the insulating uncovered glass regions. This issue was specially addressed by coating mesh with conducting metal oxides such as SnO_2 and AZO (**Chapter IIID**) and was utilized for replacing ITO in LC devices (**Chapter IVB**).

While this thesis work targets large area metal mesh based transparent conductors, the next possibility is to realize the TCE production by roll-to-roll or such bulk production methods. As the devices such as touch screen and other functional devices require patterning of metal mesh, metal deposition can be controlled by mixing templating method with other methods such as screen printing. Other possibilities include functionalization of metal wire for specific surface applications. Another prospective of this approach is to fabricate mesh networks of various functional materials with heterostructures instead of bare metals.

List of Publications

From this thesis

1. G. U Kulkarni, **S. Kiruthika**, R. Gupta, K. D. M. Rao, Towards low cost materials and methods for transparent electrodes, *Current Opinion in Chemical Engineering* **2015**, *8*, 60–68.
2. **S. Kiruthika**[#], K. D. M. Rao[#], A. Kumar, R. Gupta, G. U. Kulkarni, Metal wire network based transparent conducting electrodes fabricated using interconnected crackled layer as template, *Materials Research Express* **2014** *1*, 026301 ([#] equal contribution)
3. **S. Kiruthika**, Ritu Gupta, K. D. M. Rao, Swati Chakraborty, Nagarajan Padmavathy and G. U. Kulkarni, Large area solution processed transparent conducting electrode based on highly interconnected Cu wire network, *J. Mater. Chem. C,* **2014**, *2*, 2089
4. **S. Kiruthika**, Ritu Gupta, Aman Anand, Ankush Kumar, and G. U. Kulkarni, Fabrication of Oxidation-Resistant Metal Wire Network-Based Transparent Electrodes by a Spray-Roll Coating Process, *ACS Appl. Mater. Interfaces* **2015**, 7, 27215-27222.
5. **S. Kiruthika**, A.K. Singh, M. Janani, M. G. Sreenivasan and G. U. Kulkarni, Fabrication of Metal mesh and oxide based hybrid transparent electrodes for surface electrical uniformity, Manuscript under preparation.
6. R Gupta, K. D. M. Rao, **S. Kiruthika**, G. U. Kulkarni, Visibly Transparent Heaters, *ACS Appl. Mater. Interfaces* **2016**, *8*, 12559–12575.
7. **S. Kiruthika**, Ritu Gupta and G. U. Kulkarni, Large area defrosting windows based on electrothermal heating of highly conducting and transmitting Ag wire mesh, *RSC Adv*., **2014**, *4*, 49745.
8. **S. Kiruthika** and G. U. Kulkarni, Energy efficient hydrogel based smart windows with low cost transparent conducting electrodes, *Solar Energy Materials & Solar Cells* **2017,** *163,* 231–236
9. **S. Kiruthika**[#]**,** A. K. Singh[#]**,** I. Mondal and G. U. Kulkarni**,** Fabrication of solar and electrically adjustable smart windows for indoor light and heat modulations, Under revision in *J. Mater. Chem. C* ([#] equal contribution)
10. **S. Kiruthika**, M. Indrajit, M. Janani, A. Kumar, Vimala, Madhuri, G. Nair, S. K Prasad and G. U. Kulkarni, Manuscript under preparation.

11. **S. Kiruthika**, Chaitali Sow and G. U. Kulkarni, Transparent and flexible super-capacitors with networked electrodes, Submitted **(May 2017)**
12. **S. Kiruthika** and G U Kulkarni, Smart Electrochromo Supercapacitor With Metal Mesh Electrodes, Submitted **(May 2017)**
13. **S. Kiruthika**, S Singh, G. U. Kulkarni, Large area transparent ZnO photodetectors with Au wire network electrodes, *RSC Adv.* **2016**, *6*, 44668-44672.
14. **S. Kiruthika**[*], N Kurra[*], G. U, Kulkarni, Solution processed sun baked electrode material for flexible supercapacitors, *RSC Adv*. **2014**, *4*, 20281-20289.
15. **S. Kiruthika**, B. Radha and G. U. Kulkarni, Patterning of bimetals, alloys and transparent metal oxides by soft lithography using simple single source precursors, Manuscript under preparation.
16. **S. Kiruthika** and G. U. Kulkarni, Simple methods to fabricate highly corrosive resistant Pd_4S electrodes for supercapacitors, Manuscript under preparation**.**
17. **S. Kiruthika** and G. U. Kulkarni, Studying the Modulation in Resistance of Partially annealed Pd thiolate Films, Manuscript under preparation.

Co-authored publications:

18. B. Radha, **S. Kiruthika**, G. U. Kulkarni, Metal anion–alkyl ammonium complexes as direct write precursors to produce nanopatterns of metals, nitrides, oxides, sulfides, and alloys, *J. Am. Chem. Soc.* **2011**, *133*, 12706–12713.
19. R. Gupta, **S. Kiruthika**, K. D. M. Rao, M. Jørgensen, F. C. Krebs, G. U. Kulkarni Screen-Display-Induced Photoresponse Mapping for Large-Area Photovoltaics, *Energy Technology* **2013**, *1* , 770-775
20. MV Madsen.., R. Gupta, **S. Kiruthika**, G. U. Kulkarni, F. C. Krebs et al, Worldwide outdoor round robin study of organic photovoltaic devices and modules, *Solar Energy Materials and Solar Cells* **2014**, *130*, 281-290.
21. R. Gupta, K. D. M. Rao, K. Srivastava, A. Kumar, **S. Kiruthika**, G. U. Kulkarni, Spray coating of crack templates for the fabrication of transparent conductors and heaters on flat and curved surfaces, *ACS Appl. Mater. Interfaces* **2014**, *6*, 13688-13696.

Patent filled

1. K. D. M. Rao, R. Gupta, , B. Radha, **S. Kiruthika** and G. U. Kulkarni, "composition, substrates and methods there of" PCT application number: PCT/IB2014/059411

Book Chapter

1. "*Synthesis of Nano and Microcrystallites of Metals Using Metal-Organic Precursors"* by Giridhar U. Kulkarni, Gangaiah Mettela, and **S. Kiruthika** in *Molecular Materials,* published by CRC Press, Taylor & Francis Group